# Complete experiment analysis and Bayesian inference in physics

Dissertation

zur

Erlangung des Doktorgrades (Dr. rer. nat.)

der

Mathematisch-Naturwissenschaftlichen Fakultät

der

Rheinischen Friedrich-Wilhelms-Universität Bonn

vorgelegt von

Philipp Krönert

aus

Mainz

Bonn, September 2025

Angefertigt mit Genehmigung der Mathematisch-Naturwissenschaftlichen Fakultät
der Rheinischen Friedrich-Wilhelms-Universität Bonn

Gutachter/Betreuer: Prof. Dr. Reinhard Beck
Gutachterin: Prof. Dr. Annika Thiel

Tag der Promotion: 17.12.2025
Erscheinungsjahr: 2026

# Dedication

This dissertation is dedicated to my parents, Loni and Prof. Dr. Uwe Krönert. You always support me throughout my journey, I thank you so much.

**Haiku | Doctoral thesis**

Ideas and discussions,
reading and writing papers,
talks and conferences.

# Abstract

This thesis consists of three parts. The first part is concerned with complete experiment analysis. This is a theoretical topic within the field of Baryon spectroscopy and deals with the question of how many and which polarization observables have to be measured in order to un-ambiguously determine the underlying physical parameters of the hadronic reaction under consideration. The theorem of Moravcsik, which is based on graph theory and combinatorial methods, is applied to multiple reactions including two-pseudoscalar meson photoproduction, which is fully described by eight complex spin-amplitudes. This yields complete sets of observables, which are further reduced via numerical methods to contain only the minimal, required number of observables. The approach is appealing because the whole process can be automated, parallelized and is applicable to reactions with an arbitrary number of complex spin-amplitudes. The studies resulted in two papers, Ref. [Wunderlich et al., 2020] and Ref. [Kroenert et al., 2021], published in the journal Physical Review C.

The second part of this thesis falls likewise into the domain of Baryon spectroscopy. The application of truncated partial-wave analysis on $\eta$-photoproduction data ($\sigma_0$, $\Sigma$, $T$, $E$, $F$ and $G$) near the production threshold ($E_\gamma^{\text{lab}}$ from 750 MeV to 1250 MeV) is studied. The results of the analysis are model-independent estimates of the electromagnetic multipole parameters and predictions for not yet measured polarization observables. For the first time, truncated partial-wave analysis and Bayesian inference are combined, resulting in parameter distributions instead of point estimates and accurate error estimates for the model parameters and predictions. The application of Bayesian inference is of interest, because it is a complementary analysis approach to the Frequentist method and the interpretation of the results differ. Furthermore, through the usage of Hamiltonian Monte Carlo, which is a special method of Markov chain Monte Carlo, the structure of arising solutions, i.e. the so-called ambiguities, can be studied. The results were published in Physical Review C [Kroenert et al., 2024].

The third part of this thesis falls into the domain of Neutrino mass analysis. It is connected to the second part of the thesis in the sense that the knowledge obtained about Bayesian inference is applied to a different analysis. Hence, Bayesian inference is used to analyze the first five measurement campaigns of the Karlsruhe Tritium Neutrino experiment, i.e. KNM1, KNM2, KNM3-SAP, KNM3-NAP, KNM4-NOM, KNM4-OPT and KNM5. The analysis are performed on Asimov data as well as for the measured data. Two approaches are taken, on the one hand each of the campaigns is analyzed on an individual basis. On the other hand, a so-called chained analysis of the campaigns is performed via multiple Bayesian knowledge updates. In this method, certain marginal parameter distributions of a former fit are used as prior information for the next fit. In addition, a sensitivity analysis is performed using different priors for the squared neutrino mass. However, in order to not delay the publication of this thesis, only the results on Asimov data are shown within this thesis. A paper containing the results on measurement data and further analyses is to be published in the near future.

# Contents

# Acknowledgement

First and foremost, I would like to express my deepest gratitude to Prof. Dr. Annika Thiel for providing me the opportunity to write a doctor thesis under her excellent supervision. It was a pleasure to work together! In particular, I would like to thank Prof. Dr. Reinhard Beck for providing the financing of my doctoral position. Furthermore, I thank Priv. Doz. Dr. Bastian Kubis and Prof. Dr. Jürgen Dölz for their participation in the doctoral committee.

The working atmosphere in the group was very pleasant and thus a joy to work here. For a lot of nice conversations and the delightful teamwork I would like to thank Dr. Peter Klassen, Dr. Christian Honisch, Dr. Dennis Sauerland, Leonidas Reschke, Florian Taubert, Nadia Reinartz, Shania Müller, Peter Rosinsky and Sebastian Ciupka.

In addition, I would like to thank Dr. Marcus Grüner und Dr. Michael Lang for their general helpfulness and the nice conversations at lunch.

A special thank goes to the coauthors of my published papers, Dr. Yannick Wunderlich, Dr. Farah Afzahl and Prof. Dr. Annika Thiel. The excellent teamwork in combination with the fruitful discussions motivated me for steady improvements on the papers.

In addition, I would like to thank the following people who have taken time for discussions: Prof. Dr. Ulrike Thoma, Prof. Dr. Sebastian Neubert, Prof. Dr. Carsten Urbach, Priv. Doz. Dr. Bernard Metsch, Dr. Maxim Mai and Dr. Jan Hartmann.

I would like to thank Dr. Markus Ball, Dr. Dimitri Schaab, Dr. Yevgen Bilevych, Richard Lagemann, Christoph Winter and Candas Tezel for welcoming me so kindly at the FTD.

Without the computational infrastructure provided by the HISKP-, BAF- and Marvin cluster group the Bayesian inference would not have been possible. Especially, I would like to thank Dr. Oliver Freyermuth and Dr. Michael Hübner for their excellent support.

I would like to thank Dr. Oliver Schulz, the creator and maintainer of BAT.jl, for helping to find software solutions which made the Bayesian inference of the KATRIN neutrino mass analysis (individual and chained analysis) possible.

Last but not least, I would like to thank Prof. Dr. Susanne Mertens for providing me the opportunity to participate on the KATRIN neutrino mass analysis within her working group. The atmosphere in the KATRIN collaboration is really something special, the collaboration meetings felt always like a family reunion. In particular, I would like to thank Dr. Christoph Wiesinger, Dr. Alexey Lokhov, Dr. Magnus Schlösser, Alessandro Schwemmer, Christoph Köhler and Jan Plößner for fruitful discussions and nice evenings at the collaboration meetings. A special thanks goes to Alessandro Schwemmer for his kind help with the onboarding into the KATRIN analysis and for patiently answering so many questions of mine.

# Chapter 1

# Introduction

Physics strives for the understanding of the universe. This ranges from small-scale processes, such as quark interactions and hadron formation, to large-scale phenomena, such as the formation of neutron stars and even galaxy clusters. These processes and related phenomena are the result of four fundamental forces: gravity, weak-, electromagnetic-, and strong interaction, in combination with elementary particles. Elementary particles are the fundamental building blocks of all matter and have specific characteristics so-called quantum numbers such as electric charge, spin and parity. From today's perspective, particles are excitations of specific quantum fields, behaving like waves that propagate through space and time.

The four fundamental forces allow elementary particles to interact with each other and more interestingly to form bound systems. This results in the formation of new, stable and non-stable particles. One prominent example is the proton which was discovered by Ernest Rutherford in 1919 [Rutherford, 2010]. Another one is the neutron, which was discovered by James Chadwick in 1932 [Chadwick, 1932] (awarded a Nobel Prize in Physics in 1935). These two particles, together with electrons, are the building blocks of all stable baryonic matter in the observable universe.

Protons and neutrons themselves consist of elementary particles known as quarks. In 1964, Murray Gell-Mann [Gell-Mann, 1964] and George Zweig [Zweig, 1964] independently proposed quarks as the building blocks of protons and neutrons. This fundamental theory was experimentally verified in 1969 at the Stanford Linear Accelerator Center [Bloom et al., 1969, Breidenbach et al., 1969] using deep inelastic scattering. This achievement was awarded with a Nobel Prize for Richard Taylor, Jerome Friedman, and Henry Kendall in the year 1990.

Today a plethora of such bound states are experimentally verified, each with its distinct characteristics, and even more are predicted. The study of these composite systems of elementary particles allows to improve our understanding of the fundamental forces which shape the world around us.

Apart from bound systems of particles, other fundamental particles are of interest as well. For example the neutrino, which was predicted by Wolfgang Pauli in 1930 [Pauli, 1978] to explain the continuous $\beta$-energy spectrum as was first mea-

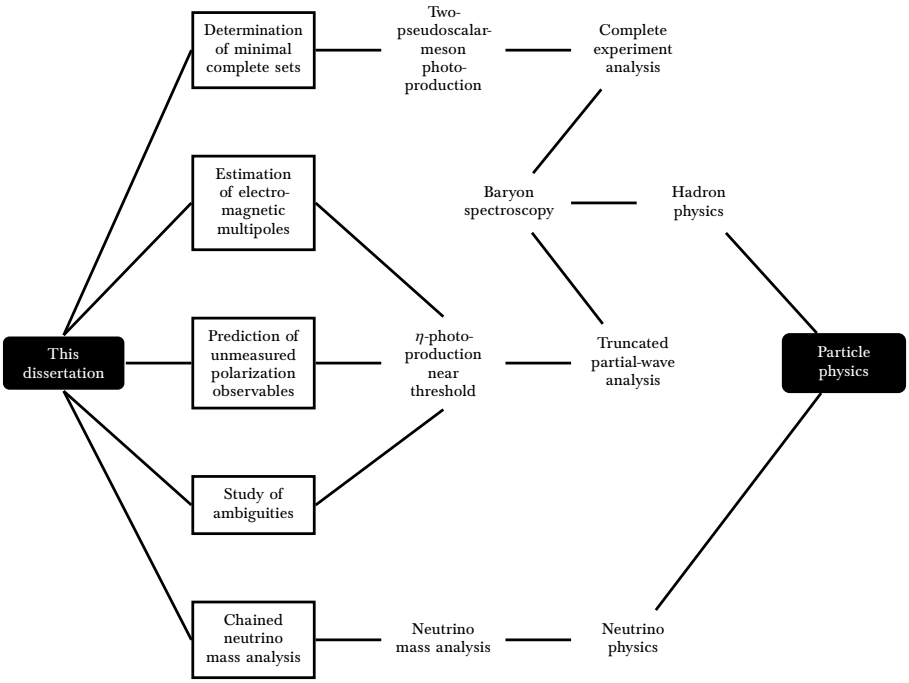


Figure 1.1: The position of this thesis in the context of particle physics is visualized. The main building blocks of this thesis are highlighted via a frame around their node.

sured by James Chadwick in 1914 [Chadwick, 1914]. The experimental verification of the neutrino was published in 1956 by Clyde Cowan and Frederick Reines et al., see Ref. [Cowan Jr et al., 1956], for which the Nobel Prize in Physics was awarded to Reines in 1995. The neutrino is of special interest, as it was first assumed to be massless and later confirmed to have a non-zero mass. However, in addition this mass is several orders of magnitude smaller than that of other fermions in the Standard Model of particle physics which might hint to physics beyond the Standard Model.

This thesis deals with bound states of quarks in the context of Baryon spectroscopy as well as with neutrino physics in the context of direct neutrino mass analysis. This includes in total three projects within these two different fields of physics. It therefore seems appropriate to visualize the position of this thesis within the larger context of particle physics and stress the connection between the two physical fields. The information is visible in Fig. 1.1.

This thesis is structured as follows: In Chapter 1, Section 1.1 the foundation for Baryon spectroscopy and the neutrino mass analysis is laid out by discussing the Standard Model of particle physics. Chapter 2 gives a general introduction to Bayesian inference, as this statistical method was heavily used in two of the three projects. In Part I of this thesis, the focus is on ambiguity analyses in Baryon spectroscopy, for which Chapter 3 gives a general introduction. Afterward, the published papers on complete experiment analysis and truncated partial wave

analysis are discussed in Chapters 4 and 5, respectively. In Part II of this thesis, the focus is on the neutrino mass analysis with KATRIN. Therefore, Chapter 6 gives a general introduction into the KATRIN experiment before in Chapter 7 the neutrino mass analysis with Bayesian inference is discussed. Finally, the thesis is summarized in Chapter 8.

## 1.1 The Standard Model of particle physics

The Standard Model (SM) of particle physics is a theoretical framework to describe and predict the phenomena within the subatomic world. It is formulated via quantum field theory (QFT) and enables the unification of the weak-, electromagnetic- and strong interaction within one framework. The gauge symmetry of the SM is written as [Thomson, 2013]:

$$\mathrm{SU}(3)_\mathrm{C} \times \mathrm{SU}(2)_\mathrm{L} \times \mathrm{U}(1)_\mathrm{Y}, \tag{1.1}$$

where $\mathrm{SU}(3)_\mathrm{C}$ corresponds to the local gauge group of the strong interaction, and $\mathrm{SU}(2)_\mathrm{L} \times \mathrm{U}(1)_\mathrm{Y}$ to the local gauge group of the electroweak interaction, which is a unification of the weak and electromagnetic interaction as proposed by Sheldon Lee Glashow, Abdus Salam and Steven Weinberg, who were awarded the Nobel Prize in Physics in 1979 [Coleman, 1979].

Gravity is usually disregarded in particle physics due to its relatively small strength in comparison to the other three interactions, i.e. it has no significant effects on the subatomic scale which can be observed [Halzen and Martin, 2008]. However, in order to describe all physical phenomena within one theoretical model, different approaches for a possible unification of gravity and the QFT of the SM are currently under investigation, in a research field called quantum gravity [Kiefer, 2012].

The Standard Model includes twelve fermionic, i.e. spin-1/2, particles consisting of six leptons and six quarks. These particles are all fundamental in the sense that they do not consist of further building blocks, just matter/energy. An overview is given in Table 1.1. In the original version of the SM the neutrinos are massless. However, later experiments, like Super-Kamiokande [Hosaka et al., 2006] and the Sudbury Neutrino Observatory [Ahmad et al., 2001] indicate massive neutrinos. Therefore, the present neutrino mass limits are shown in the table as well. This topic will be discussed in detail in Chapter 6.

The equations of motion for relativistic fermions within quantum mechanics are described by the Dirac equation. However, for each positive energy solution one with negative energy has to exist due to mathematical reasons. These are interpreted as particles and antiparticles, respectively. The existence of a corresponding antiparticle for each of the twelve particles in Table 1.1 has been experimentally verified. Antiparticles do possess the identical mass and spin and take part in the same interactions as their counterpart, but have opposite charge quantum numbers, such as electric- and color charge as well as the weak isospin.

This is of particular importance, as the quantum numbers of a particle define the types of possible interactions it can participate in. For example, all twelve fermionic particles of the SM (and the corresponding antiparticles) can interact

Table 1.1: This table lists several quantum numbers for the twelve fundamental fermions of the Standard Model of particle physics, i.e. six leptons and six quarks. The corresponding antiparticles are absent from the table. The specific values are taken from the Review of Particle Physics [Navas et al., 2024].

| **Name** | **Symbol** | **Mass in** (MeV / $c^2$) | **Electric charge** | **Color charge** | **Weak isospin** |
|---|---|---|---|---|---|
| | | Leptons | | | |
| Electron | $e^-$ | $\sim 0.511$ | -1 | no | $-1/2$ |
| Muon | $\mu^-$ | $\sim 105.658$ | -1 | no | $-1/2$ |
| Tau | $\tau^-$ | $\sim 1776.93$ | -1 | no | $-1/2$ |
| Electron neutrino | $\nu_e$ | $< 0.8 \times 10^{-6}$ | 0 | no | $+1/2$ |
| Muon neutrino | $\nu_\mu$ | $< 0.19$ | 0 | no | $+1/2$ |
| Tau neutrino | $\nu_\tau$ | $< 18.2$ | 0 | no | $+1/2$ |
| | | Quarks | | | |
| Up | u | $\sim 2.16$ | $+2/3$ | r,g,b | $+1/2$ |
| Down | d | $\sim 4.70$ | $-1/3$ | r,g,b | $-1/2$ |
| Strange | s | $\sim 93.5$ | $-1/3$ | r,g,b | $-1/2$ |
| Charm | c | $\sim 1.27 \times 10^3$ | $+2/3$ | r,g,b | $+1/2$ |
| Bottom | b | $\sim 4.18 \times 10^3$ | $-1/3$ | r,g,b | $-1/2$ |
| Top | t | $\sim 172.57 \times 10^3$ | $+2/3$ | r,g,b | $+1/2$ |

through the weak interaction, due to their non-zero weak isospin quantum number. On the other hand, out of the twelve fundamental fermions only quarks participate in the strong interaction, as they carrying a non-zero color charge. Similar, only the fermions with a non-zero electric charge quantum number interact via the electromagnetic interaction, see Table 1.1.

However, not every interaction between particles is possible. Certain conservation laws must be fulfilled, i.e. the value of a certain quantity before the interaction has to be the same after the interaction. Furthermore, certain conservation laws differ for the different types of interactions, an overview is given in Table 1.2. In general, any operator that commutes with the Hamiltonian under consideration corresponds to a conserved quantity, arising from underlying symmetries.

The interactions between fundamental particles are mediated via the exchange of so-called gauge bosons. Each type of interaction has its own gauge boson(s), which are listed in Table 1.3. The table includes two more entries, one for the Higgs boson and one for the hypothetical exchange particle of gravity, also known as the graviton.

The elementary fermionic particles/antiparticles, as well as the gauge bosons, acquire their masses via a coupling to the Higgs field $\phi$ mediated by the Higgs boson. The theoretical description is given by the Brout-Englert-Higgs (BEH) mechanism [Englert and Brout, 1964, Higgs, 1964]. In the simplest possible case, the Higgs field is a weak isospin douplet of two complex scalar fields $\phi^+$ and $\phi^0$

Table 1.2: Conserved quantities within the different types of interactions. A conserved quantity is indicated with the symbol ✓ and otherwise with the symbol ×. The energy, momentum, angular momentum, electric charge, color charge, lepton number, baryon number, and CPT are conserved in all three interactions, and therefore not explicitly listed in the table. The listing includes: the charge parity C, the parity P, time reversal T, the combination of charge parity and parity CP, the isospin I and in general the flavor quantum numbers fqn (charm, strangeness, third component of isospin, etc.). Information taken from [Povh et al., 1995].

| **Interaction** | **C** | **P** | **T** | **CP** | **I** | **fqn** |
|---|---|---|---|---|---|---|
| Strong | ✓ | ✓ | ✓ | ✓ | ✓ | ✓ |
| Electromagnetic | ✓ | ✓ | ✓ | ✓ | × | ✓ |
| Weak | × | × | × | × | × | × |

Table 1.3: This table includes the force-carrier particles, i.e. the gauge bosons of the Standard Model of particle physics. These gauge bosons mediate the interactions between elementary particles and thus are of fundamental importance. In addition, the Higgs boson and the hypothetical force carrier of gravity is shown. The specific values are taken from the Review of Particle Physics [Navas et al., 2024].

| **Interaction** | **Name** | **Symbol** | **Mass in** (GeV / $c^2$) | **Spin** | **Electric charge** | **Color charge** |
|---|---|---|---|---|---|---|
| Gauge bosons | | | | | | |
| Electromagnetic | Photon | $\gamma$ | $< 10^{-27}$ | 1 | 0 | no |
| Strong | Gluon | $g$ | 0 | 1 | 0 | r,g,b |
| Weak | W$^{\pm}$-Bosons | $W^{\pm}$ | $\sim 80.369$ | 1 | $\pm 1$ | no |
| Weak | Z-Boson | $Z^0$ | $\sim 91.188$ | 1 | 0 | no |
| Gravity | Graviton | $G$ | $< 1.76 \times 10^{-32}$ | 2 | 0 | no |
| / | Higgs boson | $H$ | $\sim 125.20$ | 0 | 0 | no |

[Workman et al., 2022, Thomson, 2013] forming the SM Higgs potential:

$$\phi := \begin{pmatrix} \phi^+ \\ \phi^0 \end{pmatrix}, \qquad V(\phi) := \mu^2 \phi^\dagger \phi + \lambda \left(\phi^\dagger \phi\right)^2. \tag{1.2}$$

If $\mu^2 < 0$ then the vacuum expectation value $v$ of the neutral, complex scalar field $\phi^0$ of the Higgs field is non-zero:

$$\langle 0|\phi|0\rangle = \frac{1}{\sqrt{2}} \begin{pmatrix} 0 \\ v \end{pmatrix}, \qquad \text{with} \qquad v^2 = \frac{-\mu^2}{\lambda}. \tag{1.3}$$

This results in an infinite set of degenerate minima for the Higgs potential, thus breaking the symmetry of the Lagrangian - a phenomenon known as spontaneous symmetry breaking. The Higgs mechanism is embedded in the $SU(2)_L \times U(1)_Y$ gauge symmetry of the electroweak interaction such that the aforementioned spontaneous symmetry breaking is generating the masses of the $W^{\pm}$ and $Z$ bosons.

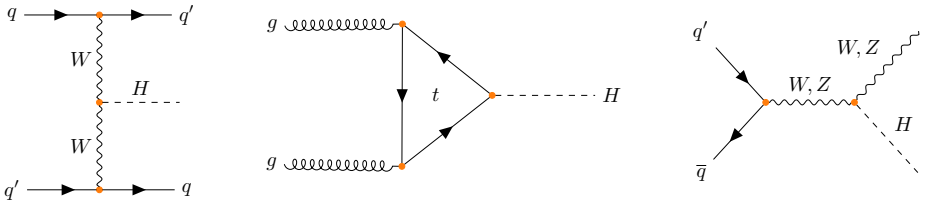


Figure 1.2: Example processes for Higgs boson production. Each graph was redrawn from [Thomson, 2013, Workman et al., 2022].

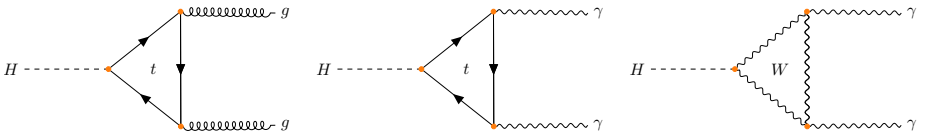


Figure 1.3: Examples processes for a Higgs boson decay. Each graph was redrawn from [Thomson, 2013].

The $W$ and $Z$ boson masses are proportional to $v$ and the gauge couplings $g_W$ and $g'$ of $SU(2)_L$ and $U(1)_Y$, respectively, whereas the mass of the photon is zero:

$$m_W = \frac{1}{2} g_W v, \qquad m_Z = \frac{1}{2} v \sqrt{g_W^2 + g'^2}, \qquad m_\gamma = 0. \tag{1.4}$$

In contrast, the elementary fermions gain mass $m_f$ via a Yukawa coupling $g_f$ to the Higgs field:

$$m_f = \frac{1}{\sqrt{2}} g_f v. \tag{1.5}$$

Thus, the masses of the gauge bosons and the elementary fermions only depend on four quantities ($v$, $g_W$, $g'$ and $g_f$), i.e. the vacuum expectation value of the Higgs field, the gauge coupling of $\mathrm{SU(2)_L}$ as well as $\mathrm{U(1)_Y}$ and the strength of the Yukawa coupling.

Furthermore, the spontaneous symmetry breaking leads to an excitation of the Higgs field $\phi$ in the form of a scalar boson called Higgs boson $H$. This particle was first proposed by Peter Higgs in 1964 [Higgs, 1964]. Its mass is given by [Thomson, 2013]:

$$m_H^2 = 2\lambda v^2. \tag{1.6}$$

The existence of this Higgs boson, and thereby the experimental verification of the BEH mechanism, was achieved in 2012 at the Large Hadron Collider at CERN [ATLAS-Collaboration et al., 2012, CMS-Collaboration et al., 2012]. Example processes for the production and decay of a Higgs boson are shown in Fig. 1.2 and Fig. 1.3, respectively. The current value for its mass was measured to be [Navas et al., 2024]:

$$m_H = (125.20 \pm 0.11)\ \mathrm{GeV}. \tag{1.7}$$

Furthermore, from the measured values of $m_W$ and $g_W$ [Thomson, 2013]:

$$g_W^2 = \frac{8 m_W^2 G_F}{\sqrt{2}}, \tag{1.8}$$

with the Fermi coupling constant [Navas et al., 2024]:

$$G_F = (1.166\,378\,8 \pm 0.000\,000\,6) \times 10^{-5}\,\mathrm{GeV}^{-2}, \tag{1.9}$$

the vacuum expectation value of the Higgs field can be calculated to be about [Thomson, 2013, Navas et al., 2024]:

$$v \approx 246\,\mathrm{GeV}. \tag{1.10}$$

All elementary particles/antiparticles couple to the Higgs field, via the Higgs boson and thereby acquire their mass. However, the neutrino masses are several magnitudes smaller than those of the other elementary particles, and it is not clear whether the neutrino masses are generated via a coupling to the Higgs field or some other kind of mechanism, like the seesaw mechanism [Thomson, 2013].

François Englert and Peter Higgs were awarded the Nobel Prize in Physics 2013 for their contribution to the BEH mechanism.

### 1.1.1 Bound states of quarks

To the present day, there is no experimental evidence for freely propagating quarks [Navas et al., 2024]. Rather, quarks are observed only indirectly, as parts of a bound system of multiple quarks. Within the SM, this observation is explained via the so-called color confinement and is assumed to originate from the self interaction of the gluons [Thomson, 2013]. The concept of color confinement states that freely propagating particles have to be color-neutral objects. To discuss this topic in more detail and its influence on the theoretically allowed bound states of quarks, it is convenient to introduce the color hypercharge $Y^c$ and the third component of the color isospin $I_3^c$ defined as follows:

$$Y^c := \frac{\lambda_8}{\sqrt{3}} \qquad \text{and} \qquad I_3^c := \frac{\lambda_3}{2}, \tag{1.11}$$

where $\lambda_3$ and $\lambda_8$ are the diagonal and thus commuting Gell-Mann matrices. The set of all eight Gell-Mann matrices are the generators of the $SU(3)_C$ symmetry group [Thomson, 2013]. The color charge of quarks can have three possible states (r, g, b), while the antiquarks have the corresponding anti-color charges ($\bar{\mathrm{r}}$, $\bar{\mathrm{g}}$, $\bar{\mathrm{b}}$), see Table 1.1. This can be visualized in the $Y^c$-$I_3^c$ plane, see Fig. 1.4.

Following the assumption of color confinement, bound states of quarks, also called hadronic states, can exist as freely propagating states if and only if they are color-neutral states. Hence, the color quantum numbers of such a state must be $I_3^c = Y^c = 0$. In addition, the application of one of the six color ladder operators (a definition in terms of Gell-Mann matrices can be found in Ref. [Halzen and Martin, 2008, Thomson, 2013]) onto the hadron color wavefunction must result in a value of zero. In other words, any freely propagating hadronic state has to be a color-singlet state [Thomson, 2013]. For example, considering all possible combinations of a color and an anticolor state, one gets eight colored states, a so-called colored octet, and one color neutral state, a so-called color-neutral singlet state, which can be written in short: $3 \otimes \bar{3} = 8 \oplus 1$. Combining three colored states, i.e. $3 \otimes 3 \otimes 3 = 10 \oplus 8 \oplus 8 \oplus 1$, gives also one color-neutral state. Such considerations can also be made for other combinations of quarks and/or antiquarks. The

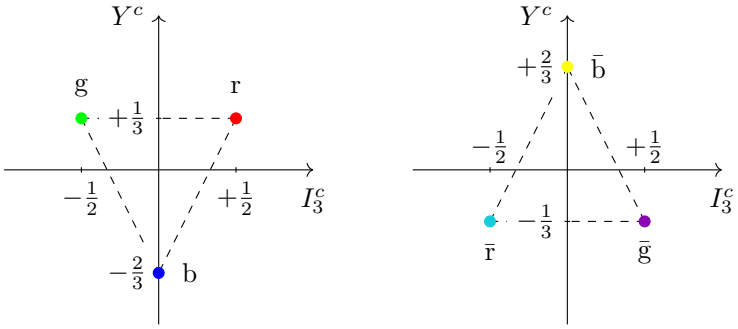


Figure 1.4: Shown are the three possible color states for quarks (r, g, b) as well as for antiquarks ($\bar{\text{r}}$, $\bar{\text{g}}$, $\bar{\text{b}}$). The definition of the color hypercharge $Y^c$ and the third component of the color isospin $I_3^c$ can be found in Eq. (1.11). Redrawn from [Thomson, 2013].

theoretically allowed combinations resulting in a color-neutral singlet state are [Gell-Mann, 1964, Thomson, 2013]:

$$\text{Mesons:} \quad |q\bar{q}\rangle\,, \tag{1.12}$$

$$\text{Baryons:} \quad |qqq\rangle\,, |\bar{q}\bar{q}\bar{q}\rangle\,, \tag{1.13}$$

$$\text{Exotics:} \quad |qq\bar{q}\bar{q}\rangle\,, |qqqq\bar{q}\rangle\,, |gg\rangle\,, |ggg\rangle\,, \text{etc.} \tag{1.14}$$

Bound states consisting of a quark-antiquark pair are called mesons while bound states made up of three quarks are called baryons. The existence of baryons and mesons are experimentally well established, see for example the 'Summary Tables' from the Review of Particle Physics [Navas et al., 2024].

However, it should be noted that the internal structure of a color neutral bound state is more complex than just consisting of multiple quarks. As an example, the proton consists of three quarks $|uud\rangle$, so-called valence quarks, which are directly responsible for the quantum numbers of the proton. The valence quarks can interact with each other by the exchange of virtual gluons which can then produce virtual quark-antiquark pairs [Thomson, 2013]. Because this happens quite often, a 'sea' of virtual quarks and antiquarks emerges, which are called sea quarks for short. These sea quarks together with the gluons contribute majorly to the momentum and the mass of the bound state. For the proton, nearly 50% of the momentum is carried by the virtual gluons [Thomson, 2013], as can be experimentally verified by measuring parton distribution functions via deep inelastic scattering.

In analogy to the color multiplets shown in Fig. 1.4, there is a compact visualization for the meson and baryon states. This time, the plane is spanned by the hypercharge $Y$, defined as the sum of the baryon- ($B$) and strangeness ($S$) quantum numbers, and the third component of the strong isospin ($I_3$). As an example, the meson and baryon states formed from the three lightest quarks (u,d,s) are shown in Fig. 1.5 and Fig. 1.6, respectively. In general, bound states with components of (u,d,s,c,b)-quarks can be formed, whereas states with t-quarks are very unlikely as the mean lifetime of a top-quark, i.e. $\tau \sim 0.5 \times 10^{-24}$ s, is believed to be too short to form a bound state [Navas et al., 2024].

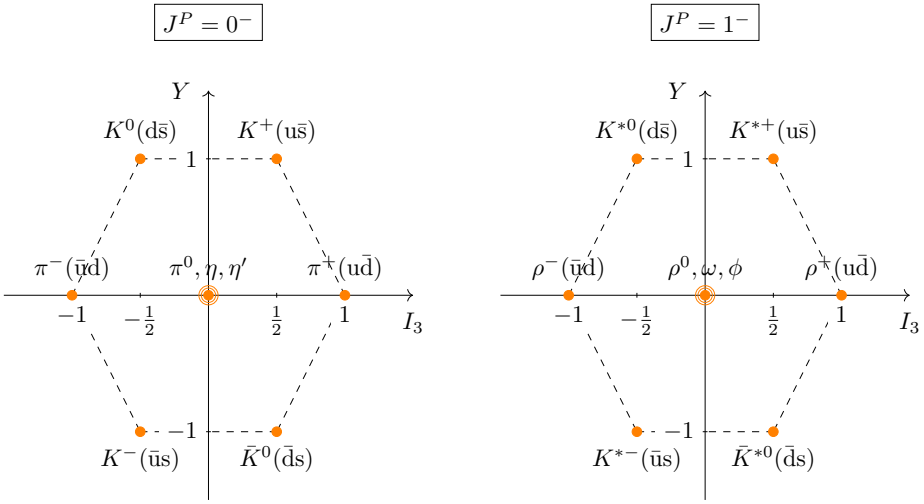


Figure 1.5: Meson ground states formed from the three lightest quarks (u,d,s). Left: Pseudoscalar meson nonet. Right: Vector meson nonet. The vertical axis shows the sum of the baryon- and strangeness quantum numbers $Y = B + S$, where the horizontal axis shows the third component of the strong isospin quantum number $I_3$. Note: $\pi^0$, $\eta$, $\eta'$, $\rho^0$, $\omega$ and $\phi$ are linear combinations of the quark states $|u\bar{u}\rangle$, $|d\bar{d}\rangle$ and $|s\bar{s}\rangle$. Redrawn from [Thomson, 2013].

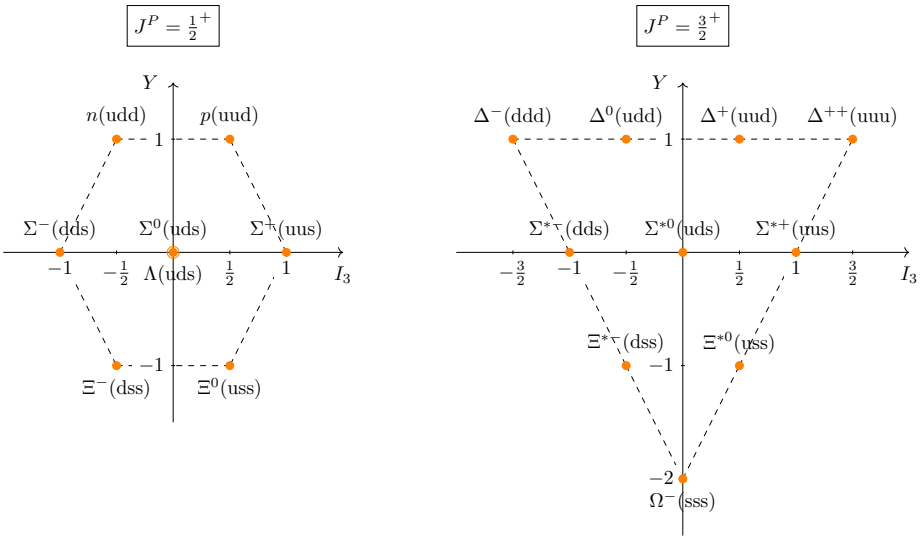


Figure 1.6: Baryon ground states formed from the three lightest quarks (u,d,s). Left: Baryon octet. Right: Baryon decuplet. The vertical axis shows the sum of the baryon- and strangeness quantum numbers $Y = B + S$, where the horizontal axis shows the third component of the strong isospin quantum number $I_3$. Redrawn from [Thomson, 2013].

In addition, the SM allows for more types of bound states with more than three quarks and/or antiquarks (tetraquark: $|q\bar{q}q\bar{q}\rangle$, pentaquark: $|q\bar{q}q\bar{q}q\rangle$) or states solely consisting of gluons (glueballs). Such exotic states are of particular research interest, as their existence could further confirm the SM or their non-existence could provide hints for physics beyond the SM. An important step in establishing the existence of exotic quark-states was the discovery of three tetraquark states $X(4274)$, $X(4500)$ and $X(4700)$ [Aaij et al., 2017] and two pentaquark states $P_c(4380)^+$ and $P_c(4450)^+$ [Aaij et al., 2015] by the LHCb collaboration.

# Chapter 2

# Bayesian inference

This chapter is structured as follows: It starts with a general introduction and motivation of Bayesian inference in Section 2.1 before moving on to the mathematical definition and an illustration of Bayes' theorem in Section 2.2. Afterward, in Section 2.3 the concept of a marginal distribution is explained and intuition for it is developed. In Section 2.4 the need for efficient and reliable numerical integration methods is discussed in order to calculate the marginal parameter distributions. Associated with this, the Markov chain Monte Carlo convergence diagnostics are discussed in detail in Section 2.5. In Section 2.6 posterior predictive checks re discussed, which are a form of model assessment in the Bayesian context.

## 2.1 Introduction

Bayesian inference (BI) is an approach to estimate the parameters of a statistical model on the basis of data. In addition to the data points, the model parameters themselves have an underlying probability distribution. This is a key difference to the well known method of maximum likelihood estimation (MLE) and is expressed in the presence of an additional term alongside the likelihood distribution, the so-called prior distribution. The likelihood distribution together with the prior distribution and a normalization factor define the posterior density, which holds all information about the problem at hand.

From the posterior density one can estimate the most likely model parameters. For example, equivalent to the MLE approach by calculating the parameter values that maximize the posterior via differentiation techniques, which is called maximum a posteriori estimation (MAP). This would result in point estimates which could be paired with additional error estimates, for example via the Hesse matrix or Monte Carlo methods.

However, in BI one is interested in the marginal distributions of the parameters. These are derived by integrating the posterior density. Hence, the results are given as distributions themselves, error estimates included.

Furthermore, BI offers an interpretation distinct from MLE with respect to the most likely parameter values. In MLE, the most likely parameter values are those

which maximize the likelihood distribution. Whereas, the marginal distribution for a specific parameter includes all of its possible values, in consideration of the possible values for all other parameters.

## 2.2 Bayes' theorem

Suppose one has measured some data $y$ and would like to extract further information from this data by employing a suitable model with parameters $\Theta$. Bayes' theorem allows for this in a unique way by treating data and parameters as probability distributions. The theorem itself reads [Bayes, 1763, Gelman et al., 2013]:

$$p(\Theta \mid y) := \frac{p(y \mid \Theta)\, p(\Theta)}{\int p(y \mid \Theta)\, p(\Theta)\, d\Theta}. \tag{2.1}$$

The equation consists of three major quantities: On the left-hand side, the posterior density $p(\Theta \mid y)$ represents the probability for the model parameters given the observed data points. From this expression the most likely model parameters are calculated, as it contains all the knowledge about the model and the data. On the right-hand side of the equation, the likelihood distribution, denoted by $p(y \mid \Theta)$, represents the probability for the observed data points given the model parameters. This component is identical between MLE and BI. Furthermore, the prior distribution $p(\Theta)$ represents the probability of the model parameters, before the actual data are taken into account. This is especially convenient for constraining the physical allowed regions of parameters or the modeling of their systematic uncertainties. The denominator in Eq. (2.1) plays the role of a normalization factor, such that the posterior is indeed a probability distribution. However, for estimating the model parameters, the normalization factor can be disregarded, as it is constant for fixed $y$:

$$p(\Theta \mid y) \propto p(y \mid \Theta)\, p(\Theta). \tag{2.2}$$

The interplay between likelihood distribution and prior distribution in forming the posterior is illustrated in Fig. 2.1. In general, the form of the posterior depends on the choice of the prior. Hence, the prior distribution is a powerful tool and has to be handled with care. In this thesis, conservative prior distributions are used, so that the likelihood distribution with the data points bring in by far the most amount of information into the statistical model. By doing this, one ensures that the final results are not dependent on the prior.

## 2.3 Marginal parameter distributions

In BI the most likely parameter values of a model, given the data, are extracted from the posterior by integrating over all but the parameter of interest. The result is called a marginal distribution. For an illustrative example consider a posterior density only dependent on two parameters $\theta_1$ and $\theta_2$:

$$p(\Theta_1, \Theta_2 \mid y). \tag{2.3}$$

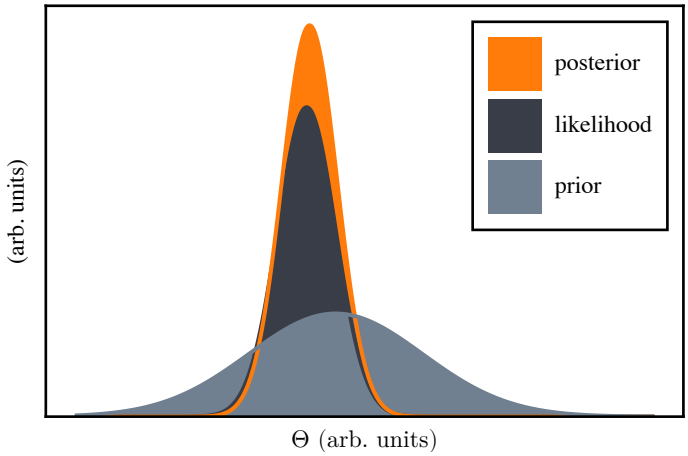


Figure 2.1: Illustration of a posterior distribution, emphasizing the combination of likelihood- and prior distribution. For this example, the posterior only depends on one parameter $\Theta$.

The marginal parameter distributions of Eq. (2.3) for $\Theta_1$ and $\Theta_2$ are defined as:

$$p(\Theta_1 \mid y) = \int p(\Theta_1, \Theta_2 \mid y)\, d\Theta_2\,, \tag{2.4}$$

$$p(\Theta_2 \mid y) = \int p(\Theta_1, \Theta_2 \mid y)\, d\Theta_1\,. \tag{2.5}$$

From these distributions, one can extract the characteristics of interest, such as: mean, median, quantile values and credible intervals, as well as the correlation between the parameters. Examples for marginal parameter distributions are shown in Fig. 2.2. The figure depicts the building up of marginal distributions with an increasing number of sampling points used to perform the integration.

## 2.4 Markov chain Monte Carlo

As explained in Section 2.3, the goal of BI is the calculation of marginal parameter distributions. In academic scenarios the integration can be done analytically, but for complex, higher-dimensional problems this becomes unfeasible. Instead, one has to rely on numerical integration.

For multivariate integrals with only a few number of variables Gaussian quadrature can be applied via a grid technique. However, for high-dimensional posteriors, as encountered within this thesis, Gaussian quadrature becomes rather quickly inefficient in terms of computation time.

Instead, stochastic methods are used to approximate the multidimensional integrals. This is a valid approach, because of the existence of a Monte Carlo central limit theorem [Geyer, 2005] and a Markov chain Monte Carlo (MCMC) central limit theorem, discussed in detail in Section 2.5.1, respectively. The term Markov chain denotes a sequence of random elements $X_1, \ldots, X_N$ when the conditional

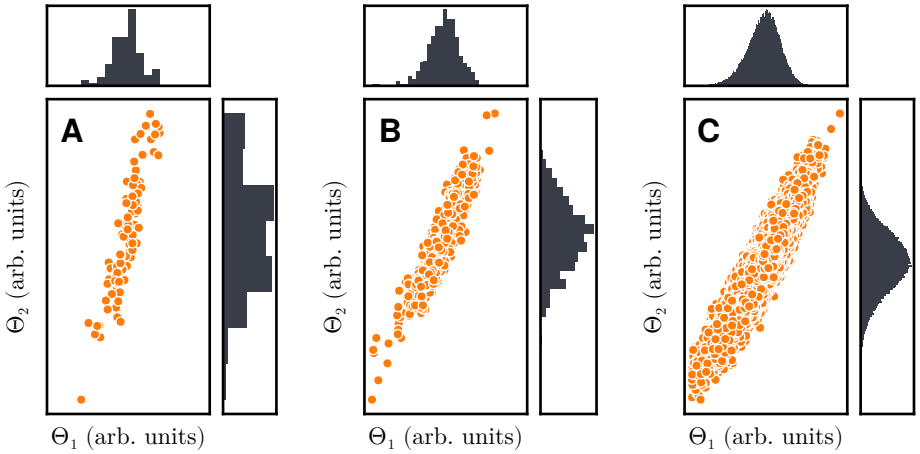


Figure 2.2: Illustration how the marginal parameter distributions are generated via the Markov chain Monte Carlo method. The posterior is assumed to have two parameters $\Theta_1$ and $\Theta_2$. The corresponding marginal parameter distributions are shown on the top and right side of each subplot. The subplots A, B and C show the first $[10^2, 10^3, 10^5]$ sampling points, respectively.

distribution of $X_k$ only depends on $X_{k-1}$ [Geyer, 2011]. However, the simplest stochastic method is ordinary Monte Carlo [Geyer, 2011]. The general procedure is to evaluate the posterior distribution at random parameter values and thus calculating the marginal parameter distributions automatically. With increasing number of samples, the marginal distributions build up and become more pronounced. An example for different stages of such a stochastic process is shown in Fig. 2.2 for $[10^2, 10^3, 10^5]$ sampling points.

The efficiency of this approach depends on the mechanism to select parameter values at which the posterior should be evaluated. Advanced methods use some form of guidance within the posterior distribution in combination with MCMC. This increases performance while retaining the stochastic properties of a central limit theorem. Within this thesis, the Hamiltonian Monte Carlo algorithm is used, which is a special MCMC method. In order to provide guidance for the MCMC chain, Hamiltonian dynamics is employed to propose new sampling points. In this way, the structure of the posterior distribution is taken into account via gradient information. This gives an advantage in performance in contrast to the random-walk Metropolis methods [Neal, 2011], especially for higher dimensional problems.

In general, the Hamiltonian $H(q, p)$ depends on the $n$-dimensional position and momentum vectors of the particles, $q$ and $p$, respectively. The Hamiltonian equations of motion are a set of differential equations, given by [Neal, 2011]:

$$\frac{\mathrm{d}q_i}{\mathrm{d}t} = \frac{\partial H(q_i, p_i)}{\partial p_i}, \qquad \frac{\mathrm{d}p_i}{\mathrm{d}t} = -\frac{\partial H(q_i, p_i)}{\partial q_i}, \tag{2.6}$$

for all $i$ from 1 to $n$. The parameters $\Theta$ of the model take the role of the position vector $q$, while for the momentum vector $p$, additional nuisance parameters $\phi$ are

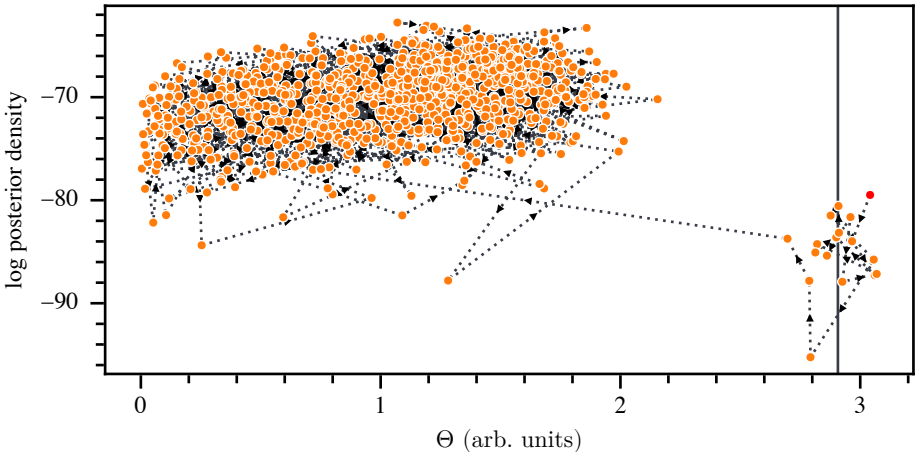


Figure 2.3: Illustration of the start and quick adaptation of a MCMC chain. Shown are the first $10^3$ sampling points, the color of the very first sampling point, at a value of $\Theta \approx 3.041$, is red. The order of sampling points is indicated via arrows. The black vertical line corresponds to the initial value of the MCMC chain.

introduced. This transforms the posterior distribution to [Gelman et al., 2013]:

$$\mathrm{p}(\Theta \mid y) \longmapsto \mathrm{p}(\Theta, \phi \mid y) = \mathrm{p}(\Theta \mid y)\, \mathrm{p}(\phi), \tag{2.7}$$

where typically $\mathrm{p}(\phi)$ is modeled as a multivariate standard normal distribution [Gelman et al., 2013]. The Hamiltonian $H(\Theta, \phi)$ is defined as the negative log posterior density:

$$H(\Theta, \phi) := -\log\big(\mathrm{p}(\Theta, \phi \mid y)\big) = -\log\big(\mathrm{p}(\Theta \mid y)\big) - \log\big(\mathrm{p}(\phi)\big). \tag{2.8}$$

In analogy to Hamiltonian dynamics, the term $-\log\big(\mathrm{p}(\phi)\big)$ is called the kinetic energy and $-\log\big(\mathrm{p}(\Theta \mid y)\big)$ the potential energy. To propose a new sampling point for MCMC, the Hamiltonian equations of motion Eq. (2.6) are solved via the Leapfrog method [Geyer, 2011], resulting in the proposals $(\Theta', \phi')$. This new sampling point is accepted with probability [Neal, 2011]:

$$\min(1, \exp[-H(\Theta', \phi') + H(\Theta, \phi)]). \tag{2.9}$$

As an example for the quick adaption of an MCMC chain, guided via HMC from low to high probability mass regions, is shown in Fig. 2.3.

## 2.5 Markov chain Monte Carlo convergence diagnostics

MCMC is inherently a stochastic method. As such, the question arises how many sampling points are necessary for a trustworthy result. To start off with, this is a non-trivial task and much more complex than for MLE or MAP.

Assuming a single MCMC chain, the marginal distributions start to be reliable, as

soon as the number of samples $N$ is high enough so that the MCMC central limit theorem holds, at which point the MCMC chain is said to have converged. To improve the monitoring of convergence, multiple MCMC chains should be started [Gelman et al., 2013] with different starting points in the parameter space. The idea is to check if all chains, at some point in time, have seen the same parameter space, i.e. the same regions of the posterior.

Multiple MCMC convergence diagnostics do exist, from simple trace plots, to more advanced methods, like the MCMC standard error (MCMCSE) or the potential scale reduction statistic $\widehat{R}$, which shall be discussed in the following. It is good practice to look at different methods to monitor the overall convergence of the sampling.

### 2.5.1 Markov chain Monte Carlo standard error

As the MCMCSE convergence diagnostic is closely related to the MCMC central limit theorem, the theorem shall be first derived and discussed. In order to develop an intuition for the MCMCSE, it is helpful to establish a link with the well-known Monte Carlo standard error (MCSE) [Geyer, 2011] of a sample $S$.

For this purpose, supposing one is interested in the expectation value of a real-valued function $g$, which depends on a random variable $X$:

$$\mu := \mathbb{E}[g(X)]. \tag{2.10}$$

Supposing furthermore, that $g(X)$ is of such a form that Eq. (2.10) can not be computed analytically. Instead, the function $g(X)$ can be approximated by drawing samples $S = g(X_1), \ldots, g(X_N)$, from which the quantity of interest can be calculated. For instance, one can estimate the expectation and variance of $g(X)$ via:

$$\hat{\mu} := \hat{\mathbb{E}}[g(X)] = \frac{1}{N}\sum_{i=1}^{N} g(X_i), \tag{2.11}$$

$$\hat{\sigma}^2 := \widehat{\mathrm{Var}}(g(X)) = \frac{1}{N}\sum_{i=1}^{N} \left(g(X_i) - \hat{\mu}\right)^2. \tag{2.12}$$

Naturally one is interested in the variance of the estimated expectation value which is given by Bienaymé's identity [Geyer, 2005]:

$$\mathrm{Var}(\hat{\mu}) = \frac{1}{N^2}\sum_{i=1}^{N}\sum_{j=1}^{N} \mathrm{Cov}(g(X_i), g(X_j)). \tag{2.13}$$

In general, the MCSE of the mean is defined as [Geyer, 2011]:

$$\mathrm{MCSE}_{\mathrm{mean}} := \sqrt{\mathrm{Var}(\hat{\mu})}. \tag{2.14}$$

The specific form of Eq. (2.14) shall be derived for the case of independent- and dependent identically distributed samples, respectively.

### Classic central limit theorem

In the classical Central limit theorem, the samples in $S$ are assumed to be independent and identically distributed [Geyer, 2011]. Thus, Eq. (2.13) simplifies to:

$$\mathrm{Var}(\hat{\mu}) = \frac{1}{N^2}\sum_{i=1}^{N}\mathrm{Var}(g(X_i)) = \frac{\mathrm{Var}(g(X))}{N}. \tag{2.15}$$

Since the sampling points are identically distributed the equality $\mathrm{Var}(g(X_i)) = \mathrm{Var}(g(X))$ holds and the MCSE of the mean, as defined in Eq. (2.14), can be estimated by using Eqs. (2.12) and (2.15), to be:

$$\widehat{\mathrm{MCSE}}_{\mathrm{mean}} := \frac{\hat{\sigma}}{\sqrt{N}}. \tag{2.16}$$

Finally, the Central limit theorem reads (as $N \to \infty$) [Geyer, 2005]:

$$\hat{\mu} \sim \mathcal{N}\left(\mu, \widehat{\mathrm{MCSE}}_{\mathrm{mean}}\right). \tag{2.17}$$

The estimated expectation value $\hat{\mu}$ is Gaussian distributed around the 'true' expectation value $\mu$ of $g(X)$ and the variance of this distribution shrinks with the number of samples with $\sqrt{N}$.

### MCMC central limit theorem

The sampling points generated via a MCMC approach are assumed to be identically distributed but are not independent of each other since a sampling point depends on the previous sampling point. Thus, the variance of $\hat{\mu}$, i.e. Eq. (2.13), involves non-zero covariance terms [Geyer, 2005]:

$$\mathrm{Var}(\hat{\mu})_{\mathrm{MCMC}} = \frac{1}{N^2}\left(\sum_{i=1}^{N}\mathrm{Var}(g(X_i)) + 2\sum_{i=1}^{N-1}\sum_{j=i+1}^{N}\mathrm{Cov}(g(X_i), g(X_j))\right). \tag{2.18}$$

If the Markov chain is a stationary stochastic process, i.e. the marginal distribution of $X_i$ is independent of $i$ [Geyer, 2011] as well as the $\mathrm{Cov}(g(X_i), g(X_{i+t}))$ (for fixed $t$) [Geyer, 2005], it follows [Geyer, 2005]:

$$\mathrm{Var}(\hat{\mu})_{\mathrm{MCMC}} = \frac{1}{N^2}\left(N\cdot\mathrm{Var}(g(X_i)) + 2\sum_{t=1}^{N-1}(N-t)\mathrm{Cov}(g(X_i), g(X_{i+t}))\right). \tag{2.19}$$

For a better understanding of the important parts of this expression, the variables $\tau_t$, the autocorrelation $\rho_t$ at lag $t$ and the effective sample size (ESS) are defined as:

$$\mathrm{ESS} := \frac{N}{\tau_t}, \tag{2.20}$$

$$\tau_t := 1 + 2\sum_{t=1}^{N-1}(1 - \frac{t}{N})\rho_t, \tag{2.21}$$

$$\rho_t := \mathrm{Corr}(g(X_i), g(X_{i+t})). \tag{2.22}$$

The steps between the two sampling points within a chain is called lag and denoted with $t$. With this definition Eq. (2.19) takes the form:

$$\mathrm{Var}(\hat{\mu})_{\mathrm{MCMC}} = \frac{\mathrm{Var}(g(X_i))}{\mathrm{ESS}}. \tag{2.23}$$

As the sampling points are assumed to be identically distributed, i.e. $\mathrm{Var}(g(X_i)) = \mathrm{Var}(g(X))$, the MCMCSE of the mean can be estimated, by using Eqs. (2.12) and (2.23), to be:

$$\widehat{\mathrm{MCMCSE}}_{\mathrm{mean}} := \frac{\hat{\sigma}}{\sqrt{\widehat{\mathrm{ESS}}}}. \tag{2.24}$$

The estimation of ESS is discussed in Section 2.5.2. In accordance with Eq. (2.17), the MCMC Central limit theorem reads [Geyer, 2005]:

$$\hat{\mu} \sim \mathcal{N}\left(\mu,\ \widehat{\mathrm{MCMCSE}}_{\mathrm{mean}}\right). \tag{2.25}$$

The central point within the derivation above, is that the expectation value of $g(X)$, i.e. Eq. (2.11), is written as a sum of random variables. Despite the fact that quantile estimates are not defined via a sum of random variables, an equivalent expression can be derived for the MCMCSE of a quantile [Vehtari et al., 2021]. Thus, after a performed Bayesian inference, one could check the relative MCMCSE error for the quantiles of interest and judge from this if more sampling points would be appropriate to achieve a better accuracy.

### 2.5.2 Effective sample size

When using MCMC methods to draw samples from a target distribution, the resulting samples within one chain are correlated. The effective sample size takes this into account by weighting the number of draws $N$ with the correlation of the samples. In the case of predominantly positive correlations, $\mathrm{ESS} < N$ while for predominantly negative correlations ESS can become larger than $N$.

The MCMC central limit theorem, i.e. Eq. (2.25), is valid for the asymptotic case where the number of sampling points $N$ goes to infinity. This influences the effective sample size, or more precisely the formula of $\tau_t$ in Eq. (2.21):

$$\lim_{N\to\infty} \tau_t = \lim_{N\to\infty} \left(1 + 2\sum_{t=1}^{N-1}(1 - \frac{t}{N})\rho_t\right) = 1 + 2\sum_{t=1}^{\infty}\rho_t. \tag{2.26}$$

In the last step, it was assumed that $\sum_{t=1}^{\infty}|\rho_t| < \infty$, i.e. the Cesáro sum of $\rho_t$ is equal to the ordinary sum [Geyer, 2005]. As an infinite number of sampling points is not achievable, the infinite sum in Eq. (2.26) should be truncated at some appropriate value $T$, also because the amount of noise increases with large lags [Geyer, 2011]. A suitable truncation order can be found for example by using an initial sequence method [Geyer, 1992].

If multiple MCMC chains $M$ are used to optimize the convergence diagnostics, the effective sample size can be defined as [Vehtari et al., 2021]:

$$\mathrm{ESS} := NM\left(1 + 2\sum_{t=1}^{T}\hat{\rho}_t\right)^{-1}. \tag{2.27}$$

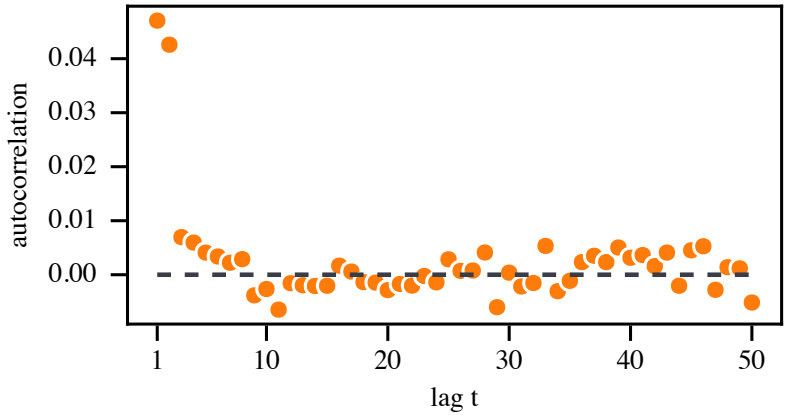


Figure 2.4: Example for the autocorrelation at lag $t$ for a chain after the burn-in period has finished. The autocorrelation at $t = 0$ is defined to be $\hat{\rho}_0 = 1$. To focus on the rapid decrease of the autocorrelation the shown lags start from $t = 1$.

Hereby, $\hat{\rho}_t$ stands for the estimated autocorrelation for multiple chains. In the case of $M$ independent MCMC chains (sampling the same target distribution) the autocorrelation for a single model parameter can be estimated as [Vehtari et al., 2021]:

$$\hat{\rho}_t := 1 - \left( W - \frac{1}{M} \sum_{m=1}^{M} s_m^2 \, \hat{\rho}_{t,m} \right), \tag{2.28}$$

with the autocorrelation $\hat{\rho}_{t,m}$ at lag $t$ of chain $m$, which can be calculated by Eq. (2.22) and the term $s_m^2$ defined in Section 2.5.3, Eq. (2.32). A typical example for the autocorrelation $\hat{\rho}_t$ after the MCMC chains have reached convergence, is shown in Fig. 2.4. Hence, the correlations rapidly decrease with increasing lag and settles around a value of zero.

### 2.5.3 Potential scale reduction statistic

The potential scale reduction statistic $\widehat{R}$ monitors the MCMC convergence via the between- and within-chain variances and is defined as [Vehtari et al., 2021]:

$$\widehat{R} := \sqrt{\frac{\widehat{var}^+}{W}}, \tag{2.29}$$

with the marginal posterior variance:

$$\widehat{var}^+ := \frac{N-1}{N} W + \frac{1}{N} B. \tag{2.30}$$

The symbol $N$ denotes the samples per chain, $M$ is the number of chains, $W$ the within-chain variance and $B$ stands for the between-chain variance. The latter two are defined as:

$$W := \frac{1}{M} \sum_{m=1}^{M} s_m^2, \qquad B := \frac{N}{M-1} \sum_{m=1}^{M} \left( \bar{\theta}^{(.m)} - \bar{\theta}^{(..)} \right)^2, \tag{2.31}$$

with the new symbols defined as:

$$s_m^2 := \frac{1}{N-1} \sum_{n=1}^{N} \left( \theta^{(nm)} - \bar{\theta}^{(.m)} \right)^2 , \tag{2.32}$$

$$\bar{\theta}^{(.m)} := \frac{1}{N} \sum_{n=1}^{N} \theta^{(nm)}, \qquad \bar{\theta}^{(..)} := \frac{1}{M} \sum_{m=1}^{M} \bar{\theta}^{(.m)}. \tag{2.33}$$

The notation $\theta^{(nm)}$ refers to the $n$-th sample from the $m$-th chain, while $\theta^{(.m)}$ represents the mean value of the $m$-th chain. Finally, $\theta^{(..)}$ denotes the mean value of all samples combined from all chains.

The most important property of Eq. (2.29) is its behavior when the number of samples $N$ approaches infinity, i.e. the limit in which the MCMC central limit theorem holds:

$$\widehat{R} \to 1, \qquad \text{for } N \to \infty. \tag{2.34}$$

Thus, after a performed Bayesian analysis one calculates $\widehat{\mathrm{R}}$ and checks how close it is to a value of one. As a rule of thump, one should achieve a $\widehat{\mathrm{R}}$ -value smaller than the empirical value of 1.01 as suggested in Ref. [Vehtari et al., 2021].

## 2.6 Posterior predictive check

In general, a posterior predictive check [Gelman et al., 2013] is useful for determining flaws within the Bayesian analysis, such as problematic data points, programming errors, systematic effects or the inadequacy of the employed model.

The central component is the probability distribution of reproduced data points $y^{\mathrm{rep}}$ given the used data $y$, which is called the posterior predictive distribution [Gelman et al., 2013, Watanabe, 2010]:

$$\begin{aligned} p(y^{\mathrm{rep}} \mid y) &:= \mathbb{E}_\Theta \left[ p\left(y^{\mathrm{rep}} \mid \Theta\right) \right], \\ &= \int p(y^{\mathrm{rep}} \mid \Theta) p(\Theta \mid y) \, \mathrm{d}\Theta \,, \end{aligned} \tag{2.35}$$

where $\mathbb{E}_\Theta[\ldots]$ denotes the expectation value over the parameter-vector $\Theta$. Hence, this allows to compare each data point $y_i$ directly with its corresponding replicated marginal distribution $p(y_i^{\mathrm{rep}} \mid y)$. Both should look similar under a reasonable model [Gelman et al., 2013]. Irregularities, such as outliers or statistically weak data points, can be detected. An example for a posterior predictive check can be seen in Fig. 2.5. The figure shows the original data points in direct comparison to the corresponding posterior predictive distributions. No systematic effects are visible in the figure and one would conclude that the model is able to describe the original data.

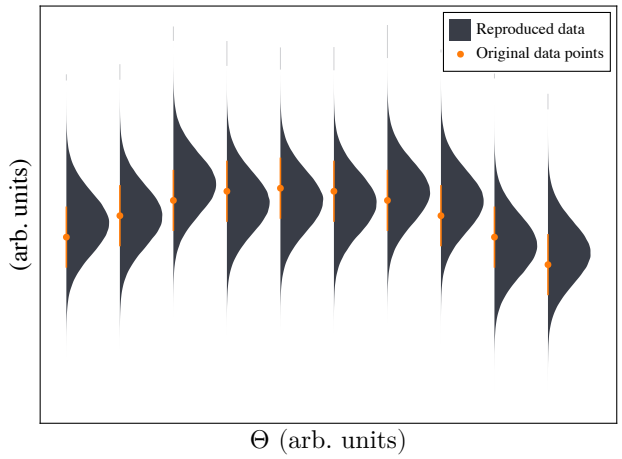


Figure 2.5: An illustration of a posterior predictive check. The original data points (orange) are compared to the posterior predictive distribution in (black).

# Part I

# Ambiguity analyses in Baryon spectroscopy

# Chapter 3

# Baryon spectroscopy

This chapter is meant as an introduction to Baryon spectroscopy and the relevant concepts necessary for the discussion of the papers in Chapters 4 and 5, which deal with ambiguity analyses. The chapter starts with a general introduction and motivation for Baryon spectroscopy in Section 3.1 laying the focus on Baryon states. This is followed by Section 3.2 in which methods for the prediction of Baryon states and the complexity of this endeavor are discussed. The measurement observables in Baryon spectroscopy, used to validate or falsify the theory predictions, are discussed in Section 3.3. A tightly connected, theoretical topic is complete experiment analyses which is outlined in Section 3.4. Finally, in Section 3.5 the connection of polarization observables and Baryon resonances is made via the introduction of partial wave analysis, a method used to extract information about Baryon resonances from the experimental available polarization data.

## 3.1 Introduction

Baryon spectroscopy (BS) is a field within particle physics, which studies the strong interaction and in particular the formation of bound states of more than two quarks, as introduced in Section 1.1.1. The majority of these bound states are so-called resonance states, which posses distinct masses and quantum numbers, and are treated as distinct particles. Their typical mean lifetime is in the order of $10^{-24}$ s, as they predominantly decay via the strong interaction. Thus, this kind of particles can not be directly detected with state-of-the-art detectors. Instead, particle colliders are used to produce resonances for example through formation experiments [Navas et al., 2024]:

$$\mathcal{I}_1 \mathcal{I}_2 \rightarrow [R] \rightarrow \mathcal{F}_1 \ldots \mathcal{F}_n, \tag{3.1}$$

with two particles in the initial state and at least two in the final state. A resonance $R$ can emerge in an intermediate step of the reaction. If and which resonance can be formed depends on the available energy within the reaction and the conserved quantities for the type of interaction, see also Table 1.2. Considering for example a photon $\mathcal{I}_1 = \gamma$ are impinging on a proton target $\mathcal{I}_2 = p$. The photon interacts electromagnetically with the quarks within the proton and transfers (part of) its energy. Due to the supplied energy, it is energetically favorable for the quarks and their bound system to change to a new bound state $R$, also called excited state.

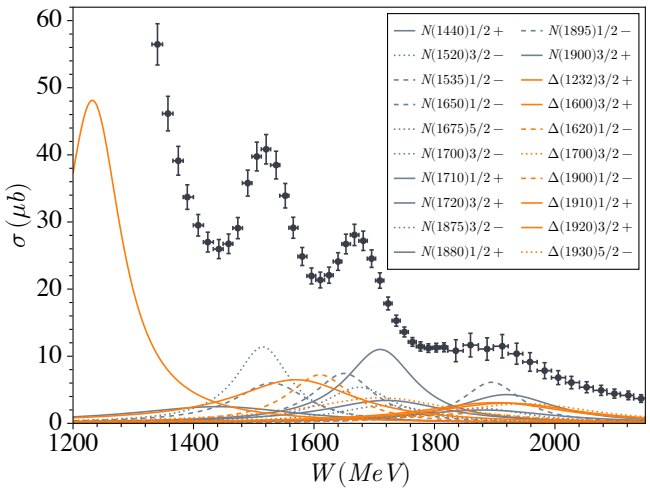


Figure 3.1: Shown is the experimental data for the total cross-section $\sigma$, as a function of the center-of-mass energy $W$, for the reaction $\gamma p \to \pi^0 p$. In addition, the contributing $N$- and $\Delta$-resonances are shown as independent Breit-Wigner distributions for partial waves with angular momenta of $\ell = 0$ (dashed), $\ell = 1$ (solid) and $\ell = 2$ (dotted) up to energies of 1930 MeV. Note: the height of the distributions do not indicate their significance. The figure is redrawn from [CBELSA/TAPS et al., 2017], with updated resonance parameters from the Review of Particle Physics [Navas et al., 2024].

The significance of resonance states and their importance for the understanding of the strong force, can for example be seen in the total cross-section $\sigma$ of a certain reaction. Figure 3.1 shows the experimental data for the total cross-section of $\pi^0$ photoproduction ($\gamma p \to \pi^0 p$) in which multiple bumps are visible. The resonances which could emerge in the reaction ($N$- and $\Delta$-resonances) are indicated as Breit-Wigner distributions. Due to reasons of visualization, only the corresponding partial wave angular momenta of $\ell = 0, 1, 2$ are taken into account. The appearance of the bumps within the total cross-section is attributed to the constructive and destructive interference of the relevant resonance states within the energy range, and thus the enhanced or suppressed production of $\pi^0 p$ in the final state of the reaction. As the coupling strength, and thus the branching ratios, of resonances are different for different initial- and final states [Navas et al., 2024], multiple reactions have to be analyzed to complete the knowledge about the plethora of Baryon resonance states. This comprises not only different single meson- but also multi meson final states. Multi meson final states are of particular importance in photoproduction for the study of higher mass resonance states. This is specifically visible in the contributions to the total cross-section for photoproduction off the proton [Thiel et al., 2022]. For center-of-mass energies $W < 1400$ MeV single meson final states contribute predominantly, whereas for $W > 1400$ MeV multi meson final states contribute the vast majority, see Fig. 1 in Ref. [Thiel et al., 2022].

Another motivation to study the excitation spectrum of baryons is that significantly more states have been predicted than experimentally verified, which is

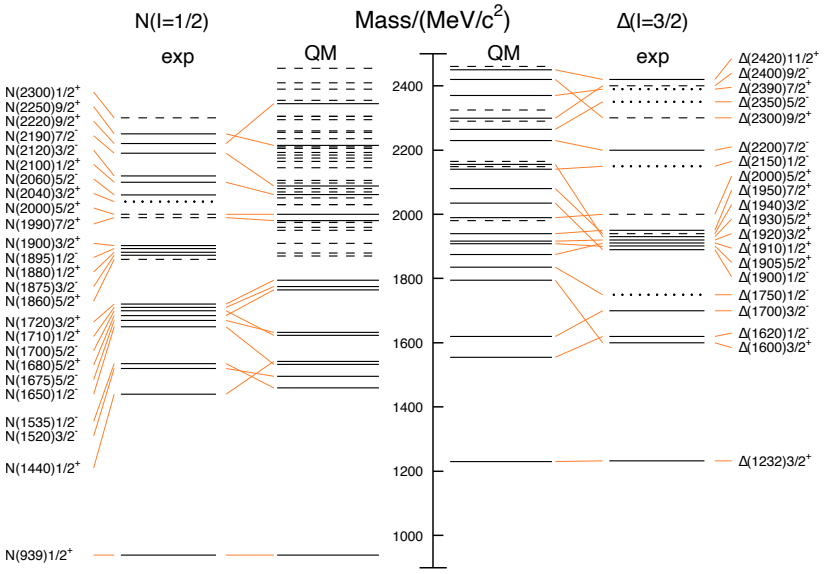


Figure 3.2: Comparison of the nucleon excitation spectrum for experimentally observed- and by a relativized quark model [Capstick, 1992, Capstick and Roberts, 1998] predicted states. (Left) In the first column one can see the spectral notation for certain resonance states. The second column shows the experimentally observed states. The certainty with which these states exist are indicated by the line style (four-star: solid line, three-star: solid line, two-star: dashed line and one-star: dotted line). See the Review of Particle Physics star-rating in Ref. [Navas et al., 2024] for further explanations. The entries of the first and second column are connected via orange lines, indicating the assignment of states. The third column lists the predicted states, some of which are assigned to states in column two. These assignments should be considered tentative. Not assigned states are indicated with dashed lines. (Right) Like the left part but reversed. Original image is from the Review of Particle Physics [Navas et al., 2024] and slightly adapted for this thesis.

also known as the 'missing-resonance' problem [Navas et al., 2024]. Figure 3.2 illustrates the assignment of experimentally observed $N$- and $\Delta$ baryon resonances to predicted states by a relativized quark model [Capstick, 1992, Capstick and Roberts, 1998]. Especially the dashed lines in the columns labeled with QM are of interest, as these are theoretically predicted states which have not been assigned to an experimentally observed state yet. Furthermore, experimentally a clustering of $N$-resonances at ~1700 MeV and ~1900 MeV is observable, the same for $\Delta$-resonances at an energy of ~1950 MeV, which is not reflected by the theoretical model [Navas et al., 2024].

## 3.2 Predicted baryon states

To begin with, the prediction of baryon resonances is a non-trivial task. As gluons carry a color charge, see Table 1.3, self-interaction Feynman diagrams play a

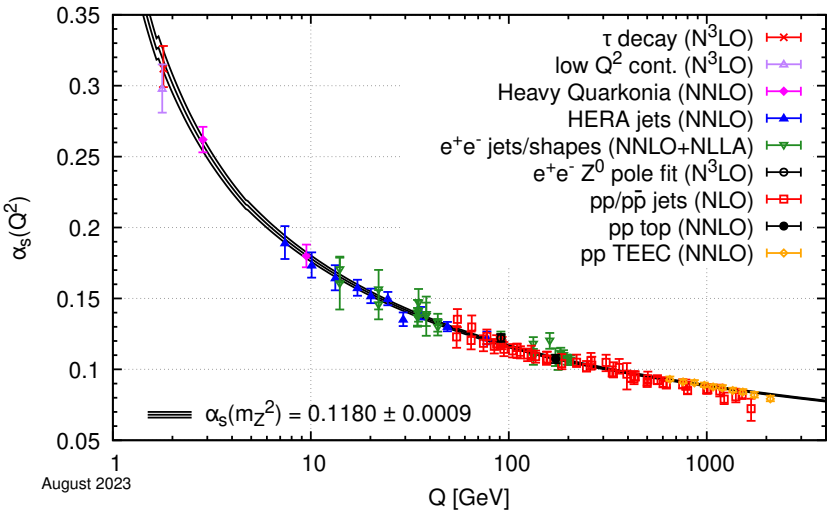


Figure 3.3: The coupling constant of the strong interaction $\alpha_s(Q^2)$ is shown as a function of the momentum transfer $Q$. The abbreviations indicate next-to-leading order (NLO), next-to-next-to-leading order (NNLO) and so on. The image is taken from the Review of Particle Physics [Navas et al., 2024].

crucial role in contrast to quantum electrodynamics or the weak interaction. These self-interaction terms lead to the well known phenomena of the running coupling constant $\alpha_s$ of the strong interaction, which is experimentally well established as can be seen in Fig. 3.3. Hence, the coupling constant of the strong interaction is dependent on the energy scale at which the experiment is performed. This functional behavior in terms of the momentum transfer $Q$ can be written as [Thomson, 2013, Halzen and Martin, 2008]:

$$\alpha_s(Q^2) := \frac{\alpha_s(\mu^2)}{1 + \frac{(11N_c - 2N_f)}{12\pi}\alpha_s(\mu^2)\log\left(\frac{Q^2}{\mu^2}\right)}, \tag{3.2}$$

with a chosen reference momentum $\mu$, $N_c$ colors and $N_f$ quark flavors. The dependence of $\alpha_s$ on $Q$ has direct implications for the study of baryon states, as the relevant energy regime is in the order of $Q \sim 1\,\text{GeV}$ and thus $\alpha_s \sim 1$ [Thomson, 2013]. Therefore, it is not possible to apply perturbation theory to solve the Lagrangian of QCD for the prediction of baryon states.

Alternative approaches to perturbation theory has to be used. One example is lattice QCD (LQCD), which was first introduced by Kenneth G. Wilson [Wilson, 1974]. The idea hereby is to solve the Lagrangian equations on a multidimensional grid, with a finite spacing between grid points (nodes) denoted with $a$. To avoid that the discretization of the problem becomes apparent in the final results, the lattice spacing $a$ should be much smaller than the spatial dimension $R$ of the object under consideration [Aitchison and Hey, 2012]. In addition, to avoid "finite size effects" [Aitchison and Hey, 2012] $R$ should be much smaller than the hypercube side length $L = aN$ with $N \in \mathbb{N}$, such that the object of interest fits into the hypercube. By convention, the quark fields $q(x)$ at a space-time point $x$ are restricted to be on the nodes, whereas gauge fields are restricted to be on

the edges, connecting the nodes [Navas et al., 2024]. An illustrative example for a two-dimensional grid is given in Fig. 3.4. The Feynman integrals appearing in this approach are calculated via MCMC methods and no perturbation theory is required [Navas et al., 2024]. In the limit of $a \rightarrow 0$, which is equivalent to "tuning the bare gauge coupling to zero according to the renormalization group" [Navas et al., 2024], the theory goes from a discretized- to a continuous space. An appealing factor is that LQCD preserves gauge invariance naturally in contrast to perturbation calculations [Navas et al., 2024]. However, it should be mentioned that particle states within a finite volume, such as in LQCD, do not decay, they only mix [Navas et al., 2024]. Hence, the prediction of resonance states form LQCD have to be taken with care. Nevertheless, an example for the prediction of nucleon resonances for multiple spin-parity configurations is shown in Fig. 3.5.

Another approach is via constituent quark models. Hereby the baryon is composed of three valence quarks which are in a static potential from the gluon gauge fields [Gross et al., 2023]. There are multiple methods to model the short-range interaction of the valence quarks, which range from "one-gluon exchange models", "pseudoscalar-meson exchange models, "instanton-induced interactions" and "the Dyson–Schwinger Bethe–Salpeter approach" [Gross et al., 2023] and therefore no pertubative methods are required. As an example, the prediction of nucleon resonances from a relativized quark model, as presented in Ref. [Capstick and Roberts, 1998], is shown in Fig. 3.2. Interestingly, the problem of missing resonances for quark models, as discussed in Section 3.1, also persists for LQCD [Thiel et al., 2022].

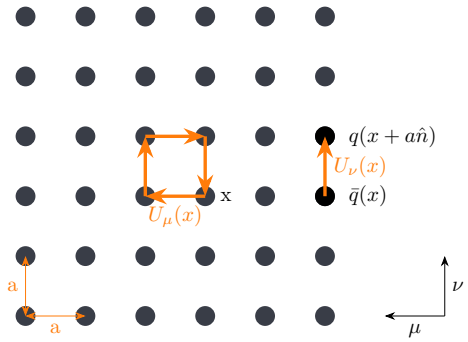


Figure 3.4: Illustration of a two-dimensional slice of the $\mu-\nu$-plane of the space-time grid, with a finite spacing of $a$ between nodes. As an example, the bilinear product $\bar{q}(x)U_\nu(x)q(x+a\hat{\nu})$, with the unit vector $\hat{\nu}$ in $\nu$-direction, connecting the quark and anti-quark fields are shown. In addition, the so-called plaquette product, which appears in the gauge action [Navas et al., 2024], is illustrated in the middle of the figure. The figure itself is redrawn and slightly adapted from [Navas et al., 2024].

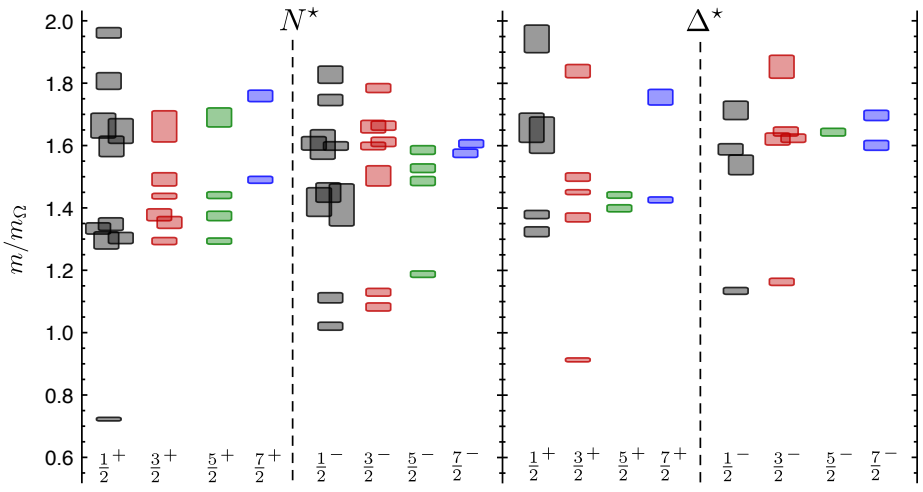


Figure 3.5: Lattice QCD predictions from Ref. [Edwards et al., 2011] for the excitation spectrum of the nucleon for different $J^P$ configurations, using an unphysical pion mass of $m_\pi = 396\,\mathrm{MeV}$. The mass $m$ of the states is given in terms of the calculated $\Omega$ mass $m_\Omega$.

Table 3.1: The 16 polarization observables for pseudoscalar meson photoproduction are grouped according to the polarization needed for their measurement (linearly polarized beam $\mathcal{B}_l$, circularly polarized beam $\mathcal{B}_\odot$, target polarization $\mathcal{T}$, recoil polarization $\mathcal{R}$). The same notation for the observables as is in Ref. [Sandorfi et al., 2011] is used.

| Category | Subcategory | Observable |
|---|---|---|
| $\diagup$ | $\diagup$ | $\sigma_0$ |
| $\mathcal{B}$ | $\mathcal{B}_l$ | $\Sigma$ |
| $\mathcal{T}$ | $\diagup$ | T |
| $\mathcal{R}$ | $\diagup$ | P |
| $\mathcal{BT}$ | $\mathcal{B}_l\mathcal{T}$ | G, H, P |
| $\mathcal{BT}$ | $\mathcal{B}_\odot\mathcal{T}$ | E, F |
| $\mathcal{BR}$ | $\mathcal{B}_l\mathcal{R}$ | $T, O_{x'}, O_{z'}$ |
| $\mathcal{BR}$ | $\mathcal{B}_\odot\mathcal{R}$ | $C_{x'}, C_{z'}$ |
| $\mathcal{TR}$ | $\diagup$ | $\Sigma, L_{x'}, L_{z'}, T_{x'}, T_{z'}$ |

## 3.3 Observables

The interplay between theory and experiment is an essential ingredient to increase our knowledge in physics. To prove or disprove predictions from theory, observables have to be measured from which directly or via further analyses, the predictions, such as baryon states, can be investigated. In BS, the measurable quantities of interest are so-called polarization observables.

The number of measurable polarization observables $N_o$ is determined by the type of reaction. More precisely, by the number of complex spin amplitudes $N_a$ required for a full mathematical description of the process at hand. These complex spin amplitudes can be understood in the following way: In general, each particle physics reaction can be fully described by the knowledge of the corresponding matrix elements $T_{fi} := \langle i|T|f\rangle$, with the initial- and final state $|i\rangle$ and $|f\rangle$. Thus, a parametrization for $T$ is required which can be experimentally determined. In BS one is typically dealing with reactions involving particles with a nonzero spin, for which $T$ can be parameterized in a model-independent way via so-called spin amplitudes.

The relation between the number of complex spin amplitudes and the number of polarization observables is $N_o := N_a^2$. For example in the case of pseudoscalar meson photoproduction $\gamma N \to \phi B$, with a beam of photons $\gamma$, a target nucleon $N$, a pseudoscalar meson $\phi$ and a recoil baryon $B$, four complex spin amplitudes are needed to describe the reaction and thus 16 observables are measurable. The observables are measurable by using different polarization configurations for the photon beam, the nucleon and the recoil baryon. The required polarization states for each observable are collected in Table 3.1. A more complex reaction is the case of two-pseudoscalar-meson photoproduction $\gamma N \to \phi_1\phi_2 B$, with two pseudoscalar mesons $\phi_i$, where eight complex spin amplitudes are required, and thus 64 polarization observables are measurable. The required spin configurations are

Table 3.2: The 64 polarization observables for two-pseudoscalar-meson photoproduction are grouped according to the polarization needed for their measurement (linearly polarized beam $\mathcal{B}_l$, circularly polarized beam $\mathcal{B}_\odot$, target polarization $\mathcal{T}$, recoil polarization $\mathcal{R}$). The notation for the observables is the one used in Ref. [Roberts and Oed, 2005]. The figure is taken from [Kroenert et al., 2021].

| Category | Subcategory | Observable |
|---|---|---|
| $\diagup$ | $\diagup$ | $I_0$ |
| $\mathcal{B}$ | $\mathcal{B}_l$ | $I^s$, $I^c$ |
| $\mathcal{B}$ | $\mathcal{B}_\odot$ | $I^\odot$ |
| $\mathcal{T}$ | $\diagup$ | $P_x, P_y, P_z$ |
| $\mathcal{R}$ | $\diagup$ | $P_{x'}, P_{y'}, P_{z'}$ |
| $\mathcal{BT}$ | $\mathcal{B}_l\mathcal{T}$ | $P^s_x, P^s_y, P^s_z, P^c_x, P^c_y, P^c_z$ |
| $\mathcal{BT}$ | $\mathcal{B}_\odot\mathcal{T}$ | $P^\odot_x, P^\odot_y, P^\odot_z$ |
| $\mathcal{BR}$ | $\mathcal{B}_l\mathcal{R}$ | $P^s_{x'}, P^s_{y'}, P^s_{z'}, P^c_{x'}, P^c_{y'}, P^c_{z'}$ |
| $\mathcal{BR}$ | $\mathcal{B}_\odot\mathcal{R}$ | $P^\odot_{x'}, P^\odot_{y'}, P^\odot_{z'}$ |
| $\mathcal{TR}$ | $\diagup$ | $O_{xx'}, O_{xy'}, O_{xz'}, O_{yx'}, O_{yy'}, O_{yz'}, O_{zx'}, O_{zy'}, O_{zz'}$ |
| $\mathcal{BTR}$ | $\mathcal{B}_l\mathcal{TR}$ | $O^s_{xx'}, O^s_{xy'}, O^s_{xz'}, O^s_{yx'}, O^s_{yy'}, O^s_{yz'}, O^s_{zx'}, O^s_{zy'}, O^s_{zz'}$ |
| $\mathcal{BTR}$ | $\mathcal{B}_l\mathcal{TR}$ | $O^c_{xx'}, O^c_{xy'}, O^c_{xz'}, O^c_{yx'}, O^c_{yy'}, O^c_{yz'}, O^c_{zx'}, O^c_{zy'}, O^c_{zz'}$ |
| $\mathcal{BTR}$ | $\mathcal{B}_\odot\mathcal{TR}$ | $O^\odot_{xx'}, O^\odot_{xy'}, O^\odot_{xz'}, O^\odot_{yx'}, O^\odot_{yy'}, O^\odot_{yz'}, O^\odot_{zx'}, O^\odot_{zy'}, O^\odot_{zz'}$ |

collected in Table 3.2. More details on the topic of required polarization states for both reactions can be found in Ref. [Sandorfi et al., 2011] and Ref. [Roberts and Oed, 2005], respectively.

Over the last decades multiple Baryon spectroscopy experiments were conducted to measure polarization observables. This includes but is not limited to: MAMI [Walcher, 1990] located in Mainz, Germany, GRAAL [Bartalini et al., 2005] located in Grenoble, France, BGOOD [Alef et al., 2020] located in Bonn, Germany, CBELSA/TAPS [Gottschall et al., 2021] located in Bonn, Germany, CLAS [Mecking et al., 2003] located in Newport News, USA, LEPS2 [Muramatsu et al., 2022] located at Harima Science Park City, Japan and many more. This international effort culminated in a large database of polarization observables. An extensive listing of measurements can be found in Ref. [Thiel et al., 2022], see Tables 7-11 for pseudoscalar meson photoproduction, Table 11 for vector meson photoproduction, Tables 12-13 for strangeness photoproduction and Tables 14-15 for two pseudoscalar meson photoproduction.

The general, mathematical definition for the polarization observables $O^\alpha$ of a reaction described by $N$ complex spin amplitudes $t_i$ is given by [Chiang and Tabakin, 1997]:

$$O^\alpha := \sum_{i,j=1}^{N} t_i^* \Gamma^\alpha_{ij} t_j, \tag{3.3}$$

with $\alpha \in [1, \ldots, N^2]$ and Hermitian $\Gamma$-matrices unique for each observable. The explicit definition for the $\Gamma$-matrices for pseudoscalar meson photoproduction

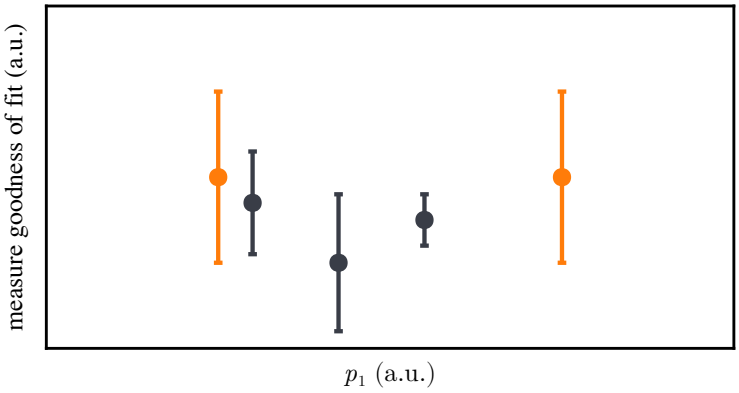


Figure 3.6: The figure shows five fit results for a hypothetical parameter $p_1$ in terms of some goodness of fit (GOF) measure. The orange points, which have the same GOF, would correspond to a severe ambiguity. The dark points are non-severe ambiguities, as their GOF tends to be smaller and can be distinguished from one another.

can be found in [Chiang and Tabakin, 1997] and for two-pseudoscalar-meson photoproduction in Ref. [Kroenert et al., 2021].

## 3.4 Complete experiment analysis

The large database of polarization observables, as introduced in Section 3.3 was brought together by an enormous effort of the Baryon spectroscopy community and is a great achievement. Having said that, a large database is not enough when it comes to the extraction of information about resonance states or transition matrix elements $T_{\mathrm{fi}}$, as it is crucial how many and which polarization observables have been measured for a certain reaction. This can directly be concluded from the mathematical definition of polarization observables in Eq. (3.3), in which the bilinear product allows for transformations of the complex spin amplitudes $t_{\mathrm{i}}$ which leave the observable invariant. Taking this observation further, there might exist transformations which leave every observable in a set $\{O^{\alpha_1},\ldots,O^{\alpha_j}\}$, with $j < N^2$, invariant. In such a situation multiple $t_{\mathrm{i}}$ exist which are capable of producing the set of observables, which is referred to as an ambiguity [Chiang and Tabakin, 1997].

Complete experiment analysis (CEA) deals with the question of how many and in particular which of the $O^{\alpha}$ need to be measured in order to determine the complex spin amplitudes $t_{\mathrm{i}}$ of a certain reaction uniquely, i.e. without ambiguities, and is thus an integral part of Baryon spectroscopy. In this context, a set of observables which does not produce any ambiguities is called a complete set of observables.

Because of the significance of CEA for BS it is a long and actively studied field of research. A CEA has been performed for multiple different processes: for example pion nucleon scattering ($N_{\mathrm{a}} = 2$) [Anisovich et al., 2013, Wunderlich et al., 2020], pseudoscalar meson photoproduction ($N_{\mathrm{a}} = 4$) [Chiang and Tabakin, 1997, Nakayama, 2019], pseudoscalar meson electroproduction ($N_{\mathrm{a}} = 6$) [Wunder-

lich et al., 2020, Wunderlich, 2021] and the photoproduction of two pseudoscalar mesons ($N_a = 8$) [Arenhövel and Fix, 2014, Kroenert et al., 2021]. It is worth mentioning, that the complexity of a CEA increases exponentially with the number of scattering amplitudes $N_a$ necessary to fully describe the reaction at hand, because the number of observables $N_o = N_a^2$ scales quadratically with it.

However, the result of a CEA is always derived under the assumption of observables without uncertainties. Which means, even when using a mathematical complete set of observables, as soon as real data are used to determine the complex spin amplitudes $t_i$, more or less severe ambiguities might occur. In practice, this translates to multiple solutions from a regression analysis which can not be easily distinguished in terms of some measure for the goodness of the fit (GOF). The problem is illustrated in Fig. 3.6. The orange points constitute a severe ambiguity, as the GOF can not be distinguished. The darker points are ambiguities as well, but less of a problem, because their GOF is smaller and can be distinguished from one another. It is assumed that the 'true' physical solution has the best GOF while ambiguities have an equal or worse GOF.

## 3.5 Partial wave analysis

The method of partial wave analysis (PWA) is an important tool in BS to extract information about resonance states, such as its mass, decay width, coupling strength and branching ratios, from experimental data.

In theoretical terms, resonance states have the property "that they appear as poles of the $S$-matrix in the complex plane on unphysical sheets,..." [Navas et al., 2024], where the $S$-matrix is a unitary operator ($S^\dagger S = \mathbb{1}$) connecting two asymptotic states, i.e. an initial state $|i\rangle$ to a final state $|f\rangle$. The $S$-matrix is typically defined as:

$$S := \mathbb{1} + 2iT, \tag{3.4}$$

with the symbol $\mathbb{1}$ denoting the case in which no interaction has taken place and $T$ representing the interaction matrix. The scattering amplitudes, which are the matrix elements of $T$ [Thiel et al., 2022], are of main interest, as these are the connections to the properties of resonances which emerged in the interaction. For reactions of the form $2 \to 2$ the so-called K-matrix approach is well suited, as it guarantees that $T$ is unitary [Navas et al., 2024]. The relations of the $T-$ and $K-$ matrix are as follows [Thiel et al., 2022]:

$$T = (\mathbb{1} - iK)^{-1} K, \tag{3.5}$$

and therefore

$$S = \frac{\mathbb{1} + iK}{\mathbb{1} - iK}. \tag{3.6}$$

An illustrative example for the imaginary part of a typical scattering amplitude is shown in Fig. 3.7, where both poles correspond to a resonance state. The mass $m_R$ and decay width $\Gamma_R$ of a resonance can be extracted via its pole position $s_R$ and the relation [Navas et al., 2024]:

$$\sqrt{s_R} = m_R - i\frac{\Gamma_R}{2}. \tag{3.7}$$

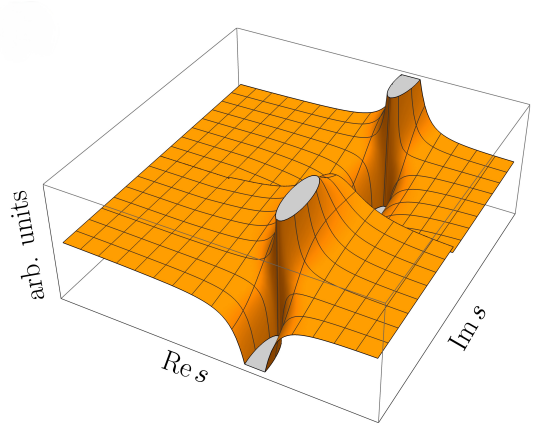


Figure 3.7: Shown is the second Riemann sheet for a typical scattering amplitude. More precisely the imaginary part of a scattering amplitude $A$ of the interaction matrix is shown as a function of the complex Mandelstam variable $s$. The two poles correspond to two resonance states. The original image is from Ref. [Navas et al., 2024] and was modified for this thesis.

Hence, in order to extract information about emerging resonances from data, the scattering amplitudes of the interaction matrix have to be modeled, and the model parameters has to be tuned by experimental data.

### 3.5.1 PWA models: BnGa, JuBo, MAID

For the modeling of the scattering amplitudes $A_i$ of the interaction $T$-matrix multiple approaches exist. This includes but is not limited to: the Bonn-Gatchina (BnGa) model [Anisovich et al., 2016], the Jülich-Bonn (JuBo) model [Rönchen et al., 2022] and the Mainz unitary isobar model (MAID) [Tiator et al., 2018].

The BnGa model uses "a dispersion-relation approach based on the N/D technique" [Anisovich et al., 2016] with the K-matrix approach and allows fitting data sets from different reactions at the same time via a coupled-channel approach [Anisovich et al., 2016]. The JuBo model is a dynamically coupled-channel model based on an effective Lagrangian and uses parametrizations for the scattering amplitudes which obeys the Lippmann-Schwinger equations [Rönchen et al., 2022]. The MAID model split the resonance and background contributions within the $T$-matrix. For the resonance part, it is assumed that the resonances can be described by a Breit-Wigner form [Tiator, 2018]. The background part is defined by a background potential involving Born terms and pion-nucleon elastic scattering amplitudes [Tiator, 2018].

A common feature of BnGa, JuBo and MAID is an energy-dependent parametrization of the scattering amplitudes. Furthermore, BnGa and JuBo are both capable of sophisticated couple-channel analysis, where MAID is in general not a coupled-channel approach [Thiel et al., 2022]. As the same resonance can show up in different reactions, the coupled-channel approach has the advantage that more data can be used to tune the parameters of the respective resonance. However,

the models also differ in the experimental data sets used to tune their respective model parameters. As such one should keep in mind, that a direct comparison between the models is rather complex.

### 3.5.2 Truncated partial-wave analysis

The ansatz of truncated partial-wave analysis (TPWA) is a model independent approach. The matrix elements of the transition matrix $T$ are not parameterized in an energy-dependent way, but rather directly fitted for each energy of interest. Because a TPWA is performed for the reaction of single pseudoscalar meson photoproduction in Chapter 5 of this thesis, a more in depth introduction to the fundamentally involved quantities seems to be appropriate. A short remark, in principle a TPWA can also be performed for example for two-pseudoscalar-meson photoproduction. The theoretical groundwork is already laid out in Ref. [Fix and Arenhövel, 2013], but because of the lack of experimental data, which would form a complete set of observables, no TPWA was performed so far.

For pseudoscalar meson photoproduction the transition matrix $T$ can be formulated as [Chew et al., 1957]:

$$T := \frac{i\vec{\sigma}\cdot\vec{\epsilon}F_1}{|\vec{\epsilon}|} + \frac{\vec{\sigma}\cdot\vec{q}\vec{\sigma}\cdot\left(\vec{k}\times\vec{\epsilon}\right)F_2 + i\vec{\sigma}\cdot\vec{k}\vec{q}\cdot\vec{\epsilon}F_3}{|\vec{\epsilon}||\vec{q}||\vec{k}|} + \frac{i\vec{\sigma}\cdot\vec{q}\vec{q}\cdot\vec{\epsilon}F_4}{|\vec{\epsilon}||\vec{q}||\vec{q}|}, \tag{3.8}$$

with the photon polarization $\vec{\epsilon}$, the three momentum of the meson $\vec{q}$ and photon $\vec{k}$. The symbol $\vec{\sigma}$ denotes a vector formed from the three Pauli spin-matrices $(\sigma_1,\sigma_2,\sigma_3)$. The four functions $F_1,\ldots,F_4$ are the so-called CGLN-amplitudes, named after the authors of the paper in Ref. [Chew et al., 1957] and depend on the energy $W$ and the scattering angle $\theta$ in the center of mass system. The definition of the CGLN-amplitudes is given by four functions [Chew et al., 1957]:

$$\begin{aligned} F_1(W,\theta) := \sum_{l=0}^{\infty} \Big\{ &[lM_{l+}(W) + E_{l+}(W)]\ P'_{l+1}(\cos\theta) \\ &+ [(l+1)M_{l-}(W) + E_{l-}(W)]\ P'_{l-1}(\cos\theta)\Big\}, \end{aligned} \tag{3.9}$$

$$F_2(W,\theta) := \sum_{l=1}^{\infty} [(l+1)M_{l+}(W) + lM_{l-}(W)]\ P'_l(\cos\theta), \tag{3.10}$$

$$\begin{aligned} F_3(W,\theta) := \sum_{l=1}^{\infty} \Big\{ &[E_{l+}(W) - M_{l+}(W)]\ P''_{l+1}(\cos\theta) \\ &+ [E_{l-}(W) + M_{l-}(W)]\ P''_{l-1}(\cos\theta)\Big\}, \end{aligned} \tag{3.11}$$

and the fourth component:

$$F_4(W,\theta) := \sum_{l=2}^{\infty} [M_{l+}(W) - E_{l+}(W) - M_{l-}(W) - E_{l-}(W)]\ P''_l(\cos\theta). \tag{3.12}$$

The symbol $l$ denotes the angular momentum of the two particle final state, $P_l$ denotes the Legendre Polynomials with their derivative $P'_l(\cos\theta) := \frac{\mathrm{d}}{\mathrm{d}\cos\theta} P_l(\cos\theta)$.

The quantities $M_{l\pm}$ and $E_{l\pm}$ are complex functions of the energy $W$ and are called magnetic and electric multipoles, respectively. The multipoles correspond to transitions to a final state with angular momentum $l$ and total angular momentum $l \pm 1/2$, initiated by magnetic or electric radiation, respectively [Chew et al., 1957].

Hence, each quantity in Eq. (3.8) is known from the experimental setup except for the multipole parameters which can be estimated via a regression analysis in order to fully, numerically describe the transition matrix $T$ for a reaction. However, as it is not possible to estimate an infinite number of model parameters in a regression analysis, a TPWA assumes that the infinite sums in Eqs. (3.9) to (3.12) can be approximated by finite sums, up to a maximal angular momentum $l_{\max}$. This assumption is valid, since multipoles coming from higher angular momenta $l$ get more and more suppressed:

$$\lim_{l\to\infty} E_{l\pm} = 0, \tag{3.13}$$

$$\lim_{l\to\infty} M_{l\pm} = 0, \tag{3.14}$$

see Eqs. (3.12) to (3.15) in Ref. [Ball, 1961]. However, an appropriate truncation order also depends on the energy $W$ of the reaction, as the multipoles also depend on the energy. That said, higher angular momenta can still couple to lower angular momenta and thus might have a non-negligible influence. Thus, an appropriate maximum angular momentum has to be determined in each analysis by comparing some goodness of fit criterion.

In the formalism of a TPWA, the 16 polarization observable $O^\alpha$ of single meson photoproduction, with the index $\alpha$ running from one to 16, can be expressed as [Wunderlich et al., 2017]:

$$\hat{O}^\alpha(W,\theta) := \sigma_0(W,\theta) O^\alpha(W,\theta) := \frac{|\vec{q}|}{|\vec{k}|} \sum_{j=\beta_\alpha}^{2l_{\max}+\beta_\alpha+\gamma_\alpha} (a_{l_{\max}})_j^\alpha(W) P_j^{\beta_\alpha}(\cos\theta) \tag{3.15}$$

with the unpolarized differential cross-section $\sigma_0$, the three momenta for the initial state photon $\vec{k}$ and the final state meson $\vec{q}$, the maximal angular momentum taken into account $l_{\max}$, the expansion coefficients $\beta_\alpha$ and $\gamma_\alpha$, the so-called Legendre coefficients $(a_{l_{\max}})_j^\alpha$ and the associated Legendre polynomials $P_j^{\beta_\alpha}$. The values of the expansion coefficients are listed in Table 3 of Ref. [Wunderlich et al., 2017] while the Legendre coefficients themselves are defined as:

$$(a_{l_{\max}})_j^\alpha(W) := \mathcal{M}^\dagger(W) C_j^\alpha \mathcal{M}(W). \tag{3.16}$$

The vector $\mathcal{M}(W)$ contains all participating complex multipoles up to $E_{l_{\max}\pm}$ and $M_{l_{\max}\pm}$. The Hermitian $4l_{\max} \times 4l_{\max}$ matrices $C_j^\alpha$ together with the multipole vectors form a bilinear product, which is a remnant from the mathematical definition of the polarization observables Eq. (3.3). The $C_j^\alpha$-matrices are of special interest as a coupling between multipoles, and thus partial-waves themselves, can directly be read of from the nonzero matrix elements. An example is shown in Table 3.3, in which two couplings between partial waves can be seen, i.e. $\langle l_{\max} = 0 | l_{\max} = 1\rangle$ and $\langle l_{\max} = 1 | l_{\max} = 2\rangle$. This can also be used to determine the dominant partial wave contributions from experimental polarization observable data, as was demonstrated in Ref. [Wunderlich et al., 2017]. The calculation of the $C_j^\alpha$-matrices is

Table 3.3: Shown are the matrix elements of the Hermitian matrix $C_1^{\sigma_0}$ for a truncation order of $l_{\max} = 2$. The contribution of different partial waves, as well as the corresponding multipoles, are indicated.

| | | $l_{\max} = 0$ | $l_{\max} = 1$ | | | $l_{\max} = 2$ | | | |
|---|---|---|---|---|---|---|---|---|---|
| | | $E_{0+}$ | $E_{1+}$ | $M_{1+}$ | $M_{1-}$ | $E_{2+}$ | $E_{2-}$ | $M_{2+}$ | $M_{2-}$ |
| $l_{\max} = 0$ | $E_{0+}$ | 0 | 3 | 1 | -1 | 0 | 0 | 0 | 0 |
| $l_{\max} = 1$ | $E_{1+}$ | 3 | 0 | 0 | 0 | 72/5 | -3/5 | 9/5 | -9/5 |
| | $M_{1+}$ | 1 | 0 | 0 | 0 | 0 | 1 | 27/5 | 3/5 |
| | $M_{1-}$ | -1 | 0 | 0 | 0 | 0 | -1 | 0 | 3 |
| $l_{\max} = 2$ | $E_{2+}$ | 0 | 72/5 | 0 | 0 | 0 | 0 | 0 | 0 |
| | $E_{2-}$ | 0 | -3/5 | 1 | -1 | 0 | 0 | 0 | 0 |
| | $M_{2+}$ | 0 | 9/5 | 27/5 | 0 | 0 | 0 | 0 | 0 |
| | $M_{2-}$ | 0 | -9/5 | 3/5 | 3 | 0 | 0 | 0 | 0 |

quite involved and shall not be discussed here. However, the formula can be found in the Appendix, Eq. (.52), of Ref. [Yannick Wunderlich, 2019], albeit an overall factor of $1/2$ is missing in the formula.

The application of a TPWA to real data in single pseudoscalar meson photoproduction, with the goal of extracting the complex multipole parameters from which predictions of not yet measured observables are deduced, is discussed in Chapter 5.

# Chapter 4

# Minimal complete sets for two-pseudoscalar-meson photoproduction

This chapter is based on the paper:

**Philipp Kroenert, Yannick Wunderlich, Farah Afzal, and Annika Thiel,**
**'Minimal complete sets for two-pseudoscalar-meson photoproduction',**
**Phys. Rev. C 103, 014607 (2021),**

which can be found in Ref. [Kroenert et al., 2021] and is included for convenience in Appendix A.1. Additionally, this chapter is partly based on the paper:

**Yannick Wunderlich, Philipp Kroenert, Farah Afzal, and Annika Thiel,**
**Moravcsik's theorem on complete sets of polarization observables reexamined,**
**Phys. Rev. C 102, 034605 (2020),**

which can be found in Ref. [Wunderlich et al., 2020].

## 4.1 Introduction

The first project of this thesis deals with the so-called complete experiment analysis (CEA) within the field of Baryon spectroscopy (BS). CEA is of particular importance for experimentalists in the field of BS, as it serves as an additional guideline on which future measurements should be pursued in order to push our understanding of the strong interaction. The overall goal of CEA is to identify how many and which polarization observables need to be measured in order to unambiguously determine the transition matrix $T$ of the reaction under consideration, as explained in Section 3.4. A set of observables which allows for this unambiguous determination is called a complete set of observables.

The reactions which are discussed in this chapter are pion-nucleon scattering

($N_a = 2$, $N_o = 4$), pseudoscalar meson photoproduction ($N_a = 4$, $N_o = 16$), pseudoscalar meson electroproduction ($N_a = 6$, $N_o = 36$) and finally two-pseudoscalar-meson photoproduction ($N_a = 8$, $N_o = 64$).

As already explained, the complexity to perform a CEA increases exponentially with the number of spin amplitudes $N_a$. Hence, for pion-nucleon scattering it is rather easy to show, via a single equation, that indeed all four polarization observables are needed to get an unambiguous result for the transition matrix [Anisovich et al., 2013]. Already for pseudoscalar meson photoproduction the situation is more complex. In total eight carefully selected polarization observables have to be measured for a complete set, as can be seen in Ref. [Chiang and Tabakin, 1997]. The calculations are quite involved but still can be performed analytically as was done in Ref. [Nakayama, 2019]. For the reaction of pseudoscalar meson electroproduction as well as for two-pseudoscalar-meson photoproduction, no comprehensive list of complete sets of polarization observables was available in the literature. Nevertheless, pioneering work on the CEA for these reactions exist, see Ref. [Tiator et al., 2017] and Ref. [Arenhövel and Fix, 2014].

In this thesis a graph theoretical approach to CEA via Moravcsik's theorem [Moravcsik, 1985] is chosen, to yield listings of complete sets of polarization observables for the before mentioned reactions. The simplicity of this analytic approach, its applicability regardless of the number of complex spin amplitudes $N_a$ in combination with its scalability (parallelization) makes it very appealing, especially for reactions which are described by more than four complex spin amplitudes.

The theorem reads as follows: Each of the complex spin amplitudes $t_i$ of the reaction is represented as a node of a graph. The edge between two nodes $t_i$ and $t_j$ can either be the real- or imaginary part of the product $t_i t_j^*$:

$$\mathrm{Re}(t_i t_j^*) = |t_i||t_j| \cos(\phi_{ij}), \tag{4.1}$$

$$\mathrm{Im}(t_i t_j^*) = |t_i||t_j| \sin(\phi_{ij}), \tag{4.2}$$

with the definition of the relative phase $\phi_{ij} = \phi_i - \phi_j$. An example for such a graph is shown in Fig. 4.1. A graph corresponds to a complete set of polarization observables if it fulfills two requirements with a detailed proof of the statements given in Appendix A of Ref. [Wunderlich et al., 2020]. First, it has to be a connected graph, which translates to fulfilling the 'consistency relation' [Nakayama, 2019] of the relative phases:

$$\phi_{12} + \phi_{23} + \cdots + \phi_{N1} = 0. \tag{4.3}$$

Second, the graph must have an odd number of edges which correspond to $\mathrm{Im}(t_i t_j^*)$ to resolve all discrete ambiguities. The reason for the second requirement can be seen as follows: The sine and cosine introduce a phase ambiguity, i.e. 'sine-type'- and 'cosine-type' ambiguities, respectively:

$$\sin(\phi_{ij}) = \sin(\pi - \phi_{ij}), \tag{4.4}$$

$$\cos(\phi_{ij}) = \cos(-\phi_{ij}). \tag{4.5}$$

First considering the case where all edges of the graph correspond to $\mathrm{Re}(t_i t_j^*)$. In such a scenario, the possible forms of Eq. (4.3) are:

$$\pm\phi_{12} \pm \phi_{23} \pm \cdots \pm \phi_{N1} = 0. \tag{4.6}$$

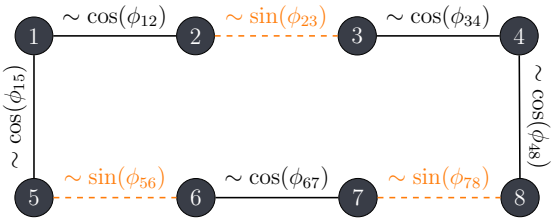


Figure 4.1: Example for a complete graph within Moravcsik's theorem [Moravcsik, 1985]. The nodes represent the eight complex spin amplitudes, necessary to fully describe the reaction of two-pseudoscalar-meson photoproduction. A solid line between node (i) and (j) corresponds to the real part of their bilinear product $\mathrm{Re}(t_i t_j^*)$, which is proportional to $\cos(\phi_{ij})$. In contrast, a dashed line corresponds to the imaginary part $\mathrm{Im}(t_i t_j^*)$ which is proportional to $\sin(\phi_{ij})$. The relative phase between the complex amplitude (i) and (j) is denoted with $\phi_{ij}$.

If a unique solution exists, for which no discrete ambiguities for the $t_i$ remain, it would be linearly independent of the remaining $2^N - 1$ possible solutions [Nakayama, 2019, Wunderlich et al., 2020]. Possible linear transformations are the multiplication with (-1) or the addition or subtraction of multiples of $2\pi$ [Wunderlich et al., 2020]. For the example in Eq. (4.6) none of the possible equations is linearly independent. Hence, a graph with all nodes corresponding to $\mathrm{Re}(t_i t_j^*)$ can not remove all discrete ambiguities. Now considering the introduction of $n$ sine-type ambiguities:

$$\pm\phi_{12} \pm \phi_{23} + \sum_{i}^{n} \begin{Bmatrix} \phi_{i,i+1} \\ \pi - \phi_{i,i+1} \end{Bmatrix} \pm \cdots \pm \phi_{N1} = 0. \tag{4.7}$$

If $n$ is an odd number, no equation can be transformed into another equation, because there is always one independent equation, due to a summand of $\pi$. However, for the case of $n$ being an even number, none of the possible equations is linearly independent. Thus, any odd number of sine-type ambiguities guarantees the resolution of all discrete ambiguities.

For completeness, the statements above are a modified version of Moravcsik's theorem as presented in Ref. [Moravcsik, 1985]. In particular, for a complete set of observables an odd number of sine-type ambiguities suffices and one does not need in addition an odd number of cosine-type ambiguities.

It follows a brief explanation on how to apply Moravcsik's theorem to extract complete set of observables. The following discussion is focused on graphs where all nodes are connected in a closed chain, and each node has exactly two edges. An example for such a graph is shown in Fig. 4.1. These type of graphs are also called cycle graphs and are "the most economical" [Moravcsik, 1985] ones to consider, as they have the lowest number of edges required for a complete set of observables.

The starting point is to construct all possible graph topologies given $N_a$ spin amplitudes. For the trivial case of $N_a = 2$ there is only one graph topology. For $N_a \geq 4$ the number of unique graph topologies is proportional to $N_a$ and given by

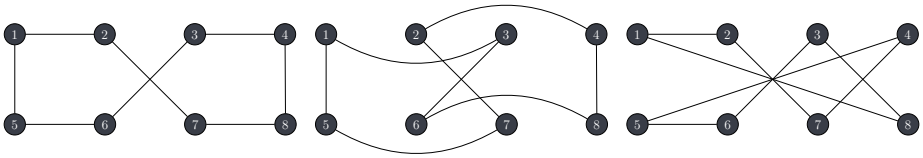

Figure 4.2: Three out of 2520 unique cycle graph topologies with eight nodes are shown. The nodes represent the eight complex spin amplitudes necessary to fully describe the reaction of two-pseudoscalar-meson photoproduction.

[Wunderlich et al., 2020]:

$$\frac{(N_\mathrm{a}-1)!}{2}. \tag{4.8}$$

The factor $N_\mathrm{a}-1$ comes from the constraint of considering only cyclic graphs, hence only $N_\mathrm{a}-1$ edges can be freely chosen. This results for $N_\mathrm{a}=4$ in 3, for $N_\mathrm{a}=6$ in 60 and for $N_\mathrm{a}=8$ in 2520 unique graph topologies. Figure 4.2 shows three exemplary graph topologies for $N_\mathrm{a}=8$.

In the next step, all possible combinations for an odd number of edges, corresponding to $\mathrm{Im}(t_i t_j^*)$, for each of the graph topologies have to be identified. The total number of suitable edge configurations is proportional to $N_\mathrm{a}$ and can be calculated by [Kroenert et al., 2021]:

$$\sum_{k=1}^{N_\mathrm{a}} \binom{N_\mathrm{a}}{k} \text{ for all odd } k \leq N_\mathrm{a}. \tag{4.9}$$

Which amounts for $N_\mathrm{a}=2$ to 2, $N_\mathrm{a}=4$ to 8, $N_\mathrm{a}=6$ to 32 and $N_\mathrm{a}=8$ to 128 possible edge configurations. An example for an edge configuration for $N_\mathrm{a}=8$ is shown in Fig. 4.1.

In the last step, the connection between the product $t_i t_j^*$ of two spin amplitudes to the polarization observables is used to extract a complete set of observables. Therefor, Eq. (3.3) can be rearranged to the following form [Wunderlich et al., 2020] and is here shown for the case of $N=8$:

$$t_i t_j^* = \frac{1}{8} \sum_{\alpha=1}^{64} \Gamma_{ij}^{\alpha} O^{\alpha}. \tag{4.10}$$

The $\Gamma$-matrices are used to mathematically define the polarization observables $O^\alpha$ in terms of Pauli matrices. For $N=8$, a complete list with the mathematical definition of the 64 polarization observables with relations to the notation of Roberts and Oed [Roberts and Oed, 2005] can be found in Table I in Ref. [Kroenert et al., 2021]. The same reference collects in Table II the definitions of the corresponding $\Gamma$-matrices. Equipped with these tools, the polarization observables required to pin down the respective sine or cosine values can be worked out. For the example

shown in Fig. 4.1 the following relations hold:

$$\sin(\phi_{23}) \curvearrowleft \{O_{s1}^{\mathrm{IV}}, O_{s2}^{\mathrm{IV}}, O_{s3}^{\mathrm{IV}}, O_{s4}^{\mathrm{IV}}\}, \tag{4.11}$$
$$\sin(\phi_{56}) \curvearrowleft \{O_{s1}^{\mathrm{III}}, O_{s2}^{\mathrm{III}}, O_{s3}^{\mathrm{III}}, O_{s4}^{\mathrm{III}}\}, \tag{4.12}$$
$$\sin(\phi_{78}) \curvearrowleft \{O_{s1}^{\mathrm{III}}, O_{s2}^{\mathrm{III}}, O_{s3}^{\mathrm{III}}, O_{s4}^{\mathrm{III}}\}, \tag{4.13}$$
$$\cos(\phi_{12}) \curvearrowleft \{O_{c1}^{\mathrm{III}}, O_{c2}^{\mathrm{III}}, O_{c3}^{\mathrm{III}}, O_{c4}^{\mathrm{III}}\}, \tag{4.14}$$
$$\cos(\phi_{15}) \curvearrowleft \{O_{c1}^{\mathrm{V}}, O_{c2}^{\mathrm{V}}, O_{c3}^{\mathrm{V}}, O_{c4}^{\mathrm{V}}\}, \tag{4.15}$$
$$\cos(\phi_{34}) \curvearrowleft \{O_{c1}^{\mathrm{III}}, O_{c2}^{\mathrm{III}}, O_{c3}^{\mathrm{III}}, O_{c4}^{\mathrm{III}}\}, \tag{4.16}$$
$$\cos(\phi_{48}) \curvearrowleft \{O_{c1}^{\mathrm{V}}, O_{c2}^{\mathrm{V}}, O_{c3}^{\mathrm{V}}, O_{c4}^{\mathrm{V}}\}, \tag{4.17}$$
$$\cos(\phi_{67}) \curvearrowleft \{O_{c1}^{\mathrm{IV}}, O_{c2}^{\mathrm{IV}}, O_{c3}^{\mathrm{IV}}, O_{c4}^{\mathrm{IV}}\}, \tag{4.18}$$

which results in the complete set of polarization observables:

$$\begin{aligned}\{&O_1^{\mathrm{I}}, O_2^{\mathrm{I}}, O_3^{\mathrm{I}}, O_4^{\mathrm{I}}, O_5^{\mathrm{I}}, O_6^{\mathrm{I}}, O_7^{\mathrm{I}}, O_8^{\mathrm{I}}, O_{s1}^{\mathrm{IV}}, O_{s2}^{\mathrm{IV}}, O_{s3}^{\mathrm{IV}}, O_{s4}^{\mathrm{IV}}, O_{c1}^{\mathrm{IV}}, O_{c2}^{\mathrm{IV}}, O_{c3}^{\mathrm{IV}}, O_{c4}^{\mathrm{IV}},\\ &O_{s1}^{\mathrm{III}}, O_{s2}^{\mathrm{III}}, O_{s3}^{\mathrm{III}}, O_{s4}^{\mathrm{III}}, O_{c1}^{\mathrm{III}}, O_{c2}^{\mathrm{III}}, O_{c3}^{\mathrm{III}}, O_{c4}^{\mathrm{III}}, O_{c1}^{\mathrm{V}}, O_{c2}^{\mathrm{V}}, O_{c3}^{\mathrm{V}}, O_{c4}^{\mathrm{V}}\}.\end{aligned} \tag{4.19}$$

Two important things can be read of from Eq. (4.19). On the one hand, all eight group I observables are in the set, despite not being required by the sine or cosine values. The reason is, that in Moravcsik's theorem it is assumed that the absolute value of all amplitudes $t_i$ are known, as is evident from Eqs. (4.1) and (4.2). The requirement can be realized by including all polarization observables expressed as sum of amplitude squares into a complete set. For two-pseudoscalar-meson photoproduction this would correspond to the eight observables of group $O^{\mathrm{I}}$ in Table 1 in Ref. [Kroenert et al., 2021], while for single pseudoscalar meson photoproduction it corresponds to the four type $\mathcal{S}$ observables as shown in Table 2 in Ref. [Kroenert et al., 2024]. However, one should keep in mind that the mathematical form of the polarization observables depends on the employed parametrization of the spin amplitudes $t_i$ in Eq. (3.3) and thus the observables defined only by amplitude squares change with a different parametrization. On the other hand, the set has a length of 28, which is larger than the empirically, minimal number of $2N_a = 16$, which is discussed further in Section 4.2.

To proof the correctness of Moravcsik's theorem, the well-known CEA results for $N_a = 2$ and $N_a = 4$ spin amplitudes were reproduced. Indeed, for $N_a = 2$ the well-known statement that all four polarization observables are needed for a complete set of observables was replicated [Wunderlich et al., 2020]. For $N_a = 4$, the situation is more complex. In total 12 non-redundant sets, each containing 10 polarization observables, were found. These sets are slightly over-complete compared to [Chiang and Tabakin, 1997], in the sense that the minimal number of polarization observables to form a complete set is eight for $N_a = 4$. It turns out, that the complete sets found in Ref. [Chiang and Tabakin, 1997] are subsets of the 12 slightly over-complete sets found by Moravcsik's theorem. From the 12 slightly over-complete sets of 10 polarization observables, all complete sets containing exactly 8 polarization observables could be extracted via a numerical algorithm, for details see the Appendix in Ref. [Kroenert et al., 2021].

In a second step, Moravcsik's theorem was applied onto pseudoscalar meson electroproduction ($N_a = 6$). In total 776 slightly over-complete sets were found.

This includes complete sets with 13 up to 18 polarization observables. All Moravcsik complete sets with in total 13 or 14 polarization observables are collected in Appendix D in Ref. [Wunderlich et al., 2020], which is the first comprehensive listing of complete sets for pseudoscalar meson electroproduction.

Finally, Moravcsik's theorem was applied to two-pseudoscalar-meson photoproduction ($N_a = 8$), which lead to the publication in Ref. [Kroenert et al., 2021], and is included in Appendix A.1.

## 4.2 Summary

Moravcsik's graph theoretical approach to CEA was first applied to pion-nucleon scattering and pseudoscalar meson photoproduction in order to reproduce the well known results for these reactions, as stated in Ref. [Anisovich et al., 2013] and Ref. [Chiang and Tabakin, 1997]. Afterward, the procedure was applied to pseudoscalar meson electroproduction, which yielded for the first time a comprehensive list of complete sets for this reaction, which are listed in Appendix D of Ref. [Wunderlich et al., 2020]. The conduction of a CEA by means of Moravcsik's theorem for pion-nucleon scattering, pseudoscalar meson photoproduction and electroproduction resulted in the publication of Ref. [Wunderlich et al., 2020] in Physical Review C. My contribution to this paper was the development of a computer program suitable to extract complete sets of polarization observables via Moravcsik's theorem. With this program I calculated the results of pion-nucleon scattering ($N_a = 3$) (mathematical example), pseudoscalar meson photoproduction ($N_a = 4$) and pseudoscalar meson electroproduction ($N_a = 6$), where $N_a$ denotes the number of complex spin amplitudes to describe the reaction. In addition, I developed the code which was used to generate the figures in the paper.

It was observed that Moravcsik's theorem yielded slightly over-complete sets for pseudoscalar meson photoproduction and electroproduction. This means that the number of polarization observables in each complete set is larger than the empirically, minimal required number of $2N_a$. Nevertheless, complete sets with the minimal length can be extracted as subsets from the slightly over-complete sets, by means of a numerical algorithm as outlined in the Appendix of Ref. [Kroenert et al., 2021].

Finally, I applied Moravcsik's theorem onto two-pseudoscalar-meson photoproduction ($N_a = 8$). In general, the polarization observables for two-pseudoscalar-meson photoproduction can be grouped into eight so-called shape classes. The shape-classes are distinguished by the position of the nonzero matrix elements of the respective $\Gamma$-matrices, see Table II in Ref. [Kroenert et al., 2021]. For an easier calculation of the 64 $\Gamma$-matrices, I worked out their definition in terms of the well-known Pauli matrices.

In total 5964 slightly over-complete sets were found, which includes complete sets with 24 up to 40 polarization observables. There are 392 non-redundant sets with a length of 24 which were used as a starting point to determine subsets with a minimal number of polarization observables still forming a complete set. Thus, the possible number of to be analyzed subsets, with the minimal length of 16 (as

the eight observables of the first shape class are always a member of a complete set), are:

$$392 \cdot \binom{16}{8} = 5\,045\,040. \tag{4.20}$$

Till the publication of the paper, 4185 complete sets with a minimal length have been found. Each of the 4185 minimal complete sets contain polarization observables from exactly four different shape classes.

In addition, an example for the algebraic derivation of complete sets for $N_a = 8$ by reference to the phase-fixing approach developed by Nakayama [Nakayama, 2019] is shown. The important steps of the method are outlined within the paper and a detailed calculation can be found in the supplement material of Ref. [Kroenert et al., 2021]. The resulting minimal complete sets are listed in Table VII of Ref. [Kroenert et al., 2021]. The derivation of these results, the writing of paragraph "B. Algebraic phase-fixing method" and the corresponding supplement material was contributed to the paper by Dr. Yannick Wunderlich.

One focus of the paper laid on the experimental verification of the identified complete sets, i.e. the measurement of a complete set in the near future. This means in particular, that a complete set should have a minimal number of triple polarization observables, as yet the first have to be measured. Therefore, the 4185 complete sets were filtered and indeed 69 complete sets with only one triple polarization observable were found and are shown in Table V of Ref. [Kroenert et al., 2021]. The only remaining triple polarization observable is $O^{\odot}_{yy'}$ and belongs to shape class I, in which all Γ-matrices are diagonal matrices. To further assist experimentalists in planning future experiments, I composed a detailed list of previous measurements in the field of two-pseudoscalar-meson photoproduction. This encompasses in total 55 measurements from eight different reactions, listed in Table IV in Ref. [Kroenert et al., 2021]. With the knowledge from this extended list of measurements, the most promising reaction is $\gamma p \to \pi^0\pi^0 p$ in combination with the complete set:

$$I^{\odot}, P_y, P_{y'}, O^{\odot}_{yy'}, O_{yy'}, P^{\odot}_{y'}, P^{\odot}_{y}, I_0, P_x, P_z, P_{x'}, P^{s}_{x}, P^{\odot}_{x}, P^{c}_{z}, P^{\odot}_{z}, P^{\odot}_{x'}. \tag{4.21}$$

From these sixteen polarization observables, already eight have been measured, and the remaining eight observables could be measured within three more experiments [Kroenert et al., 2021].

As an outlook, the outlined approach can be optimized by moving the computations on a computer cluster, to utilize the parallelization capability of the problem. Thus, all the 5 045 040 possible subsets for $N_a = 8$ could be tested for completeness. In addition, one could think of removing the last remaining triple polarization observable $O^{\odot}_{yy'}$ in the minimal complete sets, by studying alternative ways to ensure the knowledge of all absolute spin amplitude values without relying solely on polarisation observables defined by diagonal Γ-matrices.

# Chapter 5

# Truncated partial-wave analysis utilizing Bayesian inference

This chapter is based on the paper:

**Philipp Kroenert, Yannick Wunderlich, Farah Afzal, and Annika Thiel, "Truncated Partial-Wave Analysis for $\eta$-photoproduction observables via Bayesian Statistics", Phys. Rev. C 109, 045206 (2024).**

The paper can be found in Ref. [Kroenert et al., 2024] and is included for convenience in Appendix A.2.

## 5.1 Introduction

The first project of this thesis was the theoretical prediction of complete sets of polarization observables via a complete experiment analysis (CEA), which can be found in Chapter 4. However, as discussed in Section 3.4, the results of a CEA are only valid in the case of experimental data points without any uncertainty, which means for the analysis of real data one might still encounter ambiguities. Therefore, the second project of this thesis follows a complementary approach and studies the emergence of such ambiguities within a truncated partial-wave analysis (TPWA) on real data. In case of a TPWA mainly so-called accidental ambiguities arise, see Sec III.A in Ref. [Kroenert et al., 2024]. This special type of ambiguity can not be circumvented entirely and emerges from a limited numerical precision or the immanent uncertainty in experimental data. However, these accidental ambiguities often produce just minor ambiguities, i.e. those which can be clearly distinguished from the 'true' physical solution.

In general, a TPWA uses polarization data to estimate the parameters with which the matrix elements of the transition operator are modeled. In this analysis, these are the so-called multipole parameters. Compared to a full partial-wave analysis (PWA), a TPWA is less sophisticated, i.e. it is not a coupled channel approach and performs the fit at single energies. Having said that, the TPWA approach is

more straight forward and the most appealing point, it is a model independent approach, in comparison to a full PWA. For more details on this topic see Section 3.5.2.

The selection of an appropriate data set for the analysis depends on several aspects. On the one hand, the chosen data sets must form a mathematical complete set for a TPWA. On the other hand, one of the final results of the analysis is intended to be the evolution of the multipole parameters as a function of the energy. Thus, the experimental data should cover as large an energy range as possible. Considering the latest available data on polarization observables for pseudoscalar meson photoproduction, see Section 5 in [Thiel et al., 2022], the reaction $\gamma p \to \eta p$, also known as $\eta$-photoproduction, was chosen. The polarization observables $\sigma_0$, $\Sigma$, $T$, $E$, $F$ and $G$ form a complete set, see Appendix A in Ref. [Kroenert et al., 2024] (the derivation is a contribution to the paper by Dr. Yannick Wunderlich), and experimental data are available for the energies 750 MeV, 850 MeV, 950 MeV, 1050 MeV, 1150 MeV and 1250 MeV (laboratory frame) which is right above the production threshold of $E^{\text{lab}} \approx 708\,\text{MeV}$, or equivalently $W = m_\eta + m_p \approx 1486\,\text{MeV}$ in the center of mass frame. The reaction of $\eta$-photoproduction is very well suited to study $N^*$ resonances as these are the only allowed resonances in the intermediate state, because of the isospin conservation in the strong interaction.

Previous work on the application of a TPWA to meson photoproduction using real data do exist. Hereby the classical approach of Frequentist statistics was used for the analysis of emerging ambiguities and the estimation of multipole parameters. See for example, Ref. [Sandorfi et al., 2011], where the authors analyzed the reaction $\gamma p \to K^+\Lambda$, i.e. strangeness photoproduction. As the data situation at the time did not allow for the use of a complete set of observables, many ambiguities were present in the result. Another example can be found in Ref. [Yannick Wunderlich, 2019], in which experimental data of the reaction $\gamma p \to \pi^0 p$ were analyzed. In this reference, the classical approach was used as well, but first attempts were made to use the bootstrap method [Efron, 1992] for estimating the errors of the regression parameters.

In this thesis the more advanced method of Bayesian inference is combined for the first time with TPWA. Therefore, the results of the analyses, i.e. the model parameters as well as the reproduced- and predicted data are given as distributions which are accompanied by excellent error estimates. This is in contrast to the Frequentist approach, where one gets point estimates for the model parameters and has to take further steps to get accurate error estimates. An additional improvement of Bayesian inference is its ability to reveal the structure of ambiguities and their connection in parameter space. For example, in cases where multiple ambiguities, i.e. posterior modes, are traversed within one MCMC chain, they tend to have comparable log posterior densities, i.e. contribute with a comparable probability mass to the posterior, which is typically a sign of a severe ambiguity. This phenomenon is shown in Fig. 5.1, where the contributions of the two peaks on the left side of the distribution can not be distinguished, the same is true for the two peaks on the right side of the distribution.

The multimodal posterior in a TPWA, arising from the presence of ambiguities, makes the situation for monitoring the MCMC convergence diagnostics rather

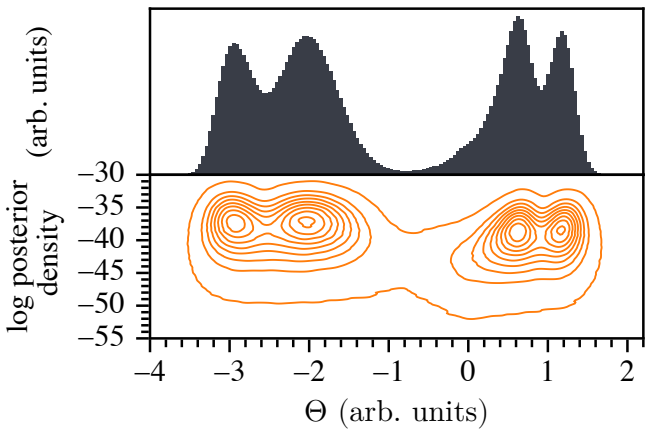


Figure 5.1: Illustration of connected ambiguities. The upper part of the figure shows the histogram of the marginal distribution of parameter Θ with four visible modes. Each mode represents one ambiguity. The lower part shows the corresponding log posterior density (LPD) as a two-dimensional histogram. The highest LPD of the two left modes can not be distinguished, and thus it is not clear which mode contributes more probability mass to the posterior, which is the definition of a severe ambiguity. The same is true for the two right modes.

complex. At first, it was not clear whether a chain has not converged yet or indeed traversed multiple relevant modes. Such a scenario is illustrated in Fig. 5.2, where the evolution of one MCMC chain is shown, exploring two distinct regions in parameter space. Furthermore, in situations where not all MCMC chains have traversed the same modes, but rather get stuck in isolated modes, a way has to be figured out how to still be able to monitor the global convergence and achieve the anticipated MCMC diagnostics. Thus, the procedure for the MCMC convergence diagnostics, see Section 2.5, had to be adapted compared to the normal approach.

## 5.2 Summary

Truncated partial-wave analyses were performed, utilizing for the first time the statistical method of Bayesian inference, for $\eta$-photoproduction and the energies 750 MeV, 850 MeV, 950 MeV, 1050 MeV, 1150 MeV and 1250 MeV (lab frame), which are just above the production threshold. Hereby, the experimental values of the six polarization observables $\sigma_0$, $\Sigma$, $T$, $E$, $F$ and $G$ were used to study the result of multiple truncation orders $l_{\max}$. In order to accomplish this, for each energy a posterior distribution was implemented, considering statistical and systematic uncertainties as well as correlations between the used data sets. The priors were chosen conservatively: uniform priors for the multipole parameters with bounds defined by the physically allowed regions of the parameters and Gaussian priors centered around a value of one for the scaling parameters, which model the systematic uncertainties. In this way, the priors are uninformative compared to the likelihood distribution but at the same time include prior physical knowledge.

First, the implemented posteriors were tested on generated data, from the Eta-

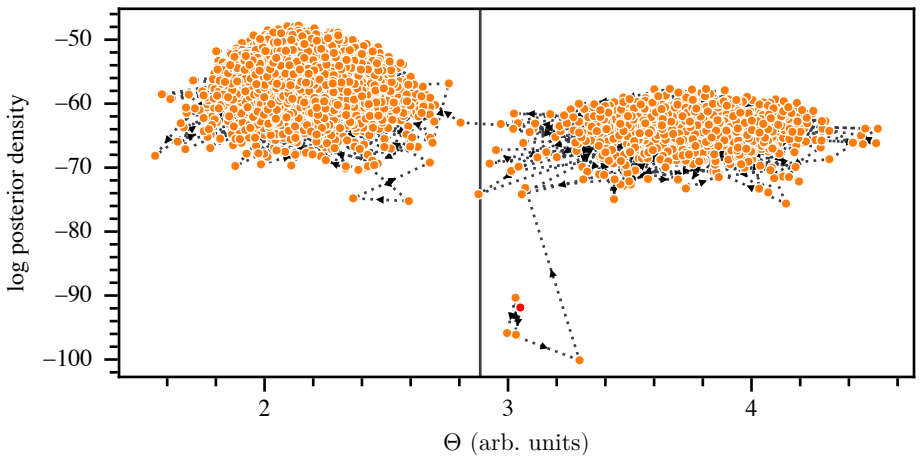


Figure 5.2: Illustration of convergence problematic with a multimodal posterior distribution. The emergence of two distinct clusters is visible, i.e. two modes in the marginal parameter distribution of Θ. The complexity lies in the assessment of whether the chain has not converged yet or the marginal distribution is indeed multimodal. Shown are the first $10^4$ sampling points, where the color of the very first sampling point is red. The order of sampling points is indicated via arrows. The black vertical line corresponds to the initial value of the MCMC chain.

MAID2018 [Tiator et al., 2018] solution, were the results of the multipoles are known a priori and can be compared to the results of the Bayesian analysis. An example for the energy of $E_\gamma^{\text{lab}} = 750\,\text{MeV}$ and a truncation order of $l_{\max} = 2$ is shown in Fig. 5.3 . The upper part of the figure depicts the solutions found for the parameter $\text{Re}(E_{0+})$ via a Monte Carlo maximum a posteriori (MAP) estimation normalized by the number of degrees of freedom. The errors were estimated via the inverted Hesse matrix. The lower part of the figure shows the solutions, i.e. the marginal distributions of $\text{Re}(E_{0+})$, found with Bayesian inference. Hereby the MAP values were used as starting points for the MCMC sampling. In total five solutions, i.e. ambiguities, are visible within Fig. 5.3. The 'best' solution according to $\chi^2/\text{ndf}$ is at a value of $\text{Re}(E_{0+}) = 19.884622\,\text{am}$. The corresponding marginal distribution (orange color) has its median value at $\text{Re}(E_{0+}) = 19.83915\,\text{am}$. Hence, to generate the data in the first place, a value of $\text{Re}(E_{0+}) = 19.8846\,\text{am}$ from EtaMAID2018 was used. Thus, the maximum likelihood estimation as well as the marginal distribution were able to recover the truth of the generated data with sufficient precision, indicating the correct working of the implemented methods.

After this sanity check, the analysis was applied to the experimentally measured data. The MCMC sampling was performed for the truncation orders $l_{\max} = 1$ and $l_{\max} = 2$ for all energies. In addition, the truncation order of $l_{\max} = 3$ was investigated for the energy of 1250 MeV. A considerable increase in accidental ambiguities could be observed, where in total 43 posterior modes were identified. This amount of ambiguities makes the securing of adequate MCMC convergence diagnostics rather complex and computationally extremely demanding. Thus, the analysis of $l_{\max} > 2$ is postponed for future research.

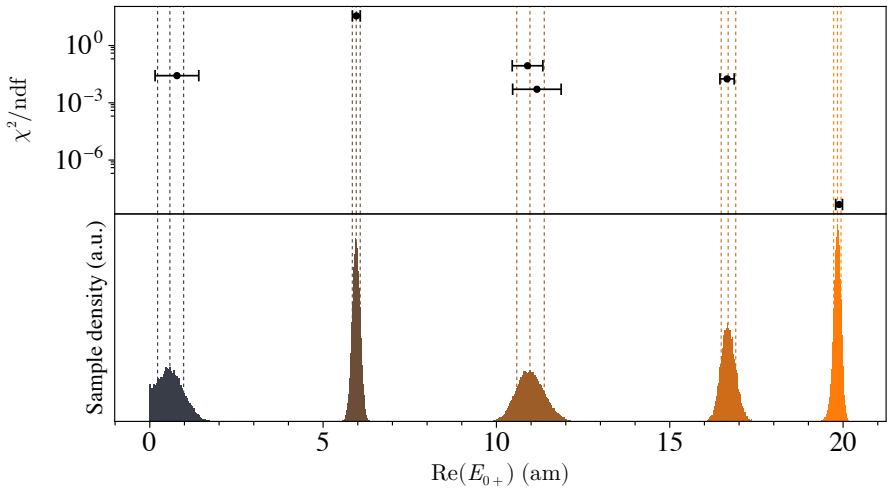


Figure 5.3: Shown is the result for Re($E_{0+}$) using a Bayesian inference with generated data for an energy of $E_\gamma^{\text{lab}} = 750\,\text{MeV}$ and a truncation order of $l_{\text{max}} = 2$. The upper part of the figure shows the results from a maximum likelihood estimation, where the errors are estimated via the Hesse matrix. The lower part of the figure depicts the marginal distributions, where the respective [15.9, 50, 84]-% quantiles are shown as dashed lines.

The electromagnetic multipole parameters were estimated as distributions and the results were compared with the MAP solutions. It was observed that MAP results with rather high $\chi^2$/ndf values are not present in the marginal parameters distributions, most likely because they are too far from the 'typical set', i.e. the region which contributes most to the expectation value of the posterior.

In a second step, reproduced data distributions were calculated from the estimated electromagnetic multipole parameters as an additional check for the models. The distributions were analyzed for systematic effects from which an appropriate maximal angular momentum of $l_{\text{max}} = 2$ was concluded, able to describe the used experimental data. At the same time, no higher angular momentum contributions were visible within the data. Closely related to this phenomenon is the impact of emerging $N^*$ resonances onto the reproduced data distributions, coming from couplings to angular momenta $\ell > 1$. It was concluded that most likely a contribution of the resonances $N(1675)5/2^-$ and/or $N(1700)3/2^-$ are visible within the used polarization observables.

In a next step, predicted data distributions are calculated from the estimated electromagnetic multipole parameters at a truncation order of $l_{\text{max}} = 2$. This includes predictions for the remaining ten polarization observables of $\eta$-photoproduction which were not included in the analysis, i.e. $H$, $P$, and the not yet measured observables $O_{x'}$, $O_{z'}$, $C_{x'}$, $C_{z'}$, $L_{x'}$, $L_{z'}$, $T_{x'}$ and $T_{z'}$. On the basis of the functional behavior of the predicted distributions over the $\cos(\theta)$-range, a list of observables was identified for each analyzed energy, which could resolve the remaining accidental ambiguities. Specifically, the polarization observable $C_{z'}$ seems promising

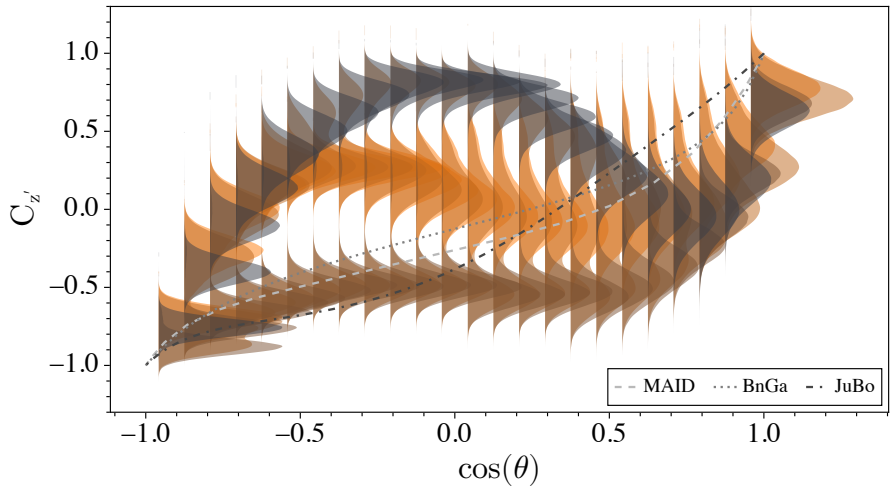


Figure 5.4: Predicted data distribution for the polarization observable $C'_z$ for an energy of $E_\gamma^{\text{lab}} = 950\,\text{MeV}$. Different solutions, i.e. ambiguities, are indicated via different colors. In addition, the solution of the partial partial-wave analysis models MAID [Tiator et al., 2018], BnGa [Anisovich et al., 2016] and JuBo [Rönchen et al., 2022] are shown for comparison.

to reduce the number of ambiguities at all six energy bins. An example is shown in Fig. 5.4, where measurement data favoring one of the three main functional behaviors would indeed help to rule out the others. Within the paper, the color coding for different ambiguities at a certain energy is kept consistent for the multipole-, reproduced- and predicted plots. Hence, the influence of a certain ambiguity onto the results can be studied.

Additionally, the model independent results of the TPWA, i.e. the evolution of the estimated multipole parameter distributions as a function of energy, as well as the predicted data distributions, are compared with the model-dependent partial-wave analysis results and predictions of BnGa [Anisovich et al., 2016], JuBo [Rönchen et al., 2022] and MAID [Tiator et al., 2018]. One example of each is shown in Fig. 5.5. Where Fig. 5.5a, the overall agreement between truncated partial-wave analysis and the partial-wave models can be seen, and Fig. 5.5b shows that different ambiguities sometimes predict a different functional behavior of the data distributions (see also Fig. 5.4). In general, the results for the multipole parameters of the approaches are consistent, except for $\text{Im}(E_{2+})$ where none of the approaches coincide.

Summarizing, for the first time truncated partial-wave analysis were combined with Bayesian inference. The utilization of MCMC sampling made it possible to study the connection between ambiguities in a new way and yields a clear indication of severe ambiguities, i.e. when multiple MCMC chains sample consistently multiple marginal modes together.

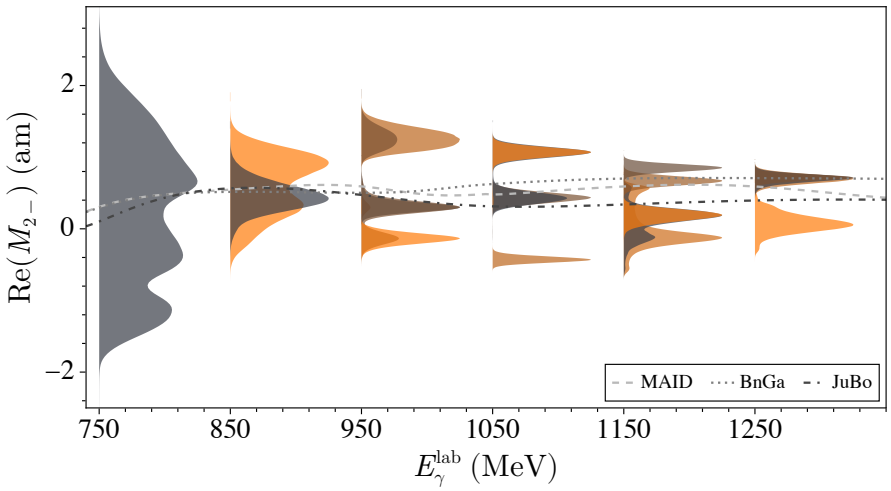


(a) Shown is the evolution of the multipole parameter Re($M_{1-}$) over the energy range of $E_\gamma^{\text{lab}}$ = [750, 1250] MeV.

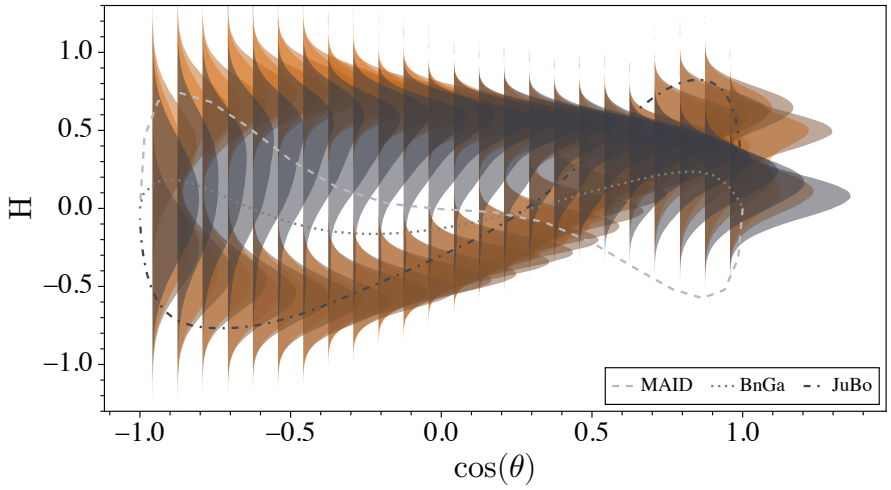


(b) Shown are the predicted data distribution of the polarization observable H for an energy of $E_\gamma^{\text{lab}}$ = 1250 MeV.

Figure 5.5: Examples for (a) the evolution of a multipole parameter with regard to the energy and (b) the predicted data distributions for the polarization observable H. Different solutions, i.e. ambiguities, are indicated via different colors (for (a) on a per-energy basis). In addition, the solution of the partial partial-wave analysis models MAID [Tiator et al., 2018], BnGa [Anisovich et al., 2016] and JuBo [Rönchen et al., 2022] are shown for comparison.

# Part II

# Neutrino mass analysis

# Chapter 6

# Neutrino mass analysis with KATRIN

The main focus of this chapter is the explanation of the measurement of the absolute mass of electron anti-neutrinos with the KArlsruhe TRItium Neutrino (KATRIN) experiment. The chapter starts with a general introduction into the topic and a motivation for massive neutrinos in Section 6.1 by discussing the mathematical framework and the experimental evidence of neutrino oscillations. Afterward, the measurement approach of the KATRIN experiment is discussed in 6.2, followed by the experimental setup with its major components in Section 6.3. In Section 6.4 the KATRIN model is discussed, i.e. the expected count rate of $\beta$-electrons from tritium decay. Section 6.5 deals with the systematic effects in the KATRIN experiment, before the mathematical form of the KATRIN likelihood is discussed in Section 6.6. Finally, the collected measurement data of the first five KATRIN campaigns are presented in Section 6.7.

## 6.1 Introduction

In the classical Standard Model of particle physics all three generations of neutrinos are massless. The very first step onto the conclusion of massive neutrinos, and an extension of the Standard Model, was a paper published by R. Davis, Jr. et al. in the year 1968, see Ref. [Davis et al., 1968], on the experimental detection of electron neutrinos $\nu_e$ originating from the sun. The experiment was located at the Homestake gold mine at Lead, South Dakota, and used the inverse $\beta$-decay $\nu_e + {}^{37}_{17}\mathrm{CL} \rightarrow {}^{37}_{18}\mathrm{Ar} + e^-$. To infer the amount of electron neutrinos coming from the sun, the produced argon atoms were chemically extracted, and their decay was closely observed [Navas et al., 2024]. The measured production rate was $0.478 \pm 0.03$ (statistical) $\pm$ 0.029 (systematic) counts per day with an expected rate in the range of 1.2 to 1.7 counts per day [Navas et al., 2024]. This massive discrepancy between expected and observed rate is known as the solar neutrino problem.

This was further investigated by the Super-Kamiokande collaboration by studying atmospheric neutrinos to see if the problem persists for this type of neutrino source. Their detection medium was a 50 kt water-Cherenkov detector situated

in the Kamioka mine in Japan [Fukuda et al., 1998] and was utilized to study neutrino interactions with nuclei $N$ via the reaction $\nu + N \rightarrow l + X$. Because the final state leptons $l$ are relativistic, they produce Cherenkov radiation, which is then detected by a fraction of the in total 11 146 photomultiplier tubes. A flux ratio, defined by the measured number of muon $n_\mu$ and electron $n_e$ like events and the corresponding theoretical expectations in the form of Monte Carlo data were found to be $R := (n_\mu/n_e)_{\text{data}}/(n_\mu/n_e)_{\text{MC}} = 0.63 \pm 0.03$ (statistical) $\pm$ 0.05 (systematic) [Fukuda et al., 1998]. In addition, the zenith angle $\theta_z$ distribution for muon like events revealed a deficit of upward going, i.e. $-1 < \cos(\theta_z) < -0.2$, events [Fukuda et al., 1998, Navas et al., 2024].

A few years later, the results from the Sudbury Neutrino Observatory (SNO) located in Canada were published. As in the case of Super-Kamiokande a water-Cherenkov detector was used, likewise situated in an old mine. By studying charged- and neutral current reactions, as well as elastic scattering, the electron-neutrino flux $\phi_e$, originating from the sun, together with the combined flux of muon- and tau-neutrinos $\phi_{\mu\tau}$ were accessible. The combined flux was measured to be $\phi_{\mu\tau} = 3.41^{+0.45}_{-0.45}$ (statistical)$^{+0.48}_{-0.45}$ (systematic) $\times 10^6\,\text{cm}^{-2}\text{s}^{-1}$, which is $5.3\,\sigma$ above the expected value of zero [Ahmad et al., 2002] and thus provides strong evidence for physics beyond the Standard Model.

### 6.1.1 Neutrino oscillation

To explain the strong discrepancies between the Standard Model predictions and the experimentally measured count rates of neutrinos, the framework of neutrino oscillations was developed. Within this theory, a neutrino with flavor $\alpha$ can transition to flavor $\beta$ with a non-zero probability, where $\alpha, \beta \in (e, \mu, \tau)$. The mixing or oscillation between neutrino flavors can be described by the unitary Pontecorvo–Maki–Nakagawa–Sakata (PMNS) matrix [Thomson, 2013]:

$$U_{\text{PMNS}} = \begin{pmatrix} U_{e1} & U_{e2} & U_{e3} \\ U_{\mu 1} & U_{\mu 2} & U_{\mu 3} \\ U_{\tau 1} & U_{\tau 2} & U_{\tau 3} \end{pmatrix}. \tag{6.1}$$

The matrix connects the neutrino states participating in the weak interaction, also called flavor-eigenstates $(\nu_e, \nu_\mu, \nu_\tau)$, with so-called mass eigenstates $(\nu_1, \nu_2, \nu_3)$:

$$\begin{pmatrix} \nu_e \\ \nu_\mu \\ \nu_\tau \end{pmatrix} = U_{\text{PMNS}} \begin{pmatrix} \nu_1 \\ \nu_2 \\ \nu_3 \end{pmatrix}. \tag{6.2}$$

The following formalism is the same for Majorana and Dirac neutrinos. Solely the free parameters of the PMNS matrix changes slightly, which can be seen by decomposing the matrix according to the oscillation parameters. In the case of Majorana neutrinos, there are six oscillation parameters, i.e. three mixing angles and three phases [Navas et al., 2024]:

$$U_{\text{PMNS}}^{\text{Majorana}} := \begin{pmatrix} 1 & 0 & 0 \\ 0 & c_{23} & s_{23} \\ 0 & -s_{23} & c_{23} \end{pmatrix} \begin{pmatrix} c_{13} & 0 & s_{13}e^{-i\delta} \\ 0 & 1 & 0 \\ -s_{13}e^{i\delta} & 0 & c_{13} \end{pmatrix} \begin{pmatrix} c_{12} & s_{12} & 0 \\ -s_{12} & c_{12} & 0 \\ 0 & 0 & 1 \end{pmatrix} \begin{pmatrix} e^{i\eta_1} & 0 & 0 \\ 0 & e^{i\eta_2} & 0 \\ 0 & 0 & 1 \end{pmatrix}. \tag{6.3}$$

In the case of Dirac neutrinos, there are four oscillation parameters, i.e. three mixing angles and one phase [Navas et al., 2024]:

$$U_{\text{PMNS}}^{\text{Dirac}} := \begin{pmatrix} 1 & 0 & 0 \\ 0 & c_{23} & s_{23} \\ 0 & -s_{23} & c_{23} \end{pmatrix} \begin{pmatrix} c_{13} & 0 & s_{13}e^{-i\delta} \\ 0 & 1 & 0 \\ -s_{13}e^{i\delta} & 0 & c_{13} \end{pmatrix} \begin{pmatrix} c_{12} & s_{12} & 0 \\ -s_{12} & c_{12} & 0 \\ 0 & 0 & 1 \end{pmatrix}. \tag{6.4}$$

The shorthand notation $s_{ij} := \sin(\theta_{ij})$, $c_{ij} := \cos(\theta_{ij})$ was used. The three mixing angles are denoted with $\theta_{\text{ij}}$, the Majorana phases with $\eta_1, \eta_2$ and the Dirac phase with $\delta$.

Equation (6.2) involves the weak eigenstates $|\nu_\alpha\rangle$ and the mass eigenstates $|\nu_k\rangle$. Hence, each weak eigenstate is a superposition of three mass eigenstates. A freely propagating neutrino state at coordinates $(x,t)$ is described in quantum theory by wave packets as [Akhmedov and Smirnov, 2009]:

$$|\nu_\alpha(x,t)\rangle := \sum_{\text{k}=1}^{3} U_{\alpha\text{k}}^{*} \Psi_{\text{k}}(x,t)\,|\nu_{\text{k}}\rangle\,, \qquad \text{with } \alpha \in \{e,\mu,\tau\}, \tag{6.5}$$

with the wave packet:

$$\Psi_{\text{k}}(x,t) := \frac{1}{(2\pi)^{3/2}} \int \mathrm{d}p\, f_{\text{k}}^{\text{S}}(p-p_{\text{k}}) e^{ipx - iE_{\text{k}}t}. \tag{6.6}$$

The function $f_{\text{k}}^{\text{S}}(p-p_{\text{k}})$ describes the momentum distribution for a neutrino produced in the source S, with mean momentum $p_{\text{k}}$. The probability for a flavor transition from state $\alpha$ to $\beta$ after the neutrino has traveled the distance $L$ is given by the absolute square of the amplitude [Akhmedov and Smirnov, 2009]:

$$P_{\nu_\alpha \to \nu_\beta}(L) := \int_{-\infty}^{\infty} \mathrm{d}t \left|A_{\alpha\beta}(L,t)\right|^2, \tag{6.7}$$

$$= \sum_{\text{kj}} U_{\alpha\text{k}}^{*} U_{\beta\text{k}} U_{\alpha\text{j}} U_{\beta\text{j}}^{*} I_{\text{kj}}(L), \tag{6.8}$$

where

$$I_{\text{kj}}(L) := \int_{-\infty}^{\infty} \mathrm{d}t\, G_{\text{k}}(L - v_{\text{g,k}}t) G_{\text{j}}^{*}(L - v_{\text{g,j}}t) e^{-i\Delta\phi_{\text{kj}}(L,t)}. \tag{6.9}$$

The symbols $v_{\text{g,k}}$ depict the group velocity of the particular wave packet of the respective neutrino mass eigenstate, and $G_{\text{k}}$ is the shape factor of the k−th neutrino mass eigenstate. The phase difference between the k-th and j-th mass eigenstate is given by:

$$\Delta\phi_{\text{kj}}(L,t) := (E_{\text{k}} - E_{\text{j}})t - (p_{\text{k}} - p_{\text{j}})L. \tag{6.10}$$

Under the assumption of relativistic neutrinos and performing a Taylor expansion of the momenta, one gets [Akhmedov and Smirnov, 2009]:

$$\Delta\phi_{\text{kj}}(L,t) = \frac{(m_{\text{k}}^2 - m_{\text{j}}^2)}{2p} L - \frac{1}{v_{\text{g}}}(L - v_{\text{g}}t)(E_{\text{k}} - E_{\text{j}}), \tag{6.11}$$

with the masses $m_k$ and $m_j$, average group velocity $v_{\text{g}}$ and average momentum $p$ of the two mass eigenstates. In general, $\left|L - v_{\text{g}}t\right|$ is smaller or equal to the length of the

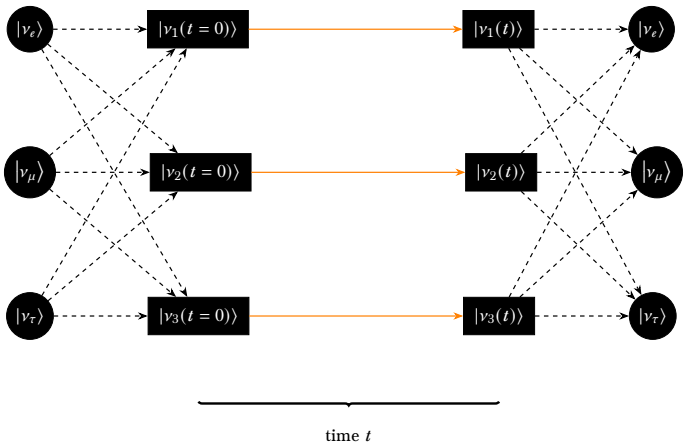


Figure 6.1: Schematic illustration of the three flavor neutrino oscillation in terms of the combination, propagation and recombination of neutrino mass eigenstates $\nu_k$. The dashed lines indicate the relative content of the neutrino flavor eigenstates. Adapted from [Smirnov, 2017].

wave packet, else the shape factors $G_\mathrm{i}$ would suppress the oscillation [Akhmedov and Smirnov, 2009]. In the case, that the neutrino oscillation length is much larger than the effective length of the wave packets, the second tern in Eq. (6.11) becomes negligible [Akhmedov and Smirnov, 2009] and the oscillation probability Eq. (6.8) takes the well known form:

$$P_{\nu_\alpha \to \nu_\beta}(L) = \sum_{\mathrm{kj}} U^*_{\alpha\mathrm{k}} U_{\beta\mathrm{k}} U_{\alpha\mathrm{j}} U^*_{\beta\mathrm{j}} e^{-i\frac{m^2_\mathrm{k} - m^2_\mathrm{j}}{2p} L}. \tag{6.12}$$

Thus, the probability for a transition of flavor state $\alpha$ into flavor state $\beta$ detected at length $L$ depends on $L$ itself, the elements of the PMNS matrix, the average momentum of the mass eigenstates and most importantly the difference of the squared masses of the mass eigenstates. This implies that at least two mass eigenstates have to have a nonzero mass for the oscillation effect to occur. A schematic illustration of neutrino oscillation, in terms of the combination, propagation and recombination of mass eigenstates is shown in Fig. 6.1.

### 6.1.2 Experimental verification of massive neutrinos

Multiple experiments are dedicated to neutrino oscillations and the measurement of the oscillation parameters in Eq. (6.12). The experiments can be grouped by the type of neutrino source and are sensitive to different oscillation parameters. The following list shows a selection: Solar neutrinos (Gallex, SNO, Borexino, SAGE), atmospheric neutrinos (IceCube, Super-Kamiokande), reactor neutrinos (KamLAND, Double-Chooz, Daya-Bay, Reno), accelerator neutrinos (MINOS, T2K, NOvA). The NuFIT collaboration [Esteban et al., 2024a] performed a global analysis, including data from more than a dozen experiments, to determine the oscillation parameters. A list of the included experiments and data points can be found in Ref. [Esteban et al., 2024b]. Among other results, the $3\,\sigma$ confidence levels for the absolute values of the PMNS matrix were calculated and are shown

Table 6.1: The $3\,\sigma$ confidence levels for the absolute values of the PMNS matrix. The shown results are with and without taking the Super-Kamiokande atmospheric (SK-atm) $\chi^2$ data [Wester et al., 2024, Super-Kamiokande-Collaboration, 2023] into account. The image is taken from [Esteban et al., 2020, Esteban et al., 2024a].

NuFIT 5.3 (2024)

$$|U|_{3\sigma}^{\text{w/o SK-atm}} = \begin{pmatrix} 0.801 \to 0.842 & 0.518 \to 0.580 & 0.142 \to 0.155 \\ 0.236 \to 0.507 & 0.458 \to 0.691 & 0.630 \to 0.779 \\ 0.264 \to 0.527 & 0.471 \to 0.700 & 0.610 \to 0.762 \end{pmatrix}$$

$$|U|_{3\sigma}^{\text{with SK-atm}} = \begin{pmatrix} 0.801 \to 0.842 & 0.518 \to 0.580 & 0.143 \to 0.155 \\ 0.244 \to 0.500 & 0.498 \to 0.690 & 0.634 \to 0.770 \\ 0.276 \to 0.521 & 0.473 \to 0.672 & 0.621 \to 0.759 \end{pmatrix}$$

in Table 6.1. In addition, Fig. 6.2 shows a two-dimensional projection of the allowed regions for the oscillation parameters, i.e. the three mixing angles, the Dirac phase and the three squared, eigenstate mass differences. The shown results were obtained under the assumption of a unitary PMNS matrix [Esteban et al., 2020, Esteban et al., 2024a].

In the year 2025, the Nobel Prize in Physics were awarded to Takaaki Kajita (Super-Kamiokande) and Arthur B. McDonald (SNO) for the discovery of neutrino oscillation. The validation of neutrino oscillations has far-reaching implications, as the mathematical framework behind it implies a non-vanishing squared mass difference ($\Delta m_{ij}^2$) between neutrinos.

However, via neutrino oscillation experiments only the mass differences of the mass eigenstates are measurable but not the absolute mass scale, which is of special interest for cosmology. Massive neutrinos contribute to the total energy density of the universe with a contribution proportional to the sum of neutrino masses $m_\nu$ [Navas et al., 2024]:

$$\Omega_\nu^0 h^2 = \frac{\sum m_\nu}{93.12\,\text{eV}}, \tag{6.13}$$

with the energy density of neutrinos today $\Omega_\nu^0$ and the Hubble constant $h$. In addition, massive neutrinos, in the form of hot dark matter, had an impact on the evolution of large-scale structures in the present universe [Giunti and Kim, 2007]. Thus, a tighter absolute mass scale would also put tighter limits on the percentage of dark matter contributed by neutrinos.

Accordingly, an experiment to pin down the neutrino mass is favorable. From cosmological data the sum of neutrino masses can be constrained to be $\sum m_\nu < 0.072\,\text{eV}$ (95% CI) [Adame et al., 2025]. However, this limit is rather model dependent and encompasses the sum of neutrinos. Another approach is the search for neutrinoless double-$\beta$-decay. This ansatz assumes that neutrinos are their own anti particles, so-called Majorana particles. An upper bound on the half-life of such a decay, which depends on the effective Majorana mass $m_{ee}$ of $\nu_e$ [Navas et al., 2024]:

$$\frac{1}{T_{1/2}} \propto m_{ee}^2, \tag{6.14}$$

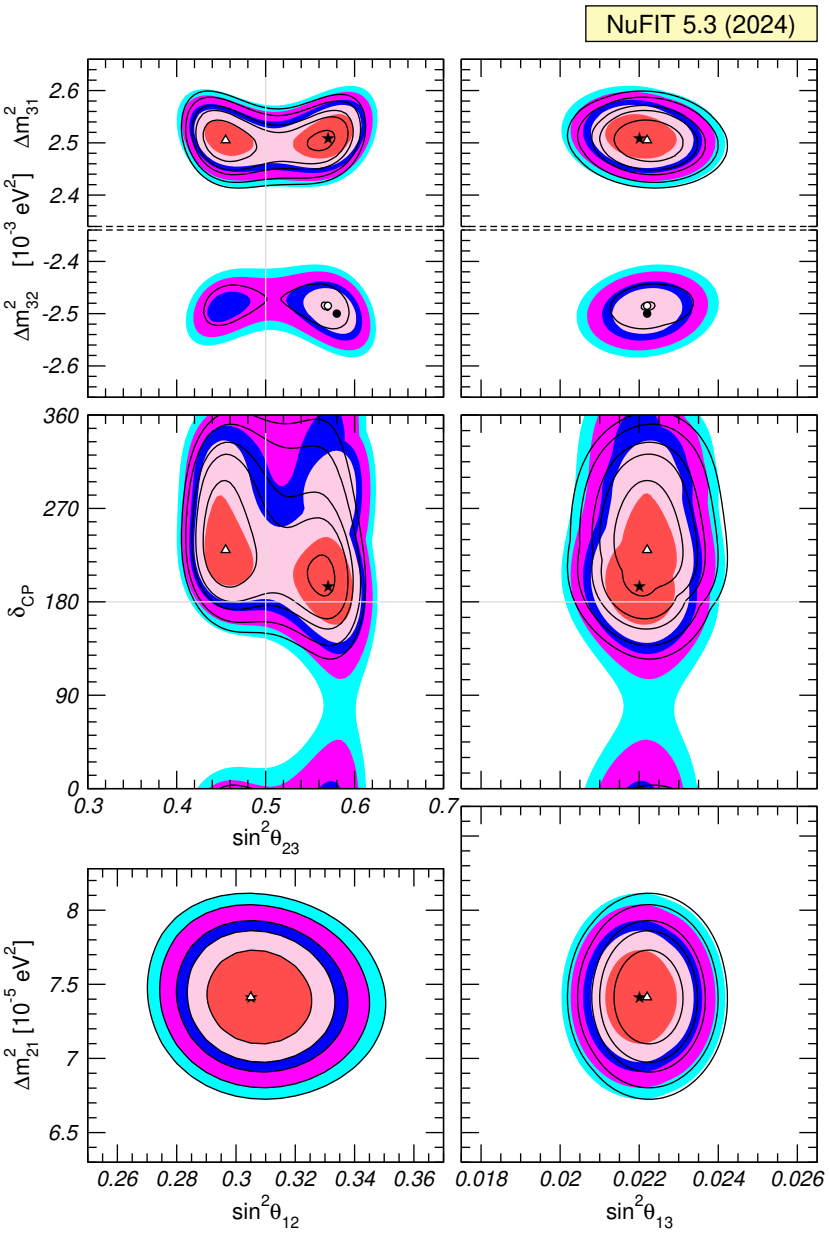


Figure 6.2: Two dimensional projections of the oscillation parameters: The three mixing angles ($\theta_{12}$, $\theta_{13}$ and $\theta_{23}$), the Dirac phase $\delta_{\mathrm{CP}}$, and the three squared mass differences ($\Delta m^2_{21}$, $\Delta m^2_{31}$ and $\Delta m^2_{32}$), defined as $\Delta m^2_{\mathrm{kj}} := m^2_{\mathrm{k}} - m^2_{\mathrm{j}}$. The contour plots show the $1\,\sigma$, $2\,\sigma$, $3\,\sigma$, 90%, and 99% confidence levels. The colored areas (black contour lines) correspond to taking (not taking) the Super-Kamiokande atmospheric $\chi^2$ data [Wester et al., 2024, Super-Kamiokande-Collaboration, 2023] into account. The image is taken from [Esteban et al., 2020, Esteban et al., 2024a].

can experimentally be determined, from which limits about $m_{ee}$ can be drawn. These are typically in the order of $m_{ee} < 180\,\text{meV}$ [Navas et al., 2024].

All in all, the results indicate a strong favor for massive neutrinos. However, because neutrino oscillation experiments measure the difference $m_i^2 - m_j^2$, the absolute neutrino mass scale is inaccessible. In the following sections, the KATRIN experiment is outlined, which pursues the goal to measure the mass directly with an unprecedented precision.

## 6.2 Measurement approach

The Karlsruhe Tritium Neutrino experiment was designed and build to measure the effective mass of electron anti-neutrinos, defined as:

$$m_\nu := \sqrt{\sum_i |U_{ei}|^2 m_i^2}, \tag{6.15}$$

with a sensitivity of 200 meV at 90% confidence level (CL) [KATRIN et al., 2022]. The symbol $U_{ei}$ indicates PMNS matrix elements involving electron neutrino contributions and $m_i$ indicates the mass of a neutrino mass eigenstate, as introduced in Eqs. (6.1) and (6.11), respectively.

KATRIN uses the $\beta$-decay of molecular tritium into a helium-3-tritium molecule, an electron and an electron anti-neutrino to perform a direct measurement of $m_\nu$ via the kinematics of the electron in the final state:

$$T_2 \rightarrow {}^3HeT^+ + e^- + \bar{\nu}_e. \tag{6.16}$$

An illustration of the kinetic energy distribution of the electron with respect to the value of $m_\nu^2$ is shown in Fig. 6.3. It is evident that a non-zero value of $m_\nu^2$ shifts the endpoint to lower values compared to the absolute endpoint $E_0$, i.e. the case of $m_\nu^2 = 0\,\text{eV}^2$. This shift is of particular significance, as it influences the shape of the distribution within the endpoint region. Hence, based on the endpoint and the resulting shape of the distribution within the endpoint region, the neutrino mass can be deduced. KATRIN uses the decay of tritium, because the $\beta$-spectrum of this decay is theoretically very well understood [Kraus et al., 2005], which minimizes systematic effects of the model prediction. Furthermore, the endpoint of tritium is rather low, which is favorable as the above-mentioned shape distortion is larger the smaller the absolute endpoint is.

Hence, the main goal is to detect electrons with energies close to the absolute endpoint energy. The experimental setup to accomplish this endeavor is outlined in the following section.

## 6.3 Experimental setup

The KATRIN experiment is designed to measure the count rate of $\beta$-electrons above a certain energy. An in depth explanation of the complete KATRIN experiment is beyond the scope of this thesis, but can be found in [Aker et al., 2021b]. In the

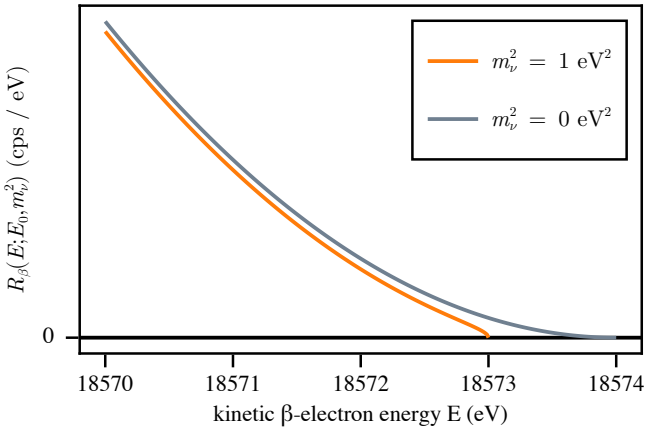


Figure 6.3: A schematic visualization of the $\beta$-electron energy spectrum near the chosen absolute endpoint of $E_0 = 18\,574$ eV. The differential decay rate $R_\beta$ as a function of the kinetic energy of the electron is shown. The difference between a zero (gray line) and a non-zero (orange line) electron anti-neutrino mass is indicated.

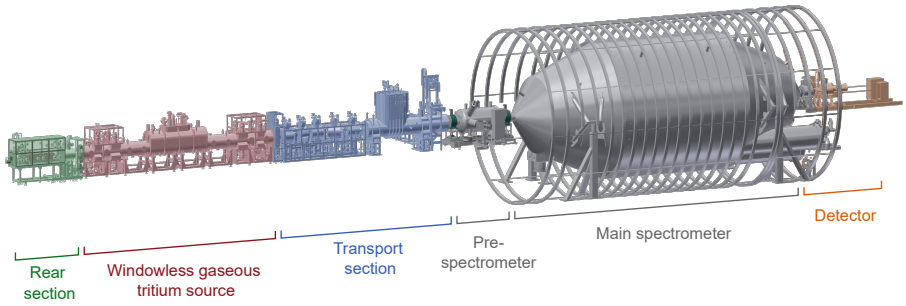


Figure 6.4: Illustration of the KATRIN experiment with its main components. Figure provided by Jaroslav Storek.

following, the main components shall be discussed briefly, which are visible in Fig. 6.4, which shows the experimental setup of the KATRIN experiment.

**Tritium source** The windowless gaseous tritium source (WGTS) consists of a 10 m tube with a diameter of 90 mm [Kleesiek et al., 2019]. The molecular tritium is provided by the Tritium Laboratory Karlsruhe and is continuously circulating within the WGTS (about 40 g per day [KATRIN et al., 2024a]). This allows the WGTS to provide up to $10^{11}$ $\beta$-electrons per second [Kleesiek et al., 2019]. To reduce the collision probability of electrons with tritium molecules, the WGTS is cooled to 30 K [KATRIN et al., 2022].

**Transport and pumping** This section guides the $\beta$-electrons from the Tritium source to the spectrometer section via magnetic fields. And more importantly, it reduces the tritium flow rate by 14 orders of magnitude [KATRIN et al., 2022]

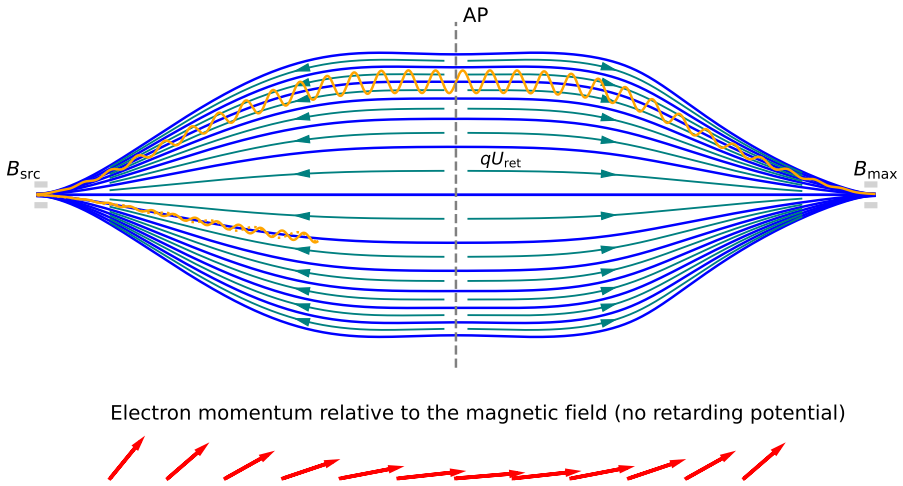


Figure 6.5: A schematic illustration of the Magnetic Adiabatic Collimation with Electrostatic (MAC-E) filter principle within the KATRIN main spectrometer. The magnetic field lines, which guide the $\beta$-electrons are shown as blue lines. The electric field, which is adjustable via the retarding voltage $U_{\text{ret}}$ is indicated as teal lines. Electrons propagating from the left to right side of the spectrometer are drawn as solid orange lines, wheres electrons traveling in the opposite direction are indicated width a dashed orange line. The analyzing plane (AP) is indicated via a vertical dashed line. The positions of the maximal magnetic field within the beamline $B_{\text{max}}$ and the magnetic field within the source $B_{\text{src}}$, i.e. the WGTS, are indicated. In addition, the $\beta$-electron momentum vector are indicated with red arrows. The figure is an adapted version of the one presented in Ref. [Lokhov et al., 2022].

via differential- and cryogenic pumping systems. This reduces the probability for collisions drastically and prevents the tritium gas from entering the main spectrometer.

**Spectrometer section** The spectrometer section consists of the pre- and the main spectrometer. Both work after the Magnetic Adiabatic Collimation with Electrostatic (MAC-E) filtering principle [KATRIN et al., 2025b]. A schematic illustration of the MAC-E filter as used in the main spectrometer is shown in Fig. 6.5. The MAC-E filter acts as a high-pass energy-filter which lets only electrons above a certain energy pass through. The working principle is as follows: The $\beta$-electrons enter the spectrometer on the left side of Fig. 6.5. Their kinetic energy consist of two components, perpendicular and parallel to the orientation of the spectrometer, i.e. $E_{\text{kin}} = E_{\perp} + E_{\parallel}$. A so-called retarding voltage $U_{\text{ret}}$ is applied to the spectrometer, creating an electric potential $qU_{\text{ret}}$, where $q$ is the electron charge. The potential and its direction is indicated with teal lines and arrow heads. Electrons run against this potential and are reflected if $E_{\text{kin}} < qU_{\text{ret}}$. However, for an optimal filtering of energies, $E_{\perp}$ must be transformed into $E_{\parallel}$ while keeping $E_{\text{kin}}$ constant. This is done adiabatically via the magnetic field within the spectrometer,

which guides the electrons. The process is indicated via the red arrows on the bottom of Fig. 6.5, which depict the momentum vector of the $\beta$-electrons. At the so-called analyzing-plane (AP) (indicated in Fig. 6.5 with a gray, dashed line) $E_\perp$ reaches its minimum ($E_\perp \ll E_\parallel$) and the momenta become aligned with the magnetic field lines [Aker et al., 2021b]. At this point, the absolute magnetic field within the spectrometer reaches its minimum and the retarding potential $qU_{\text{ret}}$ its maximum. Electrons with an energy $E_\parallel \geq qU_{\text{ret}}$ can pass through and become accelerated again by the same amount as they were decelerated before the AP. The retarding voltage $U_{\text{ret}}$ is adjustable in order to scan the region close to the endpoint $E_0$, which enables the measurement of the integrated $\beta$-spectrum.

The pre-spectrometer has a fixed energy threshold of 10.5 keV [KATRIN et al., 2025b] to filter out the majority of the low-energy electrons. Hence, these low energy electrons are not of interest for the neutrino mass measurement and could produce ionization events in the main spectrometer, thus increasing the overall background [Otten and Weinheimer, 2008]. The main spectrometer is the centerpiece of the experiment and is concerned with the energy filtering in the endpoint region of the $\beta$-energy spectrum. Therefore, the energy resolution of the main spectrometer is of upmost importance. Its mathematical form is given by [Kleesiek et al., 2019]:

$$\Delta E = E_{\text{kin}} \frac{B_{\text{ana}}}{B_{\text{max}}} \frac{\gamma + 1}{2}, \tag{6.17}$$

where $B_{\text{ana}}$ is the magnetic field at the AP, i.e. the minimal magnetic field, $B_{\text{max}}$ the maximal magnetic field and $\gamma$ the relativistic gamma factor of the electron. Choosing the magnetic fields such that $B_{\text{max}}/B_{\text{ana}} \approx 20\,000$ an energy resolution of $\Delta E \lesssim 1$ eV close to the absolute endpoint $E_0$ is achieved for the main spectrometer [Otten and Weinheimer, 2008].

**Segmented detector** The $\beta$-electrons with enough energy to pass through the main spectrometer, are finally detected at the segmented focal plane detector. A schematic figure of the detector is shown in Fig. 6.6. It consists of a 148-pixel silicon-PIN-diode array, with a detection efficiency of about 95% [KATRIN et al., 2025b]. Each pixel covers an are of 44 mm$^2$ and has a typical energy resolution of about $(1.85 \pm 0.13)$ keV (at full width at half maximum) [Aker et al., 2021b]. Thus one is able to reject counts coming from low energy background events. In addition, the focal plane detector is surrounded by two layers: First, by a muon tagging system based on multiple plastic scintillators. Second, by a two shell system. The outer shell is 3 cm thick and consists of lead to reduce the $\gamma$-background. The inner shell is 1.27 cm thick and is made of oxygen-free, high-conductivity copper to block X-rays coming from the surrounding lead shielding [Amsbaugh et al., 2015].

**Rear section** The rear section is equipped with multiple devices dedicated to monitor several parts of the whole experiment. For example the gas composition in the WGTS is monitored via Laser Raman Spectroscopy, as impurities in the form of deuterium and hydrogen can be present [Aker et al., 2021b], or the column density in the WGTS, as the energy of the $\beta$-electrons leaving the WGTS is influenced by the elastic scattering with the gas molecules [Aker et al., 2021b]. In addition, an electron gun is used for testing the KATRIN setup by producing precise electron

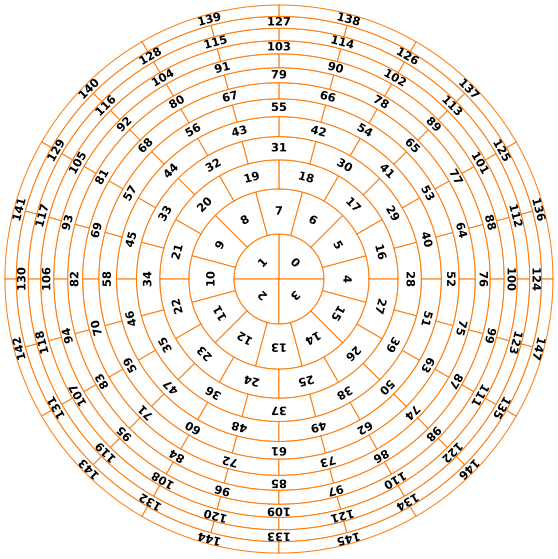

Figure 6.6: The focal plane detector of the KATRIN experiment. The detector consists of 148-pixel silicon-PIN-diodes, indicated as the drawn boxes. The shown figure is an adapted version of the one shown in Ref. [KATRIN et al., 2024a].

energies and is also suitable to monitor the stability of the column density [Aker et al., 2021b].

## 6.4 The KATRIN model

The final goal is to derive at a formula for the count rate of $\beta$-electrons, coming from molecular tritium decay, as a function of the retarding energy $qU_{\mathrm{ret}}$. The starting point is to consider the probability for a tritium molecule in state $|i\rangle$ to decay into some state $|f\rangle$. According to Fermis's golden rule, the total transition rate from initial state $|i\rangle$ to all possible discrete and continuum final states $|f\rangle$ is given by [Otten and Weinheimer, 2008]:

$$\Gamma := 2\pi \sum \int |M_{fi}|^2 \, \mathrm{d}f \, . \tag{6.18}$$

From this equation, the theoretical predicted differential $\beta$-electron energy spectrum can be derived, see Ref. [Otten and Weinheimer, 2008], and is given by [KATRIN et al., 2024a]:

$$\begin{aligned} R_\beta(E; E_0, m_\nu^2) := \frac{\mathrm{d}\Gamma}{\mathrm{d}E} = \frac{G_{\mathrm{F}}^2 |V_{\mathrm{ud}}|^2}{2\pi^3} |M_{\mathrm{nucl}}|^2 F(Z=2, E)(E + m_{\mathrm{e}}) p_{\mathrm{e}} \\ \times \sum_{\mathrm{f}} P_{\mathrm{f}} G(E, E_0 - V_{\mathrm{f}}) \epsilon_{\mathrm{f}} \sqrt{\epsilon_{\mathrm{f}}^2 - m_\nu^2} \Theta(\epsilon_{\mathrm{f}} - m_\nu). \end{aligned} \tag{6.19}$$

The symbols appearing in the formula are: The Fermi coupling constant $G_F$, the Cabibbo–Kobayashi–Maskawa (CKM) matrix element $V_{ud}$ for coupling between u- and d-quarks, the energy-independent nuclear-transition-matrix element $M_{nucl}$ of the super-allowed transition, the relativistic Fermi function $F(Z = 2, E)$ describing the Coulomb interaction of the $\beta$-decay electron and the daughter nucleus with $Z = 2$. Further symbols are the kinetic energy of the $\beta$-decay electron $E$, the momentum of the $\beta$-decay electron $p_e$, the mass of the electron $m_e$, the maximal kinetic energy of the $\beta$-decay electron $E_0$ under the assumption of massless neutrinos $m_\nu^2 = 0\,\mathrm{eV}^2$, the transition probability $P_f$ to state f, the excitation energy $V_f$ of state f, the radiative correction factor $G(E, E_0 - V_f)$ (i.e. higher-order quantum-electrodynamics contributions), the maximal neutrino energy $\epsilon_f = E_0 - E - V_f$ and the Heaviside function $\Theta(\dots)$ to ensure energy conservation [KATRIN et al., 2024a].

The integral count rate of $\beta$-electrons expected at a certain retarding energy $qU_{ret}$ is calculated by multiplying the differential decay rate with the experimental response function $f_{calc}$ and integrating over the relevant energies [KATRIN et al., 2024a]:

$$R_{\beta,\mathrm{int}}(qU_{ret}; E_0, m_\nu^2) = N_T \int_{qU_{ret}}^{E_0} R_\beta(E; E_0, m_\nu^2) f_{calc}(E, qU_{ret})\,\mathrm{d}E\,, \tag{6.20}$$

with the signal normalization $N_T$. The experimental response function is defined as [KATRIN et al., 2024a]:

$$f_{calc}(E, qU_{ret}) = \int_{\epsilon=0}^{E-qU_{ret}} \int_{\theta=0}^{\theta_{max}} \mathcal{T}(E-\epsilon, \theta, qU_{ret}) \sin(\theta) \sum_s P_s(E) f_s(\epsilon)\,\mathrm{d}\theta\,\mathrm{d}\epsilon\,, \tag{6.21}$$

which describes the probability for an emitted $\beta$-electron with energy $E$ to overcome the retarding potential and reach the focal plane detector. The symbol $\theta$ denotes the starting angle between the electron momentum and the magnetic field in the source, with its maximal value $\theta_{max} = \arcsin\left(\sqrt{B_{src}/B_{max}}\right)$ with the magnetic field in the source $B_{src}$ and the maximal magnetic field in the beamline $B_{max}$. The transmission condition of the spectrometer $\mathcal{T}$ also depends on $B_{src}$, $B_{max}$ as well as the magnetic field at the analyzing-plane $B_{ana}$. In general, the $\beta$-electrons can scatter in the WGTS s-times. The probability for this to happen and to lose overall the energy $\epsilon$ during these scatterings is denoted with $P_s(E)$ and $f_s(\epsilon)$, respectively.

Finally, the model for the predicted count rate of $\beta$-electrons from molecular tritium decay as a function of the retarding energy $qU_{ret}$ is given by [KATRIN et al., 2024a]:

$$R(qU_{ret}; A_S, R_{bg}, E_0, m_\nu^2) = A_S \times R_{\beta,\mathrm{int}}(qU_{ret}; E_0, m_\nu^2) + R_{bg}(qU_{ret}; R_{bg}). \tag{6.22}$$

This model has four free parameters: the signal normalization $A_S$, the overall background rate $R_{bg}$, the maximal kinematic energy of electrons $E_0$ within the molecular tritium decay spectrum, under the assumption of massless neutrinos, and the squared effective electron anti-neutrino mass $m_\nu^2$. All background related contributions to the count rate are encompassed in the term [KATRIN et al., 2024a]:

$$R_{bg}(qU_{ret}; R_{bg}) = R_{bg} + R_{spec,det}(qU_{ret}) + R_{RW}(qU_{ret}), \tag{6.23}$$

which includes $R_{\mathrm{bg}}$ which is a free model parameter and independent of the retarding energy, systematic contributions from the spectrometer and the focal plane detector $R_{\mathrm{spec,det}}$ as well as contributions originating from tritium deposited on the rear-wall $R_{\mathrm{RW}}$.

## 6.5 KATRIN systematic effects

Within this section, the systematic effects of the KATRIN experiment are discussed, this includes their place in the KATRIN model and their treatment in the first five KATRIN Neutrino Mass (KNM) measurement campaigns, i.e. in chronological order KNM1, KNM2, KNM3-SAP, KNM3-NAP, KNM4-NOM, KNM4-OPT and KNM5. The numerical values for the individual systematic uncertainties were determined by calibration measurements or simulations, for more details see Ref. [KATRIN et al., 2024a]. All systematic uncertainties are published in Ref. [KATRIN et al., 2025c]. This includes also correlations between systematic parameters between different KATRIN campaigns. However, as these are not relevant for the analyses performed in this thesis, they will not be discussed further. In general, the sources of systematic effects can be organized into four groups:

**Background** A major source for background events is the main spectrometer, which comes from Rydberg electrons (originating from $\alpha$-decays in the spectrometer walls), which have a volume-dependent background rate [Lokhov et al., 2022]. Hence, if the Rydberg electrons are created to the right of the AP they get accelerated towards the focal plane detector, thus increasing the background rate. To minimize this effect, the effective volume of the downstream flux tube within the main spectrometer (the volume to the right of the analyzing plane) was reduced by a different layout of the magnetic fields [Lokhov et al., 2022], thus shifting the analyzing-plane further downstream. Because of this shift, the new layout is also called shifted-analyzing-plane (SAP) configuration, and was first used in the KNM3-SAP campaign. The SAP configuration reduced the overall background by a factor of two, to typical values of $O(0.12\,\mathrm{cps})$ [Lokhov et al., 2022, KATRIN et al., 2025b]. The evolution of the flux tube volume and the impact on the analyzing-plane are shown in Fig. 6.7. In the original KATRIN design, the flux tube was spanning a large volume of the main spectrometer (blue, dotted line) [Karl, 2022]. Already in the chronological first two campaigns KNM1 and KNM2, as well as in KNM3-NAP, a decreased volume was used to reduce the before-mentioned background. This is called the nominal-AP (NAP) configuration and is indicated as a orange, dashed line in Fig. 6.7. The other campaigns are all operated with the SAP setting (green, solid line). In addition, the NAP and the SAP are indicated as a vertical gray, dashed line and a curved, green, dashed line, respectively. Regarding the background of the count rate, two systematic effects are taken into account. On the one hand, a possible dependence of the rate on the retarding energy $qU_{\mathrm{ret}}$ is taken into account via the parameter $R_{\mathrm{bg,energy}}$,which is used to calculate $R_{\mathrm{spec,det}}$ in Eq. (6.23), and is modeled as one parameter per campaign. On the other hand, due to the high voltages on the spectrometers a Penning trap between the pre- and main spectrometer emerges [KATRIN et al., 2024a]. Positive ions created from the Penning trap can find their way to the main spectrometer, producing low-energetic background electrons [KATRIN et al., 2024a]. The higher the number of stored electrons within the trap, the higher the number of background electrons [Karl,

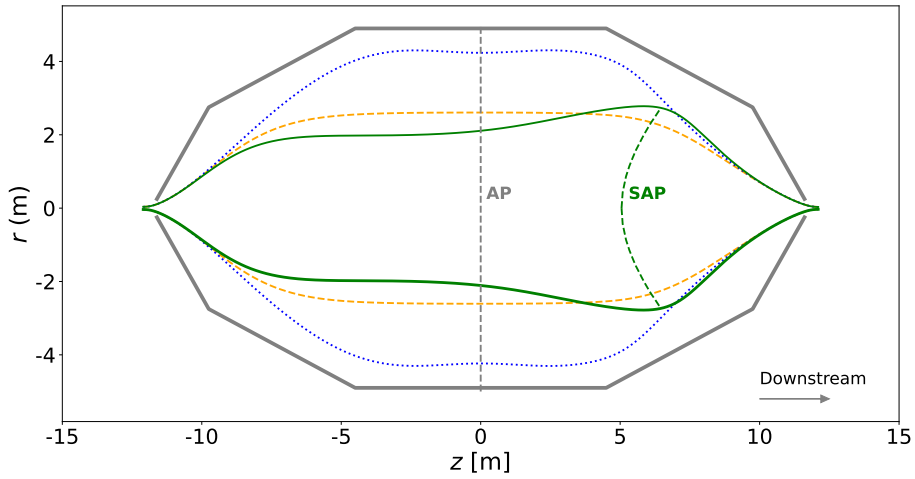


Figure 6.7: Depicted is the main spectrometer of the KATRIN experiment. The overall gray line is the outer shell of the spectrometer. The blue, dotted line corresponds to the flux tube used within the first commissioning run of KATRIN [Lokhov et al., 2022]. The blue, dashed line corresponds to the NAP-setup used in KNM1, KNM2 and KNM3-SAP. The green, solid line is the flux tube in the SAP-setup, as used in KNM3-SAP, KNM4-NOM, KNM4-OPT and KNM5. The corresponding analyzing-planes are indicated with a dashed, gray or green line, respectively. The figure is an adapted version of the one used in [Lokhov et al., 2022].

2022]. Hence, the Penning trap is emptied between scan steps [KATRIN et al., 2024a], and thus it can only emerge within the duration of a scan step. This time dependence is modeled via the parameter $R_{\mathrm{bg,time}}$, which is simply added to Eq. (6.23), with one parameter per campaign. After the campaign KNM4-NOM, with the NOMinal (NOM) setup for the pre-spectrometer, the setup was OPTimized (OPT) such that the time span for each scan step is now identical, and the pre-spectrometer voltage is lowered [KATRIN et al., 2024a] to remove the Penning trap. Hence, the parameter $R_{\mathrm{bg,time}}$ is not present in the models for KNM4-OPT and KNM5.

**Rear-wall** Tritium, originating from the WGTS, can reach the rear-wall and accumulate there, increasing the overall KATRIN background count rate. This contribution is represented with the term $R_{\mathrm{RW}}$ in Eq. (6.23) and is modeled with three parameters: 1) the real-wall signal amplitude $A_{\mathrm{RW}}$, 2) the rear-wall endpoint $E_{0,\mathrm{RW}}$ and 3) the final-state distribution (FSD) shape parameter $\mathrm{FSD}_{\mathrm{RW}}$, which effectively modifies the ratio of the ground and electronic excited final-state probabilities. In the KATRIN model, the rear-wall amplitude $A_{\mathrm{RW}}$ is modeled as one parameter per so-called detector patch. The concept of a detector patch will be explained in detail in Section 6.6. The parameters $E_{0,\mathrm{RW}}$ and $\mathrm{FSD}_{\mathrm{RW}}$ are modeled on a per campaign basis. Hence, the systematic effects of the rear-wall were discovered prior to the KNM3-SAP campaign, such that these parameters are not present in KNM1 and KNM2. However, the amount of accumulated tritium should be small enough to neglect this effect for KNM1 and KNM2.

**Tritium source** The WGTS is the source of multiple systematic effects. First, the probability to scatter s-times $P_s(E)$ in Eq. (6.21) depends on the gas density $\rho$, the total length $d$ of the WGTS and the cross-section for inelastic scattering of electrons. More precisely, the product of these quantities $\rho d\sigma$ [Aker et al., 2021a], which is modeled as one parameter per campaign. Second, longitudinal inhomogeneities in the electric potential in the WGTS can lead to different starting potentials for the $\beta$-electrons (for example at the front and the back of the WGTS). The $\beta$-electrons travel longer distances when starting their journey at the back of the WGTS, which lead to two effects: 1) on average the electrons have a different starting energy and 2) the electrons have a higher probability for multiple inelastic scattering. Hence, this leads to different starting energies for non-scattered and multi-scattered $\beta$-electrons on average, which has an impact on the spectrum [KATRIN et al., 2024a]. This energy shift $\Delta_\epsilon(\text{eV})$ between non-scattered and multi-scattered $\beta$-electrons is taken into account by replacing $f_s(\epsilon) \rightarrow f_s(\epsilon - \Delta_\epsilon)$ in Eq. (6.21) [KATRIN et al., 2024a], and is modeled as one parameter per campaign. Furthermore, the WGTS is the source of multiple effects which broaden the $\beta$-electron spectrum. On the one hand, there is the thermal motion of the tritium molecules within the WGTS which creates a Doppler broadening [KATRIN et al., 2024a]. On the other hand, there are spacial and temporal variations of the source potential which also create a broadening effect [KATRIN et al., 2024a]. These broadening effects are all summed up and enter the KATRIN model via the parameter $\sigma^2_{\text{broad}}$ in the calculation of the transition probability $P_f$ in Eq. (6.19) [Karl, 2022], which is modeled as one parameter per detector patch. In addition, the $\beta$-electrons loose energy within the tritium source, because of inelastic scattering off tritium molecules. This energy loss is modeled via three Normal distributions [Aker et al., 2021c], which is why one has in total nine model parameters, three for the amplitudes $\vec{E}_{\text{loss,amp}}$, three for the expectation values $\vec{E}_{\text{loss,exp}}$ and three for the standard deviations $\vec{E}_{\text{loss,std}}$. The parameters turn up in the definition of $f_s(\epsilon)$ in Eq. (6.21).

**Electromagnetic fields** In total three magnetic fields are subject to systematic effects: 1) the magnetic field within the tritium source $B_{\text{src}}(\text{T})$, which is modeled as one parameter per campaign, 2) the magnetic field within the analyzing plane $B_{\text{ana}}(\text{T})$, which is modeled as one parameter per detector patch, 3) the maximal magnetic field in the beamline $B_{\text{max}}(\text{T})$, which is modeled as one parameter per campaign. The fields $B_{\text{src}}$, $B_{\text{ana}}$ and $B_{\text{max}}$ are used within the KATRIN model to calculate the transmission function $\mathcal{T}$ in Eq. (6.21) [KATRIN et al., 2024a]. In addition, the fields $B_{\text{src}}$ and $B_{\text{max}}$ are used to calculate the maximal acceptance angle $\theta_{\text{max}}$ in Eq. (6.21) [KATRIN et al., 2024a]. Furthermore, there is a broadening effect through inhomogeneities of the electric potential and the magnetic field within the analyzing-plane. Hence, a certain area in the analyzing-plane is mapped onto a certain pixel of the focal plane detector. Small variations within this area of the AP could smear the transmission function $\mathcal{T}$ (see Eq. (6.21)), which depends on the energy of the $\beta$-electrons and the magnetic fields, and cause a broadening in the $\beta$-spectrum [KATRIN et al., 2024b].

## 6.6 Definition of likelihood distribution

As mentioned in Section 6.4, the KATRIN experiment measures count rates of $\beta$-electrons at certain retarding energies $qU_{\text{ret}}$. This is accomplished by counting

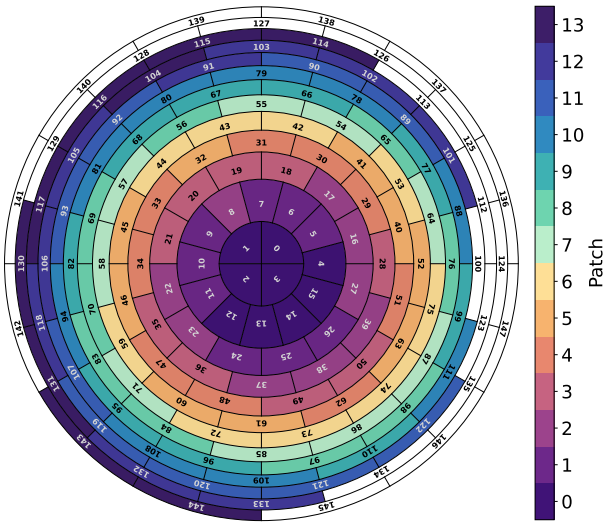


Figure 6.8: The segmentation of the focal plane detector into patches as used for the statistical model of the KATRIN SAP campaigns. The 22 white pixels are not included for the analysis. The remaining pixels are grouped into 14 patches (with 9 pixels each), indicated via color coding. Figure taken from [KATRIN et al., 2024a].

the electrons impinging onto the focal plane detector for a certain time span $t_i$, where the specific measurement time depends on the retarding energy. The measurements at different $qU_{\mathrm{ret}}$ are statistically independent, and thus the likelihood is a product of Poisson distributions [Karl et al., 2022], with the expected count rate given by Eq. (6.22).

As discussed in Section 6.3, the focal plane detector consists of 148 pixel detectors. For the NAP campaigns KNM1, KNM2 and KNM3-NAP the detector is treated as a single, so-called patch. Due to systematic effects, as discussed in Section 6.5, the SAP setup was used for the campaigns KNM3-SAP, KNM4-NOM, KNM4-OPT and KNM5. In comparison to the NAP setup, this introduced inhomogeneities of the electric potential and the magnetic field within the shifted-analyzing-plane (see green, dashed line in Fig. 6.7) [Lokhov et al., 2022]. Thus, the detector can not be treated as one large patch, like for the NAP campaigns, but rather have to be grouped into multiple patches. Pixels corresponding to approximately the same electric potential and magnetic field in the SAP are grouped into one patch. However, some pixels are excluded from the analysis (31 pixels each in KNM1 and KNM2 and 22 pixels each in KNM3 to KNM5). The reasons are a reduced flux of $\beta$-electrons due to structural components or an increased intrinsic noise [KATRIN et al., 2024a]. Hence, for the NAP campaigns one has 117 active pixels, while for the SAP campaigns the detector was grouped into 14 patches with 9 pixels each, i.e. in total 126 pixels. As an example, the distribution of the patches, and active pixels, for the SAP campaigns are shown in Fig. 6.8. In general, the pixels are statistically independent of each other [Lokhov et al., 2022] which is why the count

rate of pixels in the same patch can be summed up. However, different patches correspond to different electrical potentials and magnetic fields which has to be taken into account. Hence, each patch has an individual model, and because the detector patches are statistically independent, a product over those likelihoods can be built. Furthermore, because certain parameters such as the column density can vary drastically between campaigns [KATRIN et al., 2025b], there is one statistical model per campaign. Thus, the statistical likelihood function for a single KATRIN campaign is written as [Karl et al., 2022]:

$$\mathcal{L}(\theta) := \prod_{\text{patch}} \prod_{\text{i}} e^{-R(qU_{\text{ret,i}};\theta)t_{\text{i}}} \frac{(R(qU_{\text{ret,i}};\theta)t_{\text{i}})^{N_{\text{i}}}}{N_{\text{i}}!}, \tag{6.24}$$

where $\theta := (A_{\text{S}}, R_{\text{bg}}, E_0, m_\nu^2)$ represents the free model parameters, $N_{\text{i}}$ are the measured electron counts at retarding energy $qU_{\text{ret,i}}$ within the time span $t_{\text{i}}$ and $R$ is the expected count rate as given by Eq. (6.22).

Systematic uncertainties are taken into account by the well established pull-term method [KATRIN et al., 2025b]. For experimentally determined values in *Eq.* (6.22), such as $B_{\text{ana}}$, a systematic parameter $\theta_{\text{syst}}^{B_{\text{ana}}}$ is introduced. It is assumed that the systematic parameter is normally distributed around the experimental measured value $\theta_{\text{exp}}$ with the systematic uncertainty $\sigma_{\text{syst}}$:

$$\theta_{\text{syst}}^{B_{\text{ana}}} \sim \mathcal{N}(\theta_{\text{exp}}^{B_{\text{ana}}}, \sigma_{\text{syst}}^{B_{\text{ana}}}). \tag{6.25}$$

The procedure is similar for other measured quantities, as for example $B_{\text{src}}$ or the column density times the cross-section $\rho \text{d}\sigma$. The full pull-term, modeling all systematic uncertainties and possible correlations has the form [KATRIN et al., 2025b]:

$$\left(\vec{\theta}_{\text{syst}} - \vec{\theta}_{\text{exp}}\right)^T \Sigma_{\text{cov}}^{-1} \left(\vec{\theta}_{\text{syst}} - \vec{\theta}_{\text{exp}}\right), \tag{6.26}$$

and is multiplied with the likelihood in Eq. (6.24). All systematic parameters of KATRIN, together with their origin, are discussed in Section 6.5.

### 6.6.1 Model parameters

The model for the expected count rate of $\beta$-electrons, as introduced in Eq. (6.22), has four free model parameters. First and foremost, the squared effective electron anti-neutrino mass $m_\nu^2$ ($\text{eV}^2$), as defined in Eq. (6.15), which is modeled via one parameter throughout all measurement campaigns. Second, the effective endpoint energy $E_0$ (eV) of the $\beta$-electrons (under the assumption of massless neutrinos). Third, the overall signal normalization $A_{\text{S}}$ and fourth, the absolute background rate $R_{\text{bg}}$ of the expected count rate $R(qU_{\text{ret}})$. As already mentioned, in the nominal-analyzing-plane (NAP) setup, the same statistical model can be used for all pixels [KATRIN et al., 2024a]. However, in shifted-analyzing-plane (SAP) setup the retarding energy and the magnetic field are not constant throughout the SAP. Hence, the electrons detected in different patches have experienced different fields and electric potentials [KATRIN et al., 2024a]. This has implications on the statistical model. Because the background $E_0$ can absorb a possible offset of the retarding energy [Karl, 2022], and the patch-dependency of the background- and count rate, the parameters $E_0$, $R_{\text{bg}}$ and $A_{\text{S}}$ are modeled on a patch-wise basis, i.e.

there is an independent parameter for each of the 14 patches of the focal plane detector. In addition, there are multiple parameters to take systematic uncertainties into account, as introduced in Section 6.5. An overview over all model parameters, together with a short explanation and their appearance in the different KATRIN campaigns is presented in Table 6.2. The overall number of parameters varies between the single KATRIN measurement campaigns, from a minimum of 21 to a maximum of 102, mainly attributable to whether the NAP- or the SAP setup is used. In addition, certain systematic parameters only appear in certain campaigns. In the case of KNM1 and KNM2, the source of systematic effects from the rear wall were unknown and only included in later campaigns. Another case is the time dependent background due to the formation of a Penning trap between the pre- and main spectrometer. This systematic uncertainty is present in campaigns KNM1 to KNM4-NOM and was fully mitigated for the campaigns KNM4-OPT and KNM5.

## 6.7 KATRIN collected data

With the setup described in Section 6.3 data taking started in the year 2019 and is still ongoing to this date. The $\beta$-electron count rate at certain retarding energies $qU_{\mathrm{ret}}$ are measured in order to get the integral $\beta$-electron spectrum, such that it can be compared to its theoretical prediction, see Eq. (6.22). The integrated spectrum is scanned through measurements at different retarding energies in the range of $E_0 - 300\,\mathrm{eV} \leq qU_{\mathrm{ret}} \leq E_0 + 135\,\mathrm{eV}$, with typically 40 different $qU_{\mathrm{ret}}$ set points [KATRIN et al., 2025b]. Each such $\beta$-scan has a duration of 3 h to 3.5 h and one KATRIN campaign consist of several hundreds of these scans. Only the data in the range $r_{\mathrm{A}} = E_0 - 40\,\mathrm{eV}$ is used for the neutrino mass analysis up to now, but with the option to enlarge this analysis window in the future. The data points below $r_{\mathrm{A}}$ are used for calibrations and monitoring the experiment, while the data above $E_0$ give constraints on the overall background rate [KATRIN et al., 2025b].

The KATRIN experiment collected within the first five measurement campaigns, i.e. KNM1, KNM2, KNM3-SAP and KNM3-NAP, KNM4-NOM and KNM4-OPT as well as KNM5, a total amount of $\sim 3.6 \times 10^7$ electrons within the analysis window ($qU_{\mathrm{ret}} > E_0 - 40\,\mathrm{eV}$) [KATRIN et al., 2025b]. The measured data points are published in Ref. [KATRIN et al., 2025a], and are plotted in Fig. 6.9. In addition, an illustration of the accumulated statistics over the first five measurement campaigns is shown in Fig. 6.10.

Table 6.2: KATRIN model parameters and their number in each of the first five KATRIN measurement campaigns.

| Parameter | Unit | Description | Multiplicity | | | | | | |
|---|---|---|---|---|---|---|---|---|---|
| | | | KNM1 | KNM2 | KNM3-NAP | KNM3-SAP | KNM4-NOM | KNM4-OPT | KNM5 |
| **Free model parameters** | | | | | | | | | |
| $m_\nu^2$ | $\mathrm{eV}^2$ | Effective electron anti-neutrino mass squared | 1 | 1 | 1 | 1 | 1 | 1 | 1 |
| $E_0$ | eV | Electron endpoint energy for $m_\nu^2 = 0$ | 1 | 1 | 1 | 14 | 14 | 14 | 14 |
| $A_\mathrm{S}$ | 1 | Signal normalization | 1 | 1 | 1 | 14 | 14 | 14 | 14 |
| $R_\mathrm{bg}$ | cps | Absolute background rate | 1 | 1 | 1 | 14 | 14 | 14 | 14 |
| **Systematic parameters: rear wall** | | | | | | | | | |
| $E_{0,\mathrm{RW}}$ | eV | Rear-wall endpoint | / | / | 1 | 1 | 1 | 1 | 1 |
| $\mathrm{FSD}_\mathrm{RW}$ | 1 | Ratio of ground and excited-state probabilities | / | / | 1 | 1 | 1 | 1 | 1 |
| $A_\mathrm{RW}$ | 1 | Signal amplitude rear-wall | / | / | 1 | 14 | 14 | 14 | 14 |
| **Systematic parameters: tritium source** | | | | | | | | | |
| $\rho \mathrm{d}\sigma$ | 1 | Column density times cross-section | 1 | 1 | 1 | 1 | 1 | 1 | 1 |
| $\Delta_\epsilon$ | eV | Energy loss shift | 1 | 1 | 1 | 1 | 1 | 1 | 1 |
| $\sigma^2_\mathrm{broad}$ | $\mathrm{eV}^2$ | Broadening of (differential) spectrum | 1 | 1 | 1 | 14 | 14 | 14 | 14 |
| $E_\mathrm{loss,amp}$ | 1 | Amplitudes of the three Gaussian's | 3 | 3 | 3 | 3 | 3 | 3 | 3 |
| $E_\mathrm{loss,exp}$ | 1 | Expectations of the three Gaussian's | 3 | 3 | 3 | 3 | 3 | 3 | 3 |
| $E_\mathrm{loss,std}$ | 1 | Standard deviations of the three Gaussian's | 3 | 3 | 3 | 3 | 3 | 3 | 3 |
| **Systematic parameters: magnetic fields** | | | | | | | | | |
| $B_\mathrm{src}$ | T | Magnetic field inside the tritium source | 1 | 1 | 1 | 1 | 1 | 1 | 1 |
| $B_\mathrm{max}$ | T | Maximal magnetic field inside the beamline | 1 | 1 | 1 | 1 | 1 | 1 | 1 |
| $B_\mathrm{ana}$ | T | Magnetic field at the analyzing plane | 1 | 1 | 1 | 14 | 14 | 14 | 14 |
| **Systematic parameters: background** | | | | | | | | | |
| $R_\mathrm{bg,energy}$ | $\mathrm{cps\,eV}^{-1}$ | Energy dependence of background rate | 1 | 1 | 1 | 1 | 1 | 1 | 1 |
| $R_\mathrm{bg,time}$ | $\mathrm{cps\,s}^{-2}$ | Aggregating background rate | 1 | 1 | 1 | 1 | 1 | / | / |
| **Total number of parameters** | | | 21 | 21 | 24 | 102 | 102 | 101 | 101 |

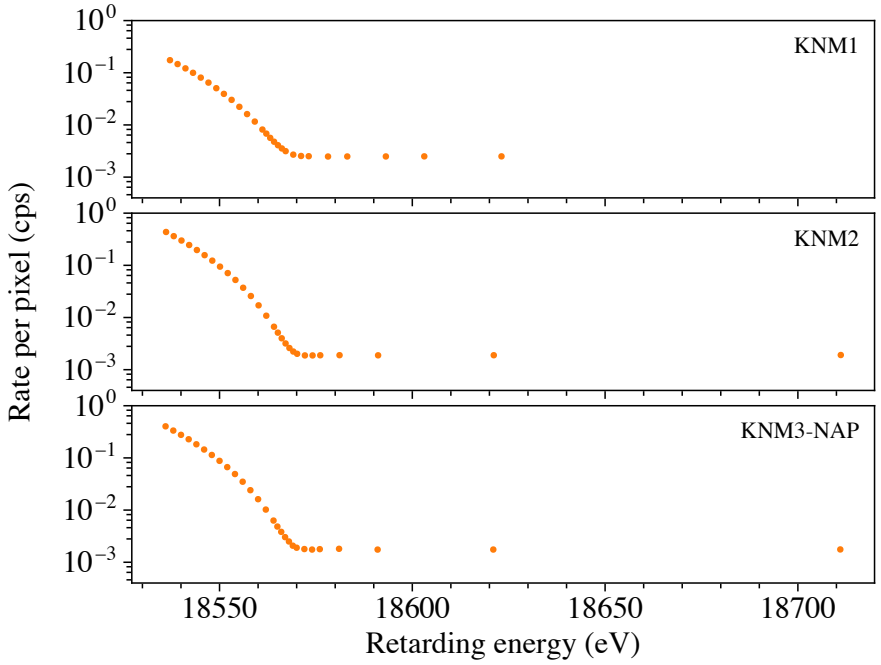


(a) NAP campaigns.

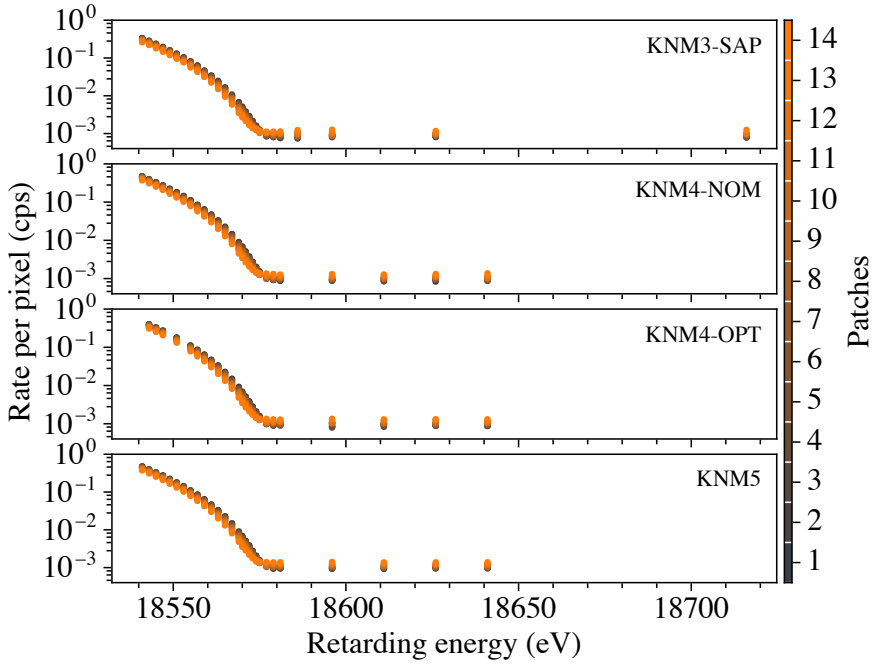


(b) SAP campaigns.

Figure 6.9: Shown are the measured data points of the first five KATRIN measurement campaigns. The graphic is grouped into NAP and SAP campaigns. The color code in part (b) corresponds to the different patches of the focal plane detector in the SAP configuration.

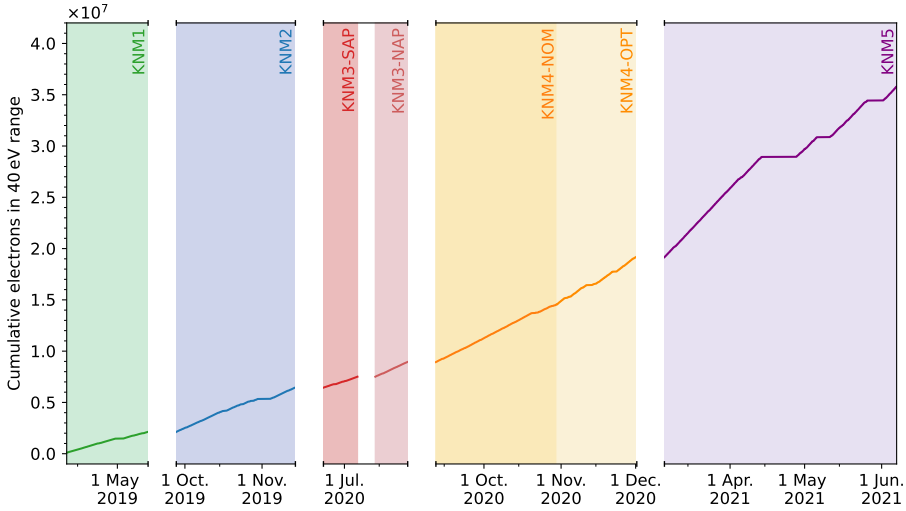


Figure 6.10: Cumulative amount of electrons collected within the analysis window ($qU_{\mathrm{ret}} > E_0 - 40\,\mathrm{eV}$) for the first five measurement campaigns. Image is taken from Ref. [KATRIN et al., 2024a].

# Chapter 7

# Neutrino mass analysis utilizing Bayesian inference

This chapter focuses on the application of Bayesian inference to extract neutrino mass bounds from the first five KATRIN measurement campaigns, i.e. KNM1, KNM2, KNM3-SAP, KNM3-NAP, KNM4-NOM, KNM4-OPT and KNM5. It starts with an introduction in Section 7.1, where the general ansatz for the analysis, the used software and the performed studies are outlined. This is followed by Section 7.2 in which explicitly the employed approach for monitoring the MCMC convergence for all performed fits and the anticipated, stringent convergence goals are addressed. Afterward, the results of applying Bayesian inference onto the individual campaigns are discussed in Section 7.3. To complement the individual analyses, the results of a combined analysis, in form of Bayesian knowledge updates, are discussed in Section 7.4. The chapter is concluded with a summary in Section 7.5.

## 7.1 Introduction

Within this chapter, the neutrino mass analysis shall be performed for the first five measurement campaigns of KATRIN utilizing the statistical method of Bayesian inference. This encompasses the analysis of the individual campaigns as well as a combined analysis in form of Bayesian knowledge updates. The analyses were all carried out as part of the KATRIN Netrium team, which is characterized by employing a neural network to evaluate the KATRIN likelihood, as defined in Section 6.6. The general description and validation of the following neural network approach, to be applied on KATRIN campaigns, can be found in [Karl et al., 2022]. In general, the neural network consists of an input layer, where the input nodes correspond to the KATRIN model parameters of the respective campaign (see Table 6.2), followed by two hidden layers, each with 128 nodes, and ends with an output layer. The nodes of the output layer corresponds to the predicted rate of $\beta$-electrons at certain retarding energies $qU_{\mathrm{ret}}$ at which the data were taken for the specific KATRIN campaign. Each layer of the neural network is fully connected to its predecessor. The activation function of the output layer is the softplus-function

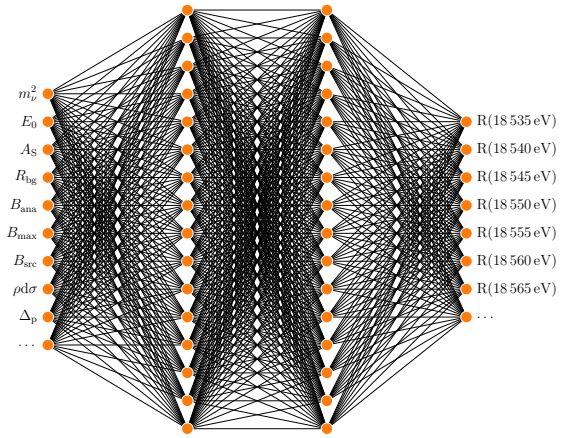


Figure 7.1: Schematic illustration of the neural network used by Netrium to evaluate the KATRIN likelihood. The inputs are numerical values of the model parameters of a specific KATRIN campaign. The two hidden layers consist of 128 nodes each (not entirely represented in the figure). The output of the neural network are the count rates at different retarding energies. Adjacent layers are fully connected. The graphic is redrawn and slightly modified from Ref. [Karl et al., 2022].

where the hidden layers use the mish-function:

$$\text{softplus}(x) = \ln\left(1 + \exp^x\right), \tag{7.1}$$

$$\text{mish}(x) = x \tanh\left(\text{softplus}(x)\right). \tag{7.2}$$

A schematic illustration for such a neural network is shown in Fig. 7.1. As described in Section 6.3, the campaigns KNM1, KNM2 and KNM3-NAP used the NAP setup, where the detector is combined to one pixel. Thus, one neural network is trained for each of the NAP campaigns. By contrast, the campaigns KNM3-SAP, KNM4-NOM, KNM4-OPT and KNM5 used the SAP setup, where the detector is modeled as consisting of 14 independent patches (see Fig. 6.8). Here, one neural network is trained per patch. In any case, a neural network is tested for its accuracy and validated by comparison to the analytic model [Karl et al., 2022].

Results achieved by the Netrium team can be compared with the results of the KaFit team, which uses the analytic computation of the KATRIN model. Thus, the Netrium team provides an additional sanity check for the KaFit results. And because the neural network approach speeds up the calculations by a factor of $\mathcal{O}(10^3)$ [Karl et al., 2022], more studies can be carried out and formerly numerically challenging approaches, such as Bayesian inference, can now be studied efficiently.

The results based on the first five measurement campaigns of KATRIN, using the Frequentist approach, were recently published in Science [KATRIN et al., 2025b]. In a next step, the KATRIN data shall be analyzed using Bayesian inference, which is a complementary analysis approach. Hence, the results do not only bare a different interpretation compared to the Frequentist approach (see Section 2.1), but also come in the form of distributions, accurate error estimates included. A detailed introduction to this topic is given in Chapter 2. The analyses were

encoded with the programming language Julia [Bezanson et al., 2017] and the high performance software "Bayesian Analysis Toolkit" (BAT) via the Julia package BAT.jl [Schulz et al., 2021] in combination with Optim.jl [Mogensen et al., 2018] and AdvancedHMC.jl [Xu et al., 2020]. Images were created using CairoMakie.jl [Danisch and Krumbiegel, 2021].

The general approach of the performed analyses is a cross-check approach between the two fitting teams, i.e. KaFit and Netrium. First each team implemented independently the scripts for the individual campaigns using their respective software and methods, i.e. different MCMC algorithms and convergence diagnostics were used. In detail, Netrium uses a neural network approach for the likelihood evaluation, Hamiltonian Monte Carlo (HMC) as MCMC algorithm and the convergence of the MCMC chains are monitored during the sampling via the Gelman-Rubin method [Schulz et al., 2021, Gelman and Rubin, 1992] and post sampling via the $\widehat{\mathrm{R}}$ and MCMCSE diagnostics. KaFit analytically evaluates the likelihood, uses the Goodman and Weare method [Goodman and Weare, 2010] as MCMC algorithm and an autocorrelation analysis to monitor the convergence diagnostics. The different methods employed by both teams strengthens the cross-check.

As a first test, the analysis for each campaign was performed on an Asimov data set. These are generated data from the analytic KATRIN model for the respective campaign with $m_\nu^2 = 0\,\mathrm{eV}^2$ while mimicking the structure of the real data. For each campaign, the impact of different priors for $m_\nu^2$ onto the marginal distribution of $m_\nu^2$ were studied for:

1. A flat prior $m_\nu^2 \sim \mathcal{U}(-10, 10)$,
2. A flat, positive prior $m_\nu^2 \sim \mathcal{U}(0, 3)$,

hereinafter referred to as (Flat) and (Flat, positive), respectively. The flat prior was chosen to complement the flat, positive prior, because the typical KATRIN Frequentist fit allows for the unphysical values $m_\nu^2 < 0\,\mathrm{eV}^2$ [Karl, 2022] as well. In this way, one can for example compare the best fit values from the Frequentist approach with the marginal modes of the Bayesian approach. To complement the analyses of different priors, the impact of including systematic effects are studied by:

1. Considering only statistical uncertainties,
2. Considering statistical and systematic uncertainties,

hereinafter referred to as (Stat. only) and (Total), respectively. This makes in total four separate analyses for each campaign.

The results from KaFit and Netrium were compared for each campaign via the quantiles of the marginal distribution of $m_\nu^2$. In case systematic structures or larger discrepancies between the numerical values were observed, further investigations were performed. Once these were resolved, the results were presented to the KATRIN collaboration. On approval by the collaboration, the fitting teams continued the analysis of the individual campaigns on real data. The results were again presented to the collaboration for approval. Once approved, the fitting teams moved on to the combined analysis of the first five KATRIN campaigns where the

cross-check procedure was repeated.

During the writing of this thesis, a paper is in preparation covering the Bayesian analysis results on real data from the Netrium and KaFit teams. This includes in total three different approaches to determine $m_\nu^2$ using all available data of the first five measurement campaigns. The analyses presented in the following are performed on Asimov data sets as well as on real data. However, in order to not delay the publication of this thesis, only the approved results for the analyses of the Asimov data sets are presented.

## 7.2 Monitoring MCMC convergence diagnostics

To achieve reliable results in Bayesian inference, the monitoring of the MCMC convergence via multiple diagnostics is crucial (see Section 2.5). The following configuration is used to monitor the MCMC convergence for the fit of the individual campaigns as well as the chained analysis. For each fit, ten independent MCMC chains are started to explore the parameter space. During the sampling, BAT.jl manages the burn-in phase automatically by using the Gelman-Rubin diagnostics for MCMC convergence. Once the burn-in phase is completed, each chain generates $10^5$ sampling points. After the sampling, the MCMC convergence is checked once more by the $\widehat{\mathrm{R}}$ and MCMCSE diagnostics [Vehtari et al., 2021]. Hereby, $\widehat{\mathrm{R}}$ is computed twice for each parameter, once focusing more on the bulk- or tail of the distribution. MCMCSE is likewise computed for each parameter, focusing on the 90 %-quantile, as the neutrino mass bound is typically given as a 90 % upper confidence level and should be as accurate as possible. The goal is to achieve a $\widehat{\mathrm{R}}$ -value smaller than the recommended, empirical value of 1.01 as suggested in Ref. [Vehtari et al., 2021] and a relative MCMCSE below 1 % for the 90 %-quantile, for each parameter of each fit.

A typical example for MCMC convergence diagnostics are shown in Fig. 7.2. It can be observed that parameters with a more narrow prior tend to have also a smaller relative MCMCSE. This is plausible, as the same amount of samples in a narrower range give a smaller sampling error compared to a broader range.

## 7.3 Individual campaigns

### 7.3.1 Introduction

The aim of Section 7.3 is to perform a neutrino mass analysis, utilizing Bayesian inference, for each of the first five KATRIN measurement campaigns individually. This has first and foremost the purpose of validating the implemented Bayesian analysis for each single campaign, before moving to more advanced approaches such as a simultaneous fit or a chained analysis via Bayesian knowledge updates. As already mentioned, only the results on Asimov data are shown within this thesis, but the analyses were performed on real data as well.

The presentation of the final results will mainly focus on the marginal distribution of $m_\nu^2$ and a representative selection of other parameters and correlation

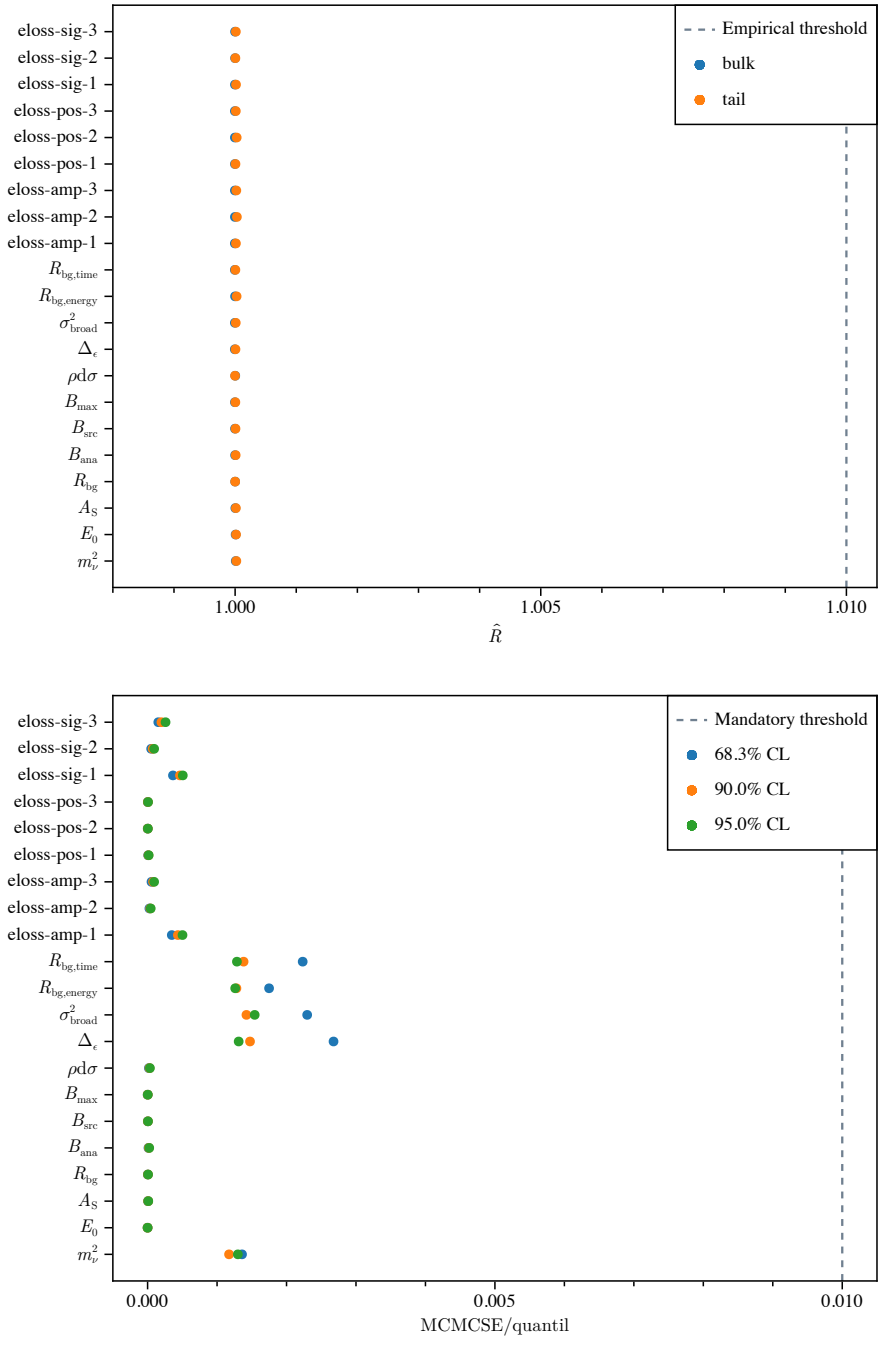


Figure 7.2: Example for a typical $\widehat{\mathrm{R}}$ and relative MCMCSE diagnostic for multiple quantiles based on a fit of KNM1. A flat, positive prior $m^2_\nu \sim \mathcal{U}(0,3)$ was used while taking statistical and systematic uncertainties into account.

plots. This is necessary, as the total number of parameters for all studied scenarios, for the first five KATRIN campaigns, is in the order of $4 \times 472$ (see Table 6.2).

### 7.3.2 MCMC convergence diagnostics

To validate the MCMC sampling, several MCMC convergence diagnostics are monitored during and after the sampling, as outlined in Section 7.2. In order to endow the statement with greater significance, the largest values from all parameters of a campaign are reported for $\widehat{\mathrm{R}}$ and the relative MCMCSE of the 90 %-quantile. The summaries of convergence diagnostics for the different fits are shown in Table B.1. From the tables it can be concluded, that for all parameters, fits and campaigns, the sampling error of the 90 %-quantile is below 0.56 % and the value for $\widehat{\mathrm{R}}$ is smaller than 1.00008. Thus, the anticipated goals of convergence are successfully reached for all fits.

### 7.3.3 Results

As a representative example, the results for the individual analysis of KNM5 are shown in Fig. 7.3. The results for the individual analysis of KNM1, KNM2 KNM3-SAP, KNM3-NAP, KNM4-NOM and KNM4-OPT can be found in Appendix B, Figs. B.7 to B.12. For each campaign the results for (Flat) and (Flat, positive) are shown. In each case, the results for (Stat. only) and (Total) can be compared in form of an overlay plot consisting of two step-histograms. For a more in depth comparison, the $q_s = [5\,\%,\ 15.9\,\%,\ 50\,\%,\ 68.3\,\%,\ 84.1\,\%,\ 90\,\%,\ 95\,\%]$ quantile values are shown in a table beneath the corresponding overlay plot.

**Summary of fits** The analysis of the Netrium results for all campaigns, and all performed fits (Flat + Stat. only), (Flat + Total), (Flat, positive + Stat. only) and (Flat, positive + Total), show the expected behavior: 1) The distributions for (Total) are slightly broader than those of (Stat. only), because more model parameters and correlations were taken into account. 2) The results of $m_\nu^2$ for (Flat) show a broader left side of the distribution, which was also observed in previous works, see Ref. [Karl, 2022]. 3) The comparison between the priors, on basis of the 90%-quantile, shows considerably larger values for (Flat, positive) than for (Flat), for all campaigns. This behavior emerges from the two distinct parameter spaces created by the distinct priors. As already stated in Section 7.1, the unphysical prior (Flat) was chosen to be able to compare the maximum a posteriori (MAP) estimate with the Frequentist best fit. For the final bounds on the neutrino mass, the physical prior (Flat, positive) should be used. Finally, the impact of the campaigns onto the overall broadening of the marginal distribution of $m_\nu^2$ is illustrated in Appendix B, Fig. B.13. The marginal distribution of $m_\nu^2$ is the broadest for KNM1, followed by KNM3-SAP and KNM3-NAP, which are on the same level, then by KNM2, KNM4-OPT, KNM4-NOM and KNM5. The ordering is the same for (Flat) and (Flat, positive) as well as the Frequentist analysis, and is compatible with the amount of statistics contributed by the single campaigns.

**Correlation between parameters** In general, the parameters of a statistical model acquire some more or less strong correlation during a regression analysis. In Fig. 7.4 a typical correlation plot for the free KATRIN model parameters ($m_\nu^2$,

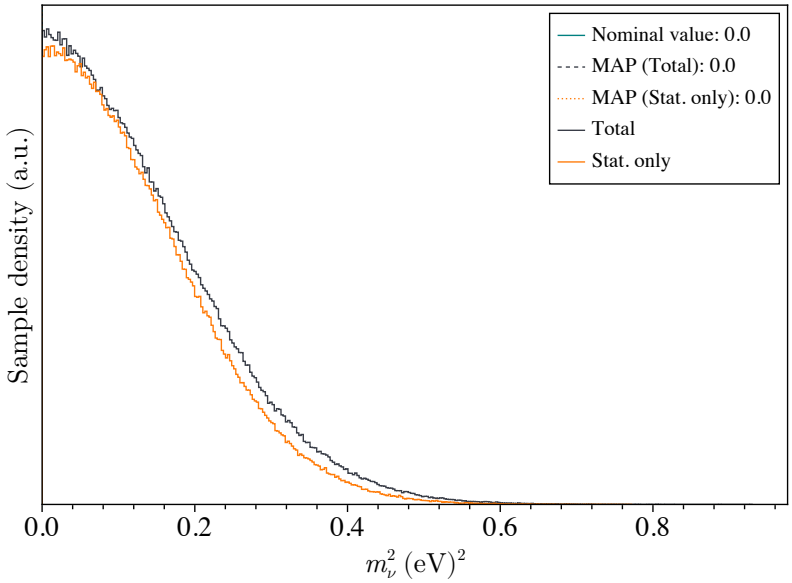


| Type | Quantile values for $m_\nu^2$ in eV$^2$ | | | | | | |
|---|---|---|---|---|---|---|---|
| | **5%** | **15.9%** | **50%** | **68.3%** | **84.1%** | **90%** | **95%** |
| **Total** | 0.0106 | 0.0342 | 0.1168 | 0.1741 | 0.2461 | 0.2882 | 0.3453 |
| **Stat. only** | 0.0103 | 0.0326 | 0.1095 | 0.1624 | 0.2283 | 0.2669 | 0.3183 |

(a) Results for a flat, positive prior: $m_\nu^2 \sim \mathcal{U}(0,3)$.

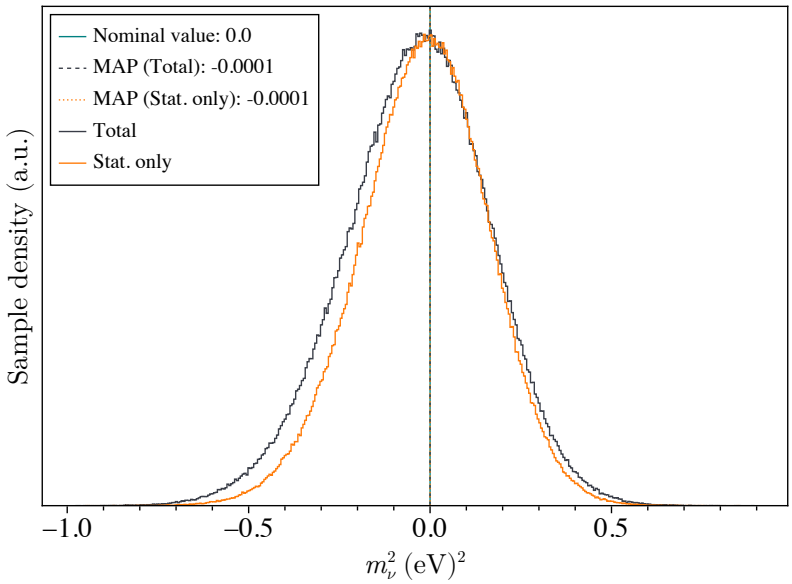


| Type | Quantile values for $m_\nu^2$ in eV$^2$ | | | | | | |
|---|---|---|---|---|---|---|---|
| | **5%** | **15.9%** | **50%** | **68.3%** | **84.1%** | **90%** | **95%** |
| **Total** | -0.3733 | -0.2337 | -0.0300 | 0.0607 | 0.1581 | 0.2102 | 0.2767 |
| **Stat. only** | -0.3162 | -0.1928 | -0.0132 | 0.0682 | 0.1552 | 0.2018 | 0.2620 |

(b) Results for a flat prior: $m_\nu^2 \sim \mathcal{U}(-10,10)$.

Figure 7.3: The results for the KATRIN campaign KNM5 are shown. Displayed are the marginal distributions of $m_\nu^2$ and the corresponding quantile values for different priors on $m_\nu^2$ as well as for (Stat. only) and (Total) fits can be compared. The nominal value and the MAP estimates are shown as vertical lines. Numbers are rounded to four digits.

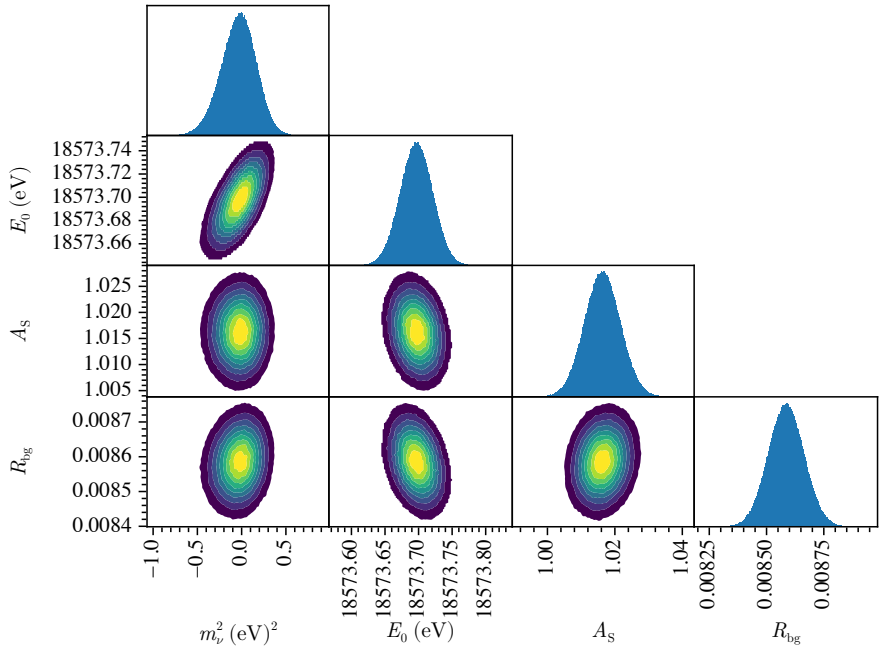


Figure 7.4: Typical example for a correlation plot of the four free model parameters. The shown results were achieved using a flat prior $m_\nu^2 \sim \mathcal{U}(-10,10)$ and taking statistical and systematic uncertainties into account. Asimov data were used.

$E_0$, $A_s$, $R_{bg}$) are shown. Typically, the correlation between $m_\nu^2$ and $E_0$ is stronger than for the other parameters. This was to be expected since the two parameters have a directer influence on each other, which can be seen in Eq. (6.19).

**Comparison Netrium and KaFit** To further validate the Netrium results, a cross-check with KaFit is performed for each individual campaign, for (Flat + Total) and (Flat, positive + Total). Hereby, one is looking at the difference of both teams in terms of the $q_s$ quantile values of the marginal distributions of $m_\nu^2$. For the comparison, the following versions of the code were used: Netrium [Schwemmer and Kroenert, 2025] and KaFit [Xu, 2025]. The sampling errors of the $q_s$ are typically in the order of $O(10^{-3}\text{eV}^2)$ or even below for both fitting teams. The results are displayed in Table 7.1. The quantile values typically differ only $O(10^{-3}\text{eV}^2)$ or below, for both priors. Nevertheless, there are three values for (Flat) and one value for (Flat, positive) which are at $\sim 1 \times 10^{-2}\,\text{eV}^2$. However, when taking the sampling error into account the difference is compatible within $O(10^{-3}\text{eV}^2)$. Overall, this is an excellent agreement between Netrium and KaFit considering the anticipated sensitivity of 200 meV for $m_\nu$ at 90 % CL.

**Maximum a posteriori estimate** To check for a correct implementation of the posterior, a MAP estimation was performed for each analysis. For all campaigns and fits, the maximal difference between the nominal value $m_\nu^2 = 0\,\text{eV}^2$ and the MAP are $O(10^{-3}\,\text{eV}^2)$ for (Flat) and $O(10^{-15}\,\text{eV}^2)$ for (Flat, positive). Hence,

Table 7.1: The quantiles of $m_\nu^2$, for the individual analysis of KNM1-5 Asimov data, are compared between Netrium and KaFit via their difference (Netrium-KaFit). The comparison is made for fits with a flat- and flat, positive prior on $m_\nu^2$. The values are rounded to four digits.

(a) For a flat prior, $m_\nu^2 \sim \mathcal{U}(-10,10)$.

| Campaign | Quantile differences of $m_\nu^2$ | | | | | | |
|---|---|---|---|---|---|---|---|
| | **5%** | **15.9%** | **50%** | **68.3%** | **84.1%** | **90%** | **95%** |
| **KNM1** | 0.0110 | 0.0086 | -0.0011 | -0.0025 | -0.0058 | -0.0051 | -0.0067 |
| **KNM2** | -0.0020 | 0.0012 | 0.0038 | 0.0049 | 0.0043 | 0.0044 | 0.0058 |
| **KNM3-SAP** | -0.0039 | 0.0057 | 0.0039 | 0.0053 | 0.0054 | 0.0076 | 0.0104 |
| **KNM3-NAP** | -0.0071 | -0.0048 | -0.0065 | -0.0055 | -0.0067 | -0.0056 | -0.0035 |
| **KNM4-NOM** | 0.0146 | 0.0040 | -0.0001 | -0.0010 | -0.0020 | -0.0011 | 0.0005 |
| **KNM4-OPT** | 0.0041 | -0.0047 | -0.0058 | -0.0034 | -0.0024 | -0.0000 | 0.0016 |
| **KNM5** | 0.0091 | 0.0062 | 0.0054 | 0.0054 | 0.0056 | 0.0059 | 0.0063 |

(b) For a flat, positive prior, $m_\nu^2 \sim \mathcal{U}(0,3)$.

| Campaign | Quantile differences of $m_\nu^2$ | | | | | | |
|---|---|---|---|---|---|---|---|
| | **5%** | **15.9%** | **50%** | **68.3%** | **84.1%** | **90%** | **95%** |
| **KNM1** | -0.0004 | 0.0001 | -0.0007 | -0.0032 | -0.0071 | -0.0081 | -0.0118 |
| **KNM2** | 0.0006 | 0.0015 | 0.0033 | 0.0044 | 0.0052 | 0.0064 | 0.0072 |
| **KNM3-SAP** | -0.0001 | 0.0000 | -0.0022 | -0.0031 | -0.0035 | -0.0037 | -0.0041 |
| **KNM3-NAP** | 0.0001 | -0.0005 | -0.0008 | -0.0011 | -0.0018 | -0.0012 | -0.0039 |
| **KNM4-NOM** | -0.0006 | -0.0012 | -0.0030 | -0.0034 | -0.0048 | -0.0048 | -0.0053 |
| **KNM4-OPT** | -0.0007 | -0.0015 | -0.0038 | -0.0041 | -0.0059 | -0.0063 | -0.0076 |
| **KNM5** | 0.0002 | 0.0008 | 0.0022 | 0.0026 | 0.0020 | 0.0024 | 0.0036 |

these differences are small enough for the anticipated $m_\nu^2$ sensitivity of 200 meV at 90% CL. Likewise, for the Frequentist analyses with Netrium, using a flat prior on $m_\nu^2$, the maximal difference between the maximum likelihood estimation (MLE) and the nominal value, are $O(10^{-3}\,\mathrm{eV}^2)$. For a flat, positive prior no comparison is available.

**Most probable value** In addition to the MAP, also the most probable value (MPV), i.e. the mode of the marginal distribution, of $m_\nu^2$ should be located at the nominal value. However, there is an inherent problem with the MPV estimation. As the MPV can not be expressed as a quantile value, it does not have an associated sampling error, which makes it hard to judge the result. To approximate the marginal distribution, independent of its actual shape, a non-parametric estimation, such as kernel density estimation (KDE), could be used. However, the thereby estimated MPV depends strongly on the used kernel and the bandwidth of the kernel function. For this reason a numerical comparison seems not to be appropriated. Nevertheless, graphically the MPV value seems indeed to be located at the nominal value for all campaigns using (Flat, positive). The same applies to all campaigns using (Flat), except for KNM3-SAP. In Appendix B, Fig. B.9 it is visible that the MPV is slightly shifted to the left from the nominal value. This shift is visible in Netrium and KaFit. A potential explanation for this phenomenon could be that this is an inherent feature of Bayesian inference itself.

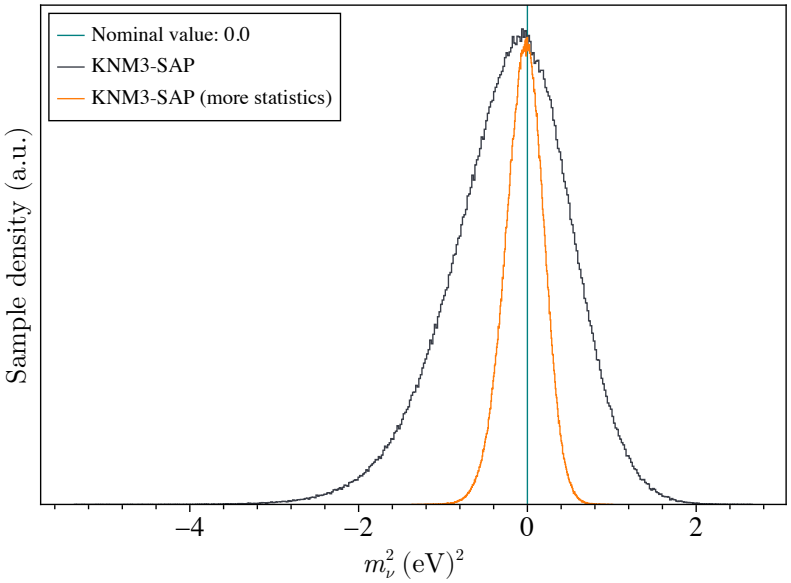


Figure 7.5: Comparison of the marginal distribution of $m_\nu^2$ for KNM3-SAP and KNM3-SAP with the statistics increased by a factor of 20.

In case the statistics would be too low, the prior distributions can have a larger impact during the marginalization which can lead to a difference between the MAP and the MPV. This possible origin is supported by the observation, that the shift disappears when increasing the statistics of KNM3-SAP, which is shown in Fig. 7.5. The comparison shows, that the KNM3-SAP campaign using more statistics can retrieve much better the nominal value than the 'normal' amount of statistics present in KNM3-SAP. Hence, this hints to a domination of the prior distribution over the likelihood distribution, which could arise from too stringent priors. However, this phenomenon is still under investigation at the moment and will be likely resolved and explained in the upcoming paper.

**Posterior predictive checks** An additional sanity check was performed in the form of posterior predictive checks, as introduced in Section 2.6. First, the reproduced data distributions (RDD) from the MAP estimation is analyzed for KNM1-5 individually for (Total) with (Flat) and (Flat, positive). Hereby, the parameter point estimates from MAP are used as input for the KATRIN model. The model itself returns a Poisson distribution for each retarding energy at which the original data points were measured. From each such predicted Poisson distribution $10^6$ samples are drawn, which form the RDDs. In order to access how well the reproduced data distributions cover the original data points, their normalized counts are compared. Hence, to be able to compare the whole energy spectrum at once, despite the counts differ by orders of magnitude, the predicted values are divided by the value of the original data point. The results are shown in Figs. 7.6 and 7.7. For the purpose of visualization and because the patches show similar results, only the result of patch one is shown for each SAP-campaign, respectively. The RDD are

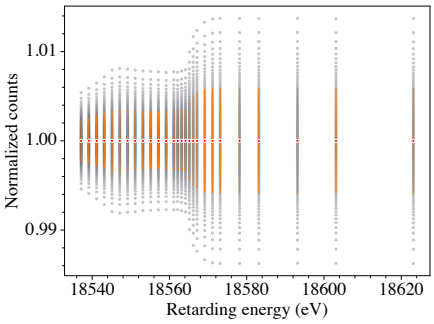


(a) KNM1.

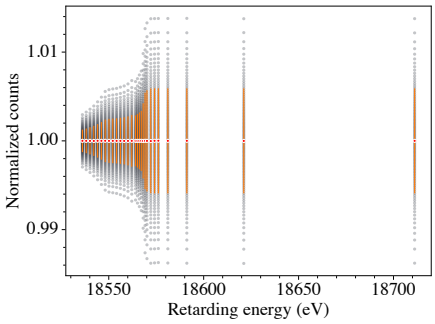


(b) KNM2.

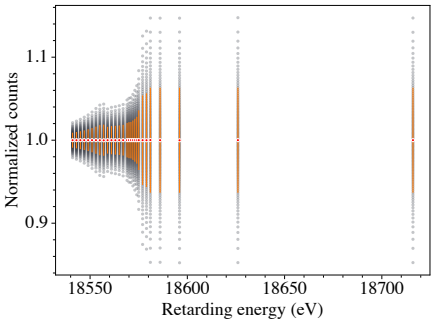


(c) KNM3-SAP.

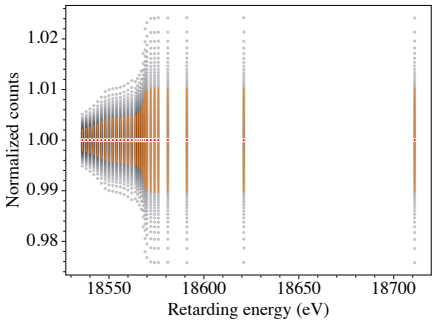


(d) KNM3-NAP.

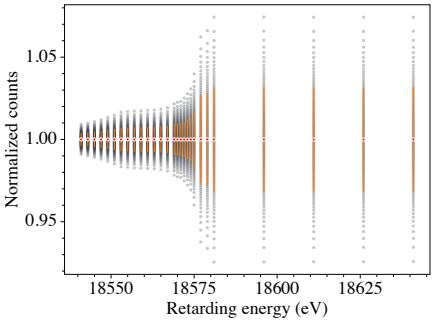


(e) KNM4-NOM.

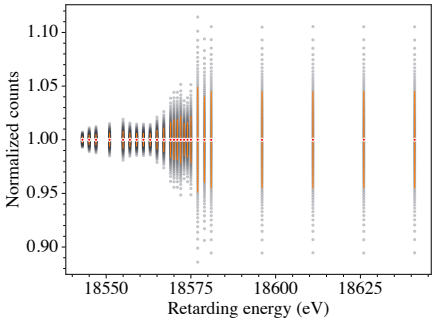


(f) KNM4-OPT.

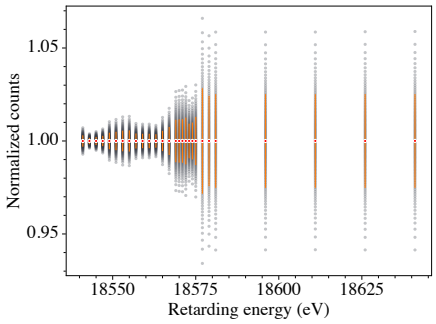


(g) KNM5.

Figure 7.6: Posterior predictive check with MAP estimates for the individual KATRIN campaigns using a flat prior $m_\nu^2 \sim \mathcal{U}(-10,10)$. The gray dots represent the reproduced data distributions, with red dots indicating the mean values. The original data points and their errors are drawn in orange. To compare all energies at once, despite the counts differing by orders of magnitude, the values at each energy were normalized by dividing by the original data point.

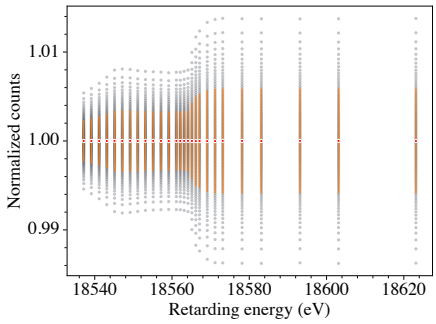


(a) KNM1.

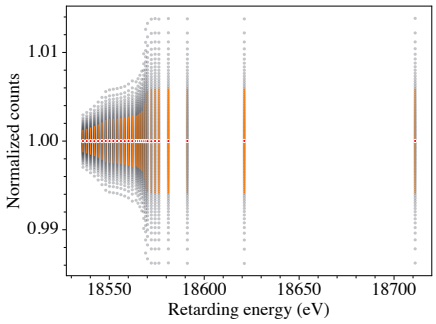


(b) KNM2.

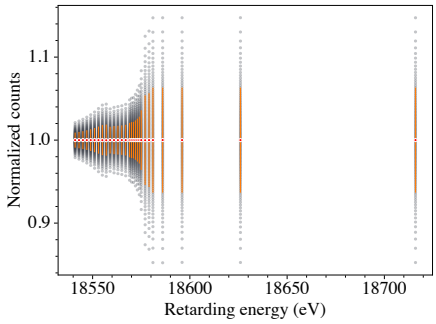


(c) KNM3-SAP.

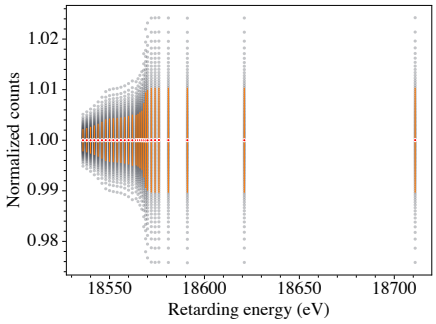


(d) KNM3-NAP.

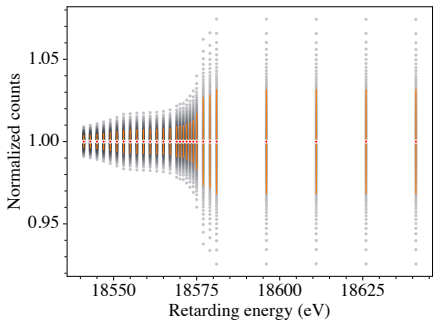


(e) KNM4-NOM.

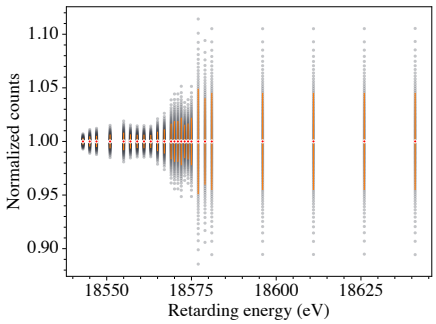


(f) KNM4-OPT.

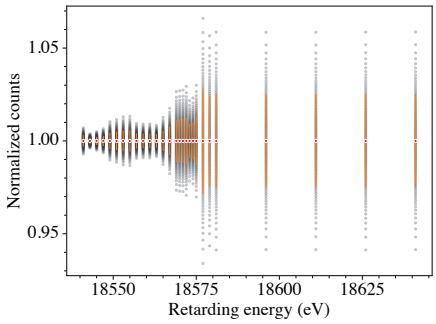


(g) KNM5.

Figure 7.7: Posterior predictive check with MAP estimates for the individual KATRIN campaigns using a flat, positive prior $m_\nu^2 \sim \mathcal{U}(0,3)$. The gray dots represent the reproduced data distributions, with red dots indicating the mean values. The original data points and their errors are drawn in orange. To compare all energies at once, despite the counts differing by orders of magnitude, the values at each energy were normalized by dividing by the original data point.

illustrated by gray dots, corresponding to 100 quantiles values of the distribution, which are equidistantly distributed in probability from 1 % up to 99 %. The mean value of each distribution is indicated with a red point. The original data points together with their uncertainties are plotted in orange.

For (Flat), as well as (Flat, positive), the RDD cover the original data points very well and no systematic effects can be seen. The maximal deviation of the mean values of the RDD to a value of one, for all energies and patches, are for (Flat) 0.02 % with typical values $O(0.001\,\%)$ and for (Flat, positive) 0.018 % with typical values $O(0.001\,\%)$. In addition, the corresponding standardized residuals were calculated and are shown in Appendix B, Figs. B.1 and B.2. The standardized residual for an energy-bin is defined as:

$$r := \frac{y^{\mathrm{rep}} - y^{\mathrm{orig}}}{\mathrm{std}(y^{\mathrm{rep}})}, \tag{7.3}$$

where $y^{\mathrm{rep}}$ is the reproduced data distribution and $y^{\mathrm{orig}}$ the original data point. Under the assumption that the differences are normally distributed, $r$ should follow a standard Normal distribution, which is illustrated as an orange curve. The standardized residual for each energy-bin is plotted as a gray curve. An excellent agreement can be observed for (Flat), as well as (Flat, positive), for all energy and patches. This validates once more the encoded models for the individual campaigns KNM1-5.

Second, the reproduced data distributions gained from the posterior samples are analyzed for KNM1-5 individually for (Flat) and (Flat, positive). In contrast to the MAP case, here exactly one sample is drawn from the predicted distribution of the model. This ensures that the resulting RDD consist of $10^6$ samples, just like in the MAP case. The results for the normalized counts are displayed in Appendix B, Figs. B.3 and B.4, and the corresponding standardized residuals in Figs. B.5 and B.6. The maximal deviation of the mean values of the RDD to a value of one considering all campaigns, energies and patches, are for (Flat) 0.114 % with typical values in $O(0.01\,\%)$ and for (Flat, positive) 0.317 % with typical values $O(0.01\,\%)$. In comparison to the MAP case, the maximal deviation became worse by one order of magnitude. The origin of this increase is an emerging systematic effect present in all campaigns, which was indeed not present in the MAP case. This phenomenon is evident in the normalized counts plots by the functional behavior of the red dots, and in the standardized residual plots as a shift of the gray distributions in comparison to the standard Normal distribution. In the case of (Flat), the systematic effect is barely visible for most of the campaigns, where for (Flat, positive) the effect is more pronounced. One possible explanation would be that the mean values of the RDD are misleading, however it was checked that the RDD indeed have a Gaussian shape and their mode can be approximated by the mean value. Furthermore, the same phenomenon is visible with the same intensity for (Stat. only) fits. These observations all hint to the conclusion, that the origin of the systematic effect is likely due to Bayesian inference itself and the integration over the priors of the free model parameters. As a further test, the analysis was performed for KNM3-SAP (Total + Flat) with 20 times increased statistics. This should resolve the systematic effect, if it originates from too stringent prior distributions. The corresponding normalized count plot is shown in Fig. 7.8. Indeed,

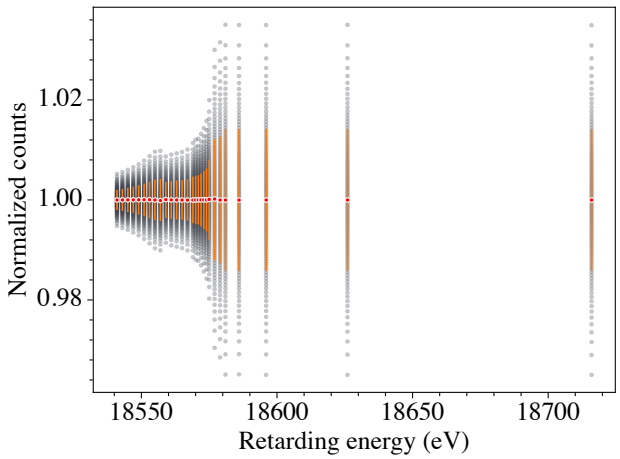


Figure 7.8: Posterior predictive check with posterior samples for KNM3-SAP with the statistics increased by a factor of 20 and using a flat prior $m_\nu^2 \sim \mathcal{U}(-10,10)$. The gray dots represent the reproduced data distributions, with red dots indicating the mean values. The original data points and their error are drawn in orange. To compare all energies at once, despite the counts differing by orders of magnitude, the values at each energy were normalized by dividing by the original data point.

the systematic effect has been reduced compared to classical KNM3-SAP. This is also reflected in the maximal deviation 0.018 % with typical values $O(0.001\,\%)$, for all energies and patches. Compared to the deviations when using KNM3-SAP with the 'normal' amount of statistics, this is a reduction by one order of magnitude. Summarizing, first studies on the origin of the systematic phenomenon were made, but the exact origin is still under investigation by Netrium and KaFit, and will be discussed in the upcoming paper.

### 7.3.4 Summary of individual analyses

The analysis of the first five KATRIN campaigns on Asimov data confirmed a correct and effective implementation of the individual models, as shown by the MAP results. The MAP value for $m_\nu^2$ retrieved the ground truth of the Asimov data within the anticipated sensitivity $O(10^{-3}\,\mathrm{eV}^2)$. Furthermore, the reproduced data distributions show an excellent agreement to the original data points and no sign of systematic effects is visible. In a next step, posterior samples were drawn utilizing a MCMC approach. The MCMC convergence diagnostics indicate an overall convergence of the MCMC chains, and the anticipated accuracy for the 90 % confidence level could be achieved for each parameter. The marginal parameter distributions of $m_\nu^2$ showed the expected behavior for fits taking only statistical uncertainties or statistical and systematic uncertainties into account, peaking at the nominal value of zero. The correlation plots behaved also as expected. To strengthen the results gained by Bayesian inference, a comparison between the two independent fitter teams Netrium and KaFit was performed. Despite KaFit and Netrium differ in the method to calculate the likelihood function, the used MCMC sampling algorithm, and the monitoring of the convergence diagnostics,

the comparison of the quantiles for the marginal distribution of $m_\nu^2$ showed a very good agreement with differences $O(10^{-3}\,\mathrm{eV}^2)$. However, two issues remain under investigation by Netrium and KaFit, where first studies has already been performed. On the one hand, the marginal parameter distribution of $m_\nu^2$ for KNM3-SAP shows a slight discrepancy between the peak of the distribution and the nominal value, when using a flat prior for $m_\nu^2$. On the other hand, the reproduced data distributions generated from posterior samples show a small systematic effect. Further studies will be performed to resolve the issues, so that their origins can be explained in the upcoming paper. Despite these ongoing investigations, it seems reasonable to move on to Bayesian knowledge updates, a more complex analysis for which the individual analysis of the KATRIN campaigns will serve as the basis.

## 7.4 Chained analysis

### 7.4.1 Introduction

Apart from fitting each KATRIN campaign on an individual basis, a combined approach is needed in order to take advantage of the full accumulated statistics of KATRIN, as illustrated in Fig. 6.10. The first approach which comes to mind is fitting the KNM1-5 data in a simultaneous fit. This was already performed with the Frequentist approach [KATRIN et al., 2025b] and can be done with Bayesian inference as well, which is, among other things, pursued in the doctor thesis of Alessandro Schwemmer.

However, there is a complementary analysis approach unique to Bayesian inference, the Bayesian knowledge update. The general idea is to forward certain information gained in one fit as prior information to a subsequent fit. In this thesis, this approach is employed to perform a chained analysis of the first five KATRIN campaigns. Hereby, the forwarded information are the marginal distributions of the forwarded model parameters and their correlations with each other.

The only model parameters which can be forwarded are those which appear identically in all fits of the chained analysis. Hence, their appearance in the statistical models is identical, and their prior distributions are independent of the campaign. For the analysis of the KNM1-5 campaigns in total 12 parameters fulfill these requirements, see Sections 6.5 and 6.6, and can be forwarded:

$$m_\nu^2,\ B_\mathrm{src},\ B_\mathrm{max},\ \vec{E}_\mathrm{loss,amp},\ \vec{E}_\mathrm{loss,exp},\ \vec{E}_\mathrm{loss,std}. \tag{7.4}$$

In the simplest case only a single parameter, namely $m_\nu^2$, is forwarded between fits. An illustration of the procedure is shown in Fig. 7.9. In a more advanced approach, all 12 parameters together with their initial correlation (as is the case for the $E_\mathrm{loss}$-parameters) or their acquired correlation during a regression can be forwarded from fit to fit.

However, the Bayesian knowledge update approach does not allow taking partially correlated fit parameters between different campaigns into account, as for example the correlation of the column density × inelastic cross section $\rho\mathrm{d}\sigma$ between KATRIN campaigns [KATRIN et al., 2024a]. The reason behind this limitation is that the model parameter describing $\rho\mathrm{d}\sigma$ in KNM1 is not present in the Netrium

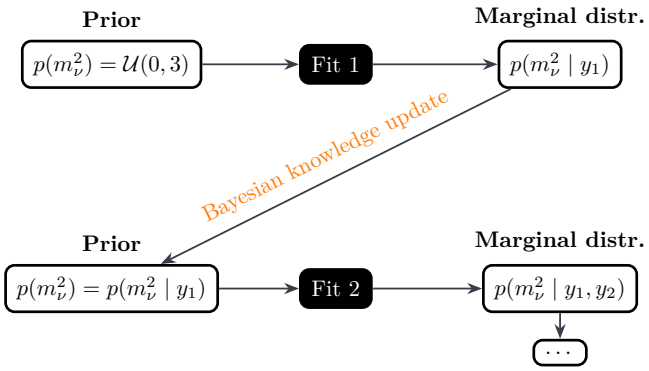


Figure 7.9: Schematic illustration of a sequential analysis based on the marginal distribution of $m_\nu^2$. The knowledge gained from the first fit step is incorporated as prior information for the subsequent fit step.

model of KNM2, and thus no correlation between these distinct parameters can be established. That said, this allows to study the impact of these correlations onto the final neutrino mass result, by comparison of the simultaneous with the chained analysis.

In Section 7.4, the influence of: 1) the ordering of the analyzed campaigns onto the final $m_\nu^2$ result, 2) forwarding a different amount of model parameters, 3) using different priors for $m_\nu^2$ in the first step of the chain and 4) using (Stat. only) or (Total) are investigated. As previously mentioned, only the results on Asimov data are shown within this thesis, but the analyses were performed on real data as well.

### 7.4.2 Order of Bayesian knowledge updates

A chained analysis involves a sequence of Bayesian knowledge updates. In the following, the impact of the ordering of the sequence onto the final, marginal distribution of a parameter $\kappa$ shall be mathematically investigated.

Suppose a simple example where the sequence consists of two steps. In the first step, one has the data set $y_1$ and model parameters $\theta_1$, which are unique for this measurement campaign. In addition, one has the forwarded parameters $\kappa$ which are identical to each campaign. It is assumed that $\kappa$ and $\theta_i$ do not have an intrinsic correlation. As the normalization of the posteriors are not relevant for the following derivation, they are omitted for the benefit of readability. Thus, one starts with the posterior distribution:

$$\mathrm{p}(\kappa, \theta_1 \mid y_1) \sim \mathrm{p}(y_1 \mid \kappa, \theta_1)\ \mathrm{p}(\theta_1)\ \mathrm{p}(\kappa)_{\mathrm{init}}, \tag{7.5}$$

from which the marginal distribution of $\kappa$:

$$\mathrm{p}(\kappa \mid y_1) = \int_{\theta_1} \mathrm{p}(\kappa, \theta_1 \mid y_1)\, \mathrm{d}\theta_1\,, \tag{7.6}$$

is used as prior for $\kappa$ in the second step of the sequence:

$$\mathrm{p}(\kappa, \theta_2 \mid y_1, y_2) \sim \mathrm{p}(y_2 \mid \kappa, \theta_2)\ \mathrm{p}(\theta_2)\ \mathrm{p}(\kappa \mid y_1). \tag{7.7}$$

Now suppose, without the loss of generality, a sequential analysis with a reversed order of analyzed measurement campaigns. This time the posterior of the first step takes the form:

$$\mathrm{p}(\kappa,\theta_2 \mid y_2) \sim \mathrm{p}(y_2 \mid \kappa,\theta_2)\ \mathrm{p}(\theta_2)\ \mathrm{p}(\kappa)_{\mathrm{init}}, \tag{7.8}$$

from which the marginal distribution of $\kappa$:

$$\mathrm{p}(\kappa \mid y_2) = \int_{\theta_2} \mathrm{p}(\kappa,\theta_2 \mid y_2)\,\mathrm{d}\theta_2\,, \tag{7.9}$$

is used as prior for $\kappa$ in the second step of the sequence:

$$\mathrm{p}(\kappa,\theta_1 \mid y_2,y_1) \sim \mathrm{p}(y_1 \mid \kappa,\theta_1)\ \mathrm{p}(\theta_1)\ \mathrm{p}(\kappa \mid y_2). \tag{7.10}$$

Compared shall be the marginal distributions of $\kappa$ at the end of the sequences:

$$\mathrm{p}(\kappa \mid y_1,y_2) \sim \mathrm{p}(\kappa)_{\mathrm{init}} \int_{\theta_2} \mathrm{p}(y_2 \mid \kappa,\theta_2)\ \mathrm{p}(\theta_2)\,\mathrm{d}\theta_2 \int_{\theta_1} \mathrm{p}(y_1 \mid \kappa,\theta_1)\ \mathrm{p}(\theta_1)\,\mathrm{d}\theta_1\,, \tag{7.11}$$

$$\mathrm{p}(\kappa \mid y_2,y_1) \sim \mathrm{p}(\kappa)_{\mathrm{init}} \int_{\theta_1} \mathrm{p}(y_1 \mid \kappa,\theta_1)\ \mathrm{p}(\theta_1)\,\mathrm{d}\theta_1 \int_{\theta_2} \mathrm{p}(y_2 \mid \kappa,\theta_2)\ \mathrm{p}(\theta_2)\,\mathrm{d}\theta_2\,, \tag{7.12}$$

which are indeed identical, because the integrals are interchangeable. More generally, the ordering of the sequence does not matter, as long as the same data $y \in \{y_1,\ldots,y_\mathrm{i},\ldots,y_\mathrm{n}\}$ and parameters $\theta \in \{\theta_1,\ldots,\theta_\mathrm{i},\ldots,\theta_\mathrm{n}\}$ are sampled throughout the sequences and the initial priors $\mathrm{p}(\kappa)_{\mathrm{init}}$ are identical. Summarizing, the marginal distributions of the forwarded parameters and their correlations, obtained in the last fit of the chain, are independent of the ordering in which the campaigns were analyzed. This statement will be further studied in Section 7.4.5.

### 7.4.3 Bayesian knowledge update with BAT

The Bayesian knowledge update makes it necessary to encode the information gained from a previous fit step somehow in the statistical model of the next fit step, which is a complex task. For the MCMC sampling the software BAT.jl [Schulz et al., 2021] is used to efficiently draw samples from the posterior. Part of this efficiency comes from the automatic choice of a parameter space suitable for the chosen MCMC algorithm [Schulz et al., 2021]. For this procedure the prior distributions have to be transformed from one variable space to another. In order to calculate automatically such a transformation, a proper prior in BAT must be defined from one of the distributions available in Distributions.jl [Besançon et al., 2021]. This restriction becomes relevant when passing on the information of one fit step to the next one.

Considering the case where all 12 parameters together with their correlations are forwarded between fits. The marginal parameter distributions after a fit are correlated with each other and must not necessarily follow a Gaussian distribution, but rather show skewness or other non-Gaussian behavior. Because currently no multivariate skew normal distribution is implemented in Distributions.jl and to be independent of non-Gaussian behavior at all, a different approach was taken. The goal is to transform the non-Gaussian multivariate, correlated distribution

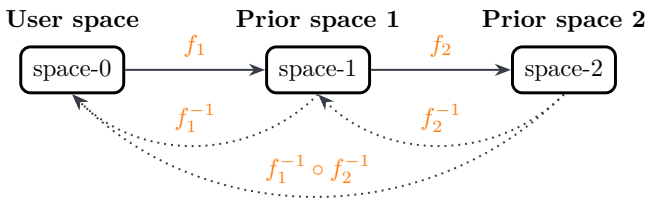


Figure 7.10: Schematic illustration for the transformation of the forwarded parameters between the three relevant parameter spaces. The involved transformation functions $f_i$ together with their back transformations $f_i^{-1}$ are shown.

of the 12 parameters to a multivariate standard normal distribution, which can be encoded as a proper prior in BAT. To do so, three parameter spaces (space-0, space-1 and space-2) are introduced. The transformation between the three spaces is illustrated in Fig. 7.10 and shall be explained in the following.

The very first step in a sequence of Bayesian knowledge updates is to define the initial prior for the forwarded parameters, which was called $p(\kappa)_{\text{init}}$ in Section 7.4.2. The variate space in which the 12 forwarded parameters take their physical form $p_0$, as given in Appendix B, Eqs. (B.1) to (B.4), are called space-0 or user space. In the first step of the chain $p_0$ is not directly used, but rather a transformation $f_1$ (from space-0 to space-1) is calculated, such that $p_1 := f_1(p_0)$ follows a multivariate standard normal distribution. This transformation is done by BAT with methods described in [Schulz et al., 2021]. The prior $p_1$ can be easily encoded in BAT and is used as actual prior in the code for the first step of the sequence. The back transformation $f_1^{-1}$ is calculated as well, as one needs to transform each input coming from $p_1$ back to space-0 before evaluating the likelihood distribution. After the MCMC sampling, the marginal distributions for the forwarded parameters are returned in space-1. These form a multivariate correlated distribution (from here on called $\mathcal{D}$) which does not necessarily follow a multivariate normal distribution, despite being close to it. Once again, to define a proper prior in BAT for the next step of the chain an additional transformation is necessary. The transformation $f_2$ (from space-1 to space-2) is calculated, such that the resulting prior $p_2 = f_2(\mathcal{D})$ follows a multivariate standard normal distribution, which can be encoded as a proper prior in BAT. Finally, the back transformation $f_1^{-1} \circ f_2^{-1}$ is applied to each input coming from $p_2$ before evaluating the likelihood distribution. In this way, the likelihood is fully defined in space-0 when it is handed over to BAT.

The transformation $f_2$ is performed in a two-step process via an affine- and a spline transformation. First, the multivariate distribution $\mathcal{D}$ is transformed to a standardized and uncorrelated multivariate distribution via the transformation [Kessy et al., 2018]:

$$Y = L_X^{-1}(X - \mathrm{E}[X]). \tag{7.13}$$

The symbol $X$ denotes the random variable of $\mathcal{D}$ and $L_X$ is the lower triangular matrix of a Cholesky decomposition of the covariance matrix of $X$. The symbol $Y$ represents the new random variable with the desired properties of $\mathbb{E}[Y] = 0$ and $\mathrm{Cov}(Y) = \mathbb{1}$. In a second step, any remaining skewness in $Y$ is removed by

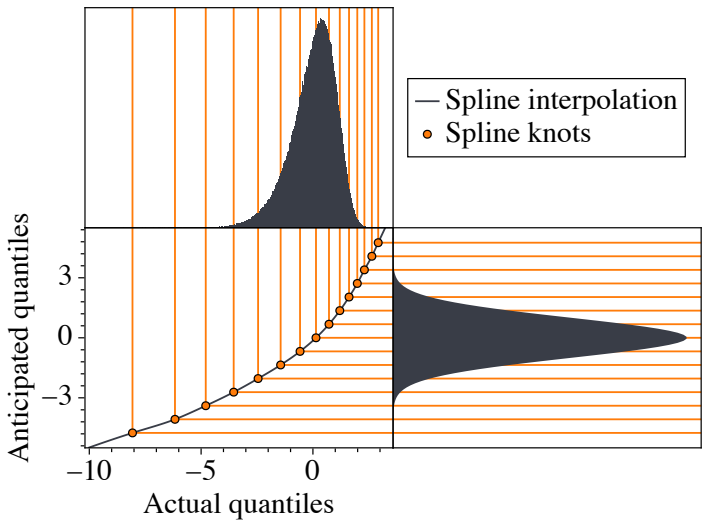


Figure 7.11: Illustration of a quadratic spline interpolation from a skewed distribution to a standard normal distribution. The upper left part of the figure shows a standardized skewed distribution, which shall be transformed to a standard normal distribution, shown in the lower right part of the figure. The spline x- and y-knots are shown as orange vertical and horizontal lines, respectively. The lower left part of the figure shows the spline knots as orange points together with the resulting interpolation function as gray line.

performing a quadratic spline interpolation on each marginal distribution of $Y$ individually. The most robust fits were achieved by choosing the spline y-knots as equidistant quantile values of the anticipated standard normal distribution, from a probability of $p = 1 \times 10^{-6}$ to $p = 1 - 1 \times 10^{-6}$. The matching quantiles of the marginal distributions are related via a cumulative distribution function. A typical spline interpolation is illustrated in Fig. 7.11, where the spline knots placement and the resulting interpolation curve are visible. An example how the forwarded parameters look before and after the transformation from space-1 to space-2 can be seen in Appendix B, Fig. B.14.

For the case in which only information about $m_\nu^2$ is forwarded between fits, the approximating of the marginal distribution was first handled by an unbinned maximum likelihood estimation. This worked well for Asimov data, but was not flexible enough for the analysis of real data. To be consistent, for real- as well as Asimov data the (affine + spline) transformation approach was utilized.

### 7.4.4 MCMC convergence diagnostics

To validate the MCMC sampling, several MCMC convergence diagnostics are monitored during and after the sampling, as outlined in Section 7.2. The convergence diagnostics are monitored for each fit of the sequential analysis and all fits have to show overall convergence. Reported are the largest values from all parameters of a campaign for $\widehat{\mathrm{R}}$ and the relative MCMCSE of the 90 %-quantile. The summaries of

Table 7.2: Maximal deviation of the mean values of the RDD to a value of one, for all energies and patches. The results are for fits taking statistical and systematic uncertainties into account.

(a) Chained analyses

| Forwarded parameters | Initial prior | Permutation | Maximal deviation | Typical deviation |
|---|---|---|---|---|
| $m_\nu^2$ only | Flat | KNM1-5 | 0.024 % | $\mathcal{O}$(0.001 %) |
| $m_\nu^2$ only | Flat | KNM5-1 | 0.006 % | $\mathcal{O}$(0.001 %) |
| $m_\nu^2$ only | Flat, positive | KNM1-5 | 0.082 % | $\mathcal{O}$(0.010 %) |
| $m_\nu^2$ only | Flat, positive | KNM5-1 | 0.025 % | $\mathcal{O}$(0.010 %) |
| $m_\nu^2$ and others | Flat | KNM1-5 | 0.026 % | $\mathcal{O}$(0.001 %) |
| $m_\nu^2$ and others | Flat | KNM5-1 | 0.006 % | $\mathcal{O}$(0.001 %) |
| $m_\nu^2$ and others | Flat, positive | KNM1-5 | 0.078 % | $\mathcal{O}$(0.010 %) |
| $m_\nu^2$ and others | Flat, positive | KNM5-1 | 0.025 % | $\mathcal{O}$(0.001 %) |

(b) Individual campaigns

| Campaign | Prior | Maximal deviation | Typical deviation |
|---|---|---|---|
| KNM1 | Flat | 0.028 % | $\mathcal{O}$(0.010 %) |
| KNM5 | Flat | 0.022 % | $\mathcal{O}$(0.001 %) |
| KNM1 | Flat, positive | 0.166 % | $\mathcal{O}$(0.010 %) |
| KNM5 | Flat, positive | 0.119 % | $\mathcal{O}$(0.010 %) |

convergence diagnostics for all performed fits are shown in Appendix B, Tables B.3 to B.5. From the tables it can be concluded, for all parameters of all performed fits, that the sampling error of the 90 %-quantile is below 0.55 % and the value for $\widehat{\mathrm{R}}$ is smaller than 1.000183. Thus, the anticipated goals of convergence, i.e. $\widehat{\mathrm{R}} < 1.01$ and MCMCSE < 1 %, are successfully reached.

### 7.4.5 Results

The results for the chained analysis, when forwarding all 12 possible parameters ($m_\nu^2$, $B_\mathrm{max}$, $B_\mathrm{src}$, $\vec{E}_\mathrm{loss,amp}$, $\vec{E}_\mathrm{loss,exp}$ and $\vec{E}_\mathrm{loss,std}$), hereinafter called ($m_\nu^2$ and others), are shown in Fig. 7.12. The results forwarding only $m_\nu^2$, hereinafter called ($m_\nu^2$ only), can be found in Appendix B, Figs. B.15 and B.16. The results of the chained analyses are discussed in the following.

**Posterior predictive checks** As in the case of the individual analyses in Section 7.3, the posterior predictive checks (PPC) are also performed for the chained approach to validate the MCMC results. Hereby, the PPC are calculated from the posterior samples and original data points of the final chain step. The corresponding normalized count plots are shown in Fig. 7.13. The figure encompasses the results of ($m_\nu^2$ and others), ($m_\nu^2$ only), each for the two permutations KNM1-5 and KNM5-1 and each for the cases (Total + Flat) and (Total + Flat, positive). The corresponding maximal and typical deviations from a value of one can be found in Table 7.2a. Comparing the campaign KNM1 with the permutation KNM5-1, and KNM5 with the permutation KNM1-5, the initial observation to be made is that typically the systematic effects are significantly mitigated within the chained analysis compared to the analysis of the individual KATRIN campaigns. The max-

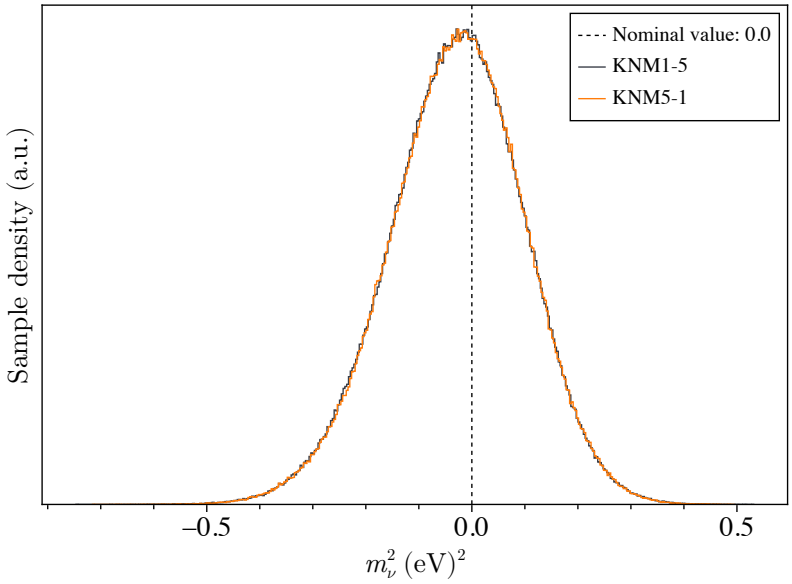


| Type | Quantile values for $m_\nu^2$ in eV$^2$ | | | | | | |
|---|---|---|---|---|---|---|---|
| | **5%** | **15.9%** | **50%** | **68.3%** | **84.1%** | **90%** | **95%** |
| **KNM1-5** | -0.2437 | -0.1547 | -0.0258 | 0.0329 | 0.0964 | 0.1301 | 0.1730 |
| **KNM5-1** | -0.2422 | -0.1538 | -0.0251 | 0.0336 | 0.0965 | 0.1302 | 0.1732 |

(a) Results for an initial flat prior: $m_\nu^2 \sim \mathcal{U}(-10,10)$.

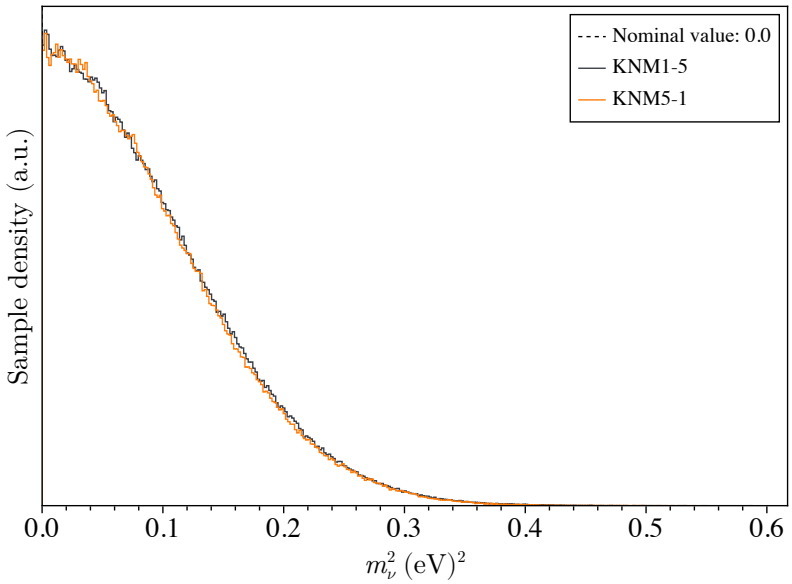


| Type | Quantile values for $m_\nu^2$ in eV$^2$ | | | | | | |
|---|---|---|---|---|---|---|---|
| | **5%** | **15.9%** | **50%** | **68.3%** | **84.1%** | **90%** | **95%** |
| **KNM1-5** | 0.0069 | 0.0224 | 0.0763 | 0.1135 | 0.1603 | 0.1873 | 0.2233 |
| **KNM5-1** | 0.0070 | 0.0223 | 0.0753 | 0.1118 | 0.1580 | 0.1851 | 0.2213 |

(b) Results for an initial flat, positive prior: $m_\nu^2 \sim \mathcal{U}(-0,3)$.

Figure 7.12: Results of the chained analysis forwarding $m_\nu^2$, $B_{\text{max}}$, $B_{\text{src}}$, $E_{\text{loss}}$ and their correlations between campaigns. The sequences KNM1 → KNM2 → KNM3-NAP → KNM3-SAP → KNM4-NOM → KNM4-OPT → KNM5 and its reversed order are compared. In addition, the results for (a) an initial flat prior $m_\nu^2 \sim \mathcal{U}(-10,10)$ and (b) an initial flat, positive prior $m_\nu^2 \sim \mathcal{U}(0,3)$ are shown.

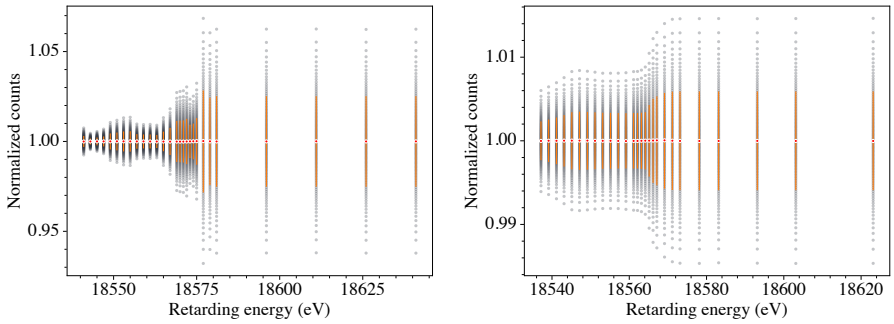


(a) Forwarding only $m_\nu^2$ with initial flat prior $m_\nu^2 \sim \mathcal{U}(-10,10)$.

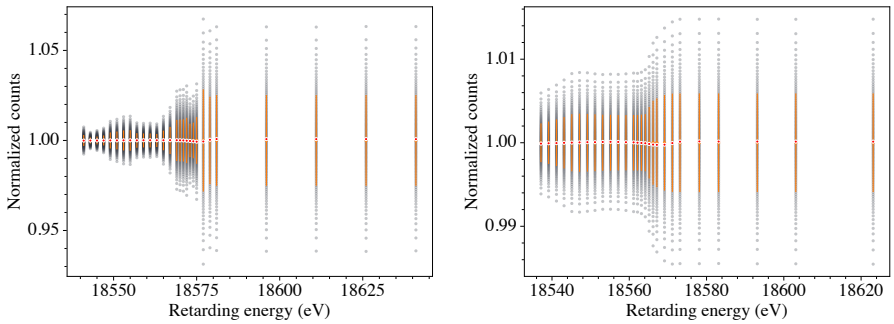


(b) Forwarding only $m_\nu^2$ with initial flat, positive prior $m_\nu^2 \sim \mathcal{U}(0,3)$.

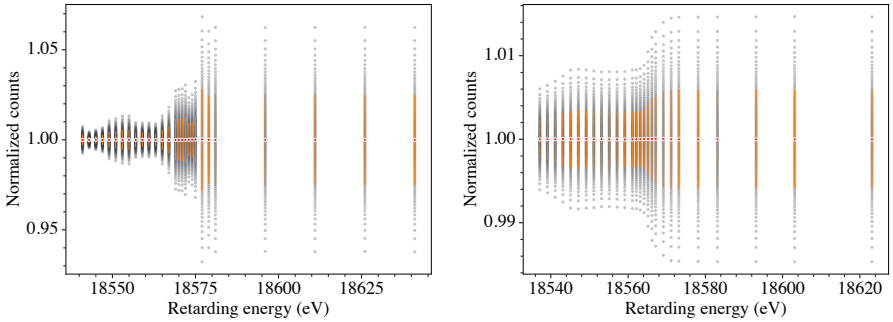


(c) Forwarding $m_\nu^2$ and others with initial flat prior $m_\nu^2 \sim \mathcal{U}(-10,10)$.

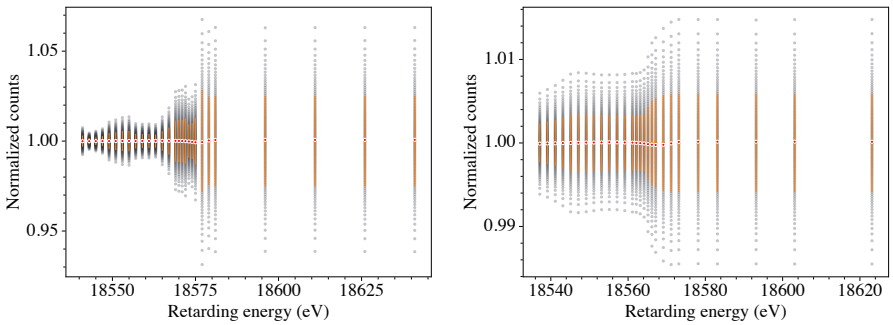


(d) Forwarding $m_\nu^2$ and others with initial flat prior $m_\nu^2 \sim \mathcal{U}(0,3)$.

Figure 7.13: Posterior predictive checks for the chained analysis using (Total). The results are shown for different amounts of forwarded parameters and different initial priors for $m_\nu^2$. Furthermore, the figures on the left-hand side correspond to a permutation of KNM1-5 while the figures on the right-hand side correspond to a permutation of KNM5-1.

Table 7.3: Compared are the final results for the chain permutations KNM1-5 and KNM5-1. For that purpose, the maximal difference of the quantiles $q_s$ = [5 %, 15.9 %, 50 %, 68.3 %, 84.1 %, 90 %, 95 %] of the final marginal distribution of $m_\nu^2$ are shown. The numbers in the column labeled "Sampling error", refer to the maximal sampling error of the quantiles and are true for both permutations KNM1-5 and KNM5-1.

| Forwarded parameters | Initial prior | Type | Quantile difference | Sampling error |
|---|---|---|---|---|
| $m_\nu^2$ only | Flat, positive | Stat. only | $\mathcal{O}(\leq 10^{-4}\mathrm{eV}^2)$ | $\mathcal{O}(\leq 10^{-4}\mathrm{eV}^2)$ |
| $m_\nu^2$ only | Flat, positive | Total | $\mathcal{O}(\leq 10^{-4}\mathrm{eV}^2)$ | $\mathcal{O}(\leq 10^{-4}\mathrm{eV}^2)$ |
| $m_\nu^2$ only | Flat | Stat. only | $\mathcal{O}(\leq 10^{-3}\mathrm{eV}^2)$ | $\mathcal{O}(10^{-4}\mathrm{eV}^2)$ |
| $m_\nu^2$ only | Flat | Total | $\mathcal{O}(\leq 10^{-3}\mathrm{eV}^2)$ | $\mathcal{O}(10^{-4}\mathrm{eV}^2)$ |
| $m_\nu^2$ and others | Flat, positive | Total | $\mathcal{O}(\leq 10^{-3}\mathrm{eV}^2)$ | $\mathcal{O}(\leq 10^{-4}\mathrm{eV}^2)$ |
| $m_\nu^2$ and others | Flat | Total | $\mathcal{O}(\leq 10^{-3}\mathrm{eV}^2)$ | $\mathcal{O}(10^{-4}\mathrm{eV}^2)$ |

imal deviations are smaller by one order of magnitude compared to their single campaign counterparts (see also Table 7.2b). Hence, the much less pronounced systematic effects and the considerably reduced maximal deviations come from the fact that the chained analysis uses the combined statistical strength of the first five KATRIN campaigns in contrast to the statistics of a single campaign. In other words, the likelihood distribution contributes much more probability mass to the posterior than the prior distributions. The behavior of the systematic effects under increased statistics was also studied for the individual fit KNM3-SAP, and yielded the same conclusion, see Section 7.3.3 and Fig. 7.8.

However, interestingly, the chained analyses of (KNM1-5 + Flat) for both ($m_\nu^2$ and others) and ($m_\nu^2$ only), show very much comparable maximal deviations with their single campaign counterparts. The reason is most likely that KNM5 has the highest statistics of the first five measurement campaigns. It appears that the likelihood distribution has enough probability mass, that even a sharper prior of $m_\nu^2$ (due to the chained analysis) does not mitigate the already low systematic effects any further.

First tests using fluctuated Asimov data, i.e. the nominal value of $m_\nu^2$ is different from zero, showed no systematic effects for the chained analysis. This will presumably also be the case for the individual campaign analyses with fluctuated Asimov data.

**Influence of different permutations** The results of the chained analyses are discussed in respect of whether different permutations give different or identical results. For this purpose, the quantiles $q_s$ = [5 %, 15.9 %, 50 %, 68.3 %, 84.1 %, 90 %, 95 %] of $m_\nu^2$, as obtained from the last fit of a chain, are compared for the two chain permutations KNM1-5 and KNM5-1 for all performed analyses. The comparison of the permutations is summarized in Table 7.3. The table shows an excellent agreement, i.e. the differences are minimal as they are in the order of the anticipated sensitivity $\mathcal{O}(10^{-3}\mathrm{eV}^2)$ or below. These results validate the mathematical result in Section 7.4.2, namely that the permutation of the chain has no impact on the final marginal distribution of a parameter.

**Summary of fits** All fits of ($m_\nu^2$ only) and ($m_\nu^2$ and others) using (Flat, positive) behave as expected. The nominal value is recovered by the peak of the distribution, and in the event that the fits were made for (Total) and (Stat. only), the quantiles for (Total) are slightly greater than those of (Stat. only). Fits using (Flat) show the same behavior as already visible in the individual campaigns, see Section 7.3.3. The mode of the marginal distribution is slightly shifted to the left of the nominal value. The observed shift is identical for both permutations and is in the same order as for the individual analysis of KNM3-SAP, as visible in Appendix B, Fig. B.9. Hence, this effect is likely caused during the chained analysis KNM3-SAP is analyzed, and is not considerably mitigated by the other fits. Interestingly, this shift is not present in the simultaneous fit approach. This is likely because all available data are fitted at once, thus there is in total enough statistics to prevent this phenomenon, as was already discussed in Section 7.3.3, and shown in Fig. 7.5. For the fit ($m_\nu^2$ only) with (Flat) and (Stat. only) no shift is observed, which was also the case for the individual campaigns with (Stat. only).

The comparison between distinct priors for $m_\nu^2$, as used in the first step of the chain, shows that for (Flat, positive) the nominal value was more robustly retrieved than for (Flat), because of the explained phenomenon with KNM3-SAP. The 90% quantiles for (Flat, positive) are always greater than that for (Flat). This phenomenon is grounded in the two distinct parameter spaces created by the distinct priors. As already stated in Section 7.1, the unphysical prior (Flat) was chosen to be able to compare the MAP with the Frequentist best fit. For the final bounds on the neutrino mass, the physical prior (Flat, positive) should be used.

Finally, the evolution of the marginal distribution of $m_\nu^2$ during a chained analysis is shown in Fig. 7.14. One can see the shrinking uncertainty, i.e. the width of the distribution, with increasing statistics for both cases (Flat) and (Flat, positive). In Fig. 7.14a, it can be seen that KNM1 as first step contributes the least amount of statistics, while with the subsequent steps the width of the distribution rapidly shrinks down. The reversed ordering of the chain is depicted in Fig. 7.14b. Here, the shrinking effect is more subtle as the chain begins with KNM5, the strongest of the five campaigns.

### 7.4.6 Summary of chained analyses

The successful implementation of a chained analysis via Bayesian knowledge updates for the first five KATRIN measurement campaigns was demonstrated on Asimov data. As for the individual analyses, an excellent Markov chain Monte Carlo convergence diagnostic was achieved in all performed analyses. Two cases are studied, one in which only the marginal distribution of $m_\nu^2$ is forwarded between chain steps, and one in which all 12 possible parameters together with their correlations are forwarded. Furthermore, the influence of the ordering of campaigns within a chained analysis onto the final result were studied. The derived mathematical result was confirmed by the analyses, in that the marginal parameter distributions are invariant under chain permutations. For fits taking statistical and systematic uncertainties into account, while using a flat prior for $m_\nu^2$, the same shift from the nominal value is observable as was for the individual analysis of KNM3-SAP. The systematic effects which already showed up in the individual analysis are also present in the chained analysis. That said, due to using the full

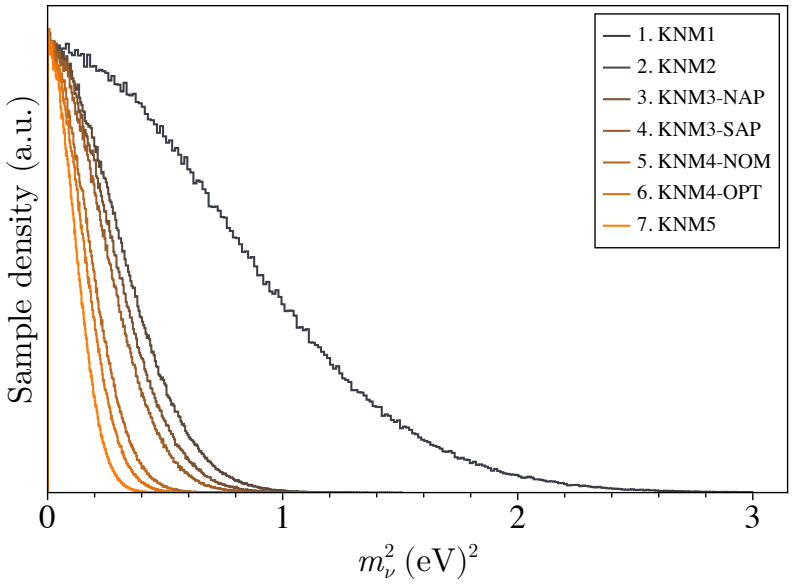


(a) Results for an initial flat, positive prior: $m_\nu^2 \sim \mathcal{U}(0,3)$. Chain sequence: KNM1-5.

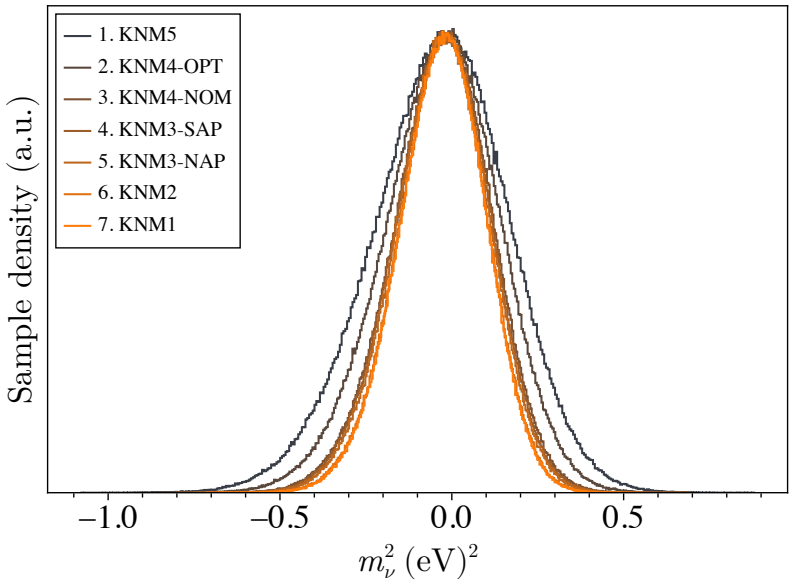


(b) Results for an initial flat prior: $m_\nu^2 \sim \mathcal{U}(-10,10)$. Chain sequence: KNM5-1.

Figure 7.14: The evolution of the marginal distribution of $m_\nu^2$ over a chained analysis is shown. Different choices for the initial prior of $m_\nu^2$ are shown. In both cases ($m_\nu^2$ and others + Total) were used.

statistical power of the first five KATRIN campaigns, the effects are much less pronounced.

## 7.5 Summary of Bayesian analyses of the first five KATRIN campaigns

In this chapter, the successful application of Bayesian inference on the first five KATRIN measurement campaigns, utilizing a neural network, was demonstrated. All shown results were gained using Asimov data and had excellent Markov chain Monte Carlo convergence diagnostics. First the analysis results of the individual KATRIN campaigns were discussed. The maximum a posteriori estimations validated the implemented scripts, as they were able to retrieve the ground truth of the Asimov data within the anticipated sensitivity $O(10^{-3}\,\mathrm{eV}^2)$ for $m_\nu^2$. To further validate the results, a comparison of the two KATRIN analysis teams Netrium and KaFit was performed using multiple quantiles of the marginal distributions of $m_\nu^2$. The agreement of both teams was excellent, with differences $O(10^{-3}\,\mathrm{eV}^2)$. This is especially a strong comparison as the methods of both teams differ in several regards: in the evaluation of the likelihood function, the utilized Markov chain Monte Carlo algorithm used for sampling and the monitoring of the Markov chain Monte Carlo convergence diagnostics. Overall, the marginal parameter distributions of $m_\nu^2$ showed the expected behavior for taking only statistical uncertainties and taking statistical and systematic uncertainties into account. In a next step, to take advantage of the full statistics of the first five measurement campaigns, a chained analysis via Bayesian knowledge updates was studied. Hereby, the impact of forwarding only information about $m_\nu^2$ from chain step to chain step, or information about all 12 suitable parameters and their correlations, were investigated. In addition, it was shown mathematically and validated via the achieved results, that the order in which the campaigns appear in the chained analysis does not have an impact onto the final marginal parameter distributions.

However, two phenomena are still under investigation by Netrium and KaFit. On the one hand, the reproduced data distributions calculated from posterior samples showed a small systematic effect, which was not observed when maximum a posteriori estimates were used for the calculation. This effect was also present in the chained analysis, but much less pronounced due to the increased statistics. On the other hand, for the campaign KNM3-SAP using a flat prior on $m_\nu^2$, the marginal mode of $m_\nu^2$ is slightly shifted to more negative values in comparison to the nominal value. The same shift was observed in the chained analysis, when in the first chain step a flat prior on $m_\nu^2$ was used. About the origin of the phenomena was reasoned. However, this is an ongoing study by both Netrium and KaFit and will be thoroughly investigated in future studies, and explained in the upcoming paper.

The analyses were also performed on the real, measured data. However, not to postpone the publication of this thesis it was decided to only show the results on Asimov data.

# Chapter 8

# Summary and conclusion

This thesis consists of three projects, which all lead, or in case of the KATRIN analysis, will lead to the publication of a paper. In the first project, theoretical ambiguity analyses were performed within the field of Baryon spectroscopy. Hereby, the theorem of Moravcsik was utilized, which is an automatable and scalable approach to obtain complete sets of polarization observables for reactions described by, in principle, an arbitrary number $N_\mathrm{a}$ of complex spin amplitudes. In order to validate the theorem, it was applied to pion-nucleon scattering ($N_\mathrm{a} = 2$) and pseudoscalar meson photoproduction ($N_\mathrm{a} = 4$) and a comparison with the well known results for these reactions were made. Afterward, the theorem was applied to pseudoscalar meson electroproduction ($N_\mathrm{a} = 6$), yielding the first lists of complete sets of observables for this reaction. Finally, the reaction of two-pseudoscalar-meson photoproduction ($N_\mathrm{a} = 8$) was studied. The concluding result was a list with 69 complete sets of polarization observables, each containing only one triple polarization observable, as these are the hardest observables to measure. In fact, no polarization observable of this type has yet been measured.

In the second project, the topic of ambiguity analysis was approached in a complementary manner by performing a truncated partial-wave analysis on measurement data from pseudoscalar meson photoproduction. This includes data of $\eta$-photoproduction for the polarization observables $\sigma_0$, $\Sigma$, $T$, $E$, $F$ and $G$, which form a complete set within the framework of truncated partial-wave analysis. Multiple energies and truncation orders were studied, resulting in the estimation of the complex electromagnetic multipole parameters, which are used to model the reaction in the first place, and predictions for all not yet measured polarization observables of $\eta$-photoproduction. The analyses were performed, for the first time, utilizing Bayesian inference. As a consequence, parameter estimations, predicted data, etc. are distributions. Furthermore, via the usage of Markov chain Monte Carlo simulation, with the Hamiltonian Monte Carlo sampling algorithm, the connection of ambiguities within the parameters space could be studied in an unprecedented way. The approach revealed that severe ambiguities tend to be sampled together, showing up as one, connected multimodal marginal distribution. However, the greatest source of complexity in the analyses arose in monitoring the Markov chain Monte Carlo convergence, attributable to the highly multimodal posteriors. To achieve reliable results, an adaptation of the typical convergence workflow was developed.

In the third project, the knowledge gained about Bayesian inference was applied to the neutrino mass analysis with KATRIN. Hereby, the first five KATRIN measurement campaigns were analyzed with Bayesian inference. At first, the analyses were performed for each campaign individually, studying different priors for $m_\nu^2$ and the influence of taking only statistical uncertainties or taking statistical and systematic uncertainties into account. Once the results were approved by the collaboration, it was moved on to a combined analysis in the form of a chained analysis, realized with Bayesian knowledge updates. Thus, making use of the full statistics of the campaigns to further reduce the effective mass limit of the electron antineutrino. The influence on the ordering of the Bayesian knowledge updates were studied, as well as the utilization of different priors for $m_\nu^2$ in the very first step of a chain. The KATRIN policy does not allow to publish a thesis containing neutrino mass results from measurement data prior to the corresponding paper. In order to not postpone the publication of this thesis, only the results based on Asimov data are shown, even though the analyses were also performed on the measured data.

# Appendix A

# Published papers

## A.1 Publication: Phys. Rev. C 103, 014607 (2021)

In the following, the paper:

**Philipp Kroenert, Yannick Wunderlich, Farah Afzal, and Annika Thiel, 'Minimal complete sets for two-pseudoscalar-meson photoproduction', Phys. Rev. C 103, 014607 (2021),**

is included.

# Minimal complete sets for two-pseudoscalar-meson photoproduction

Philipp Kroenert,* Yannick Wunderlich, Farah Afzal, and Annika Thiel
*Helmholtz Institut für Strahlen- und Kernphysik, Universität Bonn, Germany*

(Received 14 September 2020; accepted 16 December 2020; published 11 January 2021)

For photoproduction reactions with final states consisting of two pseudoscalar mesons and a spin-1/2 baryon, eight complex amplitudes need to be determined uniquely. A modified version of Moravcsik's theorem is employed for these reactions, resulting in slightly overcomplete sets of polarization observables that are able to determine the amplitudes uniquely. Further steps were taken to reduce the found sets to minimal complete sets. As a final result, multiple minimal complete sets without any remaining ambiguities are presented for the first time. These sets consist of $2N = 16$ observables, containing only one triple polarization observable.

DOI: 10.1103/PhysRevC.103.014607

## I. INTRODUCTION

The interrelation between experiment and theory is what drives science. In the field of hadron spectroscopy these are the measurement of cross sections or polarization observables and its counterpart Quantum Chromodynamics. The latter describes the transition of the initial to the final state via a transition matrix $\mathcal{T}$. This matrix comprises the employed model predictions to describe a certain process. Via so-called formation experiments (i.e., $\gamma p \to \pi\pi p$) it is possible to study the emergence of resonant states [such as $\Delta(1232)$, $N(1440)1/2+$, $N(1520)3/2-$, etc. [1]].

These states can be analyzed via partial-wave analysis (i.e., BnGa [1], MAID [2]), determining the matrix elements of $\mathcal{T}$ and comparing it to the model prediction. However, because polarization observables depend on bilinear products of the complex amplitudes [3–5], mathematical ambiguities arise [6]. Nevertheless, it is still possible to determine unique solutions by employing a complete experiment analysis [7].

Such a complete experiment analysis was performed analytically by Chiang and Tabakin in 1997 [6] for single pseudoscalar meson photoproduction. A detailed proof comprising all the relevant cases was published recently by Nakayama [8]. It should be noted that these complete experiments are an idealization for data with no uncertainty [9]. Although the process of single pseudoscalar meson photoproduction can be fully described by only four complex amplitudes [10], the calculations are nontrivial and cumbersome [8] and, furthermore, quite involved ambiguity-structures can arise.

Within this paper, the determination of complete sets of observables is studied for the reaction of two pseudoscalar meson photoproduction. The process can be described by $N = 8$ complex amplitudes and thus allows for 64 measurable polarization observables [5], which are four times as many observables as in the case of single pseudoscalar meson photoproduction [6]. This results in an exponential increase of complexity, for what reason the algebraic techniques presented in Ref. [8] are no longer appropriate, although possible (see Sec. VII B). New methods should be employed, in order to allow for an easier access to the problem of complete sets for reactions with $N > 4$.

There is an already existing work on this subject by Arenhövel and Fix [11] from 2014. On the one hand, they used the inverse function theorem to derive complete sets of 16 observables. The downside of this method is that the resulting sets might locally be free of ambiguities, but not globally. On the other hand, they used a graph theoretical approach, where a complex amplitude is represented as a node and the bilinear product as a connection between certain nodes. This method yields complete sets with 25 observables. It was then shown how to further reduce such a set to 15 observables. Although they found sets without triple polarization observables, there still remain quadratic ambiguities.

To overcome these difficulties arising from the remaining discrete mathematical ambiguities, Moravcsik's theorem [12] is employed within this paper. This theorem allows for the extraction of complete sets of observables for an arbitrary number of amplitudes. Furthermore, due to its graph-theoretical foundation, the whole algorithm can be automated [13].

The paper is structured in the following way: The starting point is a short recap of Moravcsik's theorem and its modification in Sec. II. Section III introduces the 64 polarization observables for two pseudoscalar meson photoproduction. Within Sec. IV the actual application of Moravcsik's theorem is described and illustrated with an example. Section V elaborates on the difficulties of the experimental determination of the polarization observables and gives an extensive overview of already-performed measurements in two pseudoscalar meson photoproduction. The entire analysis results in 5964 unique, but slightly overcomplete sets of observables. Their characteristics are discussed in Sec. VI. Section VII describes how to transform the slightly overcomplete sets into minimal ones (i.e., into sets containing $2N = 16$ observables). Based on these sets as well as the already-performed measure-

*Corresponding author: kroenert@hiskp.uni-bonn.de

 

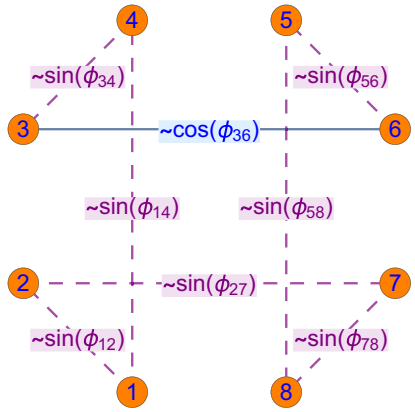


FIG. 1. Illustration of a cycle graph with eight nodes (enumerated points) and edges (solid and dashed lines). Each node represents one complex amplitude, whereas each edge connecting two nodes represents either the real (solid) or imaginary (dashed) part of the bilinear product of those nodes. The respective correlation to the relative phase $\phi_{ij}$ is indicated.

ments the most promising minimal complete set is presented in Sec. VIII. The results are summarized in Sec. IX.

## II. MORAVCSIK'S THEOREM

The main points of Moravcsik's paper [12] shall be recapped in a concise form. The basic assumption of the theorem is that the moduli of the $N$ complex amplitudes $t_i$ are known, together with the real and imaginary parts of the bilinear products $t_i t_j^*$. Furthermore, each complex amplitude $t_i$ is treated as a node of a graph whereas an edge is the real or imaginary part of the bilinear amplitude product $t_i t_j^*$ connecting both nodes. An illustration is shown in Fig. 1. Such a graph is said to correspond to a complete set of observables if it fulfills the following two requirements:

(1) it is a connected graph;
(2) it has an odd number of edges which corresponds to an imaginary part of a particular bilinear product, i.e., $\propto \mathrm{Im}(t_i t_j^*)$.

The first condition is related to the "consistency relation" of the relative phases:

$$\phi_{12} + \phi_{23} + \cdots + \phi_{N1} = 0, \tag{1}$$

which implies a summation of relative phases between all neighboring amplitudes $t_i$ [8]. Equation (1) has to hold in every case, whether the considered set is fully complete or not. The second condition is responsible for resolving the discrete ambiguities since it holds

$$\mathrm{Im}(t_i t_j^*) = |t_i||t_j| \sin(\phi_{ij}), \tag{2}$$

and that sine itself produces an ambiguity due to its periodicity:

$$\phi_{ij} \to (\phi_{ij}, \pi - \phi_{ij}). \tag{3}$$

It turns out that any odd number of such "sine-type" ambiguities resolves the discrete ambiguities, due to the summand $\pi$. The generalization to any odd number is the actual modification to Moravcsik's theorem. A proof of the original version of the theorem can be found in Ref. [12] and a quite detailed proof of the modified version of the theorem is given in Ref. [13].

The following analysis focuses on cycle graphs, i.e., connected graphs where each node has degree two. As explained in Ref. [12], "from the point of view of eliminating discrete ambiguities" these graph types are "the most economical" ones. Thus, only the minimal number of $N$ bilinear products is needed in order to eliminate all discrete ambiguities, one for each edge.

## III. POLARIZATION OBSERVABLES

The derivation of the 64 polarization observables of two pseudoscalar meson photoproduction was first published by Roberts and Oed [5]. The observables were defined in a "helicity and hybrid helicity-transversity basis" [5]. For the latter, the photon spin is still quantized along its direction of motion. For the sake of comparability, the hybrid basis shall be adopted in this paper. However, in order to work out the connection between the real (imaginary) part of the bilinear products and the relative phases $\phi_{ij}$, it is advantageous to rename the amplitudes:

$$b_1^+ \to t_1, \quad b_2^+ \to t_2, \quad b_3^+ \to t_3, \quad b_4^+ \to t_4, \tag{4}$$

$$b_1^- \to t_5, \quad b_2^- \to t_6, \quad b_3^- \to t_7, \quad b_4^- \to t_8. \tag{5}$$

Within Ref. [5], the observables are ordered according to the polarization of the photon beam, which is required to measure the respective observable. This ordering scheme is advantageous from an experimental point of view; unfortunately, it is inappropriate when studying ambiguities. Therefore, the observables are regrouped according to their mathematical structure, which yields eight groups. While the first group consists of observables solely described by the squared moduli of the amplitudes $t_i$, any other group comprises equal amounts of observables containing only cos or sin terms. The resulting expressions for the observables are listed in Table I.

For the purpose of an easier calculation, 64 $\Gamma$ matrices are introduced, which can be solely described by the identity matrix, as well as the three Pauli matrices (listed in Table II). This allows us to calculate the respective observable by the bilinear form $\langle t|\Gamma|t\rangle$ with $|t\rangle := (t_1, t_2, t_3, t_4, t_5, t_6, t_7, t_8)$, similar as in Ref. [6]. As expected, the $\Gamma$ matrices for each group share the same matrix structure. Naturally, they form an orthogonal basis and are Hermitian and unitary. Indeed, the matrices fulfill the same properties as presented in Ref. [6] (with an adapted prefactor in the orthogonality relation).

## IV. APPROACH

The results of Sec. II imply the following steps: One constructs all unique graph topologies with $N$ nodes using combinatorial methods. A few examples of possible graphs are shown in Fig. 2. The number of unique topologies is solely determined by the number of nodes (or edges), i.e., for $N \geqslant 3$ it is $N!/(2N)$ [13].

TABLE I. Definitions of the 64 polarization observables for two pseudoscalar meson photoproduction in hybrid helicity-transversity form. Here, $\phi_{ij}$ denotes the relative phase between the complex amplitudes $t_i$ and $t_j$. The notation used in the original paper of Roberts and Oed [5] is also shown. The observables are classified into eight groups according to their underlying mathematical structure. The vector $|t\rangle$ has the form $(t_1, t_2, t_3, t_4, t_5, t_6, t_7, t_8)$ and the shape of the $\Gamma$ matrices is outlined in Table II.

| Observable | Definition in terms of polar coordinates / 2 | Bilinear form | Roberts, Oed |
|---|---|---|---|
| $\mathcal{O}^{\mathrm{I}}_{1}$ | $\frac{1}{2}(\lvert t_1\rvert^2+\lvert t_2\rvert^2+\lvert t_3\rvert^2+\lvert t_4\rvert^2-\lvert t_5\rvert^2-\lvert t_6\rvert^2-\lvert t_7\rvert^2-\lvert t_8\rvert^2)$ | $\langle t\lvert\Gamma^{\mathrm{I}}_{1}\rvert t\rangle$ | $\mathrm{I}^{\odot}$ |
| $\mathcal{O}^{\mathrm{I}}_{2}$ | $\frac{1}{2}(\lvert t_1\rvert^2+\lvert t_2\rvert^2-\lvert t_3\rvert^2-\lvert t_4\rvert^2+\lvert t_5\rvert^2+\lvert t_6\rvert^2-\lvert t_7\rvert^2-\lvert t_8\rvert^2)$ | $\langle t\lvert\Gamma^{\mathrm{I}}_{2}\rvert t\rangle$ | $\mathrm{P}_{\mathrm{y}}$ |
| $\mathcal{O}^{\mathrm{I}}_{3}$ | $\frac{1}{2}(\lvert t_1\rvert^2-\lvert t_2\rvert^2+\lvert t_3\rvert^2-\lvert t_4\rvert^2+\lvert t_5\rvert^2-\lvert t_6\rvert^2+\lvert t_7\rvert^2-\lvert t_8\rvert^2)$ | $\langle t\lvert\Gamma^{\mathrm{I}}_{3}\rvert t\rangle$ | $\mathrm{P}_{\mathrm{y}'}$ |
| $\mathcal{O}^{\mathrm{I}}_{4}$ | $\frac{1}{2}(\lvert t_1\rvert^2-\lvert t_2\rvert^2-\lvert t_3\rvert^2+\lvert t_4\rvert^2-\lvert t_5\rvert^2+\lvert t_6\rvert^2+\lvert t_7\rvert^2-\lvert t_8\rvert^2)$ | $\langle t\lvert\Gamma^{\mathrm{I}}_{4}\rvert t\rangle$ | $\mathcal{O}^{\odot}_{\mathrm{yy}'}$ |
| $\mathcal{O}^{\mathrm{I}}_{5}$ | $\frac{1}{2}(\lvert t_1\rvert^2-\lvert t_2\rvert^2-\lvert t_3\rvert^2+\lvert t_4\rvert^2+\lvert t_5\rvert^2-\lvert t_6\rvert^2-\lvert t_7\rvert^2+\lvert t_8\rvert^2)$ | $\langle t\lvert\Gamma^{\mathrm{I}}_{5}\rvert t\rangle$ | $\mathcal{O}_{\mathrm{yy}'}$ |
| $\mathcal{O}^{\mathrm{I}}_{6}$ | $\frac{1}{2}(\lvert t_1\rvert^2-\lvert t_2\rvert^2+\lvert t_3\rvert^2-\lvert t_4\rvert^2-\lvert t_5\rvert^2+\lvert t_6\rvert^2-\lvert t_7\rvert^2+\lvert t_8\rvert^2)$ | $\langle t\lvert\Gamma^{\mathrm{I}}_{6}\rvert t\rangle$ | $\mathrm{P}^{\odot}_{\mathrm{y}'}$ |
| $\mathcal{O}^{\mathrm{I}}_{7}$ | $\frac{1}{2}(\lvert t_1\rvert^2+\lvert t_2\rvert^2-\lvert t_3\rvert^2-\lvert t_4\rvert^2-\lvert t_5\rvert^2-\lvert t_6\rvert^2+\lvert t_7\rvert^2+\lvert t_8\rvert^2)$ | $\langle t\lvert\Gamma^{\mathrm{I}}_{7}\rvert t\rangle$ | $\mathrm{P}^{\odot}_{\mathrm{y}}$ |
| $\mathcal{O}^{\mathrm{I}}_{8}$ | $\frac{1}{2}(\lvert t_1\rvert^2+\lvert t_2\rvert^2+\lvert t_3\rvert^2+\lvert t_4\rvert^2+\lvert t_5\rvert^2+\lvert t_6\rvert^2+\lvert t_7\rvert^2+\lvert t_8\rvert^2)$ | $\langle t\lvert\Gamma^{\mathrm{I}}_{8}\rvert t\rangle$ | $\mathrm{I}_{0}$ |
| $\mathcal{O}^{\mathrm{II}}_{\mathrm{c}1}$ | $\lvert t_1\rvert\lvert t_3\rvert\cos(\phi_{13})+\lvert t_2\rvert\lvert t_4\rvert\cos(\phi_{24})+\lvert t_5\rvert\lvert t_7\rvert\cos(\phi_{57})+\lvert t_6\rvert\lvert t_8\rvert\cos(\phi_{68})$ | $\langle t\lvert\Gamma^{\mathrm{II}}_{\mathrm{c}1}\rvert t\rangle$ | $-\mathrm{P}_{\mathrm{z}}$ |
| $\mathcal{O}^{\mathrm{II}}_{\mathrm{c}2}$ | $\lvert t_1\rvert\lvert t_3\rvert\cos(\phi_{13})+\lvert t_2\rvert\lvert t_4\rvert\cos(\phi_{24})-\lvert t_5\rvert\lvert t_7\rvert\cos(\phi_{57})-\lvert t_6\rvert\lvert t_8\rvert\cos(\phi_{68})$ | $\langle t\lvert\Gamma^{\mathrm{II}}_{\mathrm{c}2}\rvert t\rangle$ | $-\mathrm{P}^{\odot}_{\mathrm{z}}$ |
| $\mathcal{O}^{\mathrm{II}}_{\mathrm{c}3}$ | $\lvert t_1\rvert\lvert t_3\rvert\cos(\phi_{13})-\lvert t_2\rvert\lvert t_4\rvert\cos(\phi_{24})+\lvert t_5\rvert\lvert t_7\rvert\cos(\phi_{57})-\lvert t_6\rvert\lvert t_8\rvert\cos(\phi_{68})$ | $\langle t\lvert\Gamma^{\mathrm{II}}_{\mathrm{c}3}\rvert t\rangle$ | $-\mathcal{O}_{\mathrm{zy}'}$ |
| $\mathcal{O}^{\mathrm{II}}_{\mathrm{c}4}$ | $\lvert t_1\rvert\lvert t_3\rvert\cos(\phi_{13})-\lvert t_2\rvert\lvert t_4\rvert\cos(\phi_{24})-\lvert t_5\rvert\lvert t_7\rvert\cos(\phi_{57})+\lvert t_6\rvert\lvert t_8\rvert\cos(\phi_{68})$ | $\langle t\lvert\Gamma^{\mathrm{II}}_{\mathrm{c}4}\rvert t\rangle$ | $-\mathcal{O}^{\odot}_{\mathrm{zy}'}$ |
| $\mathcal{O}^{\mathrm{II}}_{\mathrm{s}1}$ | $\lvert t_1\rvert\lvert t_3\rvert\sin(\phi_{13})+\lvert t_2\rvert\lvert t_4\rvert\sin(\phi_{24})+\lvert t_5\rvert\lvert t_7\rvert\sin(\phi_{57})+\lvert t_6\rvert\lvert t_8\rvert\sin(\phi_{68})$ | $\langle t\lvert\Gamma^{\mathrm{II}}_{\mathrm{s}1}\rvert t\rangle$ | $-\mathrm{P}_{\mathrm{x}}$ |
| $\mathcal{O}^{\mathrm{II}}_{\mathrm{s}2}$ | $\lvert t_1\rvert\lvert t_3\rvert\sin(\phi_{13})+\lvert t_2\rvert\lvert t_4\rvert\sin(\phi_{24})-\lvert t_5\rvert\lvert t_7\rvert\sin(\phi_{57})-\lvert t_6\rvert\lvert t_8\rvert\sin(\phi_{68})$ | $\langle t\lvert\Gamma^{\mathrm{II}}_{\mathrm{s}2}\rvert t\rangle$ | $-\mathrm{P}^{\odot}_{\mathrm{x}}$ |
| $\mathcal{O}^{\mathrm{II}}_{\mathrm{s}3}$ | $\lvert t_1\rvert\lvert t_3\rvert\sin(\phi_{13})-\lvert t_2\rvert\lvert t_4\rvert\sin(\phi_{24})+\lvert t_5\rvert\lvert t_7\rvert\sin(\phi_{57})-\lvert t_6\rvert\lvert t_8\rvert\sin(\phi_{68})$ | $\langle t\lvert\Gamma^{\mathrm{II}}_{\mathrm{s}3}\rvert t\rangle$ | $-\mathcal{O}_{\mathrm{xy}'}$ |
| $\mathcal{O}^{\mathrm{II}}_{\mathrm{s}4}$ | $\lvert t_1\rvert\lvert t_3\rvert\sin(\phi_{13})-\lvert t_2\rvert\lvert t_4\rvert\sin(\phi_{24})-\lvert t_5\rvert\lvert t_7\rvert\sin(\phi_{57})+\lvert t_6\rvert\lvert t_8\rvert\sin(\phi_{68})$ | $\langle t\lvert\Gamma^{\mathrm{II}}_{\mathrm{s}4}\rvert t\rangle$ | $-\mathcal{O}^{\odot}_{\mathrm{xy}'}$ |
| $\mathcal{O}^{\mathrm{III}}_{\mathrm{c}1}$ | $\lvert t_1\rvert\lvert t_2\rvert\cos(\phi_{12})+\lvert t_3\rvert\lvert t_4\rvert\cos(\phi_{34})+\lvert t_5\rvert\lvert t_6\rvert\cos(\phi_{56})+\lvert t_7\rvert\lvert t_8\rvert\cos(\phi_{78})$ | $\langle t\lvert\Gamma^{\mathrm{III}}_{\mathrm{c}1}\rvert t\rangle$ | $-\mathrm{P}_{\mathrm{z}'}$ |
| $\mathcal{O}^{\mathrm{III}}_{\mathrm{c}2}$ | $\lvert t_1\rvert\lvert t_2\rvert\cos(\phi_{12})+\lvert t_3\rvert\lvert t_4\rvert\cos(\phi_{34})-\lvert t_5\rvert\lvert t_6\rvert\cos(\phi_{56})-\lvert t_7\rvert\lvert t_8\rvert\cos(\phi_{78})$ | $\langle t\lvert\Gamma^{\mathrm{III}}_{\mathrm{c}2}\rvert t\rangle$ | $-\mathrm{P}^{\odot}_{\mathrm{z}'}$ |
| $\mathcal{O}^{\mathrm{III}}_{\mathrm{c}3}$ | $\lvert t_1\rvert\lvert t_2\rvert\cos(\phi_{12})-\lvert t_3\rvert\lvert t_4\rvert\cos(\phi_{34})+\lvert t_5\rvert\lvert t_6\rvert\cos(\phi_{56})-\lvert t_7\rvert\lvert t_8\rvert\cos(\phi_{78})$ | $\langle t\lvert\Gamma^{\mathrm{III}}_{\mathrm{c}3}\rvert t\rangle$ | $-\mathcal{O}_{\mathrm{yz}'}$ |
| $\mathcal{O}^{\mathrm{III}}_{\mathrm{c}4}$ | $\lvert t_1\rvert\lvert t_2\rvert\cos(\phi_{12})-\lvert t_3\rvert\lvert t_4\rvert\cos(\phi_{34})-\lvert t_5\rvert\lvert t_6\rvert\cos(\phi_{56})+\lvert t_7\rvert\lvert t_8\rvert\cos(\phi_{78})$ | $\langle t\lvert\Gamma^{\mathrm{III}}_{\mathrm{c}4}\rvert t\rangle$ | $-\mathcal{O}^{\odot}_{\mathrm{yz}'}$ |
| $\mathcal{O}^{\mathrm{III}}_{\mathrm{s}1}$ | $\lvert t_1\rvert\lvert t_2\rvert\sin(\phi_{12})+\lvert t_3\rvert\lvert t_4\rvert\sin(\phi_{34})+\lvert t_5\rvert\lvert t_6\rvert\sin(\phi_{56})+\lvert t_7\rvert\lvert t_8\rvert\sin(\phi_{78})$ | $\langle t\lvert\Gamma^{\mathrm{III}}_{\mathrm{s}1}\rvert t\rangle$ | $\mathrm{P}_{\mathrm{x}'}$ |
| $\mathcal{O}^{\mathrm{III}}_{\mathrm{s}2}$ | $\lvert t_1\rvert\lvert t_2\rvert\sin(\phi_{12})+\lvert t_3\rvert\lvert t_4\rvert\sin(\phi_{34})-\lvert t_5\rvert\lvert t_6\rvert\sin(\phi_{56})-\lvert t_7\rvert\lvert t_8\rvert\sin(\phi_{78})$ | $\langle t\lvert\Gamma^{\mathrm{III}}_{\mathrm{s}2}\rvert t\rangle$ | $\mathrm{P}^{\odot}_{\mathrm{x}'}$ |
| $\mathcal{O}^{\mathrm{III}}_{\mathrm{s}3}$ | $\lvert t_1\rvert\lvert t_2\rvert\sin(\phi_{12})-\lvert t_3\rvert\lvert t_4\rvert\sin(\phi_{34})+\lvert t_5\rvert\lvert t_6\rvert\sin(\phi_{56})-\lvert t_7\rvert\lvert t_8\rvert\sin(\phi_{78})$ | $\langle t\lvert\Gamma^{\mathrm{III}}_{\mathrm{s}3}\rvert t\rangle$ | $\mathcal{O}_{\mathrm{yx}'}$ |
| $\mathcal{O}^{\mathrm{III}}_{\mathrm{s}4}$ | $\lvert t_1\rvert\lvert t_2\rvert\sin(\phi_{12})-\lvert t_3\rvert\lvert t_4\rvert\sin(\phi_{34})-\lvert t_5\rvert\lvert t_6\rvert\sin(\phi_{56})+\lvert t_7\rvert\lvert t_8\rvert\sin(\phi_{78})$ | $\langle t\lvert\Gamma^{\mathrm{III}}_{\mathrm{s}4}\rvert t\rangle$ | $\mathcal{O}^{\odot}_{\mathrm{yx}'}$ |
| $\mathcal{O}^{\mathrm{IV}}_{\mathrm{c}1}$ | $\lvert t_1\rvert\lvert t_4\rvert\cos(\phi_{14})+\lvert t_2\rvert\lvert t_3\rvert\cos(\phi_{23})+\lvert t_5\rvert\lvert t_8\rvert\cos(\phi_{58})+\lvert t_6\rvert\lvert t_7\rvert\cos(\phi_{67})$ | $\langle t\lvert\Gamma^{\mathrm{IV}}_{\mathrm{c}1}\rvert t\rangle$ | $\mathcal{O}_{\mathrm{zz}'}$ |
| $\mathcal{O}^{\mathrm{IV}}_{\mathrm{c}2}$ | $\lvert t_1\rvert\lvert t_4\rvert\cos(\phi_{14})+\lvert t_2\rvert\lvert t_3\rvert\cos(\phi_{23})-\lvert t_5\rvert\lvert t_8\rvert\cos(\phi_{58})-\lvert t_6\rvert\lvert t_7\rvert\cos(\phi_{67})$ | $\langle t\lvert\Gamma^{\mathrm{IV}}_{\mathrm{c}2}\rvert t\rangle$ | $\mathcal{O}^{\odot}_{\mathrm{zz}'}$ |
| $\mathcal{O}^{\mathrm{IV}}_{\mathrm{c}3}$ | $\lvert t_1\rvert\lvert t_4\rvert\cos(\phi_{14})-\lvert t_2\rvert\lvert t_3\rvert\cos(\phi_{23})+\lvert t_5\rvert\lvert t_8\rvert\cos(\phi_{58})-\lvert t_6\rvert\lvert t_7\rvert\cos(\phi_{67})$ | $\langle t\lvert\Gamma^{\mathrm{IV}}_{\mathrm{c}3}\rvert t\rangle$ | $\mathcal{O}_{\mathrm{xx}'}$ |
| $\mathcal{O}^{\mathrm{IV}}_{\mathrm{c}4}$ | $\lvert t_1\rvert\lvert t_4\rvert\cos(\phi_{14})-\lvert t_2\rvert\lvert t_3\rvert\cos(\phi_{23})-\lvert t_5\rvert\lvert t_8\rvert\cos(\phi_{58})+\lvert t_6\rvert\lvert t_7\rvert\cos(\phi_{67})$ | $\langle t\lvert\Gamma^{\mathrm{IV}}_{\mathrm{c}4}\rvert t\rangle$ | $\mathcal{O}^{\odot}_{\mathrm{xx}'}$ |
| $\mathcal{O}^{\mathrm{IV}}_{\mathrm{s}1}$ | $\lvert t_1\rvert\lvert t_4\rvert\sin(\phi_{14})+\lvert t_2\rvert\lvert t_3\rvert\sin(\phi_{23})+\lvert t_5\rvert\lvert t_8\rvert\sin(\phi_{58})+\lvert t_6\rvert\lvert t_7\rvert\sin(\phi_{67})$ | $\langle t\lvert\Gamma^{\mathrm{IV}}_{\mathrm{s}1}\rvert t\rangle$ | $\mathcal{O}_{\mathrm{xz}'}$ |
| $\mathcal{O}^{\mathrm{IV}}_{\mathrm{s}2}$ | $\lvert t_1\rvert\lvert t_4\rvert\sin(\phi_{14})+\lvert t_2\rvert\lvert t_3\rvert\sin(\phi_{23})-\lvert t_5\rvert\lvert t_8\rvert\sin(\phi_{58})-\lvert t_6\rvert\lvert t_7\rvert\sin(\phi_{67})$ | $\langle t\lvert\Gamma^{\mathrm{IV}}_{\mathrm{s}2}\rvert t\rangle$ | $\mathcal{O}^{\odot}_{\mathrm{xz}'}$ |
| $\mathcal{O}^{\mathrm{IV}}_{\mathrm{s}3}$ | $\lvert t_1\rvert\lvert t_4\rvert\sin(\phi_{14})-\lvert t_2\rvert\lvert t_3\rvert\sin(\phi_{23})+\lvert t_5\rvert\lvert t_8\rvert\sin(\phi_{58})-\lvert t_6\rvert\lvert t_7\rvert\sin(\phi_{67})$ | $\langle t\lvert\Gamma^{\mathrm{IV}}_{\mathrm{s}3}\rvert t\rangle$ | $-\mathcal{O}_{\mathrm{zx}'}$ |
| $\mathcal{O}^{\mathrm{IV}}_{\mathrm{s}4}$ | $\lvert t_1\rvert\lvert t_4\rvert\sin(\phi_{14})-\lvert t_2\rvert\lvert t_3\rvert\sin(\phi_{23})-\lvert t_5\rvert\lvert t_8\rvert\sin(\phi_{58})+\lvert t_6\rvert\lvert t_7\rvert\sin(\phi_{67})$ | $\langle t\lvert\Gamma^{\mathrm{IV}}_{\mathrm{s}4}\rvert t\rangle$ | $-\mathcal{O}^{\odot}_{\mathrm{zx}'}$ |
| $\mathcal{O}^{\mathrm{V}}_{\mathrm{c}1}$ | $\lvert t_1\rvert\lvert t_5\rvert\cos(\phi_{15})+\lvert t_2\rvert\lvert t_6\rvert\cos(\phi_{26})+\lvert t_3\rvert\lvert t_7\rvert\cos(\phi_{37})+\lvert t_4\rvert\lvert t_8\rvert\cos(\phi_{48})$ | $\langle t\lvert\Gamma^{\mathrm{V}}_{\mathrm{c}1}\rvert t\rangle$ | $-\mathrm{I}^{\mathrm{c}}$ |
| $\mathcal{O}^{\mathrm{V}}_{\mathrm{c}2}$ | $\lvert t_1\rvert\lvert t_5\rvert\cos(\phi_{15})+\lvert t_2\rvert\lvert t_6\rvert\cos(\phi_{26})-\lvert t_3\rvert\lvert t_7\rvert\cos(\phi_{37})-\lvert t_4\rvert\lvert t_8\rvert\cos(\phi_{48})$ | $\langle t\lvert\Gamma^{\mathrm{V}}_{\mathrm{c}2}\rvert t\rangle$ | $-\mathrm{P}^{\mathrm{c}}_{\mathrm{y}}$ |
| $\mathcal{O}^{\mathrm{V}}_{\mathrm{c}3}$ | $\lvert t_1\rvert\lvert t_5\rvert\cos(\phi_{15})-\lvert t_2\rvert\lvert t_6\rvert\cos(\phi_{26})+\lvert t_3\rvert\lvert t_7\rvert\cos(\phi_{37})-\lvert t_4\rvert\lvert t_8\rvert\cos(\phi_{48})$ | $\langle t\lvert\Gamma^{\mathrm{V}}_{\mathrm{c}3}\rvert t\rangle$ | $-\mathrm{P}^{\mathrm{c}}_{\mathrm{y}'}$ |
| $\mathcal{O}^{\mathrm{V}}_{\mathrm{c}4}$ | $\lvert t_1\rvert\lvert t_5\rvert\cos(\phi_{15})-\lvert t_2\rvert\lvert t_6\rvert\cos(\phi_{26})-\lvert t_3\rvert\lvert t_7\rvert\cos(\phi_{37})+\lvert t_4\rvert\lvert t_8\rvert\cos(\phi_{48})$ | $\langle t\lvert\Gamma^{\mathrm{V}}_{\mathrm{c}4}\rvert t\rangle$ | $-\mathcal{O}^{\mathrm{c}}_{\mathrm{yy}'}$ |
| $\mathcal{O}^{\mathrm{V}}_{\mathrm{s}1}$ | $\lvert t_1\rvert\lvert t_5\rvert\sin(\phi_{15})+\lvert t_2\rvert\lvert t_6\rvert\sin(\phi_{26})+\lvert t_3\rvert\lvert t_7\rvert\sin(\phi_{37})+\lvert t_4\rvert\lvert t_8\rvert\sin(\phi_{48})$ | $\langle t\lvert\Gamma^{\mathrm{V}}_{\mathrm{s}1}\rvert t\rangle$ | $-\mathrm{I}^{\mathrm{s}}$ |
| $\mathcal{O}^{\mathrm{V}}_{\mathrm{s}2}$ | $\lvert t_1\rvert\lvert t_5\rvert\sin(\phi_{15})+\lvert t_2\rvert\lvert t_6\rvert\sin(\phi_{26})-\lvert t_3\rvert\lvert t_7\rvert\sin(\phi_{37})-\lvert t_4\rvert\lvert t_8\rvert\sin(\phi_{48})$ | $\langle t\lvert\Gamma^{\mathrm{V}}_{\mathrm{s}2}\rvert t\rangle$ | $-\mathrm{P}^{\mathrm{s}}_{\mathrm{y}}$ |
| $\mathcal{O}^{\mathrm{V}}_{\mathrm{s}3}$ | $\lvert t_1\rvert\lvert t_5\rvert\sin(\phi_{15})-\lvert t_2\rvert\lvert t_6\rvert\sin(\phi_{26})+\lvert t_3\rvert\lvert t_7\rvert\sin(\phi_{37})-\lvert t_4\rvert\lvert t_8\rvert\sin(\phi_{48})$ | $\langle t\lvert\Gamma^{\mathrm{V}}_{\mathrm{s}3}\rvert t\rangle$ | $-\mathrm{P}^{\mathrm{s}}_{\mathrm{y}'}$ |
| $\mathcal{O}^{\mathrm{V}}_{\mathrm{s}4}$ | $\lvert t_1\rvert\lvert t_5\rvert\sin(\phi_{15})-\lvert t_2\rvert\lvert t_6\rvert\sin(\phi_{26})-\lvert t_3\rvert\lvert t_7\rvert\sin(\phi_{37})+\lvert t_4\rvert\lvert t_8\rvert\sin(\phi_{48})$ | $\langle t\lvert\Gamma^{\mathrm{V}}_{\mathrm{s}4}\rvert t\rangle$ | $-\mathcal{O}^{\mathrm{s}}_{\mathrm{yy}'}$ |
| $\mathcal{O}^{\mathrm{VI}}_{\mathrm{c}1}$ | $\lvert t_1\rvert\lvert t_7\rvert\cos(\phi_{17})+\lvert t_2\rvert\lvert t_8\rvert\cos(\phi_{28})+\lvert t_3\rvert\lvert t_5\rvert\cos(\phi_{35})+\lvert t_4\rvert\lvert t_6\rvert\cos(\phi_{46})$ | $\langle t\lvert\Gamma^{\mathrm{VI}}_{\mathrm{c}1}\rvert t\rangle$ | $\mathrm{P}^{\mathrm{c}}_{\mathrm{z}}$ |
| $\mathcal{O}^{\mathrm{VI}}_{\mathrm{c}2}$ | $\lvert t_1\rvert\lvert t_7\rvert\cos(\phi_{17})+\lvert t_2\rvert\lvert t_8\rvert\cos(\phi_{28})-\lvert t_3\rvert\lvert t_5\rvert\cos(\phi_{35})-\lvert t_4\rvert\lvert t_6\rvert\cos(\phi_{46})$ | $\langle t\lvert\Gamma^{\mathrm{VI}}_{\mathrm{c}2}\rvert t\rangle$ | $-\mathrm{P}^{\mathrm{s}}_{\mathrm{x}}$ |
| $\mathcal{O}^{\mathrm{VI}}_{\mathrm{c}3}$ | $\lvert t_1\rvert\lvert t_7\rvert\cos(\phi_{17})-\lvert t_2\rvert\lvert t_8\rvert\cos(\phi_{28})+\lvert t_3\rvert\lvert t_5\rvert\cos(\phi_{35})-\lvert t_4\rvert\lvert t_6\rvert\cos(\phi_{46})$ | $\langle t\lvert\Gamma^{\mathrm{VI}}_{\mathrm{c}3}\rvert t\rangle$ | $\mathcal{O}^{\mathrm{c}}_{\mathrm{zy}'}$ |
| $\mathcal{O}^{\mathrm{VI}}_{\mathrm{c}4}$ | $\lvert t_1\rvert\lvert t_7\rvert\cos(\phi_{17})-\lvert t_2\rvert\lvert t_8\rvert\cos(\phi_{28})-\lvert t_3\rvert\lvert t_5\rvert\cos(\phi_{35})+\lvert t_4\rvert\lvert t_6\rvert\cos(\phi_{46})$ | $\langle t\lvert\Gamma^{\mathrm{VI}}_{\mathrm{c}4}\rvert t\rangle$ | $-\mathcal{O}^{\mathrm{s}}_{\mathrm{xy}'}$ |
| $\mathcal{O}^{\mathrm{VI}}_{\mathrm{s}1}$ | $\lvert t_1\rvert\lvert t_7\rvert\sin(\phi_{17})+\lvert t_2\rvert\lvert t_8\rvert\sin(\phi_{28})+\lvert t_3\rvert\lvert t_5\rvert\sin(\phi_{35})+\lvert t_4\rvert\lvert t_6\rvert\sin(\phi_{46})$ | $\langle t\lvert\Gamma^{\mathrm{VI}}_{\mathrm{s}1}\rvert t\rangle$ | $\mathrm{P}^{\mathrm{s}}_{\mathrm{z}}$ |
| $\mathcal{O}^{\mathrm{VI}}_{\mathrm{s}2}$ | $\lvert t_1\rvert\lvert t_7\rvert\sin(\phi_{17})+\lvert t_2\rvert\lvert t_8\rvert\sin(\phi_{28})-\lvert t_3\rvert\lvert t_5\rvert\sin(\phi_{35})-\lvert t_4\rvert\lvert t_6\rvert\sin(\phi_{46})$ | $\langle t\lvert\Gamma^{\mathrm{VI}}_{\mathrm{s}2}\rvert t\rangle$ | $\mathrm{P}^{\mathrm{c}}_{\mathrm{x}}$ |
| $\mathcal{O}^{\mathrm{VI}}_{\mathrm{s}3}$ | $\lvert t_1\rvert\lvert t_7\rvert\sin(\phi_{17})-\lvert t_2\rvert\lvert t_8\rvert\sin(\phi_{28})+\lvert t_3\rvert\lvert t_5\rvert\sin(\phi_{35})-\lvert t_4\rvert\lvert t_6\rvert\sin(\phi_{46})$ | $\langle t\lvert\Gamma^{\mathrm{VI}}_{\mathrm{s}3}\rvert t\rangle$ | $\mathcal{O}^{\mathrm{s}}_{\mathrm{zy}'}$ |
| $\mathcal{O}^{\mathrm{VI}}_{\mathrm{s}4}$ | $\lvert t_1\rvert\lvert t_7\rvert\sin(\phi_{17})-\lvert t_2\rvert\lvert t_8\rvert\sin(\phi_{28})-\lvert t_3\rvert\lvert t_5\rvert\sin(\phi_{35})+\lvert t_4\rvert\lvert t_6\rvert\sin(\phi_{46})$ | $\langle t\lvert\Gamma^{\mathrm{VI}}_{\mathrm{s}4}\rvert t\rangle$ | $\mathcal{O}^{\mathrm{c}}_{\mathrm{xy}'}$ |
| $\mathcal{O}^{\mathrm{VII}}_{\mathrm{c}1}$ | $\lvert t_1\rvert\lvert t_6\rvert\cos(\phi_{16})+\lvert t_2\rvert\lvert t_5\rvert\cos(\phi_{25})+\lvert t_3\rvert\lvert t_8\rvert\cos(\phi_{38})+\lvert t_4\rvert\lvert t_7\rvert\cos(\phi_{47})$ | $\langle t\lvert\Gamma^{\mathrm{VII}}_{\mathrm{c}1}\rvert t\rangle$ | $\mathrm{P}^{\mathrm{c}}_{\mathrm{z}'}$ |
| $\mathcal{O}^{\mathrm{VII}}_{\mathrm{c}2}$ | $\lvert t_1\rvert\lvert t_6\rvert\cos(\phi_{16})+\lvert t_2\rvert\lvert t_5\rvert\cos(\phi_{25})-\lvert t_3\rvert\lvert t_8\rvert\cos(\phi_{38})-\lvert t_4\rvert\lvert t_7\rvert\cos(\phi_{47})$ | $\langle t\lvert\Gamma^{\mathrm{VII}}_{\mathrm{c}2}\rvert t\rangle$ | $\mathcal{O}^{\mathrm{c}}_{\mathrm{yz}'}$ |
| $\mathcal{O}^{\mathrm{VII}}_{\mathrm{c}3}$ | $\lvert t_1\rvert\lvert t_6\rvert\cos(\phi_{16})-\lvert t_2\rvert\lvert t_5\rvert\cos(\phi_{25})+\lvert t_3\rvert\lvert t_8\rvert\cos(\phi_{38})-\lvert t_4\rvert\lvert t_7\rvert\cos(\phi_{47})$ | $\langle t\lvert\Gamma^{\mathrm{VII}}_{\mathrm{c}3}\rvert t\rangle$ | $\mathrm{P}^{\mathrm{s}}_{\mathrm{x}'}$ |
| $\mathcal{O}^{\mathrm{VII}}_{\mathrm{c}4}$ | $\lvert t_1\rvert\lvert t_6\rvert\cos(\phi_{16})-\lvert t_2\rvert\lvert t_5\rvert\cos(\phi_{25})-\lvert t_3\rvert\lvert t_8\rvert\cos(\phi_{38})+\lvert t_4\rvert\lvert t_7\rvert\cos(\phi_{47})$ | $\langle t\lvert\Gamma^{\mathrm{VII}}_{\mathrm{c}4}\rvert t\rangle$ | $\mathcal{O}^{\mathrm{s}}_{\mathrm{yx}'}$ |

TABLE I. *(Continued.)*

| Observable | Definition in terms of polar coordinates / 2 | Bilinear form | Roberts, Oed |
|---|---|---|---|
| $\mathcal{O}^{\mathrm{VII}}_{\mathrm{s1}}$ | $\lvert t_1\rvert\lvert t_6\rvert\sin(\phi_{16}) + \lvert t_2\rvert\lvert t_5\rvert\sin(\phi_{25}) + \lvert t_3\rvert\lvert t_8\rvert\sin(\phi_{38}) + \lvert t_4\rvert\lvert t_7\rvert\sin(\phi_{47})$ | $\langle t\lvert\Gamma^{\mathrm{VII}}_{\mathrm{s1}}\rvert t\rangle$ | $\mathrm{P}^{\mathrm{s}}_{\mathrm{z}'}$ |
| $\mathcal{O}^{\mathrm{VII}}_{\mathrm{s2}}$ | $\lvert t_1\rvert\lvert t_6\rvert\sin(\phi_{16}) + \lvert t_2\rvert\lvert t_5\rvert\sin(\phi_{25}) - \lvert t_3\rvert\lvert t_8\rvert\sin(\phi_{38}) - \lvert t_4\rvert\lvert t_7\rvert\sin(\phi_{47})$ | $\langle t\lvert\Gamma^{\mathrm{VII}}_{\mathrm{s2}}\rvert t\rangle$ | $\mathcal{O}^{\mathrm{s}}_{\mathrm{yz}'}$ |
| $\mathcal{O}^{\mathrm{VII}}_{\mathrm{s3}}$ | $\lvert t_1\rvert\lvert t_6\rvert\sin(\phi_{16}) - \lvert t_2\rvert\lvert t_5\rvert\sin(\phi_{25}) + \lvert t_3\rvert\lvert t_8\rvert\sin(\phi_{38}) - \lvert t_4\rvert\lvert t_7\rvert\sin(\phi_{47})$ | $\langle t\lvert\Gamma^{\mathrm{VII}}_{\mathrm{s3}}\rvert t\rangle$ | $-\mathrm{P}^{\mathrm{c}}_{\mathrm{x}'}$ |
| $\mathcal{O}^{\mathrm{VII}}_{\mathrm{s4}}$ | $\lvert t_1\rvert\lvert t_6\rvert\sin(\phi_{16}) - \lvert t_2\rvert\lvert t_5\rvert\sin(\phi_{25}) - \lvert t_3\rvert\lvert t_8\rvert\sin(\phi_{38}) + \lvert t_4\rvert\lvert t_7\rvert\sin(\phi_{47})$ | $\langle t\lvert\Gamma^{\mathrm{VII}}_{\mathrm{s4}}\rvert t\rangle$ | $-\mathcal{O}^{\mathrm{c}}_{\mathrm{yx}'}$ |
| $\mathcal{O}^{\mathrm{VIII}}_{\mathrm{c1}}$ | $\lvert t_1\rvert\lvert t_8\rvert\cos(\phi_{18}) + \lvert t_2\rvert\lvert t_7\rvert\cos(\phi_{27}) + \lvert t_3\rvert\lvert t_6\rvert\cos(\phi_{36}) + \lvert t_4\rvert\lvert t_5\rvert\cos(\phi_{45})$ | $\langle t\lvert\Gamma^{\mathrm{VIII}}_{\mathrm{c1}}\rvert t\rangle$ | $-\mathcal{O}^{\mathrm{c}}_{\mathrm{zz}'}$ |
| $\mathcal{O}^{\mathrm{VIII}}_{\mathrm{c2}}$ | $\lvert t_1\rvert\lvert t_8\rvert\cos(\phi_{18}) + \lvert t_2\rvert\lvert t_7\rvert\cos(\phi_{27}) - \lvert t_3\rvert\lvert t_6\rvert\cos(\phi_{36}) - \lvert t_4\rvert\lvert t_5\rvert\cos(\phi_{45})$ | $\langle t\lvert\Gamma^{\mathrm{VIII}}_{\mathrm{c2}}\rvert t\rangle$ | $\mathcal{O}^{\mathrm{s}}_{\mathrm{xz}'}$ |
| $\mathcal{O}^{\mathrm{VIII}}_{\mathrm{c3}}$ | $\lvert t_1\rvert\lvert t_8\rvert\cos(\phi_{18}) - \lvert t_2\rvert\lvert t_7\rvert\cos(\phi_{27}) + \lvert t_3\rvert\lvert t_6\rvert\cos(\phi_{36}) - \lvert t_4\rvert\lvert t_5\rvert\cos(\phi_{45})$ | $\langle t\lvert\Gamma^{\mathrm{VIII}}_{\mathrm{c3}}\rvert t\rangle$ | $-\mathcal{O}^{\mathrm{s}}_{\mathrm{zx}'}$ |
| $\mathcal{O}^{\mathrm{VIII}}_{\mathrm{c4}}$ | $\lvert t_1\rvert\lvert t_8\rvert\cos(\phi_{18}) - \lvert t_2\rvert\lvert t_7\rvert\cos(\phi_{27}) - \lvert t_3\rvert\lvert t_6\rvert\cos(\phi_{36}) + \lvert t_4\rvert\lvert t_5\rvert\cos(\phi_{45})$ | $\langle t\lvert\Gamma^{\mathrm{VIII}}_{\mathrm{c4}}\rvert t\rangle$ | $-\mathcal{O}^{\mathrm{c}}_{\mathrm{xx}'}$ |
| $\mathcal{O}^{\mathrm{VIII}}_{\mathrm{s1}}$ | $\lvert t_1\rvert\lvert t_8\rvert\sin(\phi_{18}) + \lvert t_2\rvert\lvert t_7\rvert\sin(\phi_{27}) + \lvert t_3\rvert\lvert t_6\rvert\sin(\phi_{36}) + \lvert t_4\rvert\lvert t_5\rvert\sin(\phi_{45})$ | $\langle t\lvert\Gamma^{\mathrm{VIII}}_{\mathrm{s1}}\rvert t\rangle$ | $-\mathcal{O}^{\mathrm{s}}_{\mathrm{zz}'}$ |
| $\mathcal{O}^{\mathrm{VIII}}_{\mathrm{s2}}$ | $\lvert t_1\rvert\lvert t_8\rvert\sin(\phi_{18}) + \lvert t_2\rvert\lvert t_7\rvert\sin(\phi_{27}) - \lvert t_3\rvert\lvert t_6\rvert\sin(\phi_{36}) - \lvert t_4\rvert\lvert t_5\rvert\sin(\phi_{45})$ | $\langle t\lvert\Gamma^{\mathrm{VIII}}_{\mathrm{s2}}\rvert t\rangle$ | $-\mathcal{O}^{\mathrm{c}}_{\mathrm{xz}'}$ |
| $\mathcal{O}^{\mathrm{VIII}}_{\mathrm{s3}}$ | $\lvert t_1\rvert\lvert t_8\rvert\sin(\phi_{18}) - \lvert t_2\rvert\lvert t_7\rvert\sin(\phi_{27}) + \lvert t_3\rvert\lvert t_6\rvert\sin(\phi_{36}) - \lvert t_4\rvert\lvert t_5\rvert\sin(\phi_{45})$ | $\langle t\lvert\Gamma^{\mathrm{VIII}}_{\mathrm{s3}}\rvert t\rangle$ | $\mathcal{O}^{\mathrm{c}}_{\mathrm{zx}'}$ |
| $\mathcal{O}^{\mathrm{VIII}}_{\mathrm{s4}}$ | $\lvert t_1\rvert\lvert t_8\rvert\sin(\phi_{18}) - \lvert t_2\rvert\lvert t_7\rvert\sin(\phi_{27}) - \lvert t_3\rvert\lvert t_6\rvert\sin(\phi_{36}) + \lvert t_4\rvert\lvert t_5\rvert\sin(\phi_{45})$ | $\langle t\lvert\Gamma^{\mathrm{VIII}}_{\mathrm{s4}}\rvert t\rangle$ | $-\mathcal{O}^{\mathrm{s}}_{\mathrm{xx}'}$ |

TABLE II. Definition of the 64 Γ matrices in terms of the well-known Pauli matrices in combination with the Kronecker product. The gray shaded cells within the column "Shape-class" correspond to the nonzero matrix entries.

| Γ-matrices | Definition | Shape-class | Γ-matrices | Definition | Shape-class |
|---|---|---|---|---|---|
| $\Gamma^{\mathrm{I}}_{1}$ | $\sigma^3\otimes I_2\otimes I_2$ | 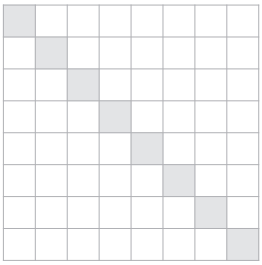 | $\Gamma^{\mathrm{V}}_{c1}$ | $\sigma^1\otimes I_2\otimes I_2$ | 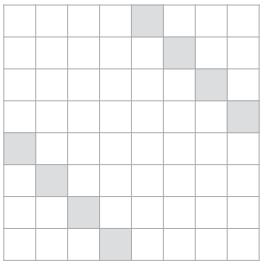 |
| $\Gamma^{\mathrm{I}}_{2}$ | $I_2\otimes\sigma^3\otimes I_2$ | | $\Gamma^{\mathrm{V}}_{c2}$ | $\sigma^1\otimes\sigma^3\otimes I_2$ | |
| $\Gamma^{\mathrm{I}}_{3}$ | $I_2\otimes I_2\otimes\sigma^3$ | | $\Gamma^{\mathrm{V}}_{c3}$ | $\sigma^1\otimes I_2\otimes\sigma^3$ | |
| $\Gamma^{\mathrm{I}}_{4}$ | $\sigma^3\otimes\sigma^3\otimes\sigma^3$ | | $\Gamma^{\mathrm{V}}_{c4}$ | $\sigma^1\otimes\sigma^3\otimes\sigma^3$ | |
| $\Gamma^{\mathrm{I}}_{5}$ | $I_2\otimes\sigma^3\otimes\sigma^3$ | | $\Gamma^{\mathrm{V}}_{s1}$ | $-\sigma^2\otimes I_2\otimes I_2$ | |
| $\Gamma^{\mathrm{I}}_{6}$ | $\sigma^3\otimes I_2\otimes\sigma^3$ | | $\Gamma^{\mathrm{V}}_{s2}$ | $-\sigma^2\otimes\sigma^3\otimes I_2$ | |
| $\Gamma^{\mathrm{I}}_{7}$ | $\sigma^3\otimes\sigma^3\otimes I_2$ | | $\Gamma^{\mathrm{V}}_{s3}$ | $-\sigma^2\otimes I_2\otimes\sigma^3$ | |
| $\Gamma^{\mathrm{I}}_{8}$ | $I_2\otimes I_2\otimes I_2$ | | $\Gamma^{\mathrm{V}}_{s4}$ | $-\sigma^2\otimes\sigma^3\otimes\sigma^3$ | |
| $\Gamma^{\mathrm{II}}_{c1}$ | $I_2\otimes\sigma^1\otimes I_2$ | 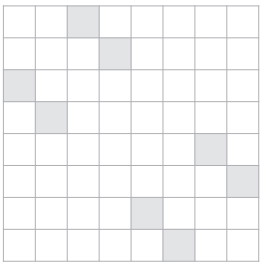 | $\Gamma^{\mathrm{VI}}_{c1}$ | $\sigma^1\otimes\sigma^1\otimes I_2$ | 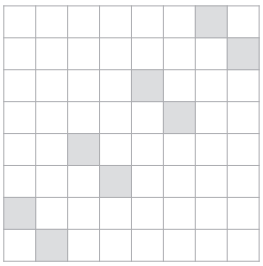 |
| $\Gamma^{\mathrm{II}}_{c2}$ | $\sigma^3\otimes\sigma^1\otimes I_2$ | | $\Gamma^{\mathrm{VI}}_{c2}$ | $-\sigma^2\otimes\sigma^2\otimes I_2$ | |
| $\Gamma^{\mathrm{II}}_{c3}$ | $I_2\otimes\sigma^1\otimes\sigma^3$ | | $\Gamma^{\mathrm{VI}}_{c3}$ | $\sigma^1\otimes\sigma^1\otimes\sigma^3$ | |
| $\Gamma^{\mathrm{II}}_{c4}$ | $\sigma^3\otimes\sigma^1\otimes\sigma^3$ | | $\Gamma^{\mathrm{VI}}_{c4}$ | $-\sigma^2\otimes\sigma^2\otimes\sigma^3$ | |
| $\Gamma^{\mathrm{II}}_{s1}$ | $-I_2\otimes\sigma^2\otimes I_2$ | | $\Gamma^{\mathrm{VI}}_{s1}$ | $-\sigma^2\otimes\sigma^1\otimes I_2$ | |
| $\Gamma^{\mathrm{II}}_{s2}$ | $-\sigma^3\otimes\sigma^2\otimes I_2$ | | $\Gamma^{\mathrm{VI}}_{s2}$ | $-\sigma^1\otimes\sigma^2\otimes I_2$ | |
| $\Gamma^{\mathrm{II}}_{s3}$ | $-I_2\otimes\sigma^2\otimes\sigma^3$ | | $\Gamma^{\mathrm{VI}}_{s3}$ | $-\sigma^2\otimes\sigma^1\otimes\sigma^3$ | |
| $\Gamma^{\mathrm{II}}_{s4}$ | $-\sigma^3\otimes\sigma^2\otimes\sigma^3$ | | $\Gamma^{\mathrm{VI}}_{s4}$ | $-\sigma^1\otimes\sigma^2\otimes\sigma^3$ | |
| $\Gamma^{\mathrm{III}}_{c1}$ | $I_2\otimes I_2\otimes\sigma^1$ | 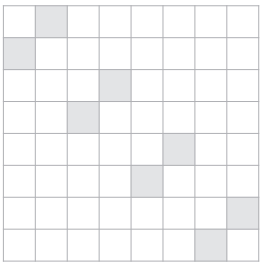 | $\Gamma^{\mathrm{VII}}_{c1}$ | $\sigma^1\otimes I_2\otimes\sigma^1$ | 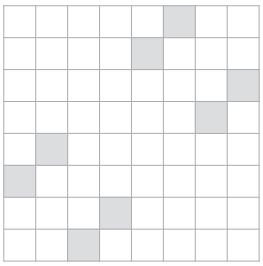 |
| $\Gamma^{\mathrm{III}}_{c2}$ | $\sigma^3\otimes I_2\otimes\sigma^1$ | | $\Gamma^{\mathrm{VII}}_{c2}$ | $\sigma^1\otimes\sigma^3\otimes\sigma^1$ | |
| $\Gamma^{\mathrm{III}}_{c3}$ | $I_2\otimes\sigma^3\otimes\sigma^1$ | | $\Gamma^{\mathrm{VII}}_{c3}$ | $-\sigma^2\otimes I_2\otimes\sigma^2$ | |
| $\Gamma^{\mathrm{III}}_{c4}$ | $\sigma^3\otimes\sigma^3\otimes\sigma^1$ | | $\Gamma^{\mathrm{VII}}_{c4}$ | $-\sigma^2\otimes\sigma^3\otimes\sigma^2$ | |
| $\Gamma^{\mathrm{III}}_{s1}$ | $-I_2\otimes I_2\otimes\sigma^2$ | | $\Gamma^{\mathrm{VII}}_{s1}$ | $-\sigma^2\otimes I_2\otimes\sigma^1$ | |
| $\Gamma^{\mathrm{III}}_{s2}$ | $-\sigma^3\otimes I_2\otimes\sigma^2$ | | $\Gamma^{\mathrm{VII}}_{s2}$ | $-\sigma^2\otimes\sigma^3\otimes\sigma^1$ | |
| $\Gamma^{\mathrm{III}}_{s3}$ | $-I_2\otimes\sigma^3\otimes\sigma^2$ | | $\Gamma^{\mathrm{VII}}_{s3}$ | $-\sigma^1\otimes I_2\otimes\sigma^2$ | |
| $\Gamma^{\mathrm{III}}_{s4}$ | $-\sigma^3\otimes\sigma^3\otimes\sigma^2$ | | $\Gamma^{\mathrm{VII}}_{s4}$ | $-\sigma^1\otimes\sigma^3\otimes\sigma^2$ | |
| $\Gamma^{\mathrm{IV}}_{c1}$ | $I_2\otimes\sigma^1\otimes\sigma^1$ | 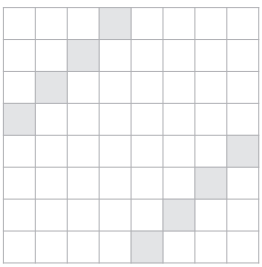 | $\Gamma^{\mathrm{VIII}}_{c1}$ | $\sigma^1\otimes\sigma^1\otimes\sigma^1$ | 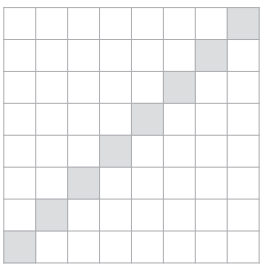 |
| $\Gamma^{\mathrm{IV}}_{c2}$ | $\sigma^3\otimes\sigma^1\otimes\sigma^1$ | | $\Gamma^{\mathrm{VIII}}_{c2}$ | $-\sigma^2\otimes\sigma^2\otimes\sigma^1$ | |
| $\Gamma^{\mathrm{IV}}_{c3}$ | $-I_2\otimes\sigma^2\otimes\sigma^2$ | | $\Gamma^{\mathrm{VIII}}_{c3}$ | $-\sigma^2\otimes\sigma^1\otimes\sigma^2$ | |
| $\Gamma^{\mathrm{IV}}_{c4}$ | $-\sigma^3\otimes\sigma^2\otimes\sigma^2$ | | $\Gamma^{\mathrm{VIII}}_{c4}$ | $-\sigma^1\otimes\sigma^2\otimes\sigma^2$ | |
| $\Gamma^{\mathrm{IV}}_{s1}$ | $-I_2\otimes\sigma^2\otimes\sigma^1$ | | $\Gamma^{\mathrm{VIII}}_{s1}$ | $-\sigma^2\otimes\sigma^1\otimes\sigma^1$ | |
| $\Gamma^{\mathrm{IV}}_{s2}$ | $-\sigma^3\otimes\sigma^2\otimes\sigma^1$ | | $\Gamma^{\mathrm{VIII}}_{s2}$ | $-\sigma^1\otimes\sigma^2\otimes\sigma^1$ | |
| $\Gamma^{\mathrm{IV}}_{s3}$ | $-I_2\otimes\sigma^1\otimes\sigma^2$ | | $\Gamma^{\mathrm{VIII}}_{s3}$ | $-\sigma^1\otimes\sigma^1\otimes\sigma^2$ | |
| $\Gamma^{\mathrm{IV}}_{s4}$ | $-\sigma^3\otimes\sigma^1\otimes\sigma^2$ | | $\Gamma^{\mathrm{VIII}}_{s4}$ | $\sigma^2\otimes\sigma^2\otimes\sigma^2$ | |

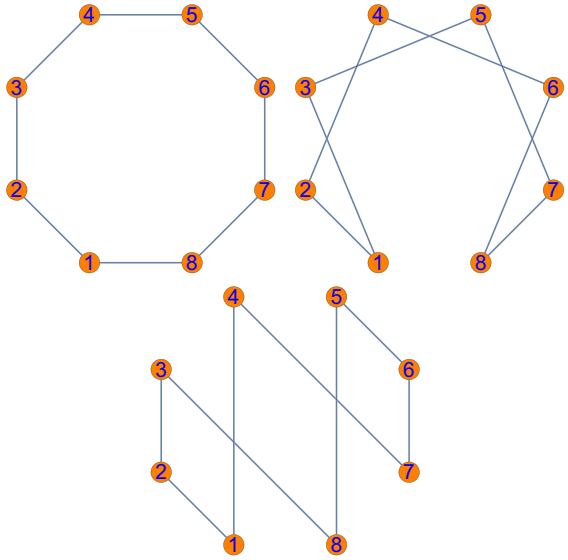


FIG. 2. Examples of graph topologies. Only three out of 2520 unique cycle graphs with eight nodes are shown.

In a second step, all possible edge configurations which yield a complete set of observables are constructed. An example is shown in Fig. 1. This is done for each unique topology. The total number of possible edge configurations can be calculated by $\sum_{k=1}^{N} \binom{N}{k}$ for all odd $k \leqslant N$.

The final step involves the mapping from bilinear forms to the actual observables. Referring again to the example in Fig. 1, the overall question is which combinations of observables can be solely described by these bilinear products (given that all amplitudes are known)? Considering Table I, the following relations are evident:

$$\sin(\phi_{12}) \mapsto \{\mathcal{O}^{\mathrm{III}}_{\mathrm{s1}}, \mathcal{O}^{\mathrm{III}}_{\mathrm{s2}}, \mathcal{O}^{\mathrm{III}}_{\mathrm{s3}}, \mathcal{O}^{\mathrm{III}}_{\mathrm{s4}}\}, \tag{6}$$

$$\sin(\phi_{34}) \mapsto \{\mathcal{O}^{\mathrm{III}}_{\mathrm{s1}}, \mathcal{O}^{\mathrm{III}}_{\mathrm{s2}}, \mathcal{O}^{\mathrm{III}}_{\mathrm{s3}}, \mathcal{O}^{\mathrm{III}}_{\mathrm{s4}}\}, \tag{7}$$

$$\sin(\phi_{56}) \mapsto \{\mathcal{O}^{\mathrm{III}}_{\mathrm{s1}}, \mathcal{O}^{\mathrm{III}}_{\mathrm{s2}}, \mathcal{O}^{\mathrm{III}}_{\mathrm{s3}}, \mathcal{O}^{\mathrm{III}}_{\mathrm{s4}}\}, \tag{8}$$

$$\sin(\phi_{78}) \mapsto \{\mathcal{O}^{\mathrm{III}}_{\mathrm{s1}}, \mathcal{O}^{\mathrm{III}}_{\mathrm{s2}}, \mathcal{O}^{\mathrm{III}}_{\mathrm{s3}}, \mathcal{O}^{\mathrm{III}}_{\mathrm{s4}}\} \tag{9}$$

$$\sin(\phi_{14}) \mapsto \{\mathcal{O}^{\mathrm{IV}}_{\mathrm{s1}}, \mathcal{O}^{\mathrm{IV}}_{\mathrm{s2}}, \mathcal{O}^{\mathrm{IV}}_{\mathrm{s3}}, \mathcal{O}^{\mathrm{IV}}_{\mathrm{s4}}\}, \tag{10}$$

$$\sin(\phi_{58}) \mapsto \{\mathcal{O}^{\mathrm{IV}}_{\mathrm{s1}}, \mathcal{O}^{\mathrm{IV}}_{\mathrm{s2}}, \mathcal{O}^{\mathrm{IV}}_{\mathrm{s3}}, \mathcal{O}^{\mathrm{IV}}_{\mathrm{s4}}\}, \tag{11}$$

$$\sin(\phi_{27}) \mapsto \{\mathcal{O}^{\mathrm{VIII}}_{\mathrm{s1}}, \mathcal{O}^{\mathrm{VIII}}_{\mathrm{s2}}, \mathcal{O}^{\mathrm{VIII}}_{\mathrm{s3}}, \mathcal{O}^{\mathrm{VIII}}_{\mathrm{s4}}\}, \tag{12}$$

$$\cos(\phi_{36}) \mapsto \{\mathcal{O}^{\mathrm{VIII}}_{\mathrm{c1}}, \mathcal{O}^{\mathrm{VIII}}_{\mathrm{c2}}, \mathcal{O}^{\mathrm{VIII}}_{\mathrm{c3}}, \mathcal{O}^{\mathrm{VIII}}_{\mathrm{c4}}\}. \tag{13}$$

Thus, the complete set of observables which corresponds to the graph configuration shown in Fig. 1 is

$$\begin{aligned}&\{\mathcal{O}^{\mathrm{I}}_{1}, \mathcal{O}^{\mathrm{I}}_{2}, \mathcal{O}^{\mathrm{I}}_{3}, \mathcal{O}^{\mathrm{I}}_{4}, \mathcal{O}^{\mathrm{I}}_{5}, \mathcal{O}^{\mathrm{I}}_{6}, \mathcal{O}^{\mathrm{I}}_{7}, \mathcal{O}^{\mathrm{I}}_{8},\\ &\mathcal{O}^{\mathrm{III}}_{\mathrm{s1}}, \mathcal{O}^{\mathrm{III}}_{\mathrm{s2}}, \mathcal{O}^{\mathrm{III}}_{\mathrm{s3}}, \mathcal{O}^{\mathrm{III}}_{\mathrm{s4}}, \mathcal{O}^{\mathrm{IV}}_{\mathrm{s1}}, \mathcal{O}^{\mathrm{IV}}_{\mathrm{s2}}, \mathcal{O}^{\mathrm{IV}}_{\mathrm{s3}}, \mathcal{O}^{\mathrm{IV}}_{\mathrm{s4}},\\ &\mathcal{O}^{\mathrm{VIII}}_{\mathrm{s1}}, \mathcal{O}^{\mathrm{VIII}}_{\mathrm{s2}}, \mathcal{O}^{\mathrm{VIII}}_{\mathrm{s3}}, \mathcal{O}^{\mathrm{VIII}}_{\mathrm{s4}}, \mathcal{O}^{\mathrm{VIII}}_{\mathrm{c1}}, \mathcal{O}^{\mathrm{VIII}}_{\mathrm{c2}}, \mathcal{O}^{\mathrm{VIII}}_{\mathrm{c3}}, \mathcal{O}^{\mathrm{VIII}}_{\mathrm{c4}}\}.\end{aligned} \tag{14}$$

In general one needs to add the observables which are solely described by moduli in order to fix the moduli of the complex amplitudes $t_i$ (see Sec. II). In this case, these are the group I observables, as shown in Table I. Thus, Eq. (14) accounts for a total of 24 observables.

TABLE III. The 64 observables are grouped into eight categories according to the polarization needed to measure these observables (beam $\mathcal{B}$, target $\mathcal{T}$, and recoil $\mathcal{R}$). The notation used in the original paper of Roberts and Oed [5] is used for the observables. The observable $\mathrm{I}_0$ corresponds to the unpolarized cross section.

| Category | Subcategory | Observables |
|---|---|---|
| | | $\mathrm{I}_0$ |
| $\mathcal{B}$ | $\mathcal{B}_\mathrm{l}$ | $\mathrm{I}^\mathrm{s}$, $\mathrm{I}^\mathrm{c}$ |
| | $\mathcal{B}_\odot$ | $\mathrm{I}^\odot$ |
| $\mathcal{T}$ | | $\mathrm{P}_\mathrm{x}$, $\mathrm{P}_\mathrm{y}$, $\mathrm{P}_\mathrm{z}$ |
| $\mathcal{R}$ | | $\mathrm{P}_{\mathrm{x}'}$, $\mathrm{P}_{\mathrm{y}'}$, $\mathrm{P}_{\mathrm{z}'}$ |
| $\mathcal{BT}$ | $\mathcal{B}_\mathrm{l}\mathcal{T}$ | $\mathrm{P}^\mathrm{s}_\mathrm{x}$, $\mathrm{P}^\mathrm{s}_\mathrm{y}$, $\mathrm{P}^\mathrm{s}_\mathrm{z}$, $\mathrm{P}^\mathrm{c}_\mathrm{x}$, $\mathrm{P}^\mathrm{c}_\mathrm{y}$, $\mathrm{P}^\mathrm{c}_\mathrm{z}$ |
| | $\mathcal{B}_\odot\mathcal{T}$ | $\mathrm{P}^\odot_\mathrm{x}$, $\mathrm{P}^\odot_\mathrm{y}$, $\mathrm{P}^\odot_\mathrm{z}$ |
| $\mathcal{BR}$ | $\mathcal{B}_\mathrm{l}\mathcal{R}$ | $\mathrm{P}^\mathrm{s}_{\mathrm{x}'}$, $\mathrm{P}^\mathrm{s}_{\mathrm{y}'}$, $\mathrm{P}^\mathrm{s}_{\mathrm{z}'}$, $\mathrm{P}^\mathrm{c}_{\mathrm{x}'}$, $\mathrm{P}^\mathrm{c}_{\mathrm{y}'}$, $\mathrm{P}^\mathrm{c}_{\mathrm{z}'}$ |
| | $\mathcal{B}_\odot\mathcal{R}$ | $\mathrm{P}^\odot_{\mathrm{x}'}$, $\mathrm{P}^\odot_{\mathrm{y}'}$, $\mathrm{P}^\odot_{\mathrm{z}'}$ |
| $\mathcal{TR}$ | | $\mathcal{O}_{\mathrm{xx}'}$, $\mathcal{O}_{\mathrm{xy}'}$, $\mathcal{O}_{\mathrm{xz}'}$, $\mathcal{O}_{\mathrm{yx}'}$, $\mathcal{O}_{\mathrm{yy}'}$, $\mathcal{O}_{\mathrm{yz}'}$, $\mathcal{O}_{\mathrm{zx}'}$ $\mathcal{O}_{\mathrm{zy}'}$, $\mathcal{O}_{\mathrm{zz}'}$ |
| $\mathcal{BTR}$ | $\mathcal{B}_\mathrm{l}\mathcal{TR}$ | $\mathcal{O}^\mathrm{s}_{\mathrm{xx}'}$, $\mathcal{O}^\mathrm{s}_{\mathrm{xy}'}$, $\mathcal{O}^\mathrm{s}_{\mathrm{xz}'}$, $\mathcal{O}^\mathrm{s}_{\mathrm{yx}'}$, $\mathcal{O}^\mathrm{s}_{\mathrm{yy}'}$, $\mathcal{O}^\mathrm{s}_{\mathrm{yz}'}$, $\mathcal{O}^\mathrm{s}_{\mathrm{zx}'}$ $\mathcal{O}^\mathrm{s}_{\mathrm{zy}'}$, $\mathcal{O}^\mathrm{s}_{\mathrm{zz}'}$ |
| | | $\mathcal{O}^\mathrm{c}_{\mathrm{xx}'}$, $\mathcal{O}^\mathrm{c}_{\mathrm{xy}'}$, $\mathcal{O}^\mathrm{c}_{\mathrm{xz}'}$, $\mathcal{O}^\mathrm{c}_{\mathrm{yx}'}$, $\mathcal{O}^\mathrm{c}_{\mathrm{yy}'}$, $\mathcal{O}^\mathrm{c}_{\mathrm{yz}'}$, $\mathcal{O}^\mathrm{c}_{\mathrm{zx}'}$ $\mathcal{O}^\mathrm{c}_{\mathrm{zy}'}$, $\mathcal{O}^\mathrm{c}_{\mathrm{zz}'}$ |
| | $\mathcal{B}_\odot\mathcal{TR}$ | $\mathcal{O}^\odot_{\mathrm{xx}'}$, $\mathcal{O}^\odot_{\mathrm{xy}'}$, $\mathcal{O}^\odot_{\mathrm{xz}'}$, $\mathcal{O}^\odot_{\mathrm{yx}'}$, $\mathcal{O}^\odot_{\mathrm{yy}'}$, $\mathcal{O}^\odot_{\mathrm{yz}'}$, $\mathcal{O}^\odot_{\mathrm{zx}'}$ $\mathcal{O}^\odot_{\mathrm{zy}'}$, $\mathcal{O}^\odot_{\mathrm{zz}'}$ |

The same result can be obtained by using the relation:

$$t_j^* t_i = \frac{1}{8} \sum_{\alpha=1}^{64} \Gamma^\alpha_{ij} \mathcal{O}^\alpha, \tag{15}$$

where $\alpha$ is an index running through the observables listed in Table I and the $\Gamma$ matrices as listed in Table II. Equation (15) is derived by using $\mathcal{O}^\alpha = \sum_{i,j=1}^{8} t_i^* \Gamma^\alpha_{ij} t_j$ in combination with the completeness relation of the $\Gamma$ matrices $\sum_{\alpha=1}^{64} \Gamma^\alpha_{ai} \Gamma^\alpha_{jb} = 8\delta_{ab}\delta_{ij}$.

## V. DATABASE FOR TWO PSEUDOSCALAR MESON PHOTOPRODUCTION

As already mentioned, 64 observables can be measured for two pseudoscalar meson photoproduction using the full three-body kinematics of the reaction. These observables can be organized into three groups: single, double, and triple polarization observables, which require either the use of a polarized beam $\mathcal{B}$, a polarized target $\mathcal{T}$, a recoil polarimeter $\mathcal{R}$, or a combination of the three. Table III gives an overview of all the observables of each category. In addition to the unpolarized cross section $\mathrm{I}_0$, there are three observables in each single polarization observable category ($\mathcal{B}$, $\mathcal{T}$, $\mathcal{R}$), nine in each double polarization observable category ($\mathcal{BT}$, $\mathcal{BR}$, and $\mathcal{TR}$) and 27 observables in the triple polarization observable category ($\mathcal{BTR}$).

The description of the full three-body kinematics requires five independent variables [14]. In this context, two planes,

the reaction plane and the decay plane, are often used [14,15]. While the reaction plane is defined by the incoming photon and one of the outgoing particles, the decay plane is spanned by the other two outgoing particles. The angle between the reaction and the decay plane is called $\phi^*$. Integrating over $\phi^*$ makes it possible to treat the three-body final state as a two-body final state, resulting in a reduced number of observables. In this case, the observables correspond to observables known from single meson photoproduction [7], e.g., category $\mathcal{B}$ reduces to $\mathrm{I}^{\mathrm{c}} = \Sigma$, category $\mathcal{T}$ to $\mathrm{P}_{\mathrm{y}} = T$, category $\mathcal{R}$ to $\mathrm{P}_{\mathrm{y}'} = P$ (this observable can be also measured as a double polarization observable $-\mathrm{P}^{\mathrm{c}}_{\mathrm{y}}$ [5]), and category $\mathcal{BT}$ to $\mathrm{P}^{\mathrm{s}}_{\mathrm{x}} = H$, $\mathrm{P}^{\mathrm{s}}_{\mathrm{z}} = G$, $\mathrm{P}^{\odot}_{\mathrm{x}} = F$, and $\mathrm{P}^{\odot}_{\mathrm{z}} = E$ [5].

In the case of single pseudoscalar meson photoproduction, quite a lot measurements were performed to determine single and double polarization observables. An extensive overview over the performed measurements, on the basis of the SAID database [16], was brought together recently by Ireland, Pasyuk, and Strakovsky [17].

A similar database does not exist yet for double pseudoscalar meson photoproduction. Thus, for the first time, an extensive overview of measurements of polarization observables for double pseudoscalar meson photoproduction is presented in Table IV.

By far the most measurements where performed for the reaction $\gamma p \to p\pi^0\pi^0$ because the reaction has the least amount of nonresonant background amplitude contributions compared with other isospin channels [1]. The most common observable is the unpolarized cross section $\mathrm{I}_0$, followed by the beam asymmetries $\mathrm{I}^{\mathrm{s}}$, $\mathrm{I}^{\mathrm{c}}$, and $\mathrm{I}^{\odot}$. Even a few double polarization observables in quasi-two-body kinematics were measured, i.e., $E$ and $H$. Until now, no triple polarization observables were extracted, as it is experimentally challenging to measure the polarization of a recoiling particle [18,19] in addition to a polarized beam and a polarized target.

However, a few words of caution are in order. One might get the impression of a huge existing database with plenty of data. It should be kept in mind that the data entries span more than half a century, thus including data with lower-performing experimental setups in comparison with the latest published polarization observables data. The collection consists mainly of measurements concerning the unpolarized cross section $\mathrm{I}_0$ (roughly 60%). Taken as a whole, the current database is not sufficient for an experimental verification of a complete experiment analysis. This issue is further discussed in Sec. VIII for experimentalists. But also for theoreticians using phenomenological models to fit and interpret the data, it is challenging and necessary to check the different data sets for consistency between different experiments and to deal with the systematic uncertainties of the data.

## VI. RESULTS FOR $N = 8$

For $N = 8$ one has 2520 unique cycle graphs, each with 128 unique edge configurations, as explained in Sec. IV. Hence, there exist in total $128 \times 2520 = 322\,560$ edge configurations which yield a complete set of observables. However, the resulting sets are not all linearly independent.

The whole algorithm was implemented in *Mathematica* [56], but can just as easily be implemented in other languages such as JULIA [57]. Filtering out the redundant sets, one is left with 5964 unique sets of observables. The length of the sets varies between the topologies as well as between different edge configurations. To be exact, it varies between a total of 24 and 40 observables.

Without loss of generality, the further analysis focuses on the 392 distinct sets with 24 observables. A numerical analysis was performed which showed that these sets are indeed complete. The applied algorithm is described in Appendix.

Further characteristics of the minimal sets according to Moravcsik involve the following:

(i) Each set inhibits at least five triple polarization observables.
(ii) The sets are constructed from four or five different shape classes.

However, these sets are slightly overcomplete since each observable depends on more than one bilinear product. According to current knowledge [11,13], a truly minimal complete set consists of $2N$ observables. Thus the task remains to reduce the slightly overcomplete sets by eight observables while retaining completeness.

## VII. REDUCTION TO MINIMAL SETS OF $2N$

### A. Numerical calculation

The smallest complete sets, which emerge from the modified version of Moravcsik's theorem, have a length of 24 (for $N = 8$). Eight of these observables cannot be omitted, namely, the group I observables, as discussed in Sec. IV. From the remaining 16 observables one constructs all possible subsets containing eight observables, which amounts to $\binom{16}{8} = 12\,870$ distinct sets.

In principle this is done for all sets with a length of 24, leading to just over five million minimal, complete set candidates. This number can be further reduced by $\approx$0.7%, by noting that sets containing only one or two distinct observable groups (apart from group I) do not correspond to a connected graph and thus do not form a complete set. There are also a few cases in which three distinct observable groups (apart from group I) are not able to form a connected graph, i.e., {II,III,IV}, {II,V,VI}, {II,VII,VIII}, {III,V,VII}, {III,VI,VIII}, {IV,V,VIII}, and {IV,VI,VII}.

However, due to the enormous number of possible candidate sets, just a minor excerpt was analyzed for this paper. The sets of interest are checked for completeness via a numerical analysis. The employed algorithm is described in Appendix.

So far, 4185 unique truly minimal sets of length $2N = 16$ have been found. There are two major differences to the slightly overcomplete sets with 24 observables. On the one hand, all sets found are constructed from exactly four different shape classes. On the other hand, truly minimal complete sets exist with a minimal number of triple polarization observables, namely only $\mathcal{O}^{I}_{4} = \mathcal{O}^{\odot}_{\mathrm{yy}'}$ from group I. Hence, this observable has to be included in every set as explained in Sec. II.

TABLE IV. A collection of polarization observable measurements for two pseudoscalar meson photoproduction. Hint: We do not distinguish the datasets according to the kinematical variable and whether is differential or total cross-section data. Further details can be found in the cited references.

| Observable | Energy range $E_\gamma^{lab}$ | Facility | Reference | Year of publication |
|---|---|---|---|---|
| | | $\gamma p \to p\pi^0\pi^0$ | | |
| $I_0$ | 309–792 MeV | TAPS at MAMI | Härter *et al.* [20] | 1997 |
| $I_0$ | 309–820 MeV | TAPS at MAMI | Wolf *et al.* [21] | 2000 |
| $I_0$ | 200–820 MeV | TAPS at MAMI | Kleber *et al.* [22] | 2000 |
| $I_0$ | 300–425 MeV | TAPS at MAMI | Kotulla *et al.* [23] | 2004 |
| $I_0$ | 309–800 MeV | CB/TAPS at MAMI | Zehr *et al.* [24] | 2012 |
| $I_0$ | 309–1400 MeV | CB/TAPS at MAMI | Kashevarov *et al.* [25] | 2012 |
| $I_0$ | 432–1374 MeV | CB/TAPS at MAMI | Dieterle *et al.* [26] | 2015 |
| $I_0$ | 400–800 MeV | DAPHNE at MAMI | Braghieri *et al.* [27] | 1995 |
| $I_0$ | 400–800 MeV | DAPHNE at MAMI | Ahrens *et al.* [28] | 2005 |
| $I_0$ | 309–820 MeV | TAPS at MAMI, CB at ELSA | Sarantsev *et al.* [29] | 2008 |
| $I_0$ | 400–1300 MeV | CB at ELSA | Thoma *et al.* [30] | 2008 |
| $I_0$ | ≈750–2500 MeV | CBELSA/TAPS at ELSA | Thiel *et al.* [31] | 2015 |
| $I_0$, $\Sigma$ | 600–2500 MeV | CB/TAPS at ELSA | Sokhoyan *et al.* [1] | 2015 |
| $I_0$, $\Sigma$ | 650–1450 MeV | GRAAL | Assafiri *et al.* [32] | 2003 |
| $\Sigma$ | 650–1450 MeV | CB at ELSA | Thoma *et al.* [30] | 2008 |
| $I^\odot$ | 560–810 MeV | CB/TAPS at MAMI | Krambrich *et al.* [33] | 2009 |
| $I^\odot$ | ≈600–1400 MeV | CB/TAPS at MAMI | Oberle *et al.* [34] | 2013 |
| $I^\odot$ | 550–820 MeV | CB/TAPS at MAMI | Zehr *et al.* [24] | 2012 |
| $E$, $\sigma_{1/2}$, $\sigma_{3/2}$ | ≈431–1455 MeV | CB/TAPS at MAMI | Dieterle *et al.* [35] | 2020 |
| $P_x$, $P_y$, $T$, $H$, $P$ | 650–2600 MeV | CBELSA/TAPS at ELSA | Seifen *et al.* [14] | 2020 |
| $I^c$, $I^s$ | 970–1650 MeV | CB/TAPS at ELSA | Sokhoyan *et al.* [1] | 2015 |
| | | $\gamma p \to p\pi^+\pi^-$ | | |
| $I_0$ | 400–800 MeV | DAPHNE at MAMI | Braghieri *et al.* [27] | 1995 |
| $I_0$ | 400–800 MeV | DAPHNE at MAMI | Ahrens *et al.* [36] | 2007 |
| $I_0$ | 370–940 MeV | LNF | Carbonara *et al.* [37] | 1976 |
| $I_0$ | 800–1100 MeV | NKS at LNS | Hirose *et al.* [38] | 2009 |
| $I_0$ | 500–4800 MeV | CEA | Crouch *et al.* [39] | 1964 |
| $I_0$ | ≈560–2560 MeV | SAPHIR at ELSA | Wu *et al.* [40] | 2005 |
| $I_0$ | ≈895–1663 MeV | CLAS at JLAB | Golovatch *et al.* [41] | 2019 |
| $I^\odot$ | 575–815 MeV | CB/TAPS at MAMI | Krambrich *et al.* [33] | 2009 |
| $I^\odot$ | 502–2350 MeV | CLAS at JLAB | Strauch *et al.* [42] | 2005 |
| $I^\odot$ | 1100–5400 MeV | CLAS at JLAB | Badui *et al.* [43] | 2016 |
| | | $\gamma p \to p\pi^0\eta$ | | |
| $I_0$ | ≈930–2500 MeV | CB/TAPS at ELSA | Gutz *et al.* [15] | 2014 |
| $I_0$ | ≈1070–2860 MeV | CB at ELSA | Horn *et al.* [44] | 2008 |
| $I_0$ | 950–1400 MeV | CB/TAPS at MAMI | Kashevarov *et al.* [45] | 2009 |
| $I_0$ | 1000–1150 MeV | GeV-$\gamma$ at LNS | Nakabayashi *et al.* [46] | 2006 |
| $I_0$, $\Sigma$ | ≈930–1500 MeV | GRAAL | Ajaka *et al.* [47] | 2008 |
| $\Sigma$ | 970–1650 MeV | CBELSA/TAPS at ELSA | Gutz *et al.* [48] | 2008 |
| $\Sigma$ | ≈1070–1550 MeV | CB/TAPS at ELSA | Gutz *et al.* [15] | 2014 |
| $I^c$, $I^s$ | 970–1650 MeV | CBELSA/TAPS at ELSA | Gutz *et al.* [49] | 2010 |
| $I^c$, $I^s$ | ≈1081–1550 MeV | CB/TAPS at ELSA | Gutz *et al.* [15] | 2014 |
| | | $\gamma p \to n\pi^+\pi^0$ | | |
| $I_0$ | 300–820 MeV | TAPS at MAMI | Langgärtner *et al.* [50] | 2001 |
| $I_0$ | ≈325–800 MeV | CB/TAPS at MAMI | Zehr *et al.* [24] | 2012 |
| $I_0$ | 400–800 MeV | DAPHNE at MAMI | Braghieri *et al.* [27] | 1995 |
| $I_0$ | 400–800 MeV | DAPHNE at MAMI | Ahrens *et al.* [51] | 2003 |
| $I^\odot$ | 520–820 MeV | CB/TAPS at MAMI | Krambrich *et al.* [33] | 2009 |
| $I^\odot$ | ≈550–820 MeV | CB/TAPS at MAMI | Zehr *et al.* [24] | 2012 |
| | | $\gamma n \to n\pi^0\pi^0$ | | |
| $I^\odot$ | ≈600–1400 MeV | CB/TAPS at MAMI | Oberle *et al.* [34] | 2013 |
| $I_0$, $\Sigma$ | ≈600–1500 MeV | GRAAL | Ajaka *et al.* [52] | 2007 |
| $I_0$ | ≈430–1371 MeV | CB/TAPS at MAMI | Dieterle *et al.* [26] | 2015 |

TABLE IV. *(Continued.)*

| Observable | Energy range $E_\gamma^{lab}$ | Facility | Reference | Year of publication |
|---|---|---|---|---|
| | | $\gamma n \to p\pi^-\pi^0$ | | |
| $I_0$ | ≈370–940 MeV | LNF | Carbonara *et al.* [37] | 1976 |
| $I_0$ | ≈450–800 MeV | DAPHNE at MAMI | Zabrodin *et al.* [53] | 1997 |
| $I_0$ | ≈500–800 MeV | DAPHNE at MAMI | Zabrodin *et al.* [54] | 1999 |
| | | $\gamma n \to n\pi^+\pi^-$ | | |
| $I_0$ | 370–940 MeV | LNF | Carbonara *et al.* [37] | 1976 |
| | | $\gamma p \to pK^+K^-$ | | |
| $I_0$ | 3000–3800 MeV | CLAS at JLAB | Lombardo *et al.* [55] | 2018 |
| $I^\odot$ | 1100–5400 MeV | CLAS at JLAB | Badui *et al.* [43] | 2016 |

In total, 69 sets with only one triple polarization observable have been found. All of them are shown in Table V. Hence, these are the most promising ones when it comes to the experimental verification of Moravcsik's theorem.

### B. Algebraic phase-fixing method

In the following, the phase-fixing approach first developed by Nakayama in a treatment of single-meson photoproduction (i.e., for $N = 4$ amplitudes) [8] is adapted to two meson photoproduction. Thus it is possible, although tedious, to derive minimal complete sets of observables with algebraic methods.

Since the full mathematical derivation is quite extensive, all mathematical details are given in the Supplemental Material [58].

One starts by combining, i.e., adding or subtracting, the observables within one shape-class in such a way that the result only depends on two relative phases. By doing this, a "decoupled" shape-class is formed. See also Table VI.

In that way, one establishes a mathematical similarity with the shape-classes in single-meson photoproduction [8,13]. For shape-class II this would be

$$\text{IIa} : \mathcal{O}^{\text{II}}_{\text{s1}} + \mathcal{O}^{\text{II}}_{\text{s2}}, \mathcal{O}^{\text{II}}_{\text{s3}} + \mathcal{O}^{\text{II}}_{\text{s4}}, \mathcal{O}^{\text{II}}_{\text{c1}} + \mathcal{O}^{\text{II}}_{\text{c2}}, \mathcal{O}^{\text{II}}_{\text{c3}} + \mathcal{O}^{\text{II}}_{\text{c4}}, \quad (16)$$

$$\text{IIb} : \mathcal{O}^{\text{II}}_{\text{s1}} - \mathcal{O}^{\text{II}}_{\text{s2}}, \mathcal{O}^{\text{II}}_{\text{s3}} - \mathcal{O}^{\text{II}}_{\text{s4}}, \mathcal{O}^{\text{II}}_{\text{c1}} - \mathcal{O}^{\text{II}}_{\text{c2}}, \mathcal{O}^{\text{II}}_{\text{c3}} - \mathcal{O}^{\text{II}}_{\text{c4}}. \quad (17)$$

The algebraic approach shown here works out only in case the observables are selected from very particular combinations of four decoupled shape-classes.

More precisely, it has to be possible to establish a "consistency relation" [cf. Eq. 1] among the relative phases belonging to all the involved decoupled shape-classes. A necessary and sufficient condition for this can be formulated in terms of the graph constructed from the relative phases (cf. Sec. II): the latter graph has to be a cycle graph.

There exist 40 possible combinations of four decoupled shape classes fulfilling these requirements and which have the following general form:

$$\{\text{Xa}, \text{Xb}, \text{Y}, \text{Z}\}. \quad (18)$$

Two examples are shown in Fig. 3, and a complete list can be found in the Supplemental Material [58]. The following derivation holds for all combinations of shape-classes of the form given in Eq. (18).

The following discussion focuses on the example case

$$\{\text{IIa}, \text{IIb}, \text{VIb}, \text{VIIIa}\}. \quad (19)$$

For the remaining 39 cases, the derivation proceeds analogously.

For the example case (19), the consistency relation reads (cf. Table VI)

$$\underbrace{\phi_{13} + \phi_{24}}_{\text{IIa}} + \underbrace{\phi_{57} + \phi_{68}}_{\text{IIb}} = \underbrace{\phi_{18} + \phi_{27}}_{\text{VIIIa}} - \underbrace{\phi_{35} - \phi_{46}}_{\text{VIb}}. \quad (20)$$

According to Nakayama [8], the "phase-fixing" procedure starts by picking a particular combination of observables from the considered combination of shape-classes, i.e., from Eq. 19. In general, one picks two observables from shape-class Xa, two from Xb and one observable each from two different shape-classes selected from the 12 remaining. For the case at hand, these are two observables from shape-class IIa, two from IIb, one from VIb, as well as one from VIIIa. For any selection of observables which has this pattern, one has to work out the remaining discrete phase-ambiguities which exist for the associated relative phases. For each combination of possible discrete ambiguities, the consistency relation (20) then has to be evaluated. In case the consistency relations of such a combination are all linearly independent [8,13], the considered set of observables is complete.

The way forward is analogous to that done in Ref. [8]. A detailed description on how to determine all possible discrete

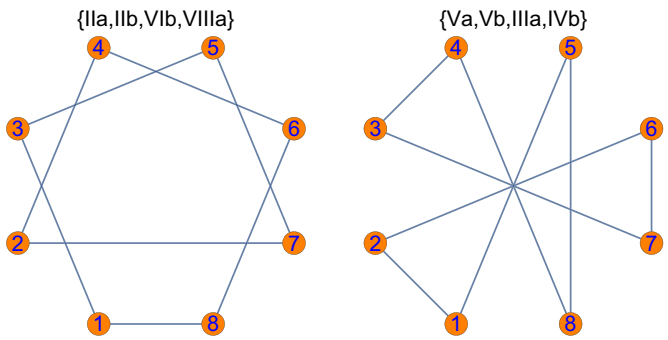


FIG. 3. Examples are shown for graph topologies which imply the possibility for a consistency relation (cf. the relative phases listed in Table VI).

TABLE V. Truly minimal sets consisting of $2N = 16$ observables with the minimal number of triple polarization observables, i.e., just $\mathcal{O}^I_4 = \mathcal{O}^{\odot}_{yy'}$. Group I observables $\{I^{\odot}, P_y, P_{y'}, \mathcal{O}^{\odot}_{yy'}, \mathcal{O}_{yy'}, P^{\odot}_{y'}, P^{\odot}_{y}, I_0\}$ are not explicitly shown because they are common to all complete sets. The notation used is analogous to that of Roberts and Oed [5].

| | | | | | | | | |
|---|---|---|---|---|---|---|---|---|
| (1) | $P_z$ | $P_{x'}$ | $P_{z'}$ | $P^s_x$ | $P^c_z$ | $P^{\odot}_z$ | $P^{\odot}_{x'}$ | $P^{\odot}_{z'}$ |
| (2) | $P_z$ | $P^s_x$ | $P^c_z$ | $P^{\odot}_z$ | $P^{\odot}_{x'}$ | $P^{\odot}_{z'}$ | $\mathcal{O}_{yx'}$ | $\mathcal{O}_{yz'}$ |
| (3) | $P_z$ | $P^s_x$ | $P^c_z$ | $P^{\odot}_{x'}$ | $P^{\odot}_{z'}$ | $\mathcal{O}_{yx'}$ | $\mathcal{O}_{yz'}$ | $\mathcal{O}_{zy'}$ |
| (4) | $P_{x'}$ | $P_{z'}$ | $P^s_x$ | $P^c_z$ | $P^{\odot}_z$ | $P^{\odot}_{x'}$ | $P^{\odot}_{z'}$ | $\mathcal{O}_{zy'}$ |
| (5) | $P^s_x$ | $P^c_z$ | $P^{\odot}_z$ | $P^{\odot}_{x'}$ | $P^{\odot}_{z'}$ | $\mathcal{O}_{yx'}$ | $\mathcal{O}_{yz'}$ | $\mathcal{O}_{zy'}$ |
| (6) | $P_x$ | $P_z$ | $P_{z'}$ | $P^s_x$ | $P^{\odot}_x$ | $P^c_z$ | $P^{\odot}_z$ | $P^{\odot}_{z'}$ |
| (7) | $P_x$ | $P_z$ | $P_{z'}$ | $P^s_x$ | $P^c_z$ | $P^{\odot}_{z'}$ | $\mathcal{O}_{xy'}$ | $\mathcal{O}_{zy'}$ |
| (8) | $P_x$ | $P_z$ | $P_{z'}$ | $P^s_x$ | $P^c_z$ | $\mathcal{O}_{xy'}$ | $\mathcal{O}_{yz'}$ | $\mathcal{O}_{zy'}$ |
| (9) | $P_{z'}$ | $P^s_x$ | $P^{\odot}_x$ | $P^c_z$ | $P^{\odot}_z$ | $P^{\odot}_{z'}$ | $\mathcal{O}_{xy'}$ | $\mathcal{O}_{zy'}$ |
| (10) | $P_{z'}$ | $P^s_x$ | $P^{\odot}_x$ | $P^c_z$ | $P^{\odot}_z$ | $\mathcal{O}_{xy'}$ | $\mathcal{O}_{yz'}$ | $\mathcal{O}_{zy'}$ |
| (11) | $P^s_x$ | $P^{\odot}_x$ | $P^c_z$ | $P^{\odot}_z$ | $P^{\odot}_{z'}$ | $\mathcal{O}_{xy'}$ | $\mathcal{O}_{yz'}$ | $\mathcal{O}_{zy'}$ |
| (12) | $P_z$ | $P^c_x$ | $P^s_x$ | $P^c_z$ | $P^s_z$ | $P^{\odot}_z$ | $P^{\odot}_{z'}$ | $\mathcal{O}_{yz'}$ |
| (13) | $P_z$ | $P^c_x$ | $P^s_x$ | $P^c_z$ | $P^s_z$ | $P^{\odot}_{z'}$ | $\mathcal{O}_{yz'}$ | $\mathcal{O}_{zy'}$ |
| (14) | $P^c_x$ | $P^s_x$ | $P^c_z$ | $P^s_z$ | $P^{\odot}_z$ | $P^{\odot}_{z'}$ | $\mathcal{O}_{yz'}$ | $\mathcal{O}_{zy'}$ |
| (15) | $P_x$ | $P_z$ | $P_{x'}$ | $P^s_x$ | $P^{\odot}_x$ | $P^c_z$ | $P^{\odot}_z$ | $P^{\odot}_{x'}$ |
| (16) | $P_x$ | $P_z$ | $P_{x'}$ | $P^s_x$ | $P^c_z$ | $P^{\odot}_{x'}$ | $\mathcal{O}_{xy'}$ | $\mathcal{O}_{zy'}$ |
| (17) | $P_x$ | $P_z$ | $P_{x'}$ | $P^s_x$ | $P^c_z$ | $\mathcal{O}_{xy'}$ | $\mathcal{O}_{yx'}$ | $\mathcal{O}_{zy'}$ |
| (18) | $P_{x'}$ | $P^s_x$ | $P^{\odot}_x$ | $P^c_z$ | $P^{\odot}_z$ | $P^{\odot}_{x'}$ | $\mathcal{O}_{xy'}$ | $\mathcal{O}_{zy'}$ |
| (19) | $P_{x'}$ | $P^s_x$ | $P^{\odot}_x$ | $P^c_z$ | $P^{\odot}_z$ | $\mathcal{O}_{xy'}$ | $\mathcal{O}_{yx'}$ | $\mathcal{O}_{zy'}$ |
| (20) | $P^s_x$ | $P^{\odot}_x$ | $P^c_z$ | $P^{\odot}_z$ | $P^{\odot}_{x'}$ | $\mathcal{O}_{xy'}$ | $\mathcal{O}_{yx'}$ | $\mathcal{O}_{zy'}$ |
| (21) | $P_z$ | $P_{x'}$ | $P_{z'}$ | $P^c_x$ | $P^s_z$ | $P^{\odot}_z$ | $P^{\odot}_{x'}$ | $P^{\odot}_{z'}$ |
| (22) | $P_z$ | $P^c_x$ | $P^s_z$ | $P^{\odot}_z$ | $P^{\odot}_{x'}$ | $P^{\odot}_{z'}$ | $\mathcal{O}_{yx'}$ | $\mathcal{O}_{yz'}$ |
| (23) | $P_z$ | $P_{x'}$ | $P_{z'}$ | $P^c_x$ | $P^s_z$ | $\mathcal{O}_{yx'}$ | $\mathcal{O}_{yz'}$ | $\mathcal{O}_{zy'}$ |
| (24) | $P_z$ | $P^c_x$ | $P^s_z$ | $P^{\odot}_{x'}$ | $P^{\odot}_{z'}$ | $\mathcal{O}_{yx'}$ | $\mathcal{O}_{yz'}$ | $\mathcal{O}_{zy'}$ |
| (25) | $P_{x'}$ | $P_{z'}$ | $P^c_x$ | $P^s_z$ | $P^{\odot}_z$ | $P^{\odot}_{x'}$ | $P^{\odot}_{z'}$ | $\mathcal{O}_{zy'}$ |
| (26) | $P^c_x$ | $P^s_z$ | $P^{\odot}_z$ | $P^{\odot}_{x'}$ | $P^{\odot}_{z'}$ | $\mathcal{O}_{yx'}$ | $\mathcal{O}_{yz'}$ | $\mathcal{O}_{zy'}$ |
| (27) | $P_z$ | $P^c_x$ | $P^s_x$ | $P^c_z$ | $P^s_z$ | $P^{\odot}_z$ | $P^{\odot}_{x'}$ | $\mathcal{O}_{yx'}$ |
| (28) | $P_z$ | $P^c_x$ | $P^s_x$ | $P^c_z$ | $P^s_z$ | $P^{\odot}_{x'}$ | $\mathcal{O}_{yx'}$ | $\mathcal{O}_{zy'}$ |
| (29) | $P^c_x$ | $P^s_x$ | $P^c_z$ | $P^s_z$ | $P^{\odot}_z$ | $P^{\odot}_{x'}$ | $\mathcal{O}_{yx'}$ | $\mathcal{O}_{zy'}$ |
| (30) | $P_x$ | $P_z$ | $P_{z'}$ | $P^c_x$ | $P^{\odot}_x$ | $P^s_z$ | $P^{\odot}_z$ | $P^{\odot}_{z'}$ |
| (31) | $P_x$ | $P_z$ | $P_{z'}$ | $P^c_x$ | $P^s_z$ | $P^{\odot}_{z'}$ | $\mathcal{O}_{xy'}$ | $\mathcal{O}_{zy'}$ |
| (32) | $P_x$ | $P_z$ | $P_{z'}$ | $P^c_x$ | $P^s_z$ | $\mathcal{O}_{xy'}$ | $\mathcal{O}_{yz'}$ | $\mathcal{O}_{zy'}$ |
| (33) | $P_{z'}$ | $P^c_x$ | $P^{\odot}_x$ | $P^s_z$ | $P^{\odot}_z$ | $P^{\odot}_{z'}$ | $\mathcal{O}_{xy'}$ | $\mathcal{O}_{zy'}$ |
| (34) | $P_{z'}$ | $P^c_x$ | $P^{\odot}_x$ | $P^s_z$ | $P^{\odot}_z$ | $\mathcal{O}_{xy'}$ | $\mathcal{O}_{yz'}$ | $\mathcal{O}_{zy'}$ |
| (35) | $P^c_x$ | $P^{\odot}_x$ | $P^s_z$ | $P^{\odot}_z$ | $P^{\odot}_{z'}$ | $\mathcal{O}_{xy'}$ | $\mathcal{O}_{yz'}$ | $\mathcal{O}_{zy'}$ |
| (36) | $P_x$ | $P_{x'}$ | $P_{z'}$ | $P^s_x$ | $P^{\odot}_x$ | $P^c_z$ | $P^{\odot}_{x'}$ | $P^{\odot}_{z'}$ |
| (37) | $P_x$ | $P^s_x$ | $P^{\odot}_x$ | $P^c_z$ | $P^{\odot}_{x'}$ | $P^{\odot}_{z'}$ | $\mathcal{O}_{yx'}$ | $\mathcal{O}_{yz'}$ |
| (38) | $P_x$ | $P^s_x$ | $P^c_z$ | $P^{\odot}_{x'}$ | $P^{\odot}_{z'}$ | $\mathcal{O}_{xy'}$ | $\mathcal{O}_{yx'}$ | $\mathcal{O}_{yz'}$ |
| (39) | $P_{x'}$ | $P_{z'}$ | $P^s_x$ | $P^{\odot}_x$ | $P^c_z$ | $P^{\odot}_{x'}$ | $P^{\odot}_{z'}$ | $\mathcal{O}_{xy'}$ |
| (40) | $P^s_x$ | $P^{\odot}_x$ | $P^c_z$ | $P^{\odot}_{x'}$ | $P^{\odot}_{z'}$ | $\mathcal{O}_{xy'}$ | $\mathcal{O}_{yx'}$ | $\mathcal{O}_{yz'}$ |
| (41) | $P_x$ | $P_z$ | $P_{x'}$ | $P^c_x$ | $P^{\odot}_x$ | $P^s_z$ | $P^{\odot}_z$ | $P^{\odot}_{x'}$ |
| (42) | $P_x$ | $P_z$ | $P_{x'}$ | $P^c_x$ | $P^s_z$ | $P^{\odot}_{x'}$ | $\mathcal{O}_{xy'}$ | $\mathcal{O}_{zy'}$ |
| (43) | $P_x$ | $P_z$ | $P_{x'}$ | $P^c_x$ | $P^s_z$ | $\mathcal{O}_{xy'}$ | $\mathcal{O}_{yx'}$ | $\mathcal{O}_{zy'}$ |
| (44) | $P_{x'}$ | $P^c_x$ | $P^{\odot}_x$ | $P^s_z$ | $P^{\odot}_z$ | $P^{\odot}_{x'}$ | $\mathcal{O}_{xy'}$ | $\mathcal{O}_{zy'}$ |
| (45) | $P_{x'}$ | $P^c_x$ | $P^{\odot}_x$ | $P^s_z$ | $P^{\odot}_z$ | $\mathcal{O}_{xy'}$ | $\mathcal{O}_{yx'}$ | $\mathcal{O}_{zy'}$ |
| (46) | $P^c_x$ | $P^{\odot}_x$ | $P^s_z$ | $P^{\odot}_z$ | $P^{\odot}_{x'}$ | $\mathcal{O}_{xy'}$ | $\mathcal{O}_{yx'}$ | $\mathcal{O}_{zy'}$ |
| (47) | $P_x$ | $P^c_x$ | $P^s_x$ | $P^{\odot}_x$ | $P^c_z$ | $P^s_z$ | $P^{\odot}_{z'}$ | $\mathcal{O}_{yz'}$ |
| (48) | $P_x$ | $P^c_x$ | $P^s_x$ | $P^c_z$ | $P^s_z$ | $P^{\odot}_{z'}$ | $\mathcal{O}_{xy'}$ | $\mathcal{O}_{yz'}$ |
| (49) | $P^c_x$ | $P^s_x$ | $P^{\odot}_x$ | $P^c_z$ | $P^s_z$ | $P^{\odot}_{z'}$ | $\mathcal{O}_{xy'}$ | $\mathcal{O}_{yz'}$ |
| (50) | $P_x$ | $P_z$ | $P^{\odot}_x$ | $P^{\odot}_z$ | $P^c_{x'}$ | $P^s_{z'}$ | $\mathcal{O}_{xz'}$ | $\mathcal{O}_{zx'}$ |
| (51) | $P_x$ | $P_z$ | $P^c_{x'}$ | $P^s_{z'}$ | $\mathcal{O}_{xy'}$ | $\mathcal{O}_{xz'}$ | $\mathcal{O}_{zx'}$ | $\mathcal{O}_{zy'}$ |
| (52) | $P^{\odot}_x$ | $P^{\odot}_z$ | $P^c_{x'}$ | $P^s_{z'}$ | $\mathcal{O}_{xy'}$ | $\mathcal{O}_{xz'}$ | $\mathcal{O}_{zx'}$ | $\mathcal{O}_{zy'}$ |
| (53) | $I^c$ | $P_x$ | $P^{\odot}_x$ | $P^c_y$ | $\mathcal{O}_{xx'}$ | $\mathcal{O}_{xz'}$ | $\mathcal{O}_{zx'}$ | $\mathcal{O}_{zz'}$ |
| (54) | $I^c$ | $P_x$ | $P^{\odot}_x$ | $P^c_{y'}$ | $\mathcal{O}_{xx'}$ | $\mathcal{O}_{xz'}$ | $\mathcal{O}_{zx'}$ | $\mathcal{O}_{zz'}$ |
| (55) | $P_x$ | $P^{\odot}_x$ | $P^c_y$ | $P^c_{y'}$ | $\mathcal{O}_{xx'}$ | $\mathcal{O}_{xz'}$ | $\mathcal{O}_{zx'}$ | $\mathcal{O}_{zz'}$ |
| (56) | $I^c$ | $P_x$ | $P^c_y$ | $\mathcal{O}_{xx'}$ | $\mathcal{O}_{xy'}$ | $\mathcal{O}_{xz'}$ | $\mathcal{O}_{zx'}$ | $\mathcal{O}_{zz'}$ |
| (57) | $I^c$ | $P_x$ | $P^c_{y'}$ | $\mathcal{O}_{xx'}$ | $\mathcal{O}_{xy'}$ | $\mathcal{O}_{xz'}$ | $\mathcal{O}_{zx'}$ | $\mathcal{O}_{zz'}$ |
| (58) | $P_x$ | $P^c_y$ | $P^c_{y'}$ | $\mathcal{O}_{xx'}$ | $\mathcal{O}_{xy'}$ | $\mathcal{O}_{xz'}$ | $\mathcal{O}_{zx'}$ | $\mathcal{O}_{zz'}$ |
| (59) | $I^c$ | $P^{\odot}_x$ | $P^c_y$ | $\mathcal{O}_{xx'}$ | $\mathcal{O}_{xy'}$ | $\mathcal{O}_{xz'}$ | $\mathcal{O}_{zx'}$ | $\mathcal{O}_{zz'}$ |
| (60) | $P^{\odot}_x$ | $P^c_y$ | $P^c_{y'}$ | $\mathcal{O}_{xx'}$ | $\mathcal{O}_{xy'}$ | $\mathcal{O}_{xz'}$ | $\mathcal{O}_{zx'}$ | $\mathcal{O}_{zz'}$ |
| (61) | $I^c$ | $P_x$ | $P^{\odot}_x$ | $P^c_{x'}$ | $P^s_{x'}$ | $P^c_{y'}$ | $P^c_{z'}$ | $P^s_{z'}$ |
| (62) | $P_x$ | $P^{\odot}_x$ | $P^c_y$ | $P^c_{x'}$ | $P^s_{x'}$ | $P^c_{y'}$ | $P^c_{z'}$ | $P^s_{z'}$ |
| (63) | $I^c$ | $P_x$ | $P^c_y$ | $P^c_{x'}$ | $P^s_{x'}$ | $P^c_{z'}$ | $P^s_{z'}$ | $\mathcal{O}_{xy'}$ |
| (64) | $I^c$ | $P^{\odot}_x$ | $P^c_y$ | $P^c_{x'}$ | $P^s_{x'}$ | $P^c_{z'}$ | $P^s_{z'}$ | $\mathcal{O}_{xy'}$ |
| (65) | $I^c$ | $P^{\odot}_x$ | $P^c_{x'}$ | $P^s_{x'}$ | $P^c_{y'}$ | $P^c_{z'}$ | $P^s_{z'}$ | $\mathcal{O}_{xy'}$ |
| (66) | $P^{\odot}_x$ | $P^c_y$ | $P^c_{x'}$ | $P^s_{x'}$ | $P^c_{y'}$ | $P^c_{z'}$ | $P^s_{z'}$ | $\mathcal{O}_{xy'}$ |
| (67) | $I^c$ | $I^s$ | $P^c_y$ | $P^s_y$ | $P^c_{x'}$ | $P^s_{z'}$ | $\mathcal{O}_{xz'}$ | $\mathcal{O}_{zx'}$ |
| (68) | $I^c$ | $I^s$ | $P^c_{x'}$ | $P^c_{y'}$ | $P^s_{y'}$ | $P^s_{z'}$ | $\mathcal{O}_{xz'}$ | $\mathcal{O}_{zx'}$ |
| (69) | $P^c_y$ | $P^s_y$ | $P^c_{x'}$ | $P^c_{y'}$ | $P^s_{y'}$ | $P^s_{z'}$ | $\mathcal{O}_{xz'}$ | $\mathcal{O}_{zx'}$ |

TABLE V. *(Continued.)*

ambiguities and determining whether a set of consistency relations is linear independent can be found in the Supplemental Material [58].

The result for the discussed example can be found in Table VII. The results shown come only from considering the left side of Eq. 20. In general, the determination of the discrete ambiguities of the left side is easier than that of the right side. So, theoretically, even more combinations are possible. Unfortunately the discussed example (19) does not yield minimal complete sets with only one triple polarization observable. Other combination of shape classes may yield the desired result where the only triple polarization observable is contained in the diagonal shape class.

TABLE VI. The 14 decoupled shape-classes IIa, IIb, ..., VIIIa, VIIIb are listed together with their corresponding pairs of relative phases.

| | |
|---|---|
| IIa $\longrightarrow \{\phi_{13}, \phi_{24}\}$ | IIb $\longrightarrow \{\phi_{57}, \phi_{68}\}$ |
| IIIa $\longrightarrow \{\phi_{12}, \phi_{34}\}$ | IIIb $\longrightarrow \{\phi_{56}, \phi_{78}\}$ |
| IVa $\longrightarrow \{\phi_{14}, \phi_{23}\}$ | IVb $\longrightarrow \{\phi_{58}, \phi_{67}\}$ |
| Va $\longrightarrow \{\phi_{15}, \phi_{26}\}$ | Vb $\longrightarrow \{\phi_{37}, \phi_{48}\}$ |
| VIa $\longrightarrow \{\phi_{17}, \phi_{28}\}$ | VIb $\longrightarrow \{\phi_{35}, \phi_{46}\}$ |
| VIIa $\longrightarrow \{\phi_{16}, \phi_{25}\}$ | VIIb $\longrightarrow \{\phi_{38}, \phi_{47}\}$ |
| VIIIa $\longrightarrow \{\phi_{18}, \phi_{27}\}$ | VIIIb $\longrightarrow \{\phi_{36}, \phi_{45}\}$ |

TABLE VII. Truly minimal complete sets, consisting of $2N = 16$ observables, obtained for the example discussed in Sec. VII B. The group I observables $\{I^{\odot}, P_y, P_{y'}, \mathcal{O}^{\odot}_{yy'}, \mathcal{O}_{yy'}, P^{\odot}_{y'}, P^{\odot}_{y}, I_0\}$ are not explicitly shown because they are common to all complete sets. The notation used is analogous to that used by Roberts and Oed [5].

| | | | | | | | |
|---|---|---|---|---|---|---|---|
| $P_x$ | $P_z$ | $P^{\odot}_x$ | $P^{\odot}_z$ | $P^{s}_z$ | $P^{c}_x$ | $\mathcal{O}^{s}_{zz'}$ | $\mathcal{O}^{c}_{xz'}$ |
| $P_x$ | $P_z$ | $P^{\odot}_x$ | $P^{\odot}_z$ | $P^{s}_z$ | $P^{c}_x$ | $\mathcal{O}^{c}_{zx'}$ | $\mathcal{O}^{s}_{xx'}$ |
| $P_x$ | $P_z$ | $P^{\odot}_x$ | $P^{\odot}_z$ | $P^{s}_z$ | $P^{c}_x$ | $\mathcal{O}^{c}_{zz'}$ | $\mathcal{O}^{s}_{xz'}$ |
| $P_x$ | $P_z$ | $P^{\odot}_x$ | $P^{\odot}_z$ | $P^{s}_z$ | $P^{c}_x$ | $\mathcal{O}^{s}_{zx'}$ | $\mathcal{O}^{c}_{xx'}$ |
| $P_x$ | $P_z$ | $P^{\odot}_x$ | $P^{\odot}_z$ | $P^{c}_z$ | $P^{s}_x$ | $\mathcal{O}^{s}_{zz'}$ | $\mathcal{O}^{c}_{xz'}$ |
| $P_x$ | $P_z$ | $P^{\odot}_x$ | $P^{\odot}_z$ | $P^{c}_z$ | $P^{s}_x$ | $\mathcal{O}^{c}_{zx'}$ | $\mathcal{O}^{s}_{xx'}$ |
| $P_x$ | $P_z$ | $P^{\odot}_x$ | $P^{\odot}_z$ | $P^{c}_z$ | $P^{s}_x$ | $\mathcal{O}^{c}_{zz'}$ | $\mathcal{O}^{s}_{xz'}$ |
| $P_x$ | $P_z$ | $P^{\odot}_x$ | $P^{\odot}_z$ | $P^{c}_z$ | $P^{s}_x$ | $\mathcal{O}^{s}_{zx'}$ | $\mathcal{O}^{c}_{xx'}$ |
| $P_x$ | $P_z$ | $P^{\odot}_x$ | $P^{\odot}_z$ | $\mathcal{O}^{s}_{zy'}$ | $\mathcal{O}^{c}_{xy'}$ | $\mathcal{O}^{s}_{zz'}$ | $\mathcal{O}^{c}_{xz'}$ |
| $P_x$ | $P_z$ | $P^{\odot}_x$ | $P^{\odot}_z$ | $\mathcal{O}^{s}_{zy'}$ | $\mathcal{O}^{c}_{xy'}$ | $\mathcal{O}^{c}_{zx'}$ | $\mathcal{O}^{s}_{xx'}$ |
| $P_x$ | $P_z$ | $P^{\odot}_x$ | $P^{\odot}_z$ | $\mathcal{O}^{s}_{zy'}$ | $\mathcal{O}^{c}_{xy'}$ | $\mathcal{O}^{c}_{zz'}$ | $\mathcal{O}^{s}_{xz'}$ |
| $P_x$ | $P_z$ | $P^{\odot}_x$ | $P^{\odot}_z$ | $\mathcal{O}^{s}_{zy'}$ | $\mathcal{O}^{s}_{xy'}$ | $\mathcal{O}^{s}_{zx'}$ | $\mathcal{O}^{c}_{xx'}$ |
| $P_x$ | $P_z$ | $P^{\odot}_x$ | $P^{\odot}_z$ | $\mathcal{O}^{c}_{zy'}$ | $\mathcal{O}^{s}_{xy'}$ | $\mathcal{O}^{s}_{zz'}$ | $\mathcal{O}^{c}_{xz'}$ |
| $P_x$ | $P_z$ | $P^{\odot}_x$ | $P^{\odot}_z$ | $\mathcal{O}^{c}_{zy'}$ | $\mathcal{O}^{s}_{xy'}$ | $\mathcal{O}^{c}_{zx'}$ | $\mathcal{O}^{s}_{xx'}$ |
| $P_x$ | $P_z$ | $P^{\odot}_x$ | $P^{\odot}_z$ | $\mathcal{O}^{c}_{zy'}$ | $\mathcal{O}^{s}_{xy'}$ | $\mathcal{O}^{c}_{zz'}$ | $\mathcal{O}^{s}_{xz'}$ |
| $P_x$ | $P_z$ | $P^{\odot}_x$ | $P^{\odot}_z$ | $\mathcal{O}^{c}_{zy'}$ | $\mathcal{O}^{s}_{xy'}$ | $\mathcal{O}^{s}_{zx'}$ | $\mathcal{O}^{c}_{xx'}$ |
| $P^{s}_z$ | $P^{c}_x$ | $\mathcal{O}_{xy'}$ | $\mathcal{O}_{zy'}$ | $\mathcal{O}^{\odot}_{xy'}$ | $\mathcal{O}^{\odot}_{zy'}$ | $\mathcal{O}^{s}_{zz'}$ | $\mathcal{O}^{c}_{xz'}$ |
| $P^{s}_z$ | $P^{c}_x$ | $\mathcal{O}_{xy'}$ | $\mathcal{O}_{zy'}$ | $\mathcal{O}^{\odot}_{xy'}$ | $\mathcal{O}^{\odot}_{zy'}$ | $\mathcal{O}^{c}_{zx'}$ | $\mathcal{O}^{s}_{xx'}$ |
| $P^{s}_z$ | $P^{c}_x$ | $\mathcal{O}_{xy'}$ | $\mathcal{O}_{zy'}$ | $\mathcal{O}^{\odot}_{xy'}$ | $\mathcal{O}^{\odot}_{zy'}$ | $\mathcal{O}^{c}_{zz'}$ | $\mathcal{O}^{s}_{xz'}$ |
| $P^{s}_z$ | $P^{c}_x$ | $\mathcal{O}_{xy'}$ | $\mathcal{O}_{zy'}$ | $\mathcal{O}^{\odot}_{xy'}$ | $\mathcal{O}^{\odot}_{zy'}$ | $\mathcal{O}^{s}_{zx'}$ | $\mathcal{O}^{c}_{xx'}$ |
| $P^{c}_z$ | $P^{s}_x$ | $\mathcal{O}_{xy'}$ | $\mathcal{O}_{zy'}$ | $\mathcal{O}^{\odot}_{xy'}$ | $\mathcal{O}^{\odot}_{zy'}$ | $\mathcal{O}^{s}_{zz'}$ | $\mathcal{O}^{c}_{xz'}$ |
| $P^{c}_z$ | $P^{s}_x$ | $\mathcal{O}_{xy'}$ | $\mathcal{O}_{zy'}$ | $\mathcal{O}^{\odot}_{xy'}$ | $\mathcal{O}^{\odot}_{zy'}$ | $\mathcal{O}^{c}_{zx'}$ | $\mathcal{O}^{s}_{xx'}$ |
| $P^{c}_z$ | $P^{s}_x$ | $\mathcal{O}_{xy'}$ | $\mathcal{O}_{zy'}$ | $\mathcal{O}^{\odot}_{xy'}$ | $\mathcal{O}^{\odot}_{zy'}$ | $\mathcal{O}^{c}_{zz'}$ | $\mathcal{O}^{s}_{xz'}$ |
| $P^{c}_z$ | $P^{s}_x$ | $\mathcal{O}_{xy'}$ | $\mathcal{O}_{zy'}$ | $\mathcal{O}^{\odot}_{xy'}$ | $\mathcal{O}^{\odot}_{zy'}$ | $\mathcal{O}^{s}_{zx'}$ | $\mathcal{O}^{c}_{xx'}$ |
| $\mathcal{O}_{xy'}$ | $\mathcal{O}_{zy'}$ | $\mathcal{O}^{\odot}_{xy'}$ | $\mathcal{O}^{\odot}_{zy'}$ | $\mathcal{O}^{s}_{zy'}$ | $\mathcal{O}^{c}_{xy'}$ | $\mathcal{O}^{s}_{zz'}$ | $\mathcal{O}^{c}_{xz'}$ |
| $\mathcal{O}_{xy'}$ | $\mathcal{O}_{zy'}$ | $\mathcal{O}^{\odot}_{xy'}$ | $\mathcal{O}^{\odot}_{zy'}$ | $\mathcal{O}^{s}_{zy'}$ | $\mathcal{O}^{c}_{xy'}$ | $\mathcal{O}^{c}_{zx'}$ | $\mathcal{O}^{s}_{xx'}$ |
| $\mathcal{O}_{xy'}$ | $\mathcal{O}_{zy'}$ | $\mathcal{O}^{\odot}_{xy'}$ | $\mathcal{O}^{\odot}_{zy'}$ | $\mathcal{O}^{s}_{zy'}$ | $\mathcal{O}^{c}_{xy'}$ | $\mathcal{O}^{c}_{zz'}$ | $\mathcal{O}^{s}_{xz'}$ |
| $\mathcal{O}_{xy'}$ | $\mathcal{O}_{zy'}$ | $\mathcal{O}^{\odot}_{xy'}$ | $\mathcal{O}^{\odot}_{zy'}$ | $\mathcal{O}^{s}_{zy'}$ | $\mathcal{O}^{c}_{xy'}$ | $\mathcal{O}^{s}_{zx'}$ | $\mathcal{O}^{c}_{xx'}$ |
| $\mathcal{O}_{xy'}$ | $\mathcal{O}_{zy'}$ | $\mathcal{O}^{\odot}_{xy'}$ | $\mathcal{O}^{\odot}_{zy'}$ | $\mathcal{O}^{c}_{zy'}$ | $\mathcal{O}^{s}_{xy'}$ | $\mathcal{O}^{s}_{zz'}$ | $\mathcal{O}^{c}_{xz'}$ |
| $\mathcal{O}_{xy'}$ | $\mathcal{O}_{zy'}$ | $\mathcal{O}^{\odot}_{xy'}$ | $\mathcal{O}^{\odot}_{zy'}$ | $\mathcal{O}^{c}_{zy'}$ | $\mathcal{O}^{s}_{xy'}$ | $\mathcal{O}^{c}_{zx'}$ | $\mathcal{O}^{s}_{xx'}$ |
| $\mathcal{O}_{xy'}$ | $\mathcal{O}_{zy'}$ | $\mathcal{O}^{\odot}_{xy'}$ | $\mathcal{O}^{\odot}_{zy'}$ | $\mathcal{O}^{c}_{zy'}$ | $\mathcal{O}^{s}_{xy'}$ | $\mathcal{O}^{c}_{zz'}$ | $\mathcal{O}^{s}_{xz'}$ |
| $\mathcal{O}_{xy'}$ | $\mathcal{O}_{zy'}$ | $\mathcal{O}^{\odot}_{xy'}$ | $\mathcal{O}^{\odot}_{zy'}$ | $\mathcal{O}^{c}_{zy'}$ | $\mathcal{O}^{s}_{xy'}$ | $\mathcal{O}^{s}_{zx'}$ | $\mathcal{O}^{c}_{xx'}$ |

## VIII. IMPLICATIONS FOR EXPERIMENTALISTS

The experimental verification of complete sets, in the framework of single pseudoscalar meson photoproduction, was studied, for example, by Ireland [9] and Vrancx *et al.* [59]. They concluded that, as soon as the data have a finite measurement uncertainty, it might not be possible to determine unique solutions for the amplitudes in case one uses a mathematical, minimal complete set of observables. It is believed that additional observables could resolve the ambiguity. Thus it is important to measure more than 16 observables [9].

Observables which are relatively easy to measure rank in the categories $\mathcal{B}$, $\mathcal{T}$, $\mathcal{BT}$ because they do not require a recoil polarimeter. Even though they form a group of 16 observables, they do not form a complete set, which was verified numerically in this study. The measurement of some well-chosen observables from the categories $\mathcal{R}$, $\mathcal{BR}$, $\mathcal{TR}$, and $\mathcal{BTR}$ is essential. Out of the 69 possible complete sets that require the measurement of only one triple polarization observable and which are listed in Table V, the sets (6), (12), (15), (27), (30), (41), and (47) contain the minimal number of recoil polarization observables, e.g., the set (15) contains the following observables:

$$\{I^{\odot}, P_y, P_{y'}, \mathcal{O}^{\odot}_{yy'}, \mathcal{O}_{yy'}, P^{\odot}_{y'}, P^{\odot}_{y}, I_0, P_x, P_z, P_{x'}, P^{s}_x, P^{\odot}_x, P^{c}_z, P^{\odot}_z, P^{\odot}_{x'}\}. \quad (21)$$

Data exist for eight of these observables [$I_0$, $I^{\odot}$, $P_x$, $P_y$, $P_{y'}$, $\mathcal{O}_{yy'} (= -I^{c})$, $P^{s}_x$, $P^{\odot}_z$] for the $p\pi^0\pi^0$ final state, albeit not having a perfect overlap of the energy and angular ranges covered by the different data sets (see Table IV). The remaining eight observables could be measured in the future in three different experiments using a linearly polarized photon beam with a longitudinally polarized target ($P_z$, $P^{c}_z$), using a circularly polarized photon beam and a transversely polarized target ($P^{\odot}_x$, $P^{\odot}_y$), and by employing a recoil polarimeter in addition to the latter configuration, the observables $P_{x'}$, $P^{\odot}_{x'}$, $P^{\odot}_{y'}$, and $\mathcal{O}^{\odot}_{yy'}$ can be obtained as well.

## IX. CONCLUSION AND OUTLOOK

Within this paper, the problem of finding complete sets for two pseudoscalar meson photoproduction was studied. For this purpose, a slightly modified version of Moravcsik's theorem was applied. This method is capable of extracting complete sets of observables in a totally automated manner. The automation capability, easy accessibility, as well as the adaptability for reactions with arbitrary $N$ are the strengths of Moravcsik's theorem. However, it turns out that the resulting sets from Moravcsik are slightly overcomplete since each observable depends on more than one bilinear product. For this reason, a numerical- as well as an algebraic method are discussed in order to reduce these sets to minimal complete sets containing $2N = 16$ observables. The characteristics of the minimal sets are discussed. Finally, 69 minimal complete sets containing the minimal number of triple polarization observables, namely only one, are presented. From these subsets in combination with the extensive overview of already performed measurements in two pseudoscalar meson photoproduction, the most promising set of observables, which could be measured in the near future, is presented.

Further studies could be performed on how Moravcsik's theorem should be adapted in order to yield directly minimal complete sets. This would decrease the numerical effort enormously and would make the theorem even more accessible.

## ACKNOWLEDGMENTS

The authors would like to thank Prof. Dr. Thoma for a fruitful discussion and constructive comments on the paper and Prof. Dr. Beck for his support.


## APPENDIX: ALGORITHM TO CHECK FOR COMPLETENESS

The following algorithm was designed by Tiator [60] and was already applied in Ref. [61]. It is used to check if a set of observables is able to resolve continuous as well as discrete ambiguities. The starting point is a system of multivariate homogeneous polynomials $f_1(\vec{t}), \ldots, f_n(\vec{t})$. The input is a vector of $N$ complex amplitudes $t_i$. Without loss of generality, the overall phase of the complex amplitudes is fixed by requiring $\mathrm{Re}(t_1) > 0$ and $\mathrm{Im}(t_1) = 0$. In a next step an $N$-dimensional solution vector $\vec{s}$ is formed. It consist of $2N - 1$ randomly chosen prime numbers within a certain range. These serve as values for the real and imaginary parts of $t_i$. Using prime numbers and increasing the range from which they are chosen should reduce the chance to land on a singularity in the solution space, where the "condition of equal magnitudes of relative phases" [8] is met.

Finally, the polynomial system

$$\begin{aligned} f_1(\vec{t}) &= g_1, \\ &\vdots \\ f_n(\vec{t}) &= g_n, \end{aligned} \tag{A1}$$

is constructed, where $g_i = f_i(\vec{s})$ is a scalar quantity. The function *NSolve* from *Mathematica* [56] is employed to solve the algebraic system for the variables $t_1, \ldots, t_N$. According to the Wolfram *Mathematica* documentation [62,63]: "For systems of algebraic equations, NSolve computes a numerical Gröbner basis using an efficient monomial ordering, then uses eigensystem methods to extract numerical roots."

The system of polynomials is said to be complete if only one solution is found which furthermore is equivalent to $\vec{s}$.


[1] V. Sokhoyan *et al.*, High-statistics study of the reaction $\gamma p \to p2\pi^0$, Eur. Phys. J. A **51**, 95 (2015).

[2] A. Fix and H. Arenhövel, Double-pion photoproduction on nucleon and deuteron, Eur. Phys. J. A **25**, 115 (2005).

[3] C. G. Fasano, F. Tabakin, and B. Saghai, Spin observables at threshold for meson photoproduction, Phys. Rev. C **46**, 2430 (1992).

[4] G. Knöchlein, D. Drechsel, and L. Tiator, Photo- and electroproduction of eta mesons, Z. Phys. A: Hadrons Nucl. **352**, 327 (1995).

[5] W. Roberts and T. Oed, Polarization observables for two-pion production off the nucleon, Phys. Rev. C **71**, 055201 (2005).

[6] W.-T. Chiang and F. Tabakin, Completeness rules for spin observables in pseudoscalar meson photoproduction, Phys. Rev. C **55**, 2054 (1997).

[7] I. Barker, A. Donnachie, and J. Storrow, Complete experiments in pseudoscalar photoproduction, Nucl. Phys. B **95**, 347 (1975).

[8] K. Nakayama, Explicit derivation of the completeness condition in pseudoscalar meson photoproduction, Phys. Rev. C **100**, 035208 (2019).

[9] D. G. Ireland, Information content of polarization measurements, Phys. Rev. C **82**, 025204 (2010).

[10] G. Chew, M. Goldberger, F. Low, and Y. Nambu, Relativistic dispersion relation approach to photomeson production, Phys. Rev. **106**, 1345 (1957).

[11] H. Arenhövel and A. Fix, Complete set of observables for photoproduction of two pseudoscalars on a nucleon, Phys. Rev. C **89**, 034003 (2014).

[12] M. J. Moravcsik, Resolving the discrete ambiguities in amplitude determinations, J. Math. Phys. **26**, 211 (1985).

[13] Y. Wunderlich, P. Kroenert, F. Afzal, and A. Thiel, Moravcsik's theorem on complete sets of polarization observables reexamined, Phys. Rev. C **102**, 034605 (2020).

[14] T. Seifen *et al.*, Measurement of polarization observables in neutral double pion photoproduction off the proton with the CBELSA/TAPS experiment, EPJ Web Conf. **241**, 01016 (2020).

[15] E. Gutz, V. Crede, V. Sokhoyan, H. van Pee, A. Anisovich, J. Bacelar, B. Bantes, O. Bartholomy, D. Bayadilov, R. Beck *et al.*, High statistics study of the reaction $\gamma p \to p\pi^0\eta$, Eur. Phys. J. A **50**, 74 (2014).

[16] W. Briscoe, M. Doering, H. Haberzettl, I. Strakovsky, and R. Workman, Said database, http://gwdac.phys.gwu.edu, accessed 16 July 2020.

[17] D. G. Ireland, E. Pasyuk, and I. Strakovsky, Photoproduction reactions and non-strange baryon spectroscopy, Prog. Part. Nucl. Phys. **111**, 103752 (2020).

[18] M. Sikora, D. Glazier, and D. Watts, Recoil polarimetry in meson photoproduction at MAMI, Chin. Phys. C **33**, 1373 (2009).

[19] K.-T. Brinkmann, Recoil polarization measurements, EPJ Web Conf. **134**, 03007 (2017).

[20] F. Härter, J. Ahrens, R. Beck, B. Krusche, V. Metag, M. Schmitz, H. Ströher, T. Walcher, and M. Wolf, Two neutral pion photoproduction off the proton between threshold and 800 MeV, Phys. Lett. B **401**, 229 (1997).

[21] M. Wolf, J. Ahrens, R. Beck, V. Hejny, J. Kellie, M. Kotulla, B. Krusche, V. Kuhr, R. Leukel, V. Metag *et al.*, Photoproduction of neutral pion pairs from the proton, Eur. Phys. J. A **9**, 5 (2000).

[22] V. Kleber, P. Achenbach, J. Ahrens, R. Beck, V. Hejny, J. Kellie, M. Kotulla, B. Krusche, V. Kuhr, R. Leukel *et al.*, Double-$\pi^0$ photoproduction from the deuteron, Eur. Phys. J. A **9**, 1 (2000).

[23] M. Kotulla, J. Ahrens, J. Annand, R. Beck, D. Hornidge, S. Janssen, B. Krusche, J. McGeorge, I. MacGregor, J. Messchendorp *et al.*, Double $\pi^0$ photoproduction off the proton at threshold, Phys. Lett. B **578**, 63 (2004).

[24] F. Zehr, B. Krusche, P. Aguar, J. Ahrens, J. Annand, H. Arends, R. Beck, V. Bekrenev, B. Boillat, A. Braghieri *et al.*, Photoproduction of $\pi^0\pi^0$- and $\pi^0\pi^+$-pairs off the proton from threshold to the second resonance region, Eur. Phys. J. A **48**, 98 (2012).

[25] V. Kashevarov, A. Fix, S. Prakhov, P. Aguar-Bartolome, J. Annand, H. Arends, K. Bantawa, R. Beck, V. Bekrenev, H. Berghäuser *et al.*, Experimental study of the $\gamma p \to \pi^0\pi^0 p$ reaction with the Crystal Ball/TAPS detector system at the Mainz microtron, Phys. Rev. C **85**, 064610 (2012).

[26] M. Dieterle, M. Oberle, J. Ahrens, J. Annand, H. Arends, K. Bantawa, P. Bartolome, R. Beck, V. Bekrenev, H. Berghäuser *et al.*, Photoproduction of $\pi^0$-pairs off protons and off neutrons, Eur. Phys. J. A **51**, 142 (2015).

[27] A. Braghieri, L. Murphy, J. Ahrens, G. Audit, N. d'Hose, V. Isbert, S. Kerhoas, M. Mac Cormick, P. Pedroni, T. Pinelli *et al.*, Total cross section measurement for the three double pion photoproduction channels on the proton, Phys. Lett. B **363**, 46 (1995).

[28] J. Ahrens, S. Altieri, J. Annand, G. Anton, H.-J. Arends, K. Aulenbacher, R. Beck, C. Bradtke, A. Braghieri, N. Degrande *et al.*, Intermediate resonance excitation in the $\gamma p \to p\pi^0\pi^0$ reaction, Phys. Lett. B **624**, 173 (2005).

[29] A. Sarantsev, M. Fuchs, M. Kotulla, U. Thoma, J. Ahrens, J. Annand, A. Anisovich, G. Anton, R. Bantes, O. Bartholomy *et al.*, New results on the Roper resonance and the P11 partial wave, Phys. Lett. B **659**, 94 (2008).

[30] U. Thoma, M. Fuchs, A. Anisovich, G. Anton, R. Bantes, O. Bartholomy, R. Beck, Y. Beloglazov, V. Crede, A. Ehmanns *et al.*, $N^*$ and $\Delta^*$ decays into $N\pi^0\pi^0$, Phys. Lett. B **659**, 87 (2008).

[31] A. Thiel, V. Sokhoyan, E. Gutz, H. van Pee, A. Anisovich, J. Bacelar, B. Bantes, O. Bartholomy, D. Bayadilov, R. Beck *et al.*, Three-Body Nature of $N*$ and $\Delta*$ Resonances from Sequential Decay Chains, Phys. Rev. Lett. **114**, 091803 (2015).

[32] Y. Assafiri, O. Bartalini, V. Bellini, J. P. Bocquet, S. Bouchigny, M. Capogni, M. Castoldi, A. D'Angelo, J. Didelez, R. Di Salvo *et al.*, Double $\pi^0$ Photoproduction on the Proton at GRAAL, Phys. Rev. Lett. **90**, 222001 (2003).

[33] D. Krambrich, F. Zehr, A. Fix, L. Roca, P. Aguar, J. Ahrens, J. Annand, H. Arends, R. Beck, V. Bekrenev *et al.*, Beam-Helicity Asymmetries in Double-Pion Photoproduction off the Proton, Phys. Rev. Lett. **103**, 052002 (2009).

[34] M. Oberle, B. Krusche, J. Ahrens, J. Annand, H. Arends, K. Bantawa, P. Bartolome, R. Beck, V. Bekrenev, H. Berghäuser *et al.*, Measurement of the beam-helicity asymmetry $I^\odot$ in the photoproduction of $\pi^0$-pairs off the proton and off the neutron, Phys. Lett. B **721**, 237 (2013).

[35] M. Dieterle, L. Witthauer, A. Fix, S. Abt, P. Achenbach, P. Adlarson, F. Afzal, P. A. Bartolome, Z. Ahmed, J. R. M. Annand *et al.*, Helicity-Dependent Cross Sections for the Photoproduction of $\pi^0$ Pairs from Nucleons, Phys. Rev. Lett. **125**, 062001 (2020).

[36] J. Ahrens, S. Altieri, J. Annand, H.-J. Arends, R. Beck, M. Blackston, C. Bradtke, A. Braghieri, N. d'Hose, H. Dutz *et al.*, First measurement of the helicity dependence for the $\gamma p \to p\pi$ reaction, Eur. Phys. J. A **34**, 11 (2007).

[37] F. Carbonara, G. Chiefari, E. Drago, G. Gialanella, L. Merola, M. Napolitano, R. Rinzivillo, G. Sciacca, V. Rossi, and G. Susinno, Analysis of $\gamma n \to n\pi^+\pi^-$ and $\gamma n \to p\pi^-\pi^0$ reactions from threshold up to 1 GeV, Nuovo Cimento A **36**, 219 (1976).

[38] K. Hirose, M. Ejima, T. Fujibayashi, Y. Fujii, K. Futatsukawa, O. Hashimoto, T. Ishikawa, S. Kameoka, H. Kanda, F. Kato *et al.*, Study of double pion photoproduction on the deuteron, Phys. Lett. B **674**, 17 (2009).

[39] H. Crouch, Jr., R. Hargraves, B. Kendall, R. Lanou, A. Shapiro, M. Widgoff, G. Fischer, A. Brenner, M. Law, E. Ronat *et al.*, Gamma-Ray Proton Interactions between 0.5 and 4.8 BeV, Phys. Rev. Lett. **13**, 636 (1964).

[40] C. Wu, J. Barth, W. Braun, J. Ernst, K.-H. Glander, J. Hannappel, N. Jöpen, H. Kalinowsky, F. Klein, F. Klein *et al.*, Photoproduction of $\rho$ mesons and $\delta$-baryons in the reaction $\gamma p \to p\pi^+\pi^-$ at energies up to $\sqrt{s} = 2.6$ GeV, Eur. Phys. J. A **23**, 317 (2005).

[41] E. Golovatch *et al.*, First results on nucleon resonance photocouplings from the $\gamma p \to \pi^+\pi^- p$ reaction, Phys. Lett. B **788**, 371 (2019).

[42] S. Strauch, B. Berman, G. Adams, P. Ambrozewicz, M. Anghinolfi, B. Asavapibhop, G. Asryan, G. Audit, H. Avakian, H. Bagdasaryan *et al.*, Beam-Helicity Asymmetries in Double-Charged-Pion Photoproduction on the Proton, Phys. Rev. Lett. **95**, 162003 (2005).

[43] R. Badui, J. Bono, L. Guo, and B. A. Raue, The beam-helicity asymmetry for $\gamma p \to pK^+K^-$ and $\gamma p \to p\pi^+\pi^-$, AIP Conf. Proc. **1735**, 040014 (2016).

[44] I. Horn, A. Anisovich, G. Anton, R. Bantes, O. Bartholomy, R. Beck, Y. Beloglazov, R. Bogendörfer, R. Castelijns, V. Crede *et al.*, Evidence for a Parity Doublet $\Delta$ (1920) P33 and $\Delta$ (1940) D33 from $\gamma p \to p\pi^0\eta$, Phys. Rev. Lett. **101**, 202002 (2008).

[45] V. Kashevarov, A. Fix, P. Aguar-Bartolomé, L. Akasoy, J. Annand, H. Arends, K. Bantawa, R. Beck, V. Bekrenev, H. Berghäuser *et al.*, Photoproduction of $\pi^0\eta$ on protons and the $\Delta(1700)$ $D_{33}$-resonance, Eur. Phys. J. A **42**, 141 (2009).

[46] T. Nakabayashi, H. Fukasawa, R. Hashimoto, T. Ishikawa, T. Iwata, H. Kanda, J. Kasagi, T. Kinoshita, K. Maeda, F. Miyahara *et al.*, Photoproduction of $\eta$ mesons off protons for $E_\gamma \leqslant 1.15$ GeV, Phys. Rev. C **74**, 035202 (2006).

[47] J. Ajaka, Y. Assafiri, O. Bartalini, V. Bellini, S. Bouchigny, M. Castoldi, A. D'Angelo, J. Didelez, R. Di Salvo, M. Döring *et al.*, Simultaneous Photoproduction of $\eta$ and $\pi^0$ Mesons on the Proton, Phys. Rev. Lett. **100**, 052003 (2008).

[48] E. Gutz, V. Sokhoyan, H. van Pee, A. Anisovich, J. Bacelar, B. Bantes, O. Bartholomy, D. Bayadilov, R. Beck, Y. Beloglazov *et al.*, Measurement of the beam asymmetry $\Sigma$ in $\pi^0\eta$ production off the proton with the CBELSA/TAPS experiment, in *NSTAR 2007*, edited by H. W. Hammer, V. Kleber, U. Thoma, and H. Schmieden (Springer, Berlin, Heidelberg, 2008), pp. 190–192.

[49] E. Gutz, V. Sokhoyan, H. van Pee, A. Anisovich, J. Bacelar, B. Bantes, O. Bartholomy, D. Bayadilov, R. Beck, Y. Beloglazov *et al.*, Photoproduction of meson pairs: First measurement of the polarization observable Is, Phys. Lett. B **687**, 11 (2010).

[50] W. Langgärtner, J. Ahrens, R. Beck, V. Hejny, M. Kotulla, B. Krusche, V. Kuhr, R. Leukel, J. D. McGregor, J. G. Messchendorp *et al.*, Direct Observation of a $\rho$ Decay of the $D_{13}(1520)$ Baryon Resonance, Phys. Rev. Lett. **87**, 052001 (2001).

[51] J. Ahrens, S. Altieri, J. Annand, G. Anton, H.-J. Arends, K. Aulenbacher, R. Beck, C. Bradtke, A. Braghieri, N. Degrande *et al.*, Helicity dependence of the $\gamma p \to n\pi^+\pi^0$ reaction in the second resonance region, Phys. Lett. B **551**, 49 (2003).

[52] J. Ajaka, Y. Assafiri, O. Bartalini, V. Bellini, S. Bouchigny, M. Castoldi, A. d'Angelo, J. Didelez, R. Di Salvo, A. Fantini *et al.*, Double $\pi^0$ photoproduction on the neutron at GRAAL, Phys. Lett. B **651**, 108 (2007).

[53] A. Zabrodin, G. Audit, R. Beck, A. Braghieri, N. D'Hose, B. Dolbilkin, S. J. Hall, V. Isbert, L. Y. Murphy, P. Pedroni *et al.*, Total cross section measurement of the $\gamma n \to p\pi^-\pi^0$ reaction, Phys. Rev. C **55**, R1617(R) (1997).

[54] A. Zabrodin, G. Audit, R. Beck, A. Braghieri, N. D'Hose, S. J. Hall, J. D. Kellie, M. MacCormick, L. Y. Murphy, A. Panzeri *et al.*, Invariant mass distributions of the $\gamma n \to p\pi^-\pi^0$ reaction, Phys. Rev. C **60**, 055201 (1999).

[55] S. Lombardo *et al.* (CLAS Collaboration), Photoproduction of $K^+K^-$ meson pairs on the proton, Phys. Rev. D **98**, 052009 (2018).

[56] Wolfram, Inc., Mathematica, Version 12.1 (Champaign, 2020).

[57] J. Bezanson, A. Edelman, S. Karpinski, and V. B. Shah, JULIA: A fresh approach to numerical computing, SIAM Rev. **59**, 65 (2017).

[58] See Supplemental Material at http://link.aps.org/supplemental/10.1103/PhysRevC.103.014607 for a demonstration of the algebraic reduction of overcomplete sets.

[59] T. Vrancx, J. Ryckebusch, T. Van Cuyck, and P. Vancraeyveld, Incompleteness of complete pseudoscalar-meson photoproduction, Phys. Rev. C **87**, 055205 (2013).

[60] L. Tiator (private communication).

[61] L. Tiator, R. L. Workman, Y. Wunderlich, and H. Haberzettl, Amplitude reconstruction from complete electroproduction experiments and truncated partial-wave expansions, Phys. Rev. C **96**, 025210 (2017).

[62] Some notes on internal implementation, https://reference.wolfram.com/language/tutorial/SomeNotesOnInternalImplementation.html, accessed 25 May 2020.

[63] I. N. Bronstein and K. A. Semendjajew, in *Taschenbuch der Mathematik*, 19th ed., edited by G. Grosche and V. Ziegler (BSB B. G. Teubner Verlagsgesellschaft, Nauka-Verlag, Leipzig, Moskau, 1979).

## A.2 Publication: Phys. Rev. C 109, 045206 (2024)

In the following, the paper:

**Philipp Kroenert, Yannick Wunderlich, Farah Afzal, and Annika Thiel, "Truncated Partia-Wave Analysis for $\eta$-photoproduction observables via Bayesian Statistics", Phys. Rev. C 109, 045206 (2024),**

is included.

# Truncated partial-wave analysis for $\eta$-photoproduction observables via Bayesian statistics

Philipp Kroenert, Yannick Wunderlich, Farah Afzal, and Annika Thiel
*Helmholtz Institut für Strahlen- und Kernphysik, Universität Bonn, D-53115 Bonn, Germany*

(Received 18 May 2023; revised 15 November 2023; accepted 6 February 2024; published 10 April 2024)

A truncated partial-wave analysis is performed for $\eta$ photoproduction off the proton using the polarization observables $\sigma_0$, $\Sigma$, $T$, $E$, $F$, and $G$. Through this approach, model-independent estimates of the electromagnetic multipole parameters are calculated. Based on these estimates, predictions are made for polarization observables that have not yet been measured. These predictions identify promising future measurements that could resolve the inherent mathematical ambiguities within the results. Bayesian inference is combined for the first time with truncated partial-wave analysis, analyzing different truncation orders for six energy bins near the $\eta p$-production threshold, i.e., $E_\gamma^{\text{lab}} \in [750, 1250]$ MeV.

DOI: 10.1103/PhysRevC.109.045206

## I. INTRODUCTION

Baryon spectroscopy is an experimental technique to acquire a better understanding of the strong interaction and its fundamental theoretical description given by quantum chromodynamics. Particles (for example, pions, real photons, as well as electrons [1]) are brought to collision with a nucleon. With a sufficiently high center-of-mass energy, the nucleon can be excited to a resonant state, which is classified as a distinct particle with certain intrinsic properties. Two well-established examples for baryon resonances are the delta resonance $\Delta(1232)3/2^+$ and the Roper resonance $N(1440)1/2^+$ [2]. As such resonances are often formed and decay via the strong interaction, their proper lifetimes are rather short; for the above examples, on the order of $10^{-24}$ s. A direct detection of resonances with state-of-the-art detectors is not possible. Instead, the analysis of the final-state particles angular distributions using partial-wave analysis (PWA), allows us to draw conclusions about the formation of the resonance and its inherent properties such as total angular momentum, mass, decay width, and parity. Up to the present day, single pseudoscalar meson photoproduction reactions are the experimentally most studied reactions in terms of baryon spectroscopy. A comprehensive overview can be found in the recently published review on light baryon spectroscopy by Thiel *et al.* [1]. The experimental data which are used as input to partial-wave analyses are called polarization observables. In single pseudoscalar meson photoproduction, there are sixteen linearly independent measurable quantities. Multiple facilities worldwide [3–7] have contributed to a large database. In addition, multiple PWA approaches [8–13] do exist for describing the data and extracting information about the resonant states. The results of this paper are compared with the $K$-matrix model of Bonn-Gatchina [9], the dynamical coupled-channel approach of Jülich-Bonn [10], and the unitarized isobar-model of Eta-MAID [11]. However, these approaches depend on an energy-dependent parametrization for the complex amplitudes [1], leading to model-dependent outcomes. For a detailed comparison of these three PWA approaches, the reader is advised to Refs. [1,14]. Resonant states can also be predicted in a purely mathematical manner via theory models based on quantum chromodynamics, such as quark models or lattice quantum chromodynamics; see, for example, Ref. [15]. However, theory models predicted significantly more states than are experimentally confirmed, predominantly in the higher-mass region, which is known as the missing-resonance problem [1]. This unsolved issue motivates further studies and the exploration of new approaches within this field of physics. In this paper, a completely model-independent analysis approach, namely, truncated partial-wave analysis (TPWA) [16–20], is employed. This avoids the bias present in other PWA approaches. In general, PWA as well as TPWA may exhibit mathematical ambiguities in their results, indicating that various solutions can effectively describe the same data points. These ambiguities arise from the intrinsic mathematical nature of the problem. As such, it is an essential step in any analysis using experimental data to check for potential ambiguities and evaluate their significance in comparison to each other. Mathematical ambiguities in TPWA were first investigated by Omelaenko [21]. A detailed treatment of the subject can be found in Refs. [18–20]. The application of TPWA to experimental data ($\pi^0$ photoproduction off the proton for the first- and second-resonance region) was conducted in detail by Wunderlich [19] using the maximum likelihood method. Among other things, the effect of measurement uncertainties on ambiguities was investigated. This paper is the first to perform a TPWA using Bayesian inference. Therefore, the results in this paper are given as distributions, as opposed to point estimates in previous PWA and TPWA approaches, allowing the uncertainty of an estimated parameter to be quantified with an unprecedented level of detail, which is of particular importance. Through this approach it becomes possible to study the phase space in more detail and, by association, the structure of the above-mentioned ambiguities. It is even possible to discover a certain connectivity between

 

different solutions, indicating problematic ambiguities. The results of this paper comprises the estimation of complex electromagnetic multipole parameters for various maximal angular momenta $\ell_{\max}$. Based on these estimations, for the first time, model-independent predictions for unmeasured polarization observables are computed.

This paper is structured as follows: a concise introduction to Bayesian statistics is given in Sec. II. An outline of TPWA, hence the foundation of the employed model, is provided in Sec. III, followed by a discussion of the mathematical ambiguities. The employed datasets are introduced and discussed in Sec. IV, accompanied by the discussion of their systematic uncertainties and correlations between the data points used. Within Sec. V the posterior distribution, centerpiece of the analyses, is introduced. Finally, the results of TPWA examined via Bayesian inference are presented in Sec. VI.

## II. BASICS OF BAYESIAN STATISTICS

The fundamental equation of Bayesian statistics is Bayes' theorem [22,23]:

$$p(\boldsymbol{\Theta} \mid \boldsymbol{y}) = \frac{p(\boldsymbol{y} \mid \boldsymbol{\Theta})\, p(\boldsymbol{\Theta})}{\int p(\boldsymbol{y} \mid \boldsymbol{\Theta})\, p(\boldsymbol{\Theta}) \mathrm{d}\boldsymbol{\Theta}}. \tag{1}$$

Herein, $\boldsymbol{\Theta}$ denotes the parameters of the model used whereas $\boldsymbol{y}$ stands for the employed data.

The posterior distribution $p(\boldsymbol{\Theta} \mid \boldsymbol{y})$ is in general a multidimensional probability distribution reflecting the probability of the model given the data. It consists of the likelihood distribution $p(\boldsymbol{y} \mid \boldsymbol{\Theta})$, comprising the data points and model predictions, and the prior distribution $p(\boldsymbol{\Theta})$, which inhibits the current knowledge about the parameters of the model, before the data are taken into consideration. The denominator in Eq. (1) plays the role of a normalization factor and can be neglected within the computations of parameter estimation as it is constant for fixed $\boldsymbol{y}$. The definitions for the likelihood distribution and prior distributions employed in this paper can be found in Secs. V A and V B.

The overall goal of each analysis is to scan the relevant regions of the posterior accurately. From this, the parameter distributions can then be extracted, i.e., their marginal distributions.[1] In general, the posterior is nontrivial and the integrals encountered in the derivation of the marginal distributions cannot be solved analytically. Instead, one can employ numerical methods, such as Markov chain Monte Carlo (MCMC) algorithms, in order to estimate the involved integrals. For instance, the Metropolis-Hastings [24,25] or the Hamiltonian Monte Carlo [26,27] algorithm can be used, of which the latter one is applied in this work. The convergence of the Markov chains[2] can be monitored by convergence diagnostics such as the potential-scale-reduction statistic $\hat{R}$ [29], Monte Carlo standard error [28] (which depends on the effective sample size [23]), and trace plots [30].

To check the plausibility of the model under consideration, a posterior predictive check can be performed [23]. Herein, replicated data distributions $\boldsymbol{y}^{\mathrm{rep}}$ are generated using the sampled parameter distributions as input for the posterior distribution, while at the same time treating the data points as unknown parameters. In contrast with maximum likelihood or maximum *a posteriori* estimation, the marginal parameter estimates of Bayesian inference are given as distributions. This allows us to quantify the uncertainty of a parameter with an unmatched level of detail. In addition, point estimates and the marginal parameter estimates of Bayesian inference differ in their underlying interpretation, making the latter an intriguing additional analysis approach.

## III. TRUNCATED PARTIAL-WAVE ANALYSIS

Within this section, the basic equations of TPWA for single pseudoscalar-meson photoproduction are outlined. For an in-depth explanation, the reader is advised to Refs. [19,20].

Polarization observables are the measurable quantities of interest in single pseudoscalar-meson photoproduction. They are used as experimental input for a TPWA. In total there are sixteen polarization observables, which can be calculated by measuring differential cross sections under different polarization states. Three groups can be distinguished: the unpolarized differential cross section, three single-polarization observables, and twelve double-polarization observables [31]. A comprehensive list of the required polarization states for each observable is given in Table I while a mathematical definition is given in Table II.

The theoretical prediction of a profile function[3] of a polarization observable depends on the energy $W$ as well as the scattering angle $\theta$ in the center-of-mass frame. It can be expressed as an expansion into the basis of associated Legendre polynomials $P_k^{\beta_\alpha}$ [20]:

$$\check{\Omega}^{\alpha}_{\mathrm{theo}}(W,\theta) = \rho \sum_{k=\beta_\alpha}^{2\ell_{\max}+\beta_\alpha+\gamma_\alpha} \mathcal{A}^{\alpha}_{k}(W)\, P_k^{\beta_\alpha}(\cos\theta). \tag{2}$$

Equation (2) includes a kinematic phase-space factor $\rho$, angular expansion parameters $\beta_\alpha$, $\gamma_\alpha$, which are fixed parameters for each of the sixteen polarization observables of pseudoscalar-meson photoproduction, and energy-dependent series coefficients $\mathcal{A}^{\alpha}_{k}$:

$$\mathcal{A}^{\alpha}_{k}(W) = \mathcal{M}^{\dagger}(W) \boldsymbol{\mathcal{C}}^{\alpha}_{k} \mathcal{M}(W). \tag{3}$$

Here, $\mathcal{M}$ denotes the complex multipole vector, which contains all participating multipoles involved for the truncation order $\ell_{\max}$. A valid choice for the definition of this vector, by

[1] The marginal distribution of $\Theta_1$ with respect to the posterior distribution $p(\Theta_1, \Theta_2 \mid \boldsymbol{y})$ is defined as $p(\Theta_1 \mid \boldsymbol{y}) = \int \mathrm{d}\Theta_2 p(\Theta_1, \Theta_2 \mid \boldsymbol{y})$ [23].

[2] "A sequence $X_1, X_2, \ldots$ of random elements of some set is a Markov chain if the conditional distribution of $X_{n+1}$ given $X_1, \ldots, X_n$ depends on $X_n$ only" [[28], p. 2].

[3] The profile function $\check{\Omega}^{\alpha}(W,\theta)$ of an observable $\Omega^{\alpha}(W,\theta)$ is defined as $\check{\Omega}^{\alpha}(W,\theta) := \sigma_0(W,\theta)\Omega^{\alpha}(W,\theta)$, where $\sigma_0$ is the unpolarized differential cross section.

TABLE I. This table collects the polarization configurations (beam, target, recoil) which allow us to measure the sixteen polarization observables of pseudoscalar meson photoproduction. In the center-of-mass coordinate system, the unprimed coordinates are chosen as follows: $\hat{z}$ axis along incident photon beam direction and $\hat{y}$ perpendicular to the reaction plane $\hat{x}$-$\hat{z}$. The primed coordinates is a rotation of the unprimed coordinates such that the final-state meson momentum points along the $\hat{z}'$ axis. The table is redrawn from Ref. [31]. A mathematical definition of the observables can be found in Table II.

| Observable | Beam polarization | Direction of target- or recoil-nucleon polarization |
|---|---|---|
| $\sigma_0$ | Unpolarized | |
| $\Sigma$ | Linear | |
| T | Unpolarized | $y$ |
| P | Unpolarized | $y'$ |
| H | Linear | $x$ |
| P | Linear | $y$ |
| G | Linear | $z$ |
| F | Circular | $x$ |
| E | Circular | $z$ |
| $O_{x'}$ | Linear | $x'$ |
| T | Linear | $y'$ |
| $O_{z'}$ | Linear | $z'$ |
| $C_{x'}$ | Circular | $x'$ |
| $C_{z'}$ | Circular | $z'$ |
| $T_{x'}$ | Unpolarized | $x, x'$ |
| $L_{x'}$ | Unpolarized | $z, x'$ |
| $\Sigma$ | Unpolarized | $y, y'$ |
| $T_{z'}$ | Unpolarized | $x, z'$ |
| $L_{z'}$ | Unpolarized | $z, z'$ |

TABLE II. The definition of the sixteen polarization observables in terms of transversity amplitudes $b_i$ are displayed. The table is adapted from Ref. [33]. The definition of the observables in terms of the required polarization configurations can be found in Table I.

| Observable | Transversity representation ($\rho$) | Type |
|---|---|---|
| $\check{\Omega}^1 = \sigma_0$ | $\frac{1}{2}(\lvert b_1\rvert^2 + \lvert b_2\rvert^2 + \lvert b_3\rvert^2 + \lvert b_4\rvert^2)$ | $\mathcal{S}$ |
| $\check{\Omega}^4 = -\check{\Sigma}$ | $\frac{1}{2}(\lvert b_1\rvert^2 + \lvert b_2\rvert^2 - \lvert b_3\rvert^2 - \lvert b_4\rvert^2)$ | |
| $\check{\Omega}^{10} = -\check{T}$ | $\frac{1}{2}(-\lvert b_1\rvert^2 + \lvert b_2\rvert^2 + \lvert b_3\rvert^2 - \lvert b_4\rvert^2)$ | |
| $\check{\Omega}^{12} = \check{P}$ | $\frac{1}{2}(-\lvert b_1\rvert^2 + \lvert b_2\rvert^2 - \lvert b_3\rvert^2 + \lvert b_4\rvert^2)$ | |
| $\check{\Omega}^3 = \check{G}$ | $\mathrm{Im}[-b_1 b_3^* - b_2 b_4^*]$ | $\mathcal{BT}$ |
| $\check{\Omega}^5 = \check{H}$ | $\mathrm{Re}[b_1 b_3^* - b_2 b_4^*]$ | |
| $\check{\Omega}^9 = -\check{E}$ | $\mathrm{Re}[b_1 b_3^* + b_2 b_4^*]$ | |
| $\check{\Omega}^{11} = \check{F}$ | $\mathrm{Im}[b_1 b_3^* - b_2 b_4^*]$ | |
| $\check{\Omega}^{14} = \check{O}_{x'}$ | $\mathrm{Re}[-b_1 b_4^* + b_2 b_3^*]$ | $\mathcal{BR}$ |
| $\check{\Omega}^7 = -\check{O}_{z'}$ | $\mathrm{Im}[-b_1 b_4^* - b_2 b_3^*]$ | |
| $\check{\Omega}^{16} = -\check{C}_{x'}$ | $\mathrm{Im}[b_1 b_4^* - b_2 b_3^*]$ | |
| $\check{\Omega}^2 = -\check{C}_{z'}$ | $\mathrm{Re}[b_1 b_4^* + b_2 b_3^*]$ | |
| $\check{\Omega}^6 = -\check{T}_{x'}$ | $\mathrm{Re}[-b_1 b_2^* + b_3 b_4^*]$ | $\mathcal{TR}$ |
| $\check{\Omega}^{13} = -\check{T}_{z'}$ | $\mathrm{Im}[b_1 b_2^* - b_3 b_4^*]$ | |
| $\check{\Omega}^8 = \check{L}_{x'}$ | $\mathrm{Im}[-b_1 b_2^* - b_3 b_4^*]$ | |
| $\check{\Omega}^{15} = \check{L}_{z'}$ | $\mathrm{Re}[-b_1 b_2^* - b_3 b_4^*]$ | |

means of electromagnetic multipoles [32], is

$$\begin{aligned}\mathcal{M}(W) = \big[&E_{0+}(W), E_{1+}(W), M_{1+}(W), M_{1-}(W),\\ &\times E_{2+}(W), E_{2-}(W), M_{2+}(W), M_{2-}(W), \ldots,\\ &\times E_{\ell_{\max}+}(W), E_{\ell_{\max}-}(W), M_{\ell_{\max}+}(W), M_{\ell_{\max}-}(W)\big].\end{aligned} \tag{4}$$

In addition, Eq. (3) contains a complex $4\ell_{\max} \times 4\ell_{\max}$ matrix $\mathcal{C}$ for each observable $\alpha$ and each summand $k$. Its general definition can be found in Ref. [19].[4] From these matrices one can not only read off the contributing partial waves but also their interferences with each other [20].

Equations (2) to (4) imply the following:

(1) The statistical analysis is performed for a single energy at a time.
(2) The polarization observable $\Omega^\alpha(W,\theta)$ and the unpolarized differential cross section $\sigma_0(W,\theta)$ have to share the same energy and angular binning.
(3) The observables $\Omega^\alpha(W,\theta)$ used within the TPWA have to share the same energy binning.
(4) As $\check{\Omega}^\alpha(W,\theta)$ is an observable, i.e., a real number, the matrices $\mathcal{C}_k^\alpha$ are Hermitian.
(5) The bilinear form of $\mathcal{A}_k^\alpha$ gives rise to mathematical ambiguities, as certain transformations leave this quantity invariant.

The last point is discussed in more detail in the following.

### A. Ambiguities

Ambiguities in PWA or TPWA refer to situations in which multiple configurations of the model parameters can describe the data points with similar levels of accuracy. This phenomenon is apparent in the reproduced data distributions in Figs. 1 and 2 where the different colored distributions, corresponding to multiple ambiguities, nearly overlap. In the following discussion, various types of mathematical ambiguities are examined and it is concluded that only so-called accidental discrete ambiguities can appear in the results of this paper.

The origin of the immanent mathematical ambiguities lies in the definition of the polarization observables. For photoproduction, they can be written in general as a bilinear product of the form [33–35]

$$\check{\Omega}^\alpha(W,\theta) = \kappa b^\dagger(W,\theta)\, \Gamma^\alpha\, b(W,\theta), \tag{5}$$

with a numerical prefactor $\kappa$, a vector $b$ of length $N_\mathrm{A}$, containing the complex spin amplitudes $b_i$, and a matrix $\Gamma^\alpha$ with dimensions $N_\mathrm{A} \times N_\mathrm{A}$. Certain transformations $T$ of the complex spin amplitudes $b_i(W,\theta) \xrightarrow{T} \tilde{b}_i(W,\theta)$ leave the bilinear product and thus the observable invariant. Hence, when all observables in a subset $\{\check{\Omega}^{\alpha_1}, \ldots, \check{\Omega}^{\alpha_n}\}$ are invariant under the same transformation, an ambiguity emerges [19,33], as the experimental distinction between $b_i$ and $\tilde{b}_i$ is not possible

[4] An overall factor of 1/2 is missing in the formula for $\mathcal{C}_k^\alpha$ in Ref. [19].

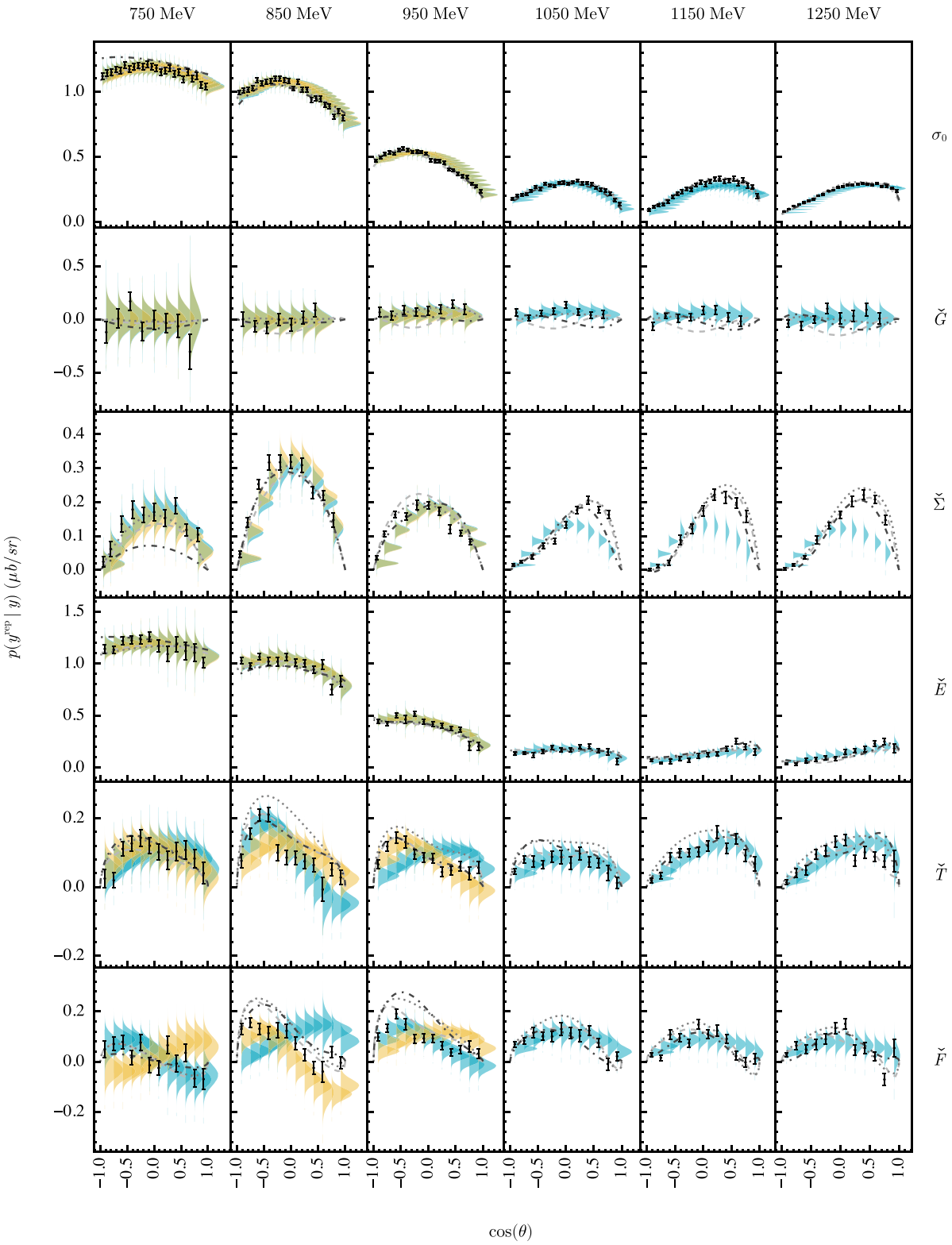


FIG. 1. Posterior predictive check for the profile functions $\sigma_0$, $\check{G}$, $\check{\Sigma}$, $\check{E}$, $\check{T}$, and $\check{F}$ for truncation order $\ell_{\max} = 1$ and energy bins $E_\gamma^{\mathrm{lab}} =$ [750, 850, 950, 1050, 1150, 1250] MeV. The reproduced data distributions for the different solutions are shown together with the original data with statistical uncertainties as black points. Each solution group is drawn in a different color and each peak of a distribution corresponds to an accidental ambiguity. In addition, the corresponding values from EtaMAID2018 [48] (dashed line), BnGa-2019 [42] (dotted line), and JüBo-2022 [47] (dash-dotted line) are shown as well.

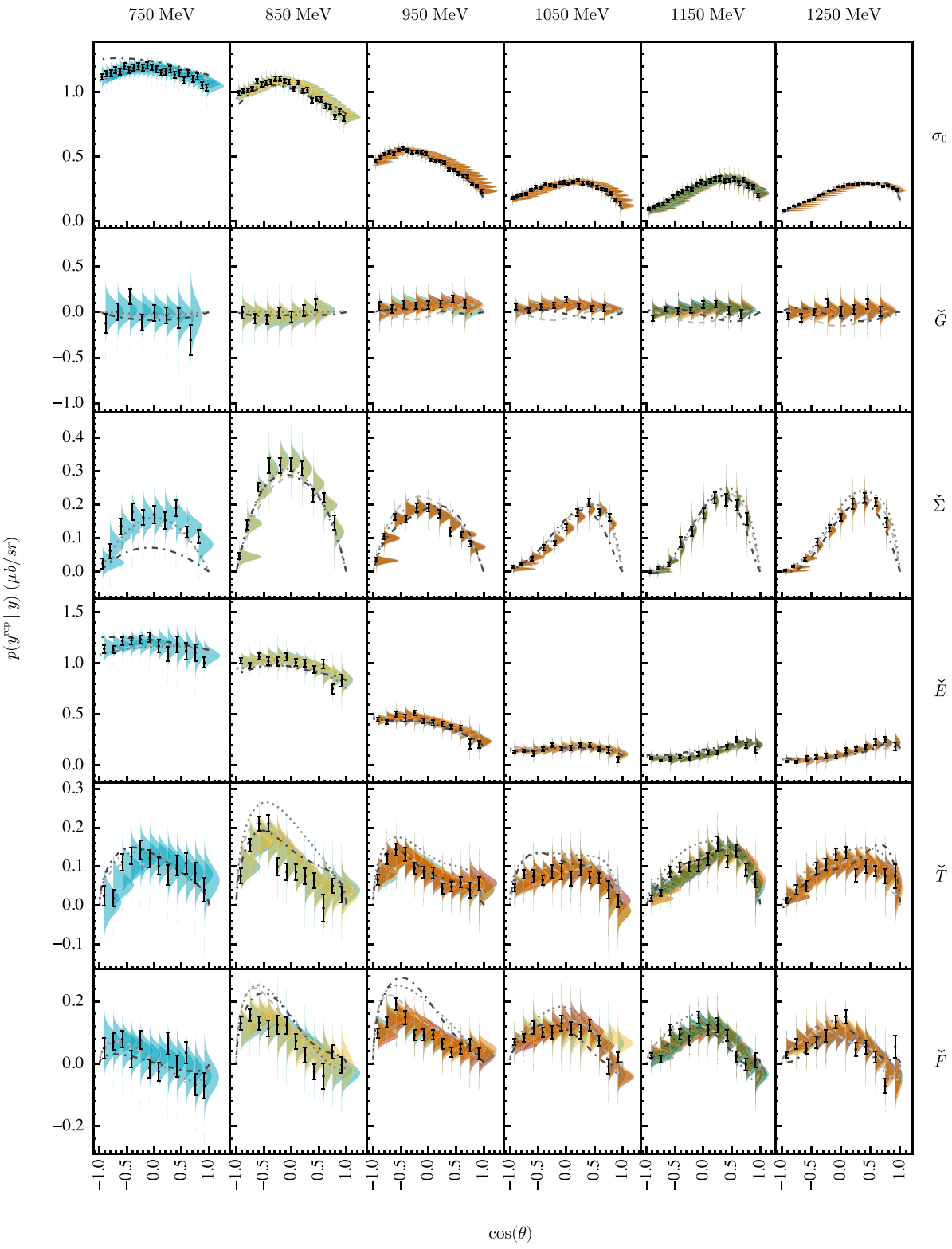


FIG. 2. Posterior predictive check for the profile functions $\sigma_0$, $\check{G}$, $\check{\Sigma}$, $\check{E}$, $\check{T}$, and $\check{F}$ for truncation order $\ell_{\max} = 2$ and energy bins $E_\gamma^{\mathrm{lab}} =$ [750, 850, 950, 1050, 1150, 1250] MeV. The reproduced data distributions for the different solutions are shown together with the original data with statistical uncertainties as black points. Each solution group is drawn in a different color and each peak of a distribution corresponds to an accidental ambiguity. In addition, the corresponding values from EtaMAID2018 [48] (dashed line), BnGa-2019 [42] (dotted line), and JüBo-2022 [47] (dash-dotted line) are shown as well.

any more. Such an ambiguity can be resolved by including a further observable $\check{\Omega}^{\alpha_k}$ into the subset, which is not invariant under the specific transformation [19,33]. There exists one special case of an ambiguity which cannot be resolved by including any further observables, namely, the simultaneous rotation of all transversity amplitudes by the same (possibly energy- and angle-dependent) phase: $b_i(W,\theta) \xrightarrow{T} e^{i\phi(W,\theta)} b_i(W,\theta)$ (see Ref. [33]). However, this continuous ambiguity can be ignored for the special case of a TPWA, since the angle-dependent part of the ambiguity is generally removed by the assumed truncation (see comments made in Ref. [36]), and the energy-dependent part is fixed by imposing certain phase conventions for the multipoles. The formalism for the remaining relevant discrete ambiguities in a TPWA is outline briefly in the following. For more information about discrete as well as continuous ambiguities in the case of the complete experiment analysis, see the paper of Chiang and Tabakin [33].

As shown by Omelaenko [19,21], in a TPWA (truncated at some finite $\ell_{\max} \geqslant 1$) the complex spin-amplitudes can be expressed (up to kinematical prefactors) as a finite product of irreducible polynomials:

$$b_1(W,\theta) \propto \prod_{k=1}^{2\ell_{\max}} \left( \tan\frac{\theta}{2} + \beta_k(W) \right), \tag{6}$$

$$b_2(W,\theta) \propto \prod_{k=1}^{2\ell_{\max}} \left( \tan\frac{\theta}{2} - \beta_k(W) \right), \tag{7}$$

$$b_3(W,\theta) \propto \prod_{k=1}^{2\ell_{\max}} \left( \tan\frac{\theta}{2} + \alpha_k(W) \right), \tag{8}$$

$$b_4(W,\theta) \propto \prod_{k=1}^{2\ell_{\max}} \left( \tan\frac{\theta}{2} - \alpha_k(W) \right), \tag{9}$$

with the complex roots $\alpha_k(W)$ and $\beta_k(W)$, which are in essence equivalent to multipoles. It can be shown [18,21,37] that the special case where $\tan(\theta/2) = 0$ implies a direct connection between the roots:

$$\prod_{i=1}^{2\ell_{\max}} \alpha_i(W) = \prod_{j=1}^{2\ell_{\max}} \beta_j(W). \tag{10}$$

All transformations $T$ which correspond to a discrete ambiguity of the four group-$\mathcal{S}$ observables $\{\sigma_0, \check{\Sigma}, \check{T}, \check{P}\}$ must also satisfy Eq. (10), which allows us to rule out a major part of the maximal possible $4^{2\ell_{\max}}$ [18] discrete ambiguity-transformations from the beginning. The so-called "double ambiguity" [18,21], which corresponds to the simultaneous complex conjugation of all roots automatically preserves the constraint in Eq. (10).

Unfortunately, there can also occur so-called accidental ambiguities. These emerge when any discrete ambiguity other than the double ambiguity of all roots approximately fulfills Eq. (10) [18]. The accidental ambiguities as well as the double ambiguity can in principle be resolved by including further observables into the analysis apart from the four group $\mathcal{S}$ observables. Candidates for observables capable of resolving the above-mentioned discrete ambiguities would be either $\check{F}$, $\check{G}$ or any of the $\mathcal{BR}$- and $\mathcal{TR}$-type observables.

The accidental ambiguities cannot be avoided for analyses of real data due to their abundance (i.e., $4^{2\ell_{\max}} - 2$ possible candidates exist for such ambiguities), and they will show up as modes within the posterior distribution and thus in the marginal parameter distributions.

In contrast with the discrete ambiguities described above, there can also exist so-called continuous ambiguities in the TPWA (in addition to the above-mentioned simultaneous phase-rotation of all transversity amplitudes, which has been ruled out), which exist on continuously connected regions within the multipole parameter space [19]. These ambiguities can occur in case an insufficiently small set of observables is analyzed, and they manifest as plateau-like structures (with possibly rounded edges) in the marginalized posterior-distributions, as opposed to the peak-like structures (or modes) originating from discrete ambiguities. The set of six observables analyzed in this work (see Sec. IV) is large enough to avoid such continuous ambiguities.

For more information about discrete ambiguities in TPWA, the paper by Omelaenko [21] and especially the subsequent work [18] is recommended. The proof of the completeness of the set of six observables analyzed in this work (Sec. IV) in the idealized case of an "exact" TPWA[5] proceeds a little bit different compared with the work by Omelaenko [21]. The proof is outlined in some detail in Sec. A.

Summarizing, accidental discrete ambiguities will likely be present within TPWA performed on real data, resulting in a multimodal likelihood and posterior distribution.

## IV. DISCUSSION OF THE DATABASE USED

A review of the currently available database on polarization observables for the reaction $\gamma p \to \eta p$ can be found in Ref. [1]. To cover the largest possible energy range and to resolve discrete mathematical ambiguities, the TPWA is performed using the six polarization observables $\sigma_0$ [38], $\Sigma$ [39], $T$ [40], $E$ [41], $F$ [40], and $G$ [42]. This choice of observables indeed resolves the discrete ambiguities of TPWA, as shown in Sec. A.

An overview of the data is given in Table III and a visualization of the phase-space coverage of the individual datasets can be found in Sec. B, Fig. 3. The available energies for the TPWA are determined by the observable with the lowest statistics [19,31], which in this case is the observable $G$. In total six energy bins are available, starting near the $\eta p$-photoproduction threshold at $E_\gamma^{\text{lab}} = 750$ MeV up to 1250 MeV, in 100 MeV steps.

As TPWA is a single-energy regression, the energy binning of each observable has to be shifted to that of $G$. The procedure is described in Ref. [19]. The advantage of this method is that no new, i.e., experimentally unobserved, data points have to be constructed, for example, via interpolation.

[5] Accidental ambiguities can be disregarded for this rather academic scenario [19].

TABLE III. Information on the experimental data, given as dimensionless asymmetries, used for the TPWA of $\gamma p \to \eta p$. Energy and angular ranges are written as intervals.

| Observable | Number of data points | $E_\gamma^{\text{lab}}$/MeV | $\cos(\theta)$ | Facility | References |
|---|---|---|---|---|---|
| $\sigma_0$ | 5736 | [723, 1571] | [−0.958, 0.958] | MAMI | Kashevarov *et al.* [38] |
| $T, F$ | 144 | [725, 1350] | [−0.917, 0.917] | MAMI | Akondi *et al.* [40] |
| $\Sigma$ | 140 | [761, 1472] | [−0.946, 0.815] | GRAAL | Bartalini *et al.* [39] |
| $E$ | 84 | [750, 1350] | [−0.917, 0.917] | MAMI | Afzal *et al.* [41,43] |
| $G$ | 47 | [750, 1250] | [−0.889, 0.667] | CBELSA/TAPS | Müller *et al.* [42] |

However, none of the observables are given as profile functions which are needed for the TPWA, see Eq. (2). Thus, the angular distribution of $\sigma_0$ has to be adjusted for each observable in order to multiply both. This is not an issue, since the very precise MAMI $\sigma_0$ dataset [38] covers a large angular range $[-0.958, 0.958]$ with a small step size $\approx 0.083$ in all available energies.

The data discussed in Sec. IV not only have statistical but also systematic uncertainties. The latter ones originate primarily from the determination of the polarization degree of the photon beam and the target nucleon, the dilution factor[6] as well as the background-subtraction procedure [38–42].

In principle, each data point has its own systematic uncertainty. However, there is no generally accepted method to model the systematic uncertainty for each data point separately. Instead, the contributions to the systematic uncertainty, which are constant over the whole angular range, are determined for each dataset. Then, the same systematic uncertainty is used for each data point within a dataset.

The contributions split up into the "general systematic uncertainty" ($\sigma_0$: 4% [[38], p. 5]), the degree of photon beam polarization (F: 2% [40], E: 2.7% [41], G: 5% [42]), and the degree of target polarization (T, F: 4% [40], E: 2.8% [41], G: 2% [42]). The authors of the polarization observable $\Sigma$ added the statistical- and systematic uncertainty in quadrature for each data point [39]. Thus, their systematic uncertainty cannot be modeled separately within this paper.

The individual systematic contributions within a dataset are combined in a conservative way. A worst-case scenario approach is employed, based on the formulas used to calculate the polarization observables, as given in the papers. In comparison with the "standard" procedure of adding the different contributions in quadrature, there are two main advantages: (1) The functional dependence is taken into account without the need to make an assumption about the distribution of the individual contributions. (2) The worst-case scenario covers the maximal and minimal impact of the systematic uncertainties, and everything in between.

As an illustrative example, suppose an observable $A$ which depends reciprocally on the degree of polarization of the photon beam $p_\gamma$ and target $p_t$, each with their own relative systematic uncertainty $\Delta_{\text{sys}}^{p_\gamma}$ and $\Delta_{\text{sys}}^{p_t}$, respectively. Then the combined, relative systematic uncertainty of $A$ would be

$$\Delta_{\text{sys}}^{A} = \max\Big(\Big|1-\big(1+\Delta_{\text{sys}}^{p_\gamma}\big)^{-1}\big(1+\Delta_{\text{sys}}^{p_t}\big)^{-1}\Big|, \Big|1-\big(1-\Delta_{\text{sys}}^{p_\gamma}\big)^{-1}\big(1-\Delta_{\text{sys}}^{p_t}\big)^{-1}\Big|\Big). \tag{11}$$

With the input taken from the references, corresponding to the respective datasets [38–42], the outlined approach results in $\Delta_{\text{sys}}^{\sigma_0} = 4.0\%$, $\Delta_{\text{sys}}^{\text{G}} = 7.4\%$, $\Delta_{\text{sys}}^{\text{E}} = 5.7\%$, $\Delta_{\text{sys}}^{\text{T}} = 4.2\%$, $\Delta_{\text{sys}}^{\text{F}} = 6.3\%$.

Due to the calculation of the profile functions, the systematic uncertainty of both datasets have to be combined as well:

$$\Delta_{\text{sys}}^{\check{A}} = \max\Big(\Big|1-\big(1+\Delta_{\text{sys}}^{A}\big)\big(1+\Delta_{\text{sys}}^{\sigma_0}\big)\Big|, \Big|1-\big(1-\Delta_{\text{sys}}^{A}\big)\big(1-\Delta_{\text{sys}}^{\sigma_0}\big)\Big|\Big). \tag{12}$$

Thus, the relative systematic uncertainties for the profile functions are $\Delta_{\text{sys}}^{\sigma_0} = 4.0\%$, $\Delta_{\text{sys}}^{\check{G}} = 11.7\%$, $\Delta_{\text{sys}}^{\check{E}} = 10.0\%$, $\Delta_{\text{sys}}^{\check{T}} = 8.3\%$, $\Delta_{\text{sys}}^{\check{F}} = 10.5\%$. The incorporation of the systematic uncertainties into the statistical model is described in more detail in Sec. V.

Furthermore, the calculation of the profile functions introduces a correlation between the unpolarized differential cross section and the profile functions, as well as among the profile functions themselves. Since certain values of $\sigma_0(W,\theta)$ were used to calculate $\check{\Omega}^\alpha(W,\theta)$, correlations were introduced between certain data points of both observables. Moreover, the same value of $\sigma_0(W,\theta)$ might be used to calculate data points of different profile functions.

The relevance of these correlations can be estimated via the Pearson correlation coefficient [44], see Eqs. (C4) and (C5) in Sec. C. The measured values of the polarization observables are used as expectation values and the corresponding squared statistical uncertainties as the variances. An example, for a correlation matrix is shown in Fig. 4. The correlations are quite small, with absolute values below $\approx 0.17$, but typically on the order of $10^{-2}$ to $10^{-3}$. An exception is the significantly higher correlation between $\sigma_0$ and $\sigma_0 \cdot E$, with minimal and maximal values of $\approx 0.29$ and $\approx 0.67$, respectively. This can be explained by the similar definition of the coefficients $\mathcal{A}_k^\alpha(W)$ of $\sigma_0$ and $\sigma_0 \cdot E$. Both having sensitivity to almost the exact same interference terms of multipoles, albeit with different strengths (see Ref. [20]). The magnitude of the correlation matrix elements as a function of the energy can be seen in Fig. 5. The corresponding covariance matrix, which is used to construct the likelihood distribution in Sec. V A, can be estimated via Eqs. (C2) and (C3) in Sec. C.

[6]The dilution factor is the ratio of polarizable free protons to all nuclei in the used target material.

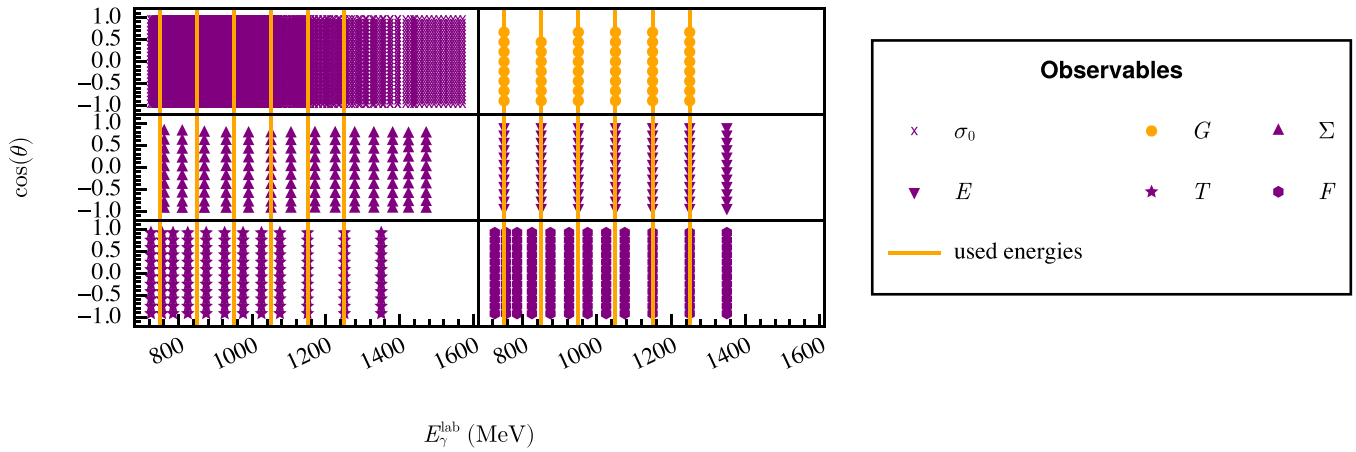


FIG. 3. Energy and angular coverage of the six observables $\sigma_0$, $\Sigma$, $G$, $E$, $T$, and $F$ [38–42] which were used for the analysis. The energies used, $E_\gamma^{\text{lab}} = [750, 850, 950, 1050, 1150, 1250]$ MeV, are determined by the observable $G$.

## V. THE POSTERIOR DISTRIBUTION

It is assumed that the utilized profile functions, constructed from the polarization observables, follow a normal distribution. The validity of this assumption is extensively discussed in Sec. D. However, the profile functions are correlated with the unpolarized differential cross section, as well as among themselves, see Sec. IV. This dependence is modeled within the likelihood distribution using a covariance matrix. In favor of a compact representation, the functional dependencies are not shown explicitly in the subsequent equations.

### A. Likelihood distribution

Combining the results of Secs. IV and D, the conditional likelihood distribution for each of the analyzed energies can be formulated as an $N$-dimensional multivariate Gaussian distribution:

$$p(\boldsymbol{y}, \boldsymbol{x} \mid \boldsymbol{\Theta}, \boldsymbol{\kappa}) = \mathcal{N}(\boldsymbol{\mu}, \boldsymbol{\Lambda}) = \frac{\exp\left(-\frac{1}{2}(\boldsymbol{y}-\boldsymbol{\mu})^{\mathrm{T}}\boldsymbol{\Lambda}^{-1}(\boldsymbol{y}-\boldsymbol{\mu})\right)}{\sqrt{(2\pi)^N|\boldsymbol{\Lambda}|}}. \tag{13}$$

Herein, the vectors $\boldsymbol{y}, \boldsymbol{x} \in \mathbb{R}^N$ contain the entirety of the $N \in \mathbb{N}$ utilized profile function data points and the corresponding $\cos(\theta)$ values at which they were measured, respectively:

$$\boldsymbol{y} = [\boldsymbol{y}^{\sigma_0}, \boldsymbol{y}^{\check{G}}, \boldsymbol{y}^{\check{\Sigma}}, \boldsymbol{y}^{\check{E}}, \boldsymbol{y}^{\check{T}}, \boldsymbol{y}^{\check{F}}], \tag{14}$$

$$\boldsymbol{x} = [\boldsymbol{x}^{\sigma_0}, \boldsymbol{x}^{\check{G}}, \boldsymbol{x}^{\check{\Sigma}}, \boldsymbol{x}^{\check{E}}, \boldsymbol{x}^{\check{T}}, \boldsymbol{x}^{\check{F}}]. \tag{15}$$

The parameters of the model can be divided into two groups. On the one hand, the real- and imaginary parts of multipoles, i.e., Eq. (4), denoted by $\boldsymbol{\Theta} \in \mathbb{R}^{8\ell_{\max}-1}$ are used to

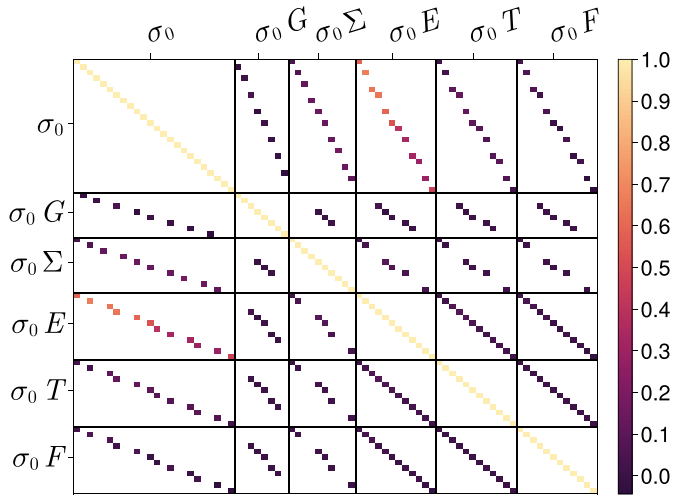


FIG. 4. Example for a correlation matrix. The correlations between the data points of the unpolarized differential cross section $\sigma_0$ and the profile functions used, as well as the correlation between the profile functions themselves, is shown for $E_\gamma^{\text{lab}} = 750$ MeV. Each square represents a certain data point. The color encodes the correlation strength ranging from $-1$ (darker colors) to $+1$ (lighter colors).

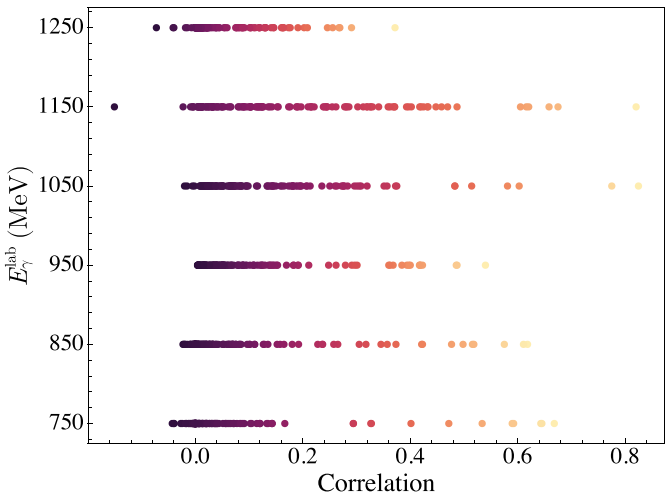


FIG. 5. Unique correlation matrix element values as a function of the laboratory frame energy. The color encodes the correlation strength ranging from $-1$ (darker colors) to $+1$ (lighter colors).

model the underlying physical process. On the other hand, the parameters $\boldsymbol{\kappa} \in \mathbb{R}^5$ which are used to model the systematic uncertainties of the involved datasets:

$$\boldsymbol{\kappa} = [\kappa^{\sigma_0}, \kappa^{\check{G}}, \kappa^{\check{E}}, \kappa^{\check{T}}, \kappa^{\check{F}}]. \tag{16}$$

The multivariate normal distribution in Eq. (13) is constructed with the model predictions $\boldsymbol{\mu} \in \mathbb{R}^N$ for the expectations of $\boldsymbol{y}$:

$$\boldsymbol{\mu}(\boldsymbol{\Theta}, \boldsymbol{\kappa}, \boldsymbol{x}) = [\kappa^{\sigma_0}\boldsymbol{\mu}^{\sigma_0}, \kappa^{\check{G}}\boldsymbol{\mu}^{\check{G}}, 1\boldsymbol{\mu}^{\check{\Sigma}}, \kappa^{\check{E}}\boldsymbol{\mu}^{\check{E}}, \kappa^{\check{T}}\boldsymbol{\mu}^{\check{T}}, \kappa^{\check{F}}\boldsymbol{\mu}^{\check{F}}]. \tag{17}$$

The $\boldsymbol{\mu}^{\alpha}(\boldsymbol{\Theta}, \boldsymbol{x}^{\alpha})$ are the model predictions for the individual profile functions, i.e., Eq. (2). Hence, in order to model the systematic uncertainties, one additional parameter per relevant dataset is introduced and multiplied with the corresponding theoretical prediction for the profile function. Thus, the model gets additional degrees of freedom to adjust for possible systematic uncertainties. However, these parameters are restricted to physical meaningful bounds, further discussed in Sec. V B. As explained in Sec. IV, the systematic uncertainty of the polarization observable $\Sigma$ cannot be modeled.

Finally, there is the covariance matrix $\boldsymbol{\Lambda} \in \mathbb{R}^{N\times N}$. Its off-diagonal terms are not identical, and therefore the data pairs are not exchangeable.[7]

### B. Prior distribution

The priors for the multipole parameters are chosen as uniform priors with bounds corresponding to the physically allowed ranges of the parameters (see Ref. [19]). Thus, the priors incorporate physical knowledge while being uninformative compared with the likelihood distribution.

In principle a uniform prior for the systematic parameters would be reasonable. However, in this case the hard boundaries in the parameter space lead to numerical issues. Thus, the prior distributions for the scaling parameters $\boldsymbol{\kappa}$ are assumed to be normally distributed and centered around the value one. The standard deviation is chosen such that[8] 99% of the distribution are within the range $1 \pm \Delta^{\alpha}_{\text{sys}}$, which results in (rounded to five digits):

$$\kappa^{\sigma_0} \sim \mathcal{N}(1, 0.01552), \tag{18}$$

$$\kappa^{\check{G}} \sim \mathcal{N}(1, 0.04542), \tag{19}$$

$$\kappa^{\check{E}} \sim \mathcal{N}(1, 0.03882), \tag{20}$$

$$\kappa^{\check{T}} \sim \mathcal{N}(1, 0.03222), \tag{21}$$

$$\kappa^{\check{F}} \sim \mathcal{N}(1, 0.04076). \tag{22}$$

This choice is in accordance with the conservative combination of the systematic uncertainties, as discussed in Sec. IV. The treatment of systematic errors within this paper is similar to that in Refs. [31,46,47].

## VI. RESULTS

Bayesian inference was utilized to extract the electromagnetic multipole parameters, as introduced in Eq. (4), for the reaction $\gamma p \to \eta p$ at energies $E_{\gamma}^{\text{lab}} = [750, 850, 950, 1050, 1150, 1250]$ MeV and truncation orders $\ell_{\max} = 1, 2$ through truncated partial-wave analysis. The procedures involved are detailed in Sec. E.

Highly multimodal posterior distributions were encountered, necessitating an adaptation of the typical MCMC convergence diagnostic workflow. The adjusted procedure is detailed in Sec. E 3. By studying the reproduced data distributions for the various truncation orders, an indication of $N^*$ resonances in the energy range from 950 to 1050 MeV is observed. Finally, utilizing the electromagnetic multipole parameter estimates, predictions were calculated[9] for the polarization observables $H$ and $P$ as well as those of group $\mathcal{BR}$ and $\mathcal{TR}$. Hence, this includes eight polarization observables that are yet to be measured. The distributions of the multipole parameters, the reproduced and predicted data are presented alongside the values of EtaMAID2018 [48], BnGa-2019 [42], and JüBo-2022 [47].

The presentation of the multipole parameter results is quite detailed and deserves an explanation. The top part shows the solutions found via Monte Carlo maximum *a posteriori* estimation and their corresponding $\chi^2/ndf$ values, together with the $1\sigma$ uncertainty (see Sec. E 1). The middle part shows the marginal-parameter distributions obtained via Bayesian inference, as explained in Secs. V and E 2. For a better comparison of the two approaches for $\ell_{\max} = 1$, the [0.16, 0.5, 0.84] quantiles of the distributions, corresponding to the median of the distribution and the $1\sigma$-uncertainty boundaries, are drawn as dashed lines through all parts of the figure. Whereas, for $\ell_{\max} = 2$ a solid vertical line is drawn for each peak of the multimodal distribution, i.e., the most probable values. The bottom part of the figure is a contour plot of the log posterior density distribution and the corresponding marginal-parameter distribution. The outermost contour line is at 1% of the maximum altitude, each subsequent line represents an 11% increase. It is assumed that a log posterior distribution centered around a higher log posterior value, corresponds to more likely parameter values because this solution contributes more probability mass to the posterior. Each solution group is drawn in a different color and each peak of a distribution corresponds to an accidental ambiguity. The color for a specific solution group is consistent between the shown figures (MCMC convergence, multipole, predictive performance plots, etc.) for a certain energy and truncation order. This

[7] If the joint probability density function $p(\boldsymbol{y}, \boldsymbol{x}|\boldsymbol{\Theta}, \boldsymbol{\kappa})$ is invariant under permutations of the data pairs $(y, x)_i$, then the data pairs are said to be exchangeable [23,45].

[8] This can be calculated by solving numerically the following equation for the standard deviation $\sigma$:

$$\int_{-\infty}^{1-\Delta^{\alpha}_{\text{sys}}} \frac{\exp\left(-\frac{1}{2}\left(\frac{x-1}{\sigma}\right)^2\right)}{\sigma\sqrt{2\pi}} dx = \frac{1-0.99}{2}.$$

[9] To get from the profile functions to the dimensionless polarization observables, the predicted distribution is divided by a certain $\sigma_0$ value, corresponding to the $\cos(\theta)$ value at which the prediction were calculated.

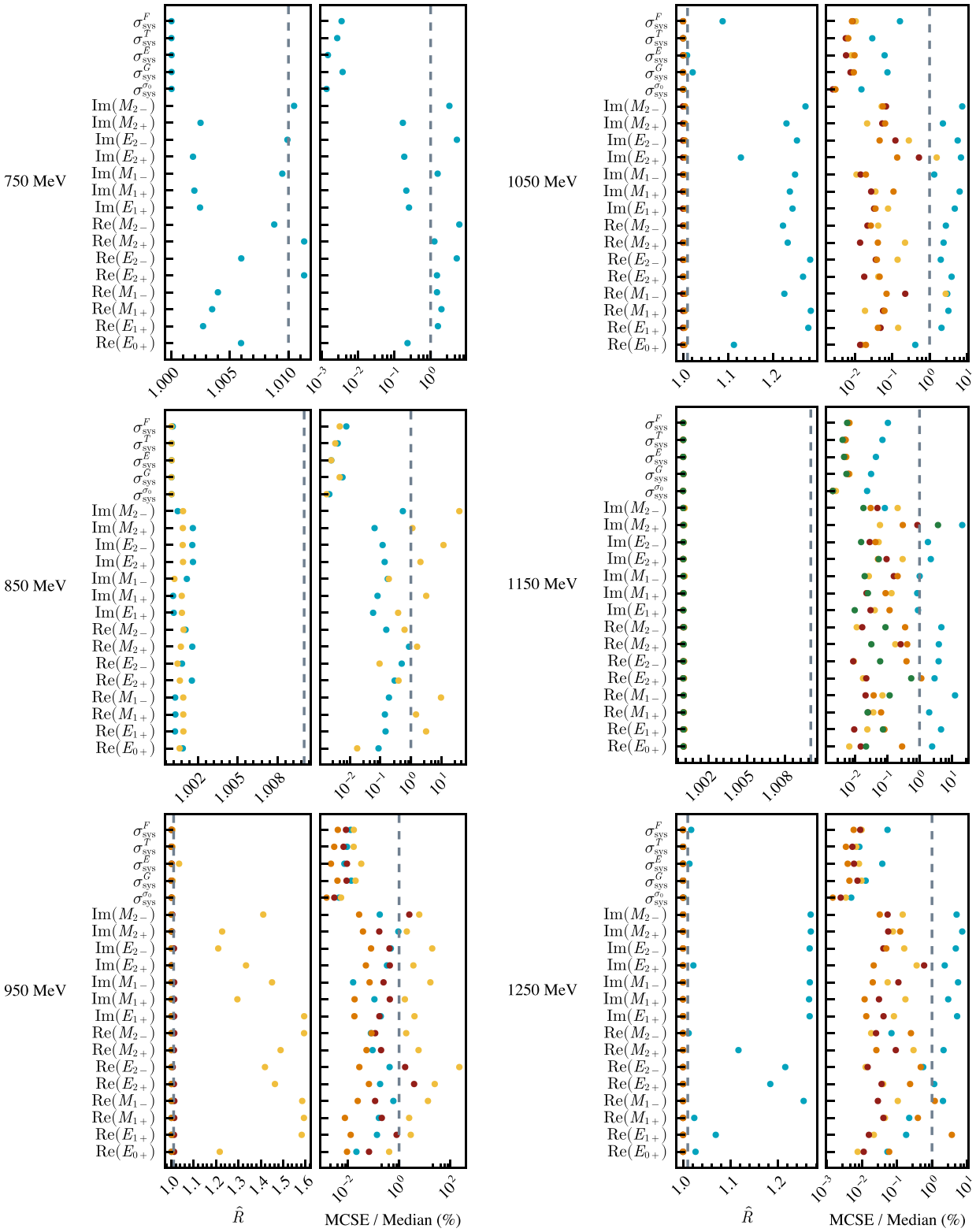


FIG. 6. MCMC convergence diagnostics for the truncation order $\ell_{\text{max}} = 2$. Shown are the potential-scale-reduction statistic $\hat{R}$ (the gray, dashed line indicates the value of 1.01) and the Monte Carlo standard error (MCSE) for the median divided by the median in percent (the gray, dashed line indicates the value of 1%). Each solution group is drawn in a different color.

means one can monitor the behavior of a specific ambiguity, ranging from the MCMC diagnostic plots in Fig. 6 to the multipole plots in Figs. 7 and 8, to the reproduced data plots in Fig. 2, up to the predicted data distribution plots in Fig. 9. The performed analyses showed, that Bayesian inference gives more insight into the relevance of ambiguities, due to the Hamiltonian Monte Carlo algorithm. When multiple chains sample consistently multiple marginal modes together, this

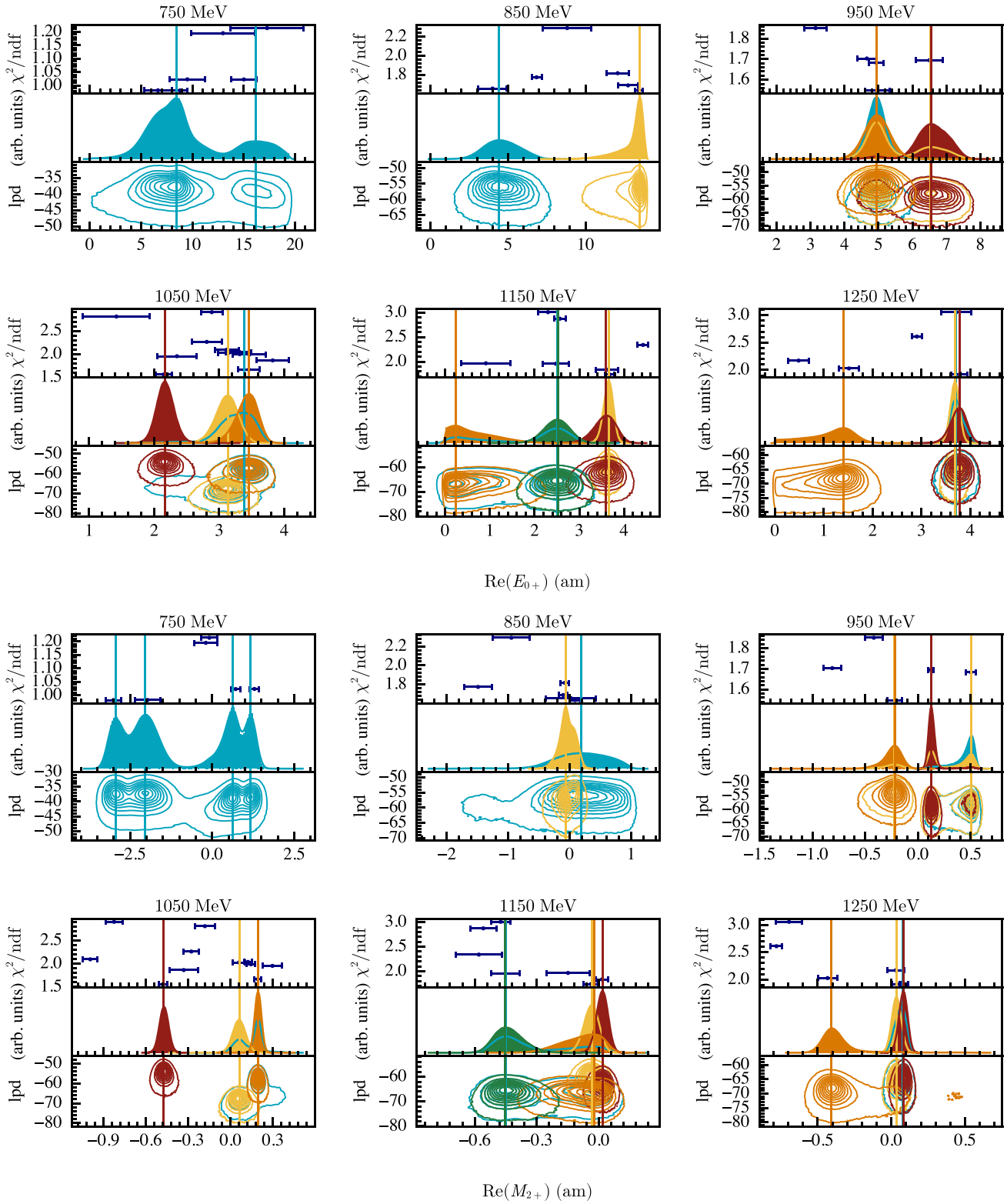


FIG. 7. Solutions of the multipole parameters Re($E_{0+}$) and Re($M_{2+}$) for a truncation order of $\ell_{\max} = 2$, for the energy bins $E_\gamma^{\text{lab}} =$ [750, 850, 950, 1050, 1150, 1250] MeV. Each solution group is drawn in a different color and each peak of a distribution corresponds to an accidental ambiguity. The different parts of the tripartite plots are explained at the beginning of Sec. VI. The natural logarithm was used to calculate the log posterior density (lpd).

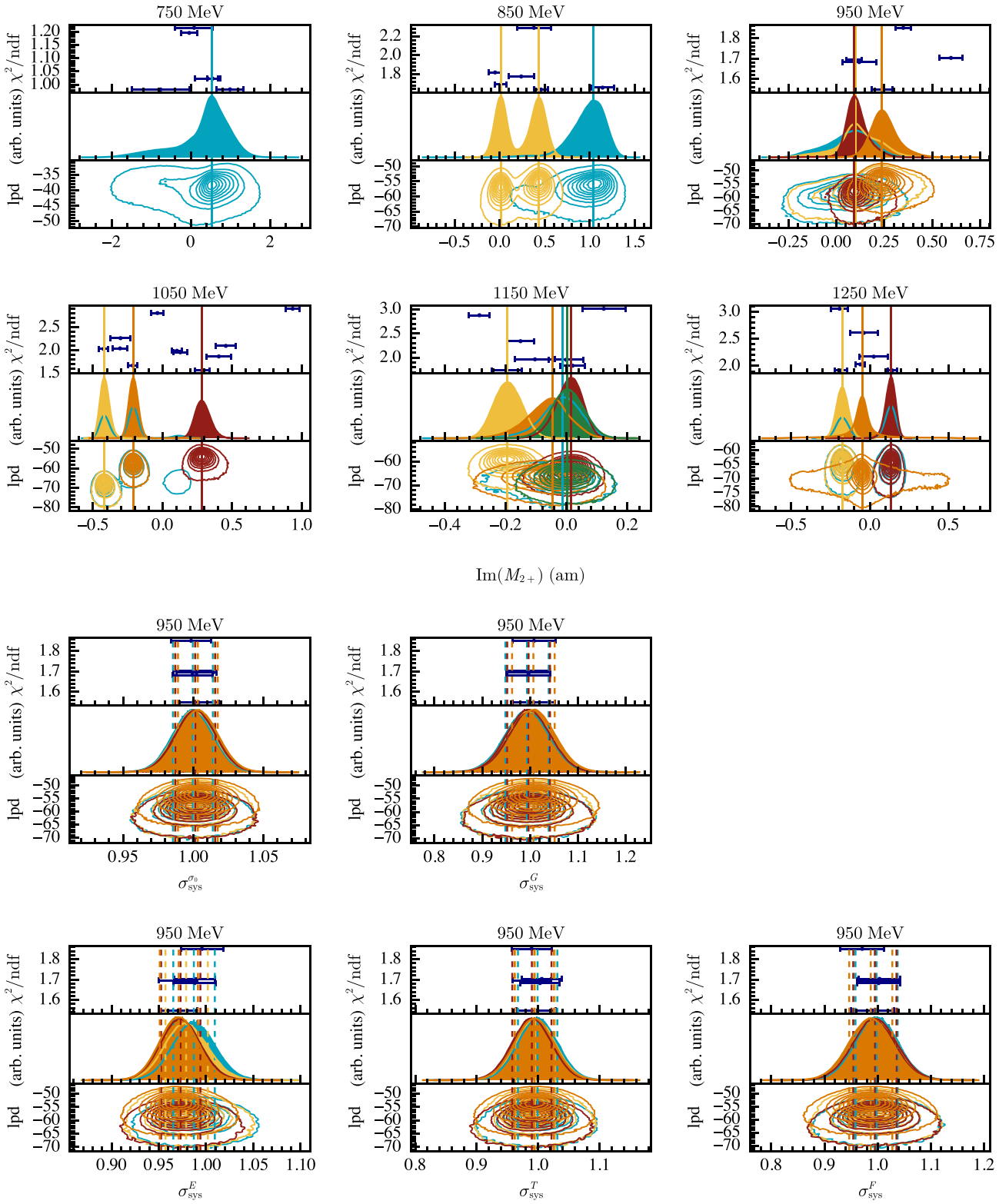


FIG. 8. Solutions of the multipole parameter $\mathrm{Im}(M_{2+})$ for a truncation order of $\ell_{\max} = 2$, for the energy bins $E_\gamma^{\mathrm{lab}} = [750, 850, 950, 1050, 1150, 1250]$ MeV. In addition, solutions of systematic parameters for a truncation order of $\ell_{\max} = 2$ for the energy bin $E_\gamma^{\mathrm{lab}} = 950$ MeV are shown. Each solution group is drawn in a different color and each peak of a distribution corresponds to an accidental ambiguity. The different parts of the tripartite plots are explained at the beginning of Sec. VI. The natural logarithm was used to calculate the log posterior density (lpd).

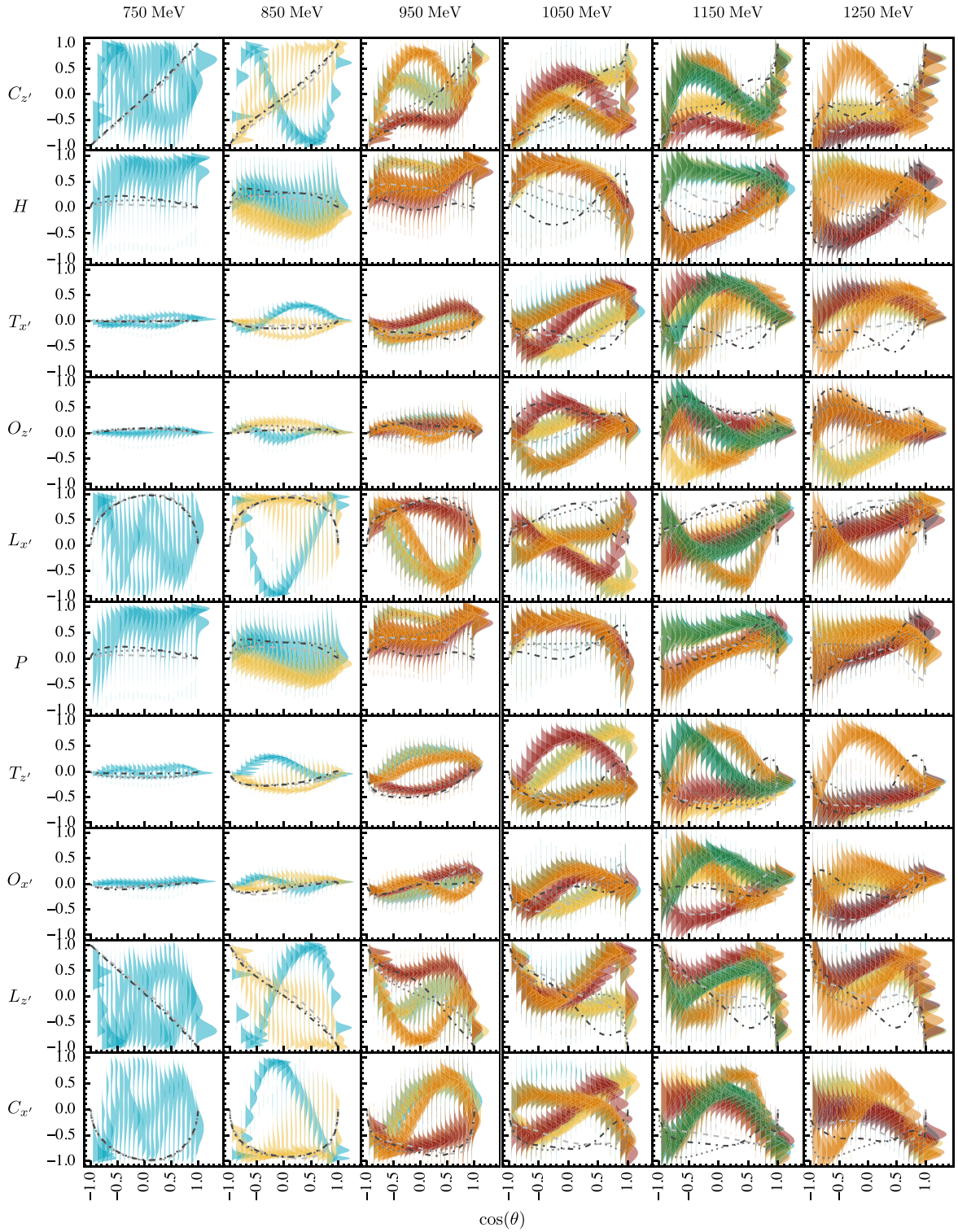


FIG. 9. Predicted data distributions for the polarization observables $C_{z'}$, $H$, $T_{x'}$, $O_{z'}$, $L_{x'}$, $P$, $T_{z'}$, $O_{x'}$, $L_{z'}$, and $C_{x'}$ for the energy bins $E_\gamma^{\text{lab}} = [750, 850, 950, 1050, 1150, 1250]$ MeV, using a truncation order of $\ell_{\text{max}} = 2$. Each solution group is drawn in a different color and each peak of a distribution corresponds to an accidental ambiguity. In addition, the corresponding values from EtaMAID2018 [48] (dashed line), BnGa-2019 [42] (dotted line), and JüBo-2022 [47] (dash-dotted line) are shown as well.

is a sign of a problematic ambiguity, as they tend to have comparable log posterior densities. As an example, consider the multipole solution for $\text{Re}(M_{2+})$ at 750 MeV in Fig. 7. This is an advantage over the maximum likelihood approach.

Within the following discussion of the results a representative selection of figures is shown. All parameter figures, for all analyzed energies and truncation orders can be found in the Supplemental Material [49].

### A. Impact of accidental ambiguities on the results

As discussed in Sec. III A, accidental ambiguities appear in the results of the marginal multipole parameter distributions, which subsequently manifest in both the replicated and predicted data distributions, as well as in the marginal systematic parameter distributions. The ambiguities are apparent as differently colored distributions, where each peak of a distribution corresponds to an accidental ambiguity. See, for example, 2 and 7 to 9. As expected, all accidental ambiguities can replicate the original data points. The corresponding reproduced data distributions are nearly identical, as illustrated in Fig. 2. The impact of ambiguities on predicted data distributions and what can be learned from it is discussed in Sec. VI F.

### B. Choice of the truncation order

At first, the regression was conducted using $\ell_{\max} = 1$. For each of the six energy bins, the number of warmup and postwarmup samples was set to $2\times10^4$, respectively. In total, $N_c = 10$ chains are started at each solution, found via the Monte Carlo maximum *a posteriori* approach. The corresponding MCMC convergence diagnostics, displayed in Sec. F, Fig. 10, support this decision, with $\hat{R} < 1.01$ and relative Monte Carlo standard error within a few percent or less.

For each energy bin above 950 MeV, specifically 1050, 1150, and 1250 MeV, the measured $\sigma_0$ data are systematically higher for $\cos(\theta) > 0$ compared with the TPWA predictions. Furthermore, the TPWA predictions for $\check{\Sigma}$ do not resemble the original data points at all, as shown in Fig. 1. It appears that the statistical model utilized with truncation order $\ell_{\max} = 1$ cannot adequately replicate data points for all observables. An elucidation for this phenomenon is provided in Sec. VI C.

To enhance the data description flexibility of the TPWA model, the truncation order was increased to $\ell_{\max} = 2$, and the regression was re-executed. To obtain the desired MCMC convergence diagnostics for each of the six energy bins, it was necessary to increase the number of warmup and postwarmup samples to $5\times10^4$, respectively. $N_c$ remains the same as for $\ell_{\max} = 1$. The corresponding MCMC convergence diagnostics are displayed in Sec. F, Fig. 6. Special phenomena that occur are discussed in detail in Sec. F. The TPWA model with a truncation order of $\ell_{\max} = 2$ effectively describes the original data points as evinced by the data distributions reproduced in Fig. 2.

In general, it is preferable to set the truncation order $\ell_{\max}$ as high as possible, because lower partial waves can interfere with higher ones, leading to non-negligible contributions. However, increasing the truncation order also increases the number of accidental ambiguities. For example, with $\ell_{\max} = 3$ and 1250 MeV, 43 posterior modes were identified. This results in a situation that demands a large number of numerical computations to achieve the desired MCMC convergence diagnostics. Additionally, the visual assessment of clustering becomes challenging due to the large number of required chains. Furthermore, the statistical quality of the combined datasets do not permit observations of any $F$-wave contributions, such as those from the $N(1680)5/2^+$ [2] resonance at $E_\gamma^{\text{lab}} \approx 1035$ MeV. Due to these considerations, this paper focuses on $\ell_{\max} = 2$, while truncation orders with $\ell_{\max} > 2$ are reserved for future research.

### C. Indication of $N^*$ resonances

To summarize, the model with $\ell_{\max} = 1$ is inadequate in replicating the original data points for $\sigma_0$ and $\check{\Sigma}$ for the energies above 950 MeV. This phenomenon could be explained by an emerging resonance in the energy range between 950 and 1050 MeV that couples to an orbital angular momentum $\ell > 1$ and predominantly contributes to $\sigma_0$ and $\check{\Sigma}$. Since isospin is a conserved quantity in the strong interaction, the reaction of $\eta$ photoproduction serves as an isospin filter, meaning that for the subsequent discussion, only $N^*$ resonances require consideration. There are two $N^*$ resonances which fulfill the conservation laws, couple to $\ell = 2$, and fall within the required energy range (taking into account the Breit-Wigner width [2] of the resonances). These resonances are $N(1675)5/2^-$ [2] at $E_\gamma^{\text{lab}} \approx 1026$ MeV and $N(1700)3/2^-$ [2] at $E_\gamma^{\text{lab}} \approx 1071$ MeV.

There is also a resonance which opens up already at $E_\gamma^{\text{lab}} \approx 762$ MeV, specifically $N(1520)3/2^-$ [2]. However, this resonance has a branching ratio to $\eta N$ [2] that is $\approx$10 times smaller than those of $N(1675)5/2^-$ and $N(1700)3/2^-$. The datasets employed do not appear to possess the necessary sensitivity to see a contribution of $N(1520)3/2^-$.

### D. Multipole parameters

The solutions for $E_{0+}$ and $M_{2+}$ are shown as representative examples of the multipole parameters in Figs. 7 and 8. The figures for all multipole parameters are available in the Supplemental Material [49]. Typically, the peaks of the marginal distributions are in agreement with the first few "best" *a posteriori* estimates. However, not every *a posteriori* solution has a corresponding peak within the marginal distributions. This could be due to two potential reasons. On the one hand, the interpretation of a marginal distribution differs from that of a maximum *a posteriori* estimate. On the other hand, the reason may lie within the Hamiltonian Monte Carlo algorithm [26,27], where it has been observed that some of the starting values are not in close proximity to the "typical set"[10] [50] but adjust rapidly. An example is shown in Fig. 11.

Within Fig. 12, the fifteen multipole parameters are graphed based on the laboratory energy of the photon. The corresponding values of EtaMAID2018 [48], BnGa-2019 [42], and JüBo-2022 [47] are also shown. For a detailed comparison of the various solution clusters and their relevance, readers are encouraged to refer to the tripartite multipole parameter figures in Figs. 7 and 8 and the Supplemental Material in Ref. [49].

[10]The "typical set" are the regions of the posterior which contribute the most to its expectation value.

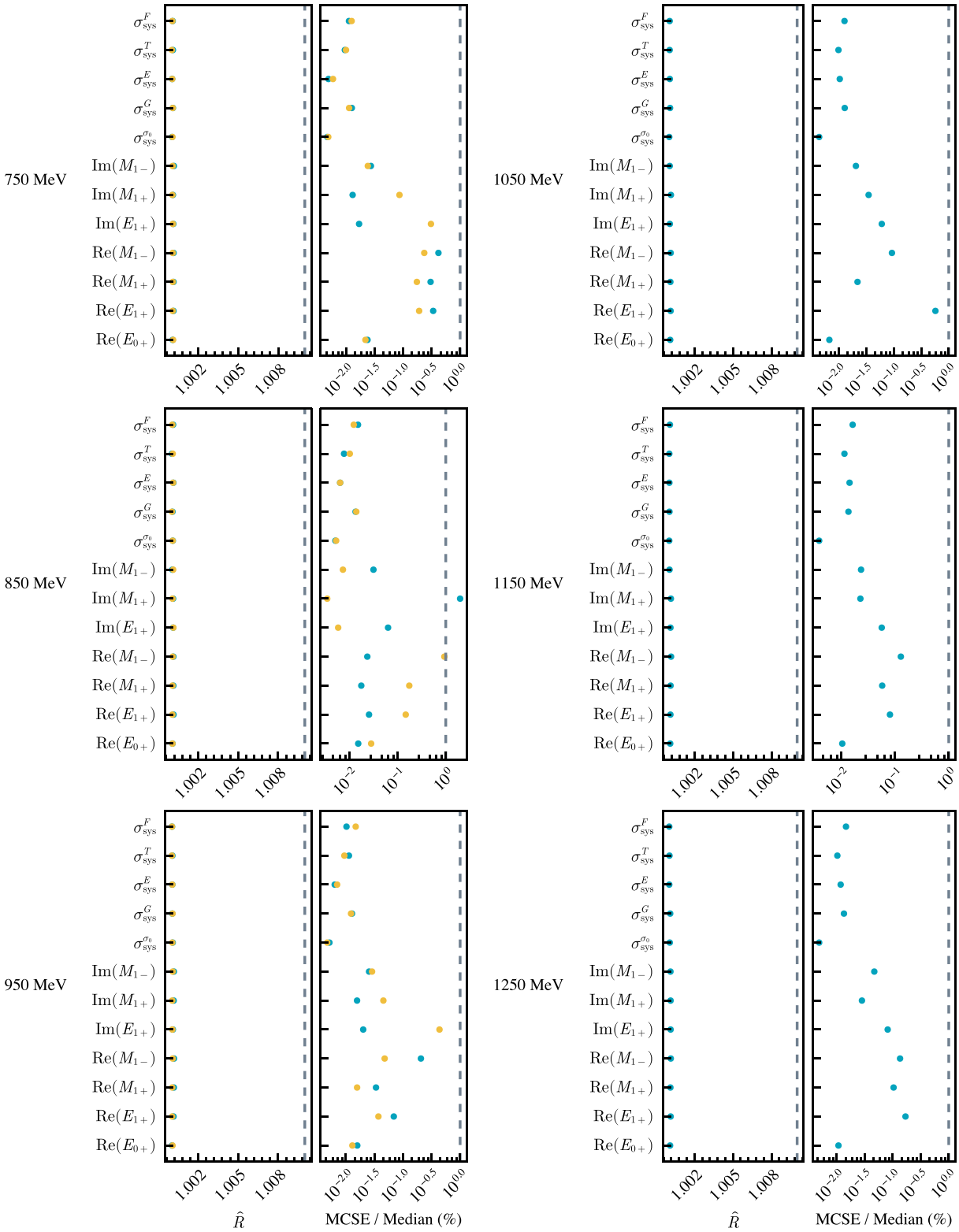


FIG. 10. MCMC convergence diagnostics for the truncation order $\ell_{\max} = 1$. Shown are the potential-scale-reduction statistic $\hat{R}$ (the gray, dashed line indicates the value of 1.01) and the Monte Carlo standard error (MCSE) for the median divided by the median in percent (the gray, dashed line indicates the value of 1%). Each solution group is drawn in a different color.

### *d1. Comparison with MAID, BnGa, and JuBo*

In general, the paper's results align well with the values of EtaMAID2018, BnGa-2019, and JüBo-2022. However, there are two noteworthy exceptions.

First, for the multipole parameter $\mathrm{Im}(E_{2+})$, none of the PWA values align with each other nor with the TPWA results of this paper. Second, the three PWAs report a value of ≈20 mfm for the multipole parameter $\mathrm{Re}(E_{0+})$ at 750 MeV. This

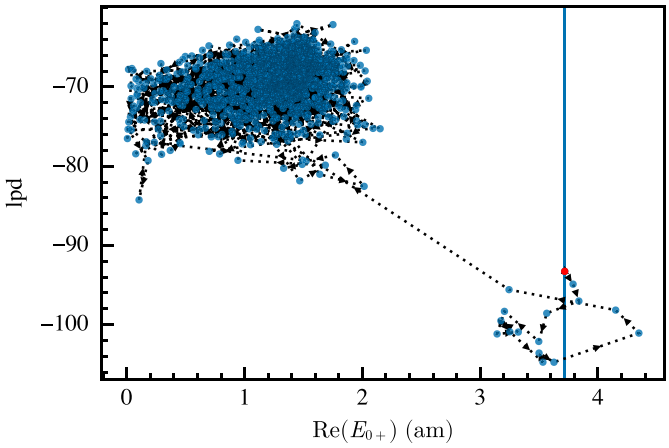


FIG. 11. Illustration of the first 1000 sampling points of a chain with initial value at 3.7 (the blue vertical line). The first sampling point is drawn in red. The chain converges from its starting point to a more likely solution, i.e., with higher log posterior density (lpd) value. The natural logarithm was used to calculate the lpd.

significant value of $E_{0+}$ close to the $\eta p$-production threshold results from the dominant $N(1535)1/2^-$ resonance, which couples to the $S$-wave $E_{0+}$. The datasets of $\eta$ photoproduction (see Sec. IV) utilized in this analysis do not emphasize such high values. Although the marginal parameter distribution does indeed have a nonzero probability at ≈19 mfm, the most likely values are around 8.5 mfm. This unexpected difference may have multiple causes. On the one hand, both BnGa-2019 and JüBo-2022 are coupled-channel analyses that involve a variety of final states simultaneously [14]. On the other hand, EtaMAID2018, BnGa-2019, and JüBo-2022 use the $\pi N$ partial-wave amplitudes from SAID [14] as input, which includes the $N(1535)1/2^-$ resonance [51].

In contrast, the current analysis is not a coupled-channel analysis nor does it rely on the SAID solutions. The values of the multipole parameters are exclusively obtained from the $\eta$-photoproduction datasets presented in Sec. IV.

In addition, the TPWA relies on single-energy regression, which implies that solely the available data points at a particular energy bin can be utilized in the analysis. As the PWAs do not follow this restriction, the complete available datasets can be utilized. This is particular important for the differential cross section, where the increased data can have a significant impact on the regression.

Furthermore, although a dominant $S$-wave $E_{0+}$ results in a nearly constant maximal allowed value of one for the observable $E$ for all angles, the inverse conclusion does not always hold true. For example, the observable $E$ cannot differentiate between $S$-wave $E_{0+}$ and $P$-wave $M_{1-}$ since both can lead to these maximum values of $E$. As shown in our results for 750 MeV (see Fig. 12), the expected strength of $E_{0+}$ has migrated to other multipoles, such as $M_{1-}$.

Improved statistics of the datasets involved in terms of the angular range or the inclusion of additional observables in future analyses, may shift the probability mass of the distribution of Re($E_{0+}$) at 750 MeV towards the values of EtaMAID2018, BnGa-2019, and JüBo-2022.

### E. Systematic parameters

The systematic parameters are all around the intended value of one. Each marginal distribution, for all systematic parameters and for all analyzed energy bins, is exclusively unimodal. Examples can be found in Fig. 8 and the Supplemental Material [49].

### F. Predicted data distributions

Using the estimated multipole parameters, predictions for polarization observables were calculated which were not utilized in this analysis. These include the observables $H$, $P$ as well as all eight observables of the groups $\mathcal{BR}$ and $\mathcal{TR}$ that have yet to be measured [1]. The predicted data distributions are displayed in Fig. 9. The distributions are within the physical bounds between $-1$ and 1 and their overall course over the angular range shows the correct tendency at $\cos(\theta) = \pm 1$ towards the mathematically expected values [18].

An interesting effect can be observed. The predicted data distributions for the various ambiguities, show specific functional trajectories over the angular range. In contrast, for the reproduced data plots, the distributions were almost identical for different ambiguities. If there were experimental data related to one of the predicted observables that supports only one of the specific functional trends throughout the angular range, it would eliminate any other ambiguity.

According to this criterion, potentially significant polarization observables have been chosen for upcoming experiments and are consolidated in Table IV. In particular, the polarization observable $C_{z'}$ seems suitable to reduce the ambiguities at all six energy bins.

## VII. SUMMARY AND OUTLOOK

A TPWA was conducted for $\eta$-meson photoproduction off the proton near the production threshold. Model-independent estimates of electromagnetic multipole parameters were determined, allowing the first model-independent calculation of predictions of unmeasured polarization observables. Based on these results, promising future measurements were identified with the aim of minimizing remaining ambiguities.

The datasets used in this study demonstrate clear $D$-wave contributions above $E_\gamma^{\text{lab}} = 950$ MeV, but are not sensitive to $F$-wave or higher partial-wave contributions.

For the first time, this study combined TPWA with Bayesian inference. The posterior distributions were highly multimodal, necessitating adaptations to monitor the MCMC convergence diagnostics. Despite its simplicity and use of fewer data, the TPWA approach maintains model-independence and achieves results consistent with the PWAs of MAID2018, BnGa-2019, and JüBo-2022.

In general, resonances can be extracted from multipole parameters. However, for a precise extraction of the resonance parameters the current resolution of the combined datasets is not sufficient. In a subsequent study, the TPWA approach could be combined with the Laurent + Pietarinen parametrization for every multipole parameter [52] in order

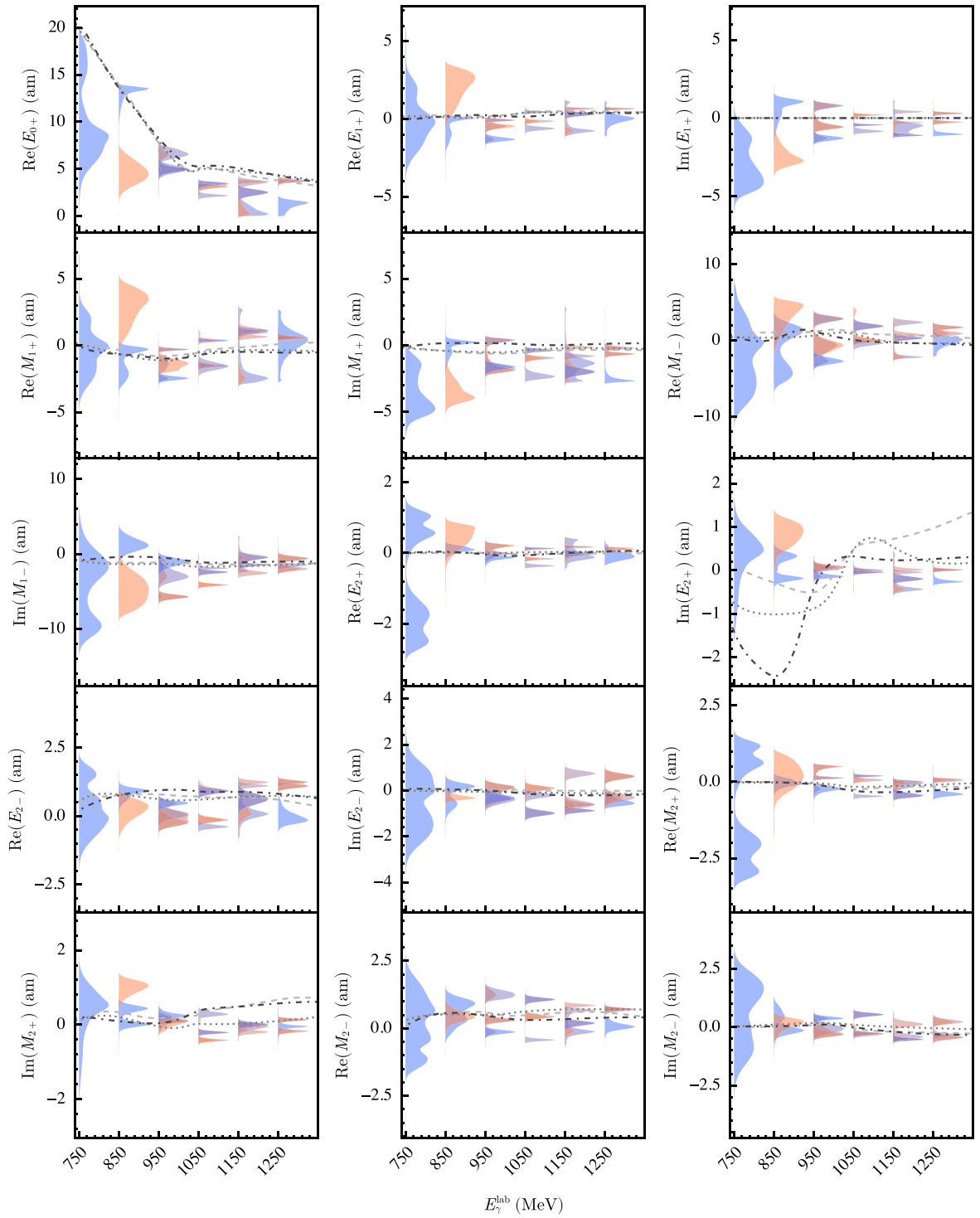


FIG. 12. Marginal multipole solutions for the truncation order $\ell_{\max} = 2$ for the energy bins $E_\gamma^{\text{lab}} = [750, 850, 950, 1050, 1150, 1250]$ MeV. In addition, the multipole parameter predictions from EtaMAID2018 [48] (dashed line), BnGa-2019 [42], (dotted line) and JüBo-2022 [47] (dash-dotted line) are shown as well. The relevance of a solution is represented by a transition from sienna (less relevant) to blue (more relevant) hues. However, for a detailed comparison between the solutions and their relevance to each other, the reader is advised to the tripartite multipole parameter figures in Figs. 7 and 8 and Ref. [49].

to extract resonance parameters. In addition, the role of the prior distribution with regard to resolving the mathematical ambiguities could be investigated.

## ACKNOWLEDGMENTS

The authors would like to thank Professor Dr. Sebastian Neubert, Professor Dr. Carsten Urbach, and Dr. Jan Hartmann

TABLE IV. Promising polarization observable candidates to resolve the ambiguities for truncation order $\ell_{\max} = 2$. The corresponding predicted data distributions are shown in Fig. 9.

| $E_\gamma^{\text{lab}}$ (MeV) | Observables |
|---|---|
| 750 | $C_{z'}, C_{x'}, L_{x'}, L_{z'}$ |
| 850 | $C_{z'}, C_{x'}, L_{x'}, L_{z'}, T_{x'}, T_{z'}$ |
| 950 | $C_{z'}, C_{x'}, L_{x'}, L_{z'}, T_{z'}$ |
| 1050 | $C_{z'}, C_{x'}, L_{x'}, O_{z'}, T_{z'}$ |
| 1150 | $C_{z'}, O_{x'}, T_{x'}, T_{z'}$ |
| 1250 | $C_{z'}$ |

for several fruitful discussions. Furthermore, special thanks go to Professor Dr. Reinhard Beck for his support.

## APPENDIX A: DISCRETE AMBIGUITIES OF THE ANALYZED SET OF SIX POLARIZATION OBSERVABLES

Within this Appendix, the discrete partial-wave ambiguities of the six observables $\{\sigma_0, \check{\Sigma}, \check{T}, \check{F}, \check{G}, \check{E}\}$ analyzed within this work (cf. Sec. IV and Table III) are discussed. It is argued that this specific set is mathematically complete in a TPWA. As has been demonstrated already in other works (e.g., Ref. [19]), such mathematical considerations can still serve as a useful precursor to analyses of real data.

The following discussion is based on the "Omelaenko formalism" [21]. The basic definitions of the sixteen observables in pseudoscalar meson photoproduction, expressed in the transversity basis, are used. The expressions are collected in Table II.

### 1. Discrete ambiguities of the group-$\mathcal{S}$ observables in truncated partial-wave analysis

As is well known from Omelaenko's work, in the case of a truncated partial-wave analysis with maximum angular momentum $\ell_{\max}$, the four transversity amplitudes can be expressed in terms of linear factorizations:

$$b_1(\theta) = -\mathcal{C}\, a_{2L}\, \frac{\exp\left(-i\frac{\theta}{2}\right)}{(1+t^2)^L} \prod_{k=1}^{2L} (t+\beta_k), \tag{A1}$$

$$b_2(\theta) = -\mathcal{C}\, a_{2L}\, \frac{\exp\left(i\frac{\theta}{2}\right)}{(1+t^2)^L} \prod_{k=1}^{2L} (t-\beta_k), \tag{A2}$$

$$b_3(\theta) = \mathcal{C}\, a_{2L}\, \frac{\exp\left(-i\frac{\theta}{2}\right)}{(1+t^2)^L} \prod_{k=1}^{2L} (t+\alpha_k), \tag{A3}$$

$$b_4(\theta) = \mathcal{C}\, a_{2L}\, \frac{\exp\left(i\frac{\theta}{2}\right)}{(1+t^2)^L} \prod_{k=1}^{2L} (t-\alpha_k), \tag{A4}$$

where $t = \tan(\theta/2)$ (with the center-of-mass scattering angle $\theta$) and $\{\alpha_k, \beta_k\}$ are the Gersten-Omelaenko roots, which are, in essence, equivalent to multipoles.

Furthermore, all permissible solutions have to satisfy Omelaenko's constraint, i.e., Eq. (10). The solution theory for the case where all four group-$\mathcal{S}$ observables have been selected, and thus only ambiguities of the four moduli $|b_1|$, $|b_2|$, $|b_3|$, $|b_4|$ have to be considered, has been worked out at length in Ref. [19]. This solution theory leads to the known complete sets of five (e.g., $\{\sigma_0, \check{\Sigma}, \check{T}, \check{P}, \check{F}\}$). In the following section, the special case where less than four diagonal observables are selected is considered.

### 2. Discrete ambiguities of the three group-$\mathcal{S}$ observables $\{\sigma_0, \Sigma, T\}$

The set of observables used within this work contains only three simultaneously diagonalized observables ($\sigma_0$, $\check{\Sigma}$, $\check{T}$, see Table II). Therefore, one has to investigate which kinds of discrete ambiguities are allowed by this set of three observables, using the root-formalism described in Appendix A 1. For this purpose, one can look at the "minimal" linear combinations of squared moduli:

$$\sigma_0 - \check{\Sigma} = 2(|b_1|^2 + |b_2|^2), \tag{A5}$$

$$\sigma_0 + \check{\Sigma} = 2(|b_3|^2 + |b_4|^2), \tag{A6}$$

$$\sigma_0 + \check{T} = 2(|b_1|^2 + |b_4|^2), \tag{A7}$$

$$\sigma_0 - \check{T} = 2(|b_2|^2 + |b_3|^2), \tag{A8}$$

$$-\check{\Sigma} + \check{T} = 2(|b_1|^2 - |b_3|^2), \tag{A9}$$

$$-\check{\Sigma} - \check{T} = 2(|b_2|^2 - |b_4|^2). \tag{A10}$$

Upon reducing the problem to the nonredundant amplitudes $b_2$ and $b_4$ in the TPWA [by using $b_4(W,\theta) = b_3(W,-\theta)$ and $b_2(W,\theta) = b_1(W,-\theta)$, cf. Eq. (6) to (9)], one obtains

$$\sigma_0 - \check{\Sigma} \propto \prod_{k=1}^{2\ell_{\max}} (t+\alpha_k^*)(t+\alpha_k) + \prod_{k=1}^{2\ell_{\max}} (t-\alpha_k^*)(t-\alpha_k), \tag{A11}$$

$$\sigma_0 + \check{\Sigma} \propto \prod_{k=1}^{2\ell_{\max}} (t+\beta_k^*)(t+\beta_k) + \prod_{k=1}^{2\ell_{\max}} (t-\beta_k^*)(t-\beta_k), \tag{A12}$$

$$\sigma_0 + \check{T} \propto \prod_{k=1}^{2\ell_{\max}} (t+\alpha_k^*)(t+\alpha_k) + \prod_{k=1}^{2\ell_{\max}} (t-\beta_k^*)(t-\beta_k), \tag{A13}$$

$$\sigma_0 - \check{T} \propto \prod_{k=1}^{2\ell_{\max}} (t-\alpha_k^*)(t-\alpha_k) + \prod_{k=1}^{2\ell_{\max}} (t+\beta_k^*)(t+\beta_k), \tag{A14}$$

$$-\check{\Sigma} + \check{T} \propto \prod_{k=1}^{2\ell_{\max}} (t+\alpha_k^*)(t+\alpha_k) - \prod_{k=1}^{2\ell_{\max}} (t+\beta_k^*)(t+\beta_k), \tag{A15}$$

$$-\check{\Sigma} - \check{T} \propto \prod_{k=1}^{2\ell_{\max}} (t-\alpha_k^*)(t-\alpha_k) - \prod_{k=1}^{2\ell_{\max}} (t-\beta_k^*)(t-\beta_k). \tag{A16}$$

The problem is now to find out which kinds of discrete ambiguity transformations, when applied to the roots $\{\alpha_k, \beta_k\}$, leave the full set of quantities Eqs. (A11) to (A16) invariant, while also satisfying the multiplicative constraint Eq. (10).

The first set of transformations which comes to mind is given by the well-known double ambiguity:

$$\alpha_k \to \alpha_k^* \text{ and } \beta_k \to \beta_k^* \ \forall\, k = 1, \ldots, 2\ell_{\max}. \tag{A17}$$

But other transformations may also be possible in addition, since the observable $\check{P}$ is missing from the full diagonalizable set $\{\sigma_0, \check{\Sigma}, \check{T}, \check{P}\}$. Ideas that one would have to test are, for instance, exchange symmetries

$$\alpha_k \to \beta_k \text{ and } \beta_k \to \alpha_k \ \forall\, k = 1, \ldots, 2\ell_{\max}, \tag{A18}$$

sign changes

$$\alpha_k \to -\alpha_k \text{ and } \beta_k \to -\beta_k \ \forall\, k = 1, \ldots, 2\ell_{\max}, \tag{A19}$$

or combinations of both

$$\alpha_k \to -\alpha_k^* \text{ and } \beta_k \to -\beta_k^* \ \forall\, k = 1, \ldots, 2\ell_{\max}. \tag{A20}$$

All of these ideas indeed do not violate the constraint Eq. (10). In case any such additional symmetry of the quantities Eqs. (A11) to (A16) were found, the next step would be to test which of the remaining three observables $\{F, G, E\}$ resolves the symmetry. Neither of the proposed symmetries Eqs. (A18) to (A20) leaves all the six quantities Eqs. (A11) to (A16) invariant. It remains to be asked whether such additional symmetries actually exist. In case they do not exist, the discussion would be simplified significantly [since $\check{F}$ and $\check{G}$ in this case already resolve the double ambiguity Eq. (A17)]. Due to information-theoretical reasons, it only seems permissible to simultaneously use three of the quantities from Eqs. (A11) to (A16), i.e., to use three new quantities obtained via invertible and linear transformations from the three diagonal initial observables $\{\sigma_0, \check{\Sigma}, \check{T}\}$.

As an example, one can select the three quantities given by Eqs. (A11) to (A13). The full set of discrete ambiguity-transformations, which, when applied to the roots $\{\alpha_k, \beta_k\}$, leaves Eqs. (A11) and (A12) invariant while maintaining the constraint in Eq. (10), is given by the two transformations in Eqs. (A17) and (A19). Under the exchange symmetry Eq. (A18), Eqs. (A11) and (A12) are transformed into each other and thus are not invariant.

Now considering additionally the quantity in Eq. (A13), one can see that while the transformation Eq. (A17) leaves this quantity invariant, transformation Eq. (A19) does not. This only leaves one possible conclusion, namely, that also for the case of only three diagonal observables $\{\sigma_0, \check{\Sigma}, \check{T}\}$, or equivalently the three new quantities in Eqs. (A11) and (A13), the double ambiguity is the only relevant discrete ambiguity of the problem.[11]

The argument given above can be repeated for any other case where a combination of three quantities from the six definitions Eq. (A11) to (A16) is taken as a starting point. None of the other starting combinations is necessary for a proof, since this would give a redundant derivation, with the same outcome.

### 3. Completeness of the set $\{\sigma_0, \check{\Sigma}, \check{T}, \check{F}, \check{G}, \check{E}\}$

It has already been shown in Refs. [18,19] that the observables $\check{F}$ and $\check{G}$ change sign under the double-ambiguity transformation.

All the arguments made up to this point prove that the set $\{\sigma_0, \check{\Sigma}, \check{T}, \check{F}, \check{G}, \check{E}\}$ is free of discrete ambiguities in the TPWA. Assuming furthermore that this set of six observables has no continuous ambiguities, the set is complete.

## APPENDIX B: COVERED PHASE SPACE OF THE DATA USED

The phase-space coverages of the polarization observable data used are illustrated in Fig. 3. For a detailed description of the data see Secs. IV and III. The vertical orange lines correspond to the energy bins of the statistically weakest polarization observable $G$ and indicate by which amount the dataset of another observable has to be shifted to match these energies.

## APPENDIX C: ON THE CORRELATION OF PROFILE FUNCTIONS

The correlation of two random variables $X$ and $Y$ can be calculated using the Pearson correlation coefficient defined as [44]

$$\mathrm{Corr}(X, Y) = \frac{\mathrm{Cov}(X, Y)}{\sqrt{\mathrm{Var}[X]\mathrm{Var}[Y]}}, \tag{C1}$$

with their respective variances Var and the covariance Cov between the two random variables. Under the assumption that the dimensionless observables do not have any correlation with each other, the covariance of the unpolarized differential cross-section $\sigma_0(W, \theta)$ (denoted with $X$) and a profile function [denoted $Y' = XY$ because $\sigma_0(W, \theta)$ was used to calculate the profile function] is

$$\begin{aligned} \mathrm{Cov}(X, Y') &= \mathrm{E}[XXY] - \mathrm{E}[X]\mathrm{E}[XY] \\ &= (\mathrm{E}[X^2] - \mathrm{E}[X]^2)\mathrm{E}[Y] \\ &= \mathrm{Var}[X]\mathrm{E}[Y]. \end{aligned} \tag{C2}$$

And similarly for the covariance of one profile function (denoted as $Y' = XY$) to another (denoted $Z' = XZ$):

$$\begin{aligned} \mathrm{Cov}(Y', Z') &= \mathrm{E}[XYXZ] - \mathrm{E}[XY]\mathrm{E}[XZ] \\ &= (\mathrm{E}[X^2] - \mathrm{E}[X]^2)\mathrm{E}[Y]\mathrm{E}[Z] \\ &= \mathrm{Var}[X]\mathrm{E}[Y]\mathrm{E}[Z]. \end{aligned} \tag{C3}$$

Substituting Eqs. (C2) and (C3), respectively, into Eq. (C1) the correlation for both cases is

$$\mathrm{Corr}(X, Y') = \sqrt{\frac{\mathrm{Var}[X]}{\mathrm{Var}[Y']}}\mathrm{E}[Y], \tag{C4}$$

$$\mathrm{Corr}(Y', Z') = \frac{\mathrm{Var}[X]}{\sqrt{\mathrm{Var}[Y']\mathrm{Var}[Z']}}\mathrm{E}[Y]\mathrm{E}[Z]. \tag{C5}$$

[11] This statement is of course only true in case transformations Eqs. (A17) and (A19) are indeed the only possible discrete ambiguities of the quantities in Eqs. (A11) and (A12) and that no further such discrete ambiguities exist. This seems plausible when considering equations Eqs. (A11) and (A12), in combination with the constraint in Eq. (10).

## APPENDIX D: UNDERLYING ASSUMPTIONS

An enormous strength of Bayesian statistics is its clarity about the underlying assumptions and how these evolve into the statistical model used. In general one has $N$ data pairs $(y, x)_i$, where the two components can be distinguished as follows:

(1) The random variables $\boldsymbol{y} = (y_1, \ldots, y_N)$ follow a certain distribution. In this context, these correspond to the values of the profile functions of the polarization observables $\check{\Omega}^{\alpha}(W, \theta)$.
(2) The explanatory variables [23] $\boldsymbol{x} = (x_1, \ldots, x_N)$ do not belong to any probability distribution. In this context, these are the angular values $\cos(\theta_i)$ at which the $y_i$ were measured.

The underlying distribution of $\boldsymbol{y}$ is of upmost importance because it defines the shape of the likelihood function and, by association, the structure of the parameter space. It is therefore essential to examine the distribution from which $\boldsymbol{y}$ originates and discuss the validity of the assumptions involved. Hereby, an understanding of the data acquisition as well as the subsequent analysis, to extract values for the polarization observables, is mandatory. For this reason, special emphasis is placed on their discussion within this paper.

The polarization observables used within this analysis originate from measurements at multiple experimental facilities: ELSA [5], MAMI [53], and GRAAL [54]. The measured quantities are count rates, corresponding to differential cross sections, from which then, one or multiple polarization observables can be extracted. The two most common methods are a "binned chi-square fit" and an "unbinned maximum-likelihood fit" [41]. For the first case, it is common to use an asymmetry of the form

$$A \propto \frac{N_1 - N_2}{N_1 + N_2}, \tag{D1}$$

where $N_1$, $N_2$ are normalized count rates of reconstructed $\gamma p \to \eta p$ events for different polarization states [39,40]. This has the advantage that systematic effects, for example, from the reconstruction efficiency, cancel out.

Certainly, the distribution of this asymmetry is not explicitly addressed in any of the analyses concerning polarization observables which the authors have encountered up to this point. However, since the distribution of $A$ determines the structure of the likelihood distribution, it is mandatory to study its proper form.

The count rates $N_1, N_2$ are Poisson-distributed random variables. If the expectation value, typically denoted as $\lambda$, is high enough, the distribution goes over to a Gaussian distribution. In the case of the data used here, this should be a good assumption.

The sum or difference of two independent Gaussian distributed random variables, as present in Eq. (D1), is again Gaussian distributed, which can be shown, for example, using characteristic functions.

However, the ratio of two, eventually correlated, Gaussian distributions $Z = X/Y$ is far more complicated. A general treatment can be found in Ref. [55]. Additionally a closed-form expression is given in Eq. (G3), of Appendix G 1. Indeed, there exist Gaussian shapes for the asymmetry $A$ in certain limits, but there exists also the possibility for a bimodal distribution [55]. Therefore, the shape of the asymmetry $A$ has to be checked for the absence of a bimodal structure. To use $\chi^2$ as likelihood function, the distribution should be well approximated by a Gaussian distribution. These checks can be performed by inserting the corresponding values for the expectation values $(\mu_x, \mu_y)$, standard deviations $(\sigma_x, \sigma_y)$ and correlation $(\rho)$ into the formula for $Z$ and its transformation, see Ref. [55], or by using Eq. (G3).

An alternative approach, where the utilization of such an asymmetry can be circumvented, is the already mentioned "unbinned maximum-likelihood fit." Albeit, in contrast with the first method, the detector acceptance has to be taken into account [41], which is possible [56]. Within this approach, the likelihood distribution can be modeled appropriately using Poisson distributions.

Summarizing, it is advantageous to use the unbinned maximum-likelihood fit for future analyses in order to extract values for the polarization observables.

However, the distribution of the extracted polarization observables not only depends on the shape of the used likelihood function but also implicitly on the method used to estimate the parameter uncertainties. Again, the distribution of the parameters is rarely explicitly discussed within papers such as the references cited in Table III. The error analysis of MINUIT uses by default the HESSE approach [57], which assumes an asymptotic approximation to a Gaussian distribution for the parameters under consideration. Thus, it is likely that the parameters were assumed to be Gaussian distributed. Another indication in the same direction is that all data used within the present analysis (cf. Table III) do have symmetric statistical uncertainties [38–42].

The profile functions $\check{\Omega}^{\alpha}$ are calculated by a product of random variables. However, even when these two random variables are independent and Gaussian distributed, the result is not always a Gaussian, only when one of the standard deviations is very small, see Ref. [19] or Appendix G 2. Fortunately, this is the case for $\sigma_0$ as it is the observable in $p\eta$ photoproduction with an unprecedented accuracy.

## APPENDIX E: ANALYSIS STEPS

This section explains in detail the analysis steps in order to determine the complex multipole parameters using Bayesian inference.

The posterior, which was in all of the analyses explicitly multimodal, and the goal to analyze the structure of the mathematical ambiguities present a major challenge with respect to the sampling of the posterior distribution. On the one hand, posteriors with multiple modes connected by regions of low posterior density persuade the Markov chains to get stuck within a certain mode, unable to explore multiple ones [23]. This results in drastically[12] failing MCMC convergence diag-

[12]This behavior was to be expected since $\hat{R}$ is a measure whether all chains have converged to the same distribution.

nostics, such as the potential-scale-reduction statistic $\hat{R}$. On the other hand, the number of possible modes increases exponentially with the truncation order $\ell_{\max}$. An upper limit can be given by $2^{4\ell_{\max}} - 2$, as this is the maximal possible number of accidental ambiguities of the four group-$\mathcal{S}$ observables [note that the bulk of this number is probably not realized as actual ambiguities due to the multiplicative constraint Eq. (10)] [19]. Capturing consistently all modes of the marginal posterior distributions via a large number of chains, with randomized starting values is computationally inefficient. Furthermore, randomized starting values will lead to traceplots where one cannot distinguish between chains that have not converged yet and chains which have explored more than one mode. An illustrative example is shown in Fig. 11.

These difficulties can be overcome by specifying well chosen starting values for the MCMC algorithm, explained in more detail in Appendixes E 2 and E 3. On that account, certain parts of the typical Bayesian workflow [58] had to be adapted.

#### 1. Monte Carlo maximum *a posteriori* estimation

To compare between different solutions, found within the same analysis, it is important to find all modes of the marginal posterior distributions, especially the global maximum. As already mentioned, the number of accidental ambiguities rises exponentially with the truncation order. Thus, the utilization of an optimization routine is substantially more efficient[13] than a large number of MCMC chains. With this in mind, a Monte Carlo maximum *a posteriori* estimation of the proposed posterior is employed as a preparatory step for the Bayesian inference procedure. The results of the following approach are cross-checked via an implementation in *Mathematica* [59], using the Levenberg-Marquard algorithm [60,61], as well as in Julia [62] using the L-BFGS-algorithm [63–67] via Optim.jl [68].

At first, one needs to fix the overall phase of the multipoles due to the bilinear product in Eq. (3). Indeed, without such a constraint the minimization algorithms would have convergence problems because the solutions are no longer located at isolated points in the parameter space but on continuous connected regions. Without loss of generality, a valid choice is $\mathrm{Re}(E_{0+}) > 0$, $\mathrm{Im}(E_{0+}) = 0$ [19]. Second, the minimization algorithm is performed for $n$ different starting values. The starting values are chosen within the physically allowed parameter space, which solely depends on the total cross section $\sigma_{\mathrm{tot}}$ [19,69]. Fortunately, the unpolarized differential cross section is the most accurately measured observable in $p\eta$ photoproduction [1], thus yielding accurate limits. An appropriate amount of $n$ equidistant points is chosen on each axis of this $(8\ell_{\max} - 1)$-dimensional hyper-rectangle, such that the volume is sufficiently covered. Each of these parameter configurations is then used as starting values for the minimization algorithm.

Finally, the nonredundant solutions, of the $n$ possible mode candidates can be extracted via a clustering algorithm. Hereby, all values of the multipole parameters are rounded to six digits. Then the unique solution vectors can be filtered out. A rough estimate for the uncertainty of each parameter solution is calculated via the inverse of the Hesse matrix [70], i.e., assuming a Gaussian shape of the parameters.

#### 2. Sampling of the posterior

Within this work, the well-established probabilistic programming software Stan [71] has been used to encode the model employed and to run the posterior sampling with the state-of-the-art Hamiltonian Monte Carlo algorithm [26,27] in combination with the No-U-Turn sampler [72]. The employed Stan model can be found in the Supplemental Material Ref. [49].

For each mode of the posterior distribution, determined within Sec. E 1, $N_{\mathrm{c}}$ chains are sampled with starting values for the multipole and systematic parameters equal to the corresponding $(8\ell_{\max} + 4)$-dimensional solution vector. This approach ensures adequate sampling of all marginal posterior modes and enables again a meaningful convergence diagnostics, further discussed in Appendix E 3. Hence, this is true as long as the posterior modes are in the vicinity of the "typical set,"[14] which is the case in this paper.

The following tuning parameters of the Hamiltonian Monte Carlo algorithm and the No-U-Turn sampler are adapted to the problem at hand. The average Metropolis acceptance probability $\delta \in [0, 1]$ is increased from its default value of 0.8 to $\delta = 0.99$. Thus, preferring a more fine-grained sampling, i.e., smaller leapfrog[15] steps $\epsilon$ [72], over the additional computation time. The maximum tree depth, with a default value of 10, is increased to 50, so that the algorithm can explore even challenging posterior regions without hitting the termination conditions [71].

#### 3. Monitor Markov chain Monte Carlo convergence

Naturally one is interested in how well the structure of the posterior was explored by the applied MCMC algorithm. The goal is to diagnose whether all Markov chains have explored the same part of the posterior distribution [23], i.e., whether the obtained distribution is reliable or accrued due to a random effect. This can be monitored by convergence diagnostics such as the potential-scale-reduction statistic $\hat{R}$ [29] and Monte Carlo standard error [28] (which depends on the effective sample size [23]). Within this work, the adapted versions of these diagnostics, as proposed by Vehtari *et al.* [73], are employed. In addition, trace plots [30] can be used to monitor the behavior of chains which explore multiple marginal modes. For each of these diagnostics, it is essential to use multiple chains [30,73] for a reliable result.

However, a multimodal posterior provides some pitfalls. As already mentioned at the beginning of Appendix E, the Markov chains can get stuck in certain, isolated modes. Thus not all chains would have seen the same parts of the posterior

[13] Integration is far more computation-intensive than differentiation.

[14] An illustration of the typical set can be found in Ref. [50].

[15] This refers to one parameter of the leapfrog integrator; see, for example, Ref. [27].

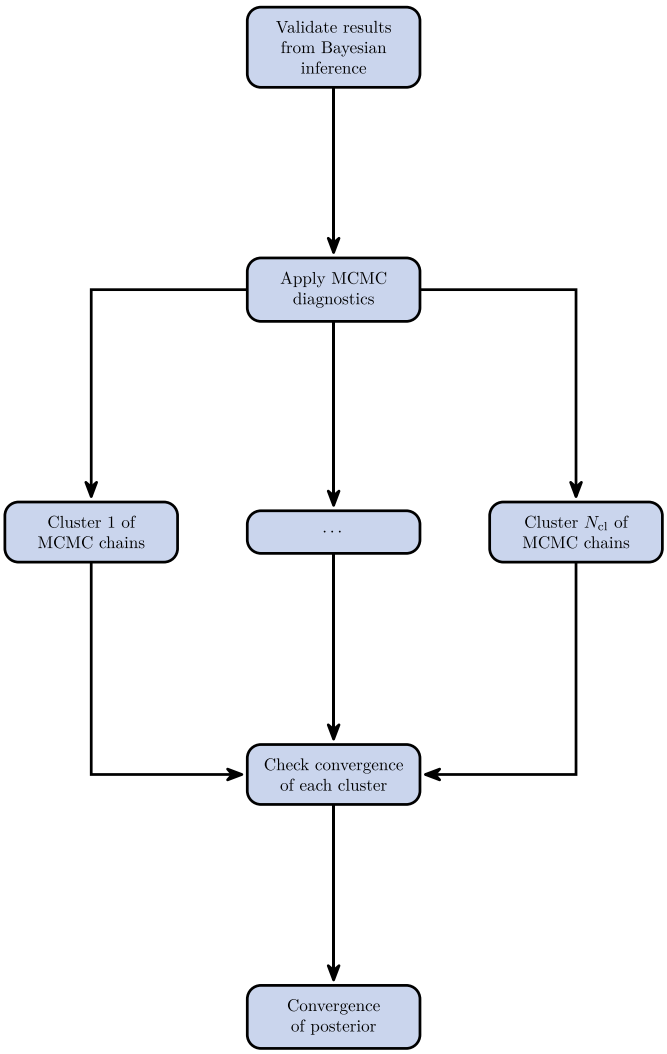


FIG. 13. Adapted workflow to monitor MCMC convergence due to a multimodal posterior.

distribution and the convergence diagnostics would indicate that the chains have not converged. Therefore, in case a multimodal posterior is studied, where all modes are of interest, the usual methods are not applicable. An adaptation has to be made. Under the assumption that all modes of the posterior were found via Monte Carlo maximum *a posteriori* estimation, see Appendix E 1, the following strategy is employed: A schematic representation of the adapted approach can be found in Fig. 13. Instead of applying the convergence diagnostics to all chains at once, the chains are clustered into groups according to their sampled parameter space and the convergence diagnostics are then applied onto each group separately.[16] Consequently, the convergence for the whole posterior is monitored.

The chains can be grouped according to their similarity as follows: To avoid problems during the clustering process, coming from high-dimensional data [75], a dimensional reduction of the chains is performed. Each chain, consisting of $S$ sampling points, is characterized via a vector of its quantiles, in this case the [0.1, 0.2, 0.3, 0.4, 0.5, 0.6, 0.7, 0.8, 0.9] quantiles. Subsequently, the corresponding distance matrix [76] of the quantile vectors is calculated using the Euclidean metric. The constructed matrix serves as input for the Density-Based Spatial Clustering of Applications with Noise (DBSCAN) algorithm [77]. The minimal cluster size should be at least two, as this is the minimal amount of chains required to perform the $\hat{R}$ diagnostic [30]. An appropriate $\epsilon$ neighborhood for the DBSCAN algorithm can be graphically determined, for example, by visualizing the Euclidean distances of the quantile vectors to each other. Afterwards, the correct clustering of chains can be checked visually. Alternatively, the two-sample Kolmogorov-Smirnov test [78] or the $K$-Sample Anderson-Darling test [79] could be employed to compare two distributions with each other.

The outlined approach still allows us to adjust the number of chains $N_{\mathrm{c}}$ per group and the sampling points $S$ in order to gain adequate convergence diagnostics and the desired precision for the parameter estimates. Within this paper, one is aiming for $\hat{R} < 1.01$ [73] and a relative Monte Carlo standard error in the region of a few percent.

#### 4. Analysis of generated data

It is crucial to prove the correct implementation and validity of the used model. An ideal testing scenario would be the *a priori* knowledge of the correct outcome of the analysis using the model under consideration. Therefore the PWA solution EtaMAID2018 [48] is employed for the electromagnetic multipoles in Eq. (4) up to the desired truncation order $\ell_{\max}$. By these means, pseudodata for the profile functions $\check{\Omega}^{\alpha}(W, \theta)$ are generated via Eq. (2) for certain energies and angular positions for the observables $\sigma_0$, $\Sigma$, $T$, $E$, $F$, and $G$. These data were used as input for the TPWA following the described steps in Appendixes E 1 to E 3. This analysis yielded again the EtaMAID2018 multipole solutions, indicating a correct implementation.

## APPENDIX F: CONVERGENCE DIAGNOSTICS

MCMC convergence diagnostics for the truncation orders $\ell_{\max} = 1$ and $\ell_{\max} = 2$ for all analyzed energies are shown in Figs. 10 and 6. The anticipated values for the potential-scale-reduction statistic $\hat{R} \leqslant 1.01$ and the relative Monte Carlo standard error (MCSE) of the median in the range of a few percent were achieved for both truncation orders. The diagnostics for 750 MeV are satisfactory, despite their slightly elevated values, which are the result of the highly multimodal marginal parameter distribution. However, certain convergence diagnostics for $\ell_{\max} = 2$ suggest that some groups of chains have not yet converged, indicating a specific phenomenon that will be discussed below. Hence, the four energies $E_{\gamma}^{\mathrm{lab}} =$ [950, 1050, 1150, 1250] MeV look suspicious. In each case one group of chains show $\hat{R}$ values way above 1.01 and relative Monte Carlo standard errors of over 100%. This results from two modes separated in phase space by a small region of low probability, so that the Metropolis acceptance probability [27] for a transition between the two high-probability regions

[16] A similar approach was used in Ref. [74].

is quite small but nonzero. Hence, just a small number of chains is able to explore both marginal modes at once, which is the reason for the suspicious convergence diagnostics. For the case of 1050 MeV, the blue distribution corresponds to a cluster with just one group member. Hence, it is not possible to calculate an $\hat{R}$ value for this cluster. It is important to note that this behavior cannot be prevented because it is inherently a random effect. As an example how such a phenomenon manifests within a parameter distribution, see the blue distribution of $\mathrm{Im}(M_{2+})$ at 1250 MeV in Fig. 8. Despite their convergence diagnostics, these types of distributions are shown within the multipole parameter and posterior predictive plots for their illustrative purposes.

## APPENDIX G: PROBABILITY DISTRIBUTIONS FOR THE QUOTIENT AND PRODUCT OF TWO GAUSSIAN RANDOM VARIABLES

Assuming the original observables to follow a Gaussian probability distribution up to a very good approximation, the result of forming the quotient and/or product is generally non-Gaussian. This Appendix collects some basic facts about the quotient and the product distributions and considers some limiting cases.

### 1. The quotient distribution: $Z := X/Y$

Given are two independent, uncorrelated, Gaussian distributed random variables $X$ and $Y$:

$$X \sim \mathcal{N}(\mu_X, \sigma_X), \quad Y \sim \mathcal{N}(\mu_Y, \sigma_Y), \tag{G1}$$

together with the integral defining the probability distribution function of the quotient variable $Z := X/Y$ [80],

$$\begin{aligned} \mathrm{P}_{X/Y}(u) &= \int_{-\infty}^{\infty} \mathrm{d}x \int_{-\infty}^{\infty} \mathrm{d}y \delta\left(\frac{x}{y} - u\right) \\ &\quad \times \frac{\exp\left[-\frac{1}{2}\left(\frac{(x-\mu_X)^2}{\sigma_X^2} + \frac{(y-\mu_Y)^2}{\sigma_Y^2}\right)\right]}{2\pi\sigma_X\sigma_Y} \\ &= \int_{-\infty}^{\infty} \mathrm{d}y |y| \frac{\exp\left[-\frac{1}{2}\left(\frac{(uy-\mu_X)^2}{\sigma_X^2} + \frac{(y-\mu_Y)^2}{\sigma_Y^2}\right)\right]}{2\pi\sigma_X\sigma_Y}, \end{aligned} \tag{G2}$$

*Mathematica* yields the following result (for positive values of $\sigma_X$ and $\sigma_Y$):

$$\begin{aligned} \mathrm{P}_{X/Y}(u) &= f_1(u) \cdot \{\sqrt{2}\, f_2(u)\, c \\ &\quad + \sqrt{\pi}\, f_3(u)\, \mathrm{erf}(f_4(u)) \exp[f_4(u)^2]\}, \end{aligned} \tag{G3}$$

with the declarations

$$f_1(u) := \frac{\exp\left[-\frac{1}{2}\left(\frac{\mu_X^2}{\sigma_X^2} + \frac{\mu_Y^2}{\sigma_Y^2}\right)\right]}{\sqrt{2}\pi\, f_2(u)^3}, \tag{G4}$$

$$f_2(u) := \sqrt{\sigma_X^2 + \sigma_Y^2 u^2}, \tag{G5}$$

$$f_3(u) := \mu_Y\sigma_X^2 + \mu_X\sigma_Y^2 u, \tag{G6}$$

$$f_4(u) := \frac{f_3(u)}{\sqrt{2}\, f_2(u)\, c}, \tag{G7}$$

$$c := \sigma_X\sigma_Y \tag{G8}$$

and the error function "erf" [81]. In the following, two limiting cases for Eq. (G3) are analyzed: first, the vanishing of the expectation values (i.e., $\mu_X = \mu_Y = 0$):

$$\mathrm{P}_{X/Y}(u) = \frac{\sigma_X\sigma_Y}{\pi\left(\sigma_X^2 + \sigma_Y^2 u^2\right)}. \tag{G9}$$

This is a result which is known from earlier publications on the quotient distribution, for instance [82].

Second, considering also unit standard deviations (i.e., $\sigma_X = \sigma_Y = 1$) the result Eq. (G9) further simplifies to

$$\mathrm{P}_{X/Y}(u) = \frac{1}{\pi(1+u^2)}. \tag{G10}$$

This is the well-known Cauchy distribution.

### 2. The product distribution: $Z := XY$

Similar to Eq. (G2) the probability-distribution function for the product of two independent, uncorrelated Gaussian distributed random variables can be written [83] as

$$\begin{aligned} \mathrm{P}_{XY}(u) &= \int_{-\infty}^{\infty} \mathrm{d}x \int_{-\infty}^{\infty} \mathrm{d}y \delta(xy - u) \\ &\quad \times \frac{\exp\left[-\frac{1}{2}\left(\frac{(x-\mu_X)^2}{\sigma_X^2} + \frac{(y-\mu_Y)^2}{\sigma_Y^2}\right)\right]}{2\pi\sigma_X\sigma_Y}. \end{aligned} \tag{G11}$$

By introducing an integral-representation for the $\delta$ function

$$\delta(xy-u) = \int_{-\infty}^{+\infty} \frac{\mathrm{d}k}{2\pi} e^{ik(xy-u)} = \int_{-\infty}^{+\infty} \frac{\mathrm{d}k}{2\pi} e^{ikxy} e^{-iku}, \tag{G12}$$

one can bring Eq. (G11) into the following form:

$$\mathrm{P}_{XY}(u) = \int_{-\infty}^{+\infty} \frac{\mathrm{d}k}{2\pi} e^{-iku} F_k[\mu_X, \sigma_X; \mu_Y, \sigma_Y], \tag{G13}$$

where

$$\begin{aligned} F_k[\mu_X, \sigma_X; \mu_Y, \sigma_Y] &= \int_{-\infty}^{\infty} \mathrm{d}x \int_{-\infty}^{\infty} \mathrm{d}y e^{ikxy} \\ &\quad \times \frac{\exp\left[-\frac{1}{2}\left(\frac{(x-\mu_X)^2}{\sigma_X^2} + \frac{(y-\mu_Y)^2}{\sigma_Y^2}\right)\right]}{2\pi\sigma_X\sigma_Y}. \end{aligned} \tag{G14}$$

This characteristic function can be solved analytically:

$$\begin{aligned} &F_k[\mu_X, \sigma_X; \mu_Y, \sigma_Y] \\ &= \int_{-\infty}^{\infty} \mathrm{d}y \exp\left[-\frac{1}{2}ky\left(k\sigma_X^2 y - 2i\mu_X\right)\right] \frac{\exp\left[-\frac{(y-\mu_Y)^2}{2\sigma_Y^2}\right]}{\sqrt{2\pi}\sigma_Y} \\ &= \frac{\exp\left[-\frac{k\left(k\mu_Y^2\sigma_X^2 + k\mu_X^2\sigma_Y^2 - 2i\mu_X\mu_Y\right)}{2+2k^2\sigma_X^2\sigma_Y^2}\right]}{\sqrt{1+k^2\sigma_X^2\sigma_Y^2}}. \end{aligned} \tag{G15}$$

The final result has the shape of a Fourier integral:

$$\mathrm{P}_{XY}(u) = \int_{-\infty}^{+\infty} \frac{dk}{2\pi} \exp\left[-iku\right] \times \frac{\exp\left[-\frac{k\left(k\mu_Y^2\sigma_X^2 + k\mu_X^2\sigma_Y^2 - 2i\mu_X\mu_Y\right)}{2+2k^2\sigma_X^2\sigma_Y^2}\right]}{\sqrt{1+k^2\sigma_X^2\sigma_Y^2}}. \tag{G16}$$

In analogy to the quotient distribution, the limiting case $\mu_X = \mu_Y = 0$ shall be analyzed. The Fourier coefficients become

$$F_k[0, \sigma_X; 0, \sigma_Y] = \frac{1}{\sqrt{1+k^2\sigma_X^2\sigma_Y^2}}. \tag{G17}$$

The result for the product distribution can in this case be written with a modified Bessel function of the second kind $K_n(z)$:

$$\mathrm{P}_{XY}(u) = \frac{K_0\left(\frac{|u|}{\sigma_X\sigma_Y}\right)}{\pi\sigma_X\sigma_Y}. \tag{G18}$$

This is the analog of Eq. (G9) from the case of the quotient distribution. For unit standard deviations, Eq. (G18) becomes simply $K_0(|u|)/\pi$, which is the analog of Eq. (G10).

For the product distribution, especially one limiting case is of interest for this paper, namely, where the standard deviation of one random variable almost vanishes (i.e., $\sigma_Y \to 0$). The characteristic function becomes

$$\lim_{\sigma_Y \to 0} F_k = \exp\left(-\frac{k\left(k\mu_Y^2\sigma_X^2 - 2i\mu_X\mu_Y\right)}{2}\right). \tag{G19}$$

Substituting Eq. (G19) into Eq. (G16) and solving the integral gives the result:

$$\mathrm{P}_{XY}(u) = \frac{\exp\left(-\frac{(u-\mu_X\mu_Y)^2}{2\mu_Y^2\sigma_X^2}\right)}{\sqrt{2\pi}|\mu_Y||\sigma_X|}, \tag{G20}$$

which is indeed a Gaussian probability distribution function. This result is used in Appendix D.


[1] A. Thiel, F. Afzal, and Y. Wunderlich, Light Baryon spectroscopy, Prog. Part. Nucl. Phys. **125**, 103949 (2022).

[2] R. L. Workman *et al.* (Particle Data Group), Review of particle physics, Prog. Theor. Exp. Phys. **2022**, 083C01 (2022).

[3] R. Haensel, European synchrotron radiation facility, Nucl. Instrum. Methods Phys. Res. Sect. A **266**, 1 (1988).

[4] T. Walcher, The Mainz microtron facility MAMI, Prog. Part. Nucl. Phys. **24**, 189 (1990).

[5] W. Hillert, The Bonn electron stretcher accelerator ELSA: Past and future, in *Many Body Structure of Strongly Interacting Systems*, edited by H. Arenhövel, H. Backe, D. Drechsel, J. Friedrich, K.-H. Kaiser, and T. Walcher (Springer, Berlin, Heidelberg, 2006), pp. 139–148.

[6] C. W. Leemann, D. R. Douglas, and G. A. Krafft, The continuous electron beam accelerator facility: CEBAF at the Jefferson laboratory, Ann. Rev. Nucl. Part. Sci. **51**, 413 (2001).

[7] C. Yamanaka, Super photon ring-8 and its application to FEL, Nucl. Instrum. Methods Phys. Res. Sect. A **318**, 239 (1992).

[8] R. A. Arndt, W. J. Briscoe, I. I. Strakovsky, and R. L. Workman, Extended partial-wave analysis of $\pi n$ scattering data, Phys. Rev. C **74**, 045205 (2006).

[9] A. Anisovich, R. Beck, E. Klempt, V. Nikonov, A. Sarantsev, and U. Thoma, Properties of baryon resonances from a multichannel partial wave analysis, Eur. Phys. J. A **48**, 1 (2012).

[10] D. Rönchen, M. Döring, and U.-G. Meißner, The impact of $K^+\Lambda$ photoproduction on the resonance spectrum, Eur. Phys. J. A **54**, 1 (2018).

[11] D. Drechsel, O. Hanstein, S. Kamalov, and L. Tiator, A unitary isobar model for pion photo- and electroproduction on the proton up to 1 GeV, Nucl. Phys. A **645**, 145 (1999).

[12] T. Sato and T.-S. H. Lee, Meson-exchange model for $\pi$N scattering and $\gamma$N $\to \pi$N reaction, Phys. Rev. C **54**, 2660 (1996).

[13] A. Švarc, M. Hadžimehmedović, H. Osmanović, J. Stahov, L. Tiator, and R. L. Workman, Introducing the Pietarinen expansion method into the single-channel pole extraction problem, Phys. Rev. C **88**, 035206 (2013).

[14] A. Anisovich, R. Beck, M. Döring, M. Gottschall, J. Hartmann, V. Kashevarov, E. Klempt, U.-G. Meißner, V. Nikonov, M. Ostrick *et al.*, The impact of new polarization data from Bonn, Mainz and Jefferson laboratory on multipoles, Eur. Phys. J. A **52**, 284 (2016).

[15] M. Ronniger and B. C. Metsch, Effects of a spin-flavour-dependent interaction on the baryon mass spectrum, Eur. Phys. J. A **47**, 162 (2011).

[16] V. F. Grushin, Photoproduction of pions on low-energy protons: Complete experiments and multipole analysis, in *Photoproduction of Pions on Nucleons and Nuclei*, edited by A. A. Komar (Nova Science, New York, 1989), p. 1.

[17] L. Tiator, Towards a model-independent partial wave analysis for pseudoscalar meson photoproduction, AIP Conf. Proc. **1432**, 162 (2012).

[18] Y. Wunderlich, R. Beck, and L. Tiator, The complete-experiment problem of photoproduction of pseudoscalar mesons in a truncated partial-wave analysis, Phys. Rev. C **89**, 055203 (2014).

[19] Y. Wunderlich, Ph.D. thesis, Rheinische Friedrich-Wilhelms-Universität Bonn, 2019 (unpublished).

[20] Y. Wunderlich, F. Afzal, A. Thiel, and R. Beck, Determining the dominant partial wave contributions from angular distributions of single- and double-polarization observables in pseudoscalar meson photoproduction, Eur. Phys. J. A **53**, 86 (2017).

[21] A. Omelaenko, Ambiguities of the multipole analysis of neutral-pion photoproduction from nucleons, Sov. J. Nucl. Phys. **34**, 406 (1981).

[22] T. Bayes, LII. An essay towards solving a problem in the doctrine of chances. By the late Rev. Mr. Bayes, F. R. S. communicated by Mr. Price, in a letter to John Canton, A. M. F. R. S, Philos. Trans. R. Soc. **53**, 370 (1763).

[23] A. Gelman, J. B. Carlin, H. S. Stern, D. B. Dunson, A. Vehtari, and D. B. Rubin, *Bayesian Data Analysis* (CRC Press, New York, 2013).

[24] N. Metropolis, A. W. Rosenbluth, M. N. Rosenbluth, A. H. Teller, and E. Teller, Equation of state calculations by fast computing machines, J. Chem. Phys. **21**, 1087 (1953).

[25] W. K. Hastings, Monte Carlo sampling methods using Markov chains and their applications, Biometrika **57**, 97 (1970).

[26] S. Duane, A. Kennedy, B. J. Pendleton, and D. Roweth, Hybrid Monte Carlo, Phys. Lett. B **195**, 216 (1987).

[27] R. M. Neal, *MCMC using Hamiltonian Dynamics*, in *Handbook of Markov Chain Monte Carlo*, 1st ed. (CRC Press, Boca Raton, 2011).

[28] C. J. Geyer, Introduction to Markov chain Monte Carlo, in *Handbook of Markov Chain Monte Carlo*, 1st ed. (CRC Press, Boca Raton, 2011).

[29] A. Gelman and D. B. Rubin, Inference from iterative simulation using multiple sequences, Stat. Sci. **7**, 457 (1992).

[30] A. Gelman and K. Shirley, Inference from simulations and monitoring convergence, in *Handbook of Markov Chain Monte Carlo*, 1st ed. (CRC Press, Boca Raton, 2011).

[31] A. M. Sandorfi, S. Hoblit, H. Kamano, and T.-S. H. Lee, Determining pseudoscalar meson photoproduction amplitudes from complete experiments, J. Phys. G **38**, 053001 (2011).

[32] G. F. Chew, M. L. Goldberger, F. E. Low, and Y. Nambu, Relativistic dispersion relation approach to photomeson production, Phys. Rev. **106**, 1345 (1957).

[33] W.-T. Chiang and F. Tabakin, Completeness rules for spin observables in pseudoscalar meson photoproduction, Phys. Rev. C **55**, 2054 (1997).

[34] P. Kroenert, Y. Wunderlich, F. Afzal, and A. Thiel, Minimal complete sets for two-pseudoscalar-meson photoproduction, Phys. Rev. C **103**, 014607 (2021).

[35] M. Pichowsky, Ç. Şavkli, and F. Tabakin, Polarization observables in vector meson photoproduction, Phys. Rev. C **53**, 593 (1996).

[36] Y. Wunderlich, A. Švarc, R. L. Workman, L. Tiator, and R. Beck, Toward an understanding of discrete ambiguities in truncated partial-wave analyses, Phys. Rev. C **96**, 065202 (2017).

[37] R. L. Workman, L. Tiator, Y. Wunderlich, M. Döring, and H. Haberzettl, Amplitude reconstruction from complete photoproduction experiments and truncated partial-wave expansions, Phys. Rev. C **95**, 015206 (2017).

[38] V. L. Kashevarov, P. Ott, S. Prakhov, P. Adlarson, F. Afzal, Z. Ahmed, C. S. Akondi, J. R. M. Annand, H. J. Arends, R. Beck, A. Braghieri, W. J. Briscoe, F. Cividini, R. Codling, C. Collicott, S. Costanza, A. Denig, E. J. Downie, M. Dieterle, M. I. Ferretti Bondy, and L. Zana (A2 Collaboration at MAMI), Study of $\eta$ and $\eta'$ photoproduction at MAMI, Phys. Rev. Lett. **118**, 212001 (2017).

[39] O. Bartalini, V. Bellini, J. Bocquet, P. Calvat, M. Capogni, L. Casano, M. Castoldi, A. d'Angelo, J.-P. Didelez, R. Di Salvo *et al.*, Measurement of $\eta$ photoproduction on the proton from threshold to 1500 MeV, Eur. Phys. J. A **33**, 169 (2007).

[40] C. S. Akondi, J. R. M. Annand, H. J. Arends, R. Beck, A. Bernstein, N. Borisov, A. Braghieri, W. J. Briscoe, S. Cherepnya, C. Collicott, S. Costanza, E. J. Downie, M. Dieterle, A. Fix, L. V. Fil'kov, S. Garni, D. I. Glazier, W. Gradl, G. Gurevich, P. Hall Barrientos, and M. Wolfes (A2 Collaboration at MAMI), Measurement of the transverse target and beam-target asymmetries in $\eta$ meson photoproduction at MAMI, Phys. Rev. Lett. **113**, 102001 (2014).

[41] F. N. Afzal, Ph.D. thesis, Rheinische Friedrich-Wilhelms-Universität Bonn, 2019 (unpublished).

[42] J. Müller, J. Hartmann, M. Grüner, F. Afzal, A. Anisovich, B. Bantes, D. Bayadilov, R. Beck, M. Becker, Y. Beloglazov, A. Berlin, M. Bichow, S. Böse, K.-T. Brinkmann, T. Challand, V. Crede, F. Dietz, M. Dieterle, P. Drexler, H. Dutz *et al.*, New data on $\vec{\gamma}\vec{p} \to \eta p$ with polarized photons and protons and their implications for $N* \to N\eta$ decays, Phys. Lett. B **803**, 135323 (2020).

[43] F. Afzal *et al.* (A2 Collaboration) (unpublished).

[44] E. W. Weisstein, Statistical correlation, From MathWorld–A Wolfram Web Resource. https://mathworld.wolfram.com/StatisticalCorrelation.html, accessed: 2022-05-30.

[45] B. O'Neill, Exchangeability, correlation, and Bayes' effect, Int. Stat. Rev. **77**, 241 (2009).

[46] M. Döring, J. Revier, D. Rönchen, and R. L. Workman, Correlations of $\pi n$ partial waves for multireaction analyses, Phys. Rev. C **93**, 065205 (2016).

[47] D. Rönchen, M. Döring, U.-G. Meißner, and C.-W. Shen, Light baryon resonances from a coupled-channel study including $\mathbf{K\Sigma}$ photoproduction, Eur. Phys. J. A **58**, 229 (2022).

[48] L. Tiator, M. Gorchtein, V. L. Kashevarov, K. Nikonov, M. Ostrick, M. Hadžimehmedović, R. Omerović, H. Osmanović, J. Stahov, and A. Švarc, Eta and etaprime photoproduction on the nucleon with the isobar model EtaMAID2018, Eur. Phys. J. A **54**, 210 (2018).

[49] See Supplemental Material at http://link.aps.org/supplemental/10.1103/PhysRevC.109.045206 for all parameter figures and the implementation of the used model within Stan.

[50] M. Betancourt, A Conceptual Introduction to Hamiltonian Monte Carlo (2017).

[51] R. L. Workman, R. A. Arndt, W. J. Briscoe, M. W. Paris, and I. I. Strakovsky, Parameterization dependence of $t$-matrix poles and eigenphases from a fit to $\pi n$ elastic scattering data, Phys. Rev. C **86**, 035202 (2012).

[52] A. Švarc and R. L. Workman, Laurent + Pietarinen partial-wave analysis, Phys. Rev. C **108**, 014615 (2023).

[53] K.-H. Kaiser, K. Aulenbacher, O. Chubarov, M. Dehn, H. Euteneuer, F. Hagenbuck, R. Herr, A. Jankowiak, P. Jennewein, H.-J. Kreidel, U. Ludwig-Mertin, M. Negrazus, S. Ratschow, S. Schumann, M. Seidl, G. Stephan, and A. Thomas, The 1.5 GeV harmonic double-sided microtron at Mainz University, Nucl. Instrum. Methods Phys. Res. Sect. A **593**, 159 (2008).

[54] O. Bartalini, V. Bellini, J. Bocquet, M. Capogni, L. Casano, M. Castoldi, P. Calvat, A. d'Angelo, R. Di Salvo, A. Fantini *et al.*, Measurement of $\pi$ photoproduction on the proton from 550 to 1500 MeV at GRAAL, Eur. Phys. J. A **26**, 399 (2005).

[55] G. Marsaglia, Ratios of normal variables, J. Stat. Softw. **16**, 1 (2006).

[56] Jan Hartmann, Ph.D. thesis, Rheinische Friedrich-Wilhelms-Universität Bonn, 2017 (unpublished).

[57] F. James and M. Roos, MINUIT: A system for function minimization and analysis of the parameter errors and correlations, Comput. Phys. Commun. **10**, 343 (1975).

[58] A. Gelman, A. Vehtari, D. Simpson, C. C. Margossian, B. Carpenter, Y. Yao, L. Kennedy, J. Gabry, P.-C. Bürkner, and M. Modrák, Bayesian workflow, arXiv:2011.01808.

[59] W. R. Inc., Mathematica, Version 12.2 (2020), Champaign, IL.

[60] K. Levenberg, A method for the solution of certain non-linear problems in least squares, Q. Appl. Math. **2**, 164 (1944).

[61] D. W. Marquardt, An algorithm for least-squares estimation of nonlinear parameters, J. Soc. Ind. Appl. Math. **11**, 431 (1963).

[62] J. Bezanson, A. Edelman, S. Karpinski, and V. B. Shah, Julia: A fresh approach to numerical computing, SIAM Rev. **59**, 65 (2017).

[63] C. G. Broyden, The convergence of a class of double-rank minimization algorithms 1. General considerations, IMA J. Appl. Math. **6**, 76 (1970).
[64] R. Fletcher, A new approach to variable metric algorithms, Comput. J. **13**, 317 (1970).
[65] D. Goldfarb, A family of variable-metric methods derived by variational means, Math. Comput. **24**, 23 (1970).
[66] D. F. Shanno, Conditioning of quasi-Newton methods for function minimization, Math. Comput. **24**, 647 (1970).
[67] J. Nocedal, Updating quasi-Newton matrices with limited storage, Math. Comput. **35**, 773 (1980).
[68] P. Mogensen and A. Riseth, Optim: A mathematical optimization package for Julia, J. Open Source Software **3**, 615 (2018).
[69] D. Dreschsel and L. Tiator, Threshold pion photoproduction on nucleons, J. Phys. G **18**, 449 (1992).
[70] R. J. Barlow, *Statistics: A Guide to the Use of Statistical Methods in the Physical Sciences* (John Wiley & Sons, 1993), Vol. 29.
[71] S. D. Team, Stan modeling language users guide and reference manual, version 2.28, https://mc-stan.org (2022).
[72] M. D. Hoffman and A. Gelman, The No-U-Turn sampler: Adaptively setting path lengths in Hamiltonian Monte Carlo, J. Mach. Learn. Res. **15**, 1593 (2014).
[73] A. Vehtari, A. Gelman, D. Simpson, B. Carpenter, and P.-C. Bürkner, Rank-normalization, folding, and localization: An improved $\widehat{R}$ for assessing convergence of MCMC (with discussion), Bayesian Anal. **16**, 667 (2021).
[74] Y.-C. Zhu, Z. Sun, and Q.-L. He, Clustering-based convergence diagnostic for multi-modal identification in parameter estimation of chromatography model with parallel MCMC, arXiv:2107.07203.
[75] K. B. Jonathan, J. Goldstein, R. Ramakrishnan, and U. Shaft, When is "nearest neighbor" meaningful? in *International Conference on Database Theory* (Springer, Berlin, Heidelberg, 1999), Vol. 1540, pp. 217–235.
[76] R. L. Graham and H. O. Pollak, On the addressing problem for loop switching, Bell Syst. Tech. J. **50**, 2495 (1971).
[77] M. Ester, H.-P. Kriegel, J. Sander, and X. Xu, A density-based algorithm for discovering clusters in large spatial databases with noise, in KDD-96 Proceedings (1996), Vol. 96, pp. 226–231.
[78] Kolmogorov–Smirnov test, *The Concise Encyclopedia of Statistics* (Springer, New York, 2008), pp. 283–287.
[79] F. W. Scholz and M. A. Stephens, $K$-sample Anderson-Darling tests, J. Am. Stat. Assoc. **82**, 918 (1987).
[80] E. W. Weisstein, Normal ratio distribution, From MathWorld–A Wolfram Web Resource. https://mathworld.wolfram.com/NormalRatioDistribution.html, accessed: 2022-09-02.
[81] E. W. Weisstein, Error function, From MathWorld–A Wolfram Web Resource.https://mathworld.wolfram.com/Erf.html, accessed: 2022-09-02.
[82] J. H. Curtiss, On the distribution of the quotient of two chance variables, Ann. Math. Stat. **12**, 409 (1941).
[83] E. W. Weisstein, Normal product distribution, From MathWorld–A Wolfram Web Resource. https://mathworld.wolfram.com/NormalProductDistribution.html, accessed: 2022-09-02.

# Appendix B

# Neutrino mass analysis

## B.1 Individual campaigns

### B.1.1 MCMC convergence diagnostics

The Markov chain Monte Carlo convergence diagnostics for the individual KATRIN analyses are shown in Table B.1.

### B.1.2 Posterior predictive checks

The following posterior predictive checks correspond to the individual KATRIN campaigns using (Total). Standardized residuals for the reproduced data distributions using the MAP estimate are shown in Figs. B.1 and B.2. Normalized counts using posterior samples are displayed in Figs. B.3 and B.4. The standardized residuals for posterior samples are displayed in Figs. B.5 and B.6.

### B.1.3 Results

The results of the performed analysis on the first five KATRIN campaigns can be found in Figs. B.7 to B.12. The results for KNM5 are shown in the main text in Fig. 7.3. In addition, Fig. B.13 compares the individual result within one plot.

Table B.1: Summary of MCMC convergence diagnostics for the fit of individual campaigns. The largest values from all parameters of a campaign are reported for $\widehat{\mathrm{R}}$ and the relative MCMCSE for the 90%-quantile. The diagnostics are shown for different priors of $m_\nu^2$ when taking only statistical uncertainties or statistical and systematic uncertainties into account. Asimov data were analyzed.

(a) Flat prior $m_\nu^2 \sim \mathcal{U}(-10,10)$ and considering only statistical uncertainties.

| **Campaign** | $\widehat{\mathbf{R}}$ | **MCMCSE for 90%-quantile** |
|---|---|---|
| KNM1 | $\leq 1.000032$ | $\leq 0.26\%$ |
| KNM2 | $\leq 1.000036$ | $\leq 0.25\%$ |
| KNM3-SAP | $\leq 1.000028$ | $\leq 0.23\%$ |
| KNM3-NAP | $\leq 1.000026$ | $\leq 0.24\%$ |
| KNM4-NOM | $\leq 1.000023$ | $\leq 0.21\%$ |
| KNM4-OPT | $\leq 1.000022$ | $\leq 0.20\%$ |
| KNM5 | $\leq 1.000018$ | $\leq 0.20\%$ |

(b) Flat prior $m_\nu^2 \sim \mathcal{U}(-10,10)$ and considering statistical and systematic uncertainties.

| **Campaign** | $\widehat{\mathbf{R}}$ | **MCMCSE for 90%-quantile** |
|---|---|---|
| KNM1 | $\leq 1.000047$ | $\leq 0.16\%$ |
| KNM2 | $\leq 1.000018$ | $\leq 0.18\%$ |
| KNM3-SAP | $\leq 1.000053$ | $\leq 0.54\%$ |
| KNM3-NAP | $\leq 1.000023$ | $\leq 0.19\%$ |
| KNM4-NOM | $\leq 1.000064$ | $\leq 0.48\%$ |
| KNM4-OPT | $\leq 1.000040$ | $\leq 0.53\%$ |
| KNM5 | $\leq 1.000079$ | $\leq 0.26\%$ |

(c) Flat, positive prior $m_\nu^2 \sim \mathcal{U}(0,3)$ and considering only statistical uncertainties.

| **Campaign** | $\widehat{\mathbf{R}}$ | **MCMCSE for 90%-quantile** |
|---|---|---|
| KNM1 | $\leq 1.000032$ | $\leq 0.15\%$ |
| KNM2 | $\leq 1.000022$ | $\leq 0.15\%$ |
| KNM3-SAP | $\leq 1.000021$ | $\leq 0.13\%$ |
| KNM3-NAP | $\leq 1.000029$ | $\leq 0.15\%$ |
| KNM4-NOM | $\leq 1.000015$ | $\leq 0.12\%$ |
| KNM4-OPT | $\leq 1.000021$ | $\leq 0.11\%$ |
| KNM5 | $\leq 1.000020$ | $\leq 0.12\%$ |

(d) Flat, positive prior $m_\nu^2 \sim \mathcal{U}(0,3)$ and considering statistical and systematic uncertainties.

| **Campaign** | $\widehat{\mathbf{R}}$ | **MCMCSE for 90%-quantile** |
|---|---|---|
| KNM1 | $\leq 1.000029$ | $\leq 0.15\%$ |
| KNM2 | $\leq 1.000028$ | $\leq 0.16\%$ |
| KNM3-SAP | $\leq 1.000030$ | $\leq 0.55\%$ |
| KNM3-NAP | $\leq 1.000017$ | $\leq 0.16\%$ |
| KNM4-NOM | $\leq 1.000051$ | $\leq 0.48\%$ |
| KNM4-OPT | $\leq 1.000048$ | $\leq 0.50\%$ |
| KNM5 | $\leq 1.000056$ | $\leq 0.17\%$ |

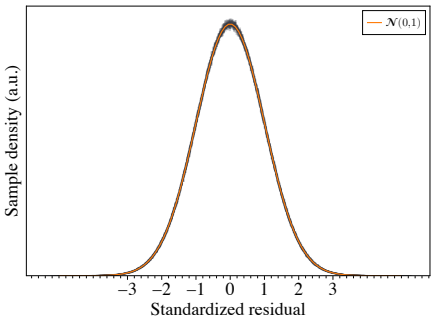


(a) KNM1.

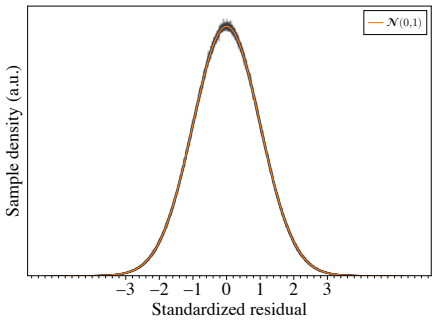


(b) KNM2.

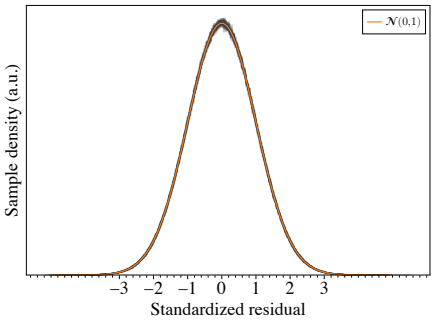


(c) KNM3-SAP.

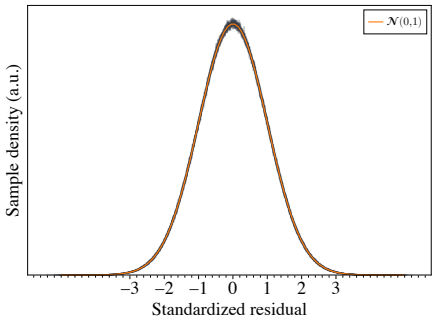


(d) KNM3-NAP.

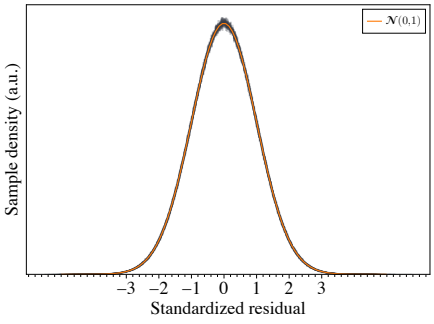


(e) KNM4-NOM.

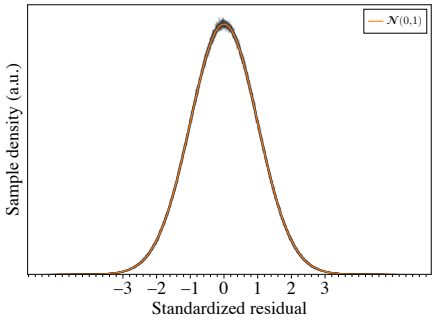


(f) KNM4-OPT.

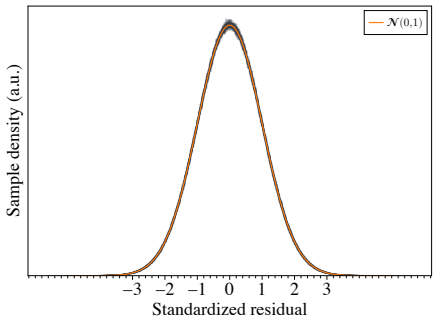


(g) KNM5.

Figure B.1: Posterior predictive check with MAP estimates for the individual KATRIN campaigns using a flat prior $m_\nu^2 \sim \mathcal{U}(-10,10)$. Shown are the standardized residuals for all energies in the form of gray step histograms. The residual distributions should follow a standard Normal distribution, indicated with an orange curve.

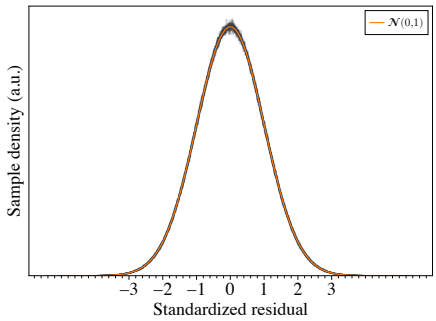


(a) KNM1.

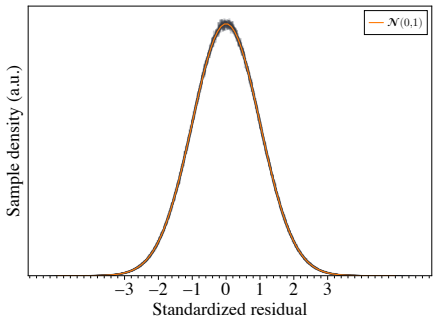


(b) KNM2.

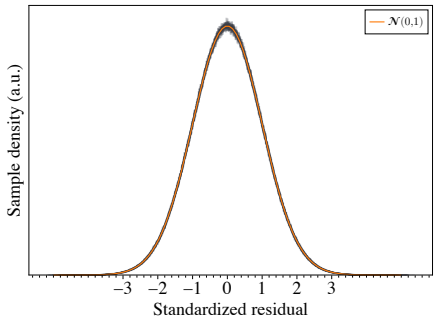


(c) KNM3-SAP.

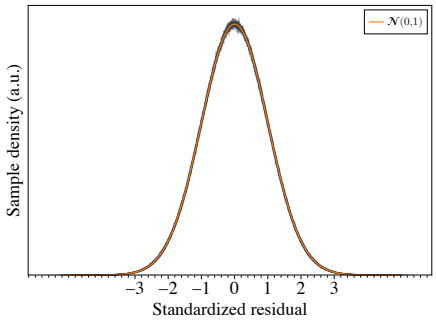


(d) KNM3-NAP.

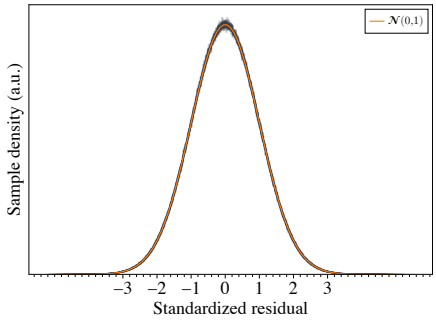


(e) KNM4-NOM.

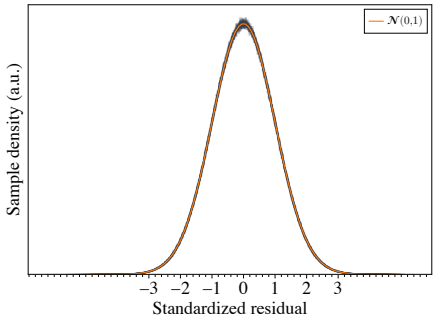


(f) KNM4-OPT.

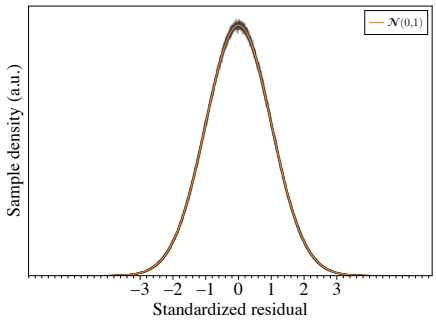


(g) KNM5.

Figure B.2: Posterior predictive check with MAP estimates for the individual KATRIN campaigns using a flat, positive prior $m_\nu^2 \sim \mathcal{U}(0,3)$. Shown are the standardized residuals for all energies in the form of gray step histograms. The residual distributions should follow a standard Normal distribution, indicated with an orange curve.

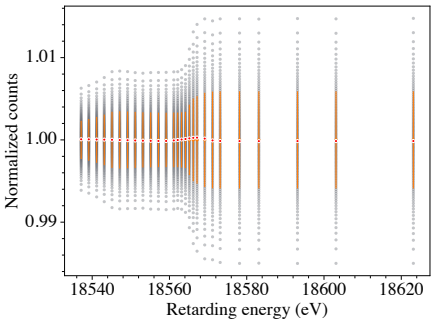


(a) KNM1.

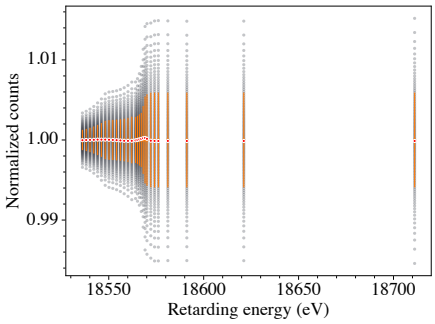


(b) KNM2.

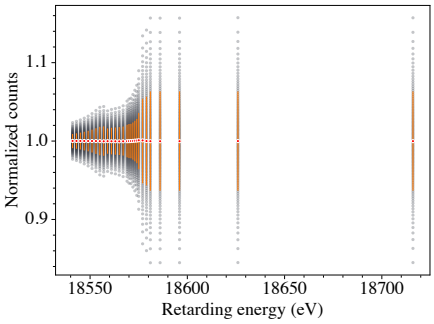


(c) KNM3-SAP.

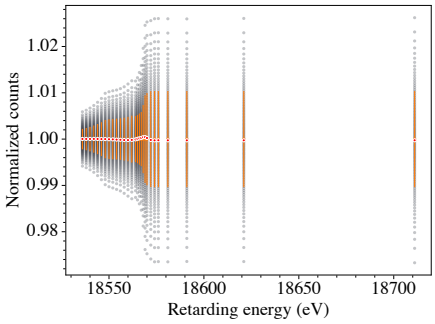


(d) KNM3-NAP.

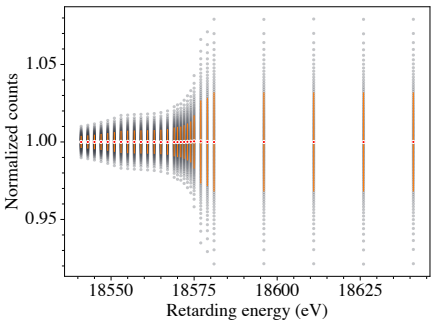


(e) KNM4-NOM.

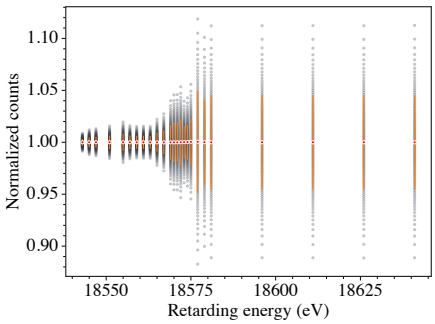


(f) KNM4-OPT.

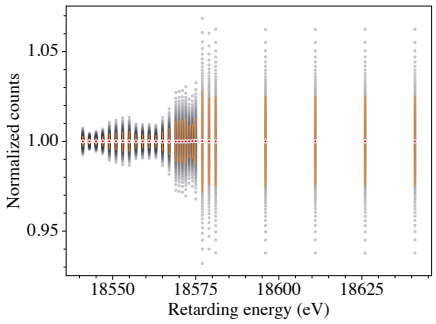


(g) KNM5.

Figure B.3: Posterior predictive check with posterior samples for the individual KATRIN campaigns using a flat prior $m_\nu^2 \sim \mathcal{U}(-10,10)$. The gray dots represent the reproduced data distributions, with red dots indicating the mean values. The original data points and their errors are drawn in orange. To compare all energies at once, despite the counts differing by orders of magnitude, the values at each energy were normalized by dividing by the original data point.

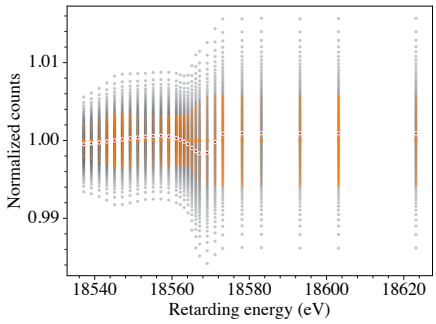


(a) KNM1.

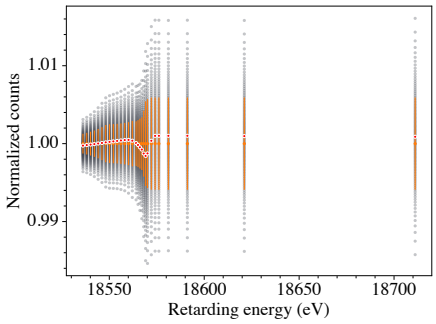


(b) KNM2.

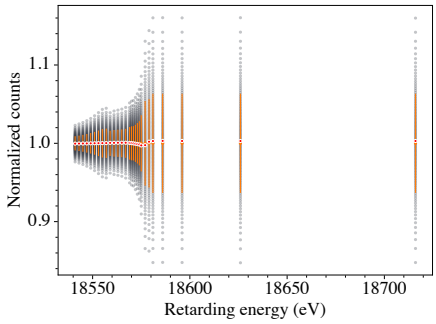


(c) KNM3-SAP.

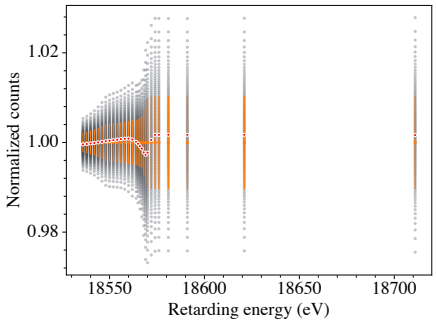


(d) KNM3-NAP.

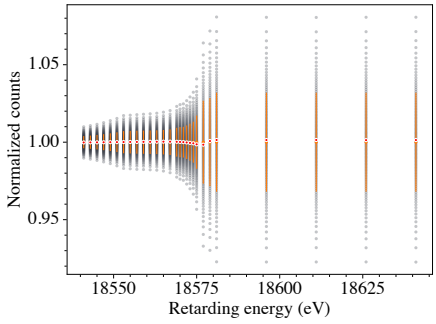


(e) KNM4-NOM.

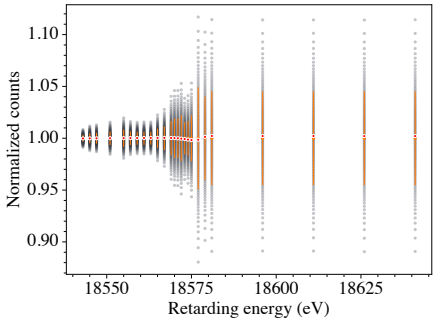


(f) KNM4-OPT.

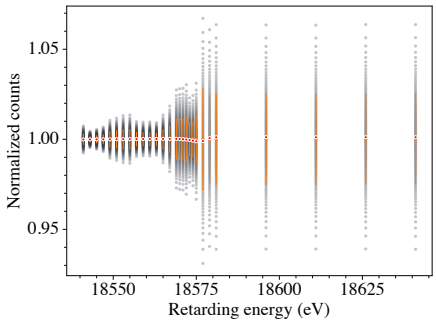


(g) KNM5.

Figure B.4: Posterior predictive check with posterior samples for the individual KATRIN campaigns using a flat, positive prior $m_\nu^2 \sim \mathcal{U}(0,3)$. The gray dots represent the reproduced data distributions, with red dots indicating the mean values. The original data points and their errors are drawn in orange. To compare all energies at once, despite the counts differing by orders of magnitude, the values at each energy were normalized by dividing by the original data point.

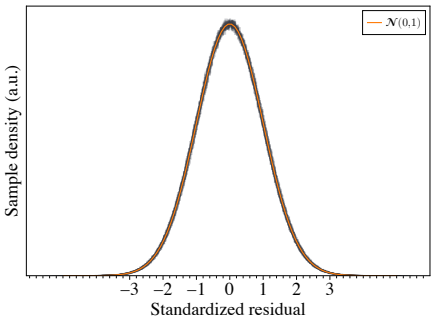


(a) KNM1.

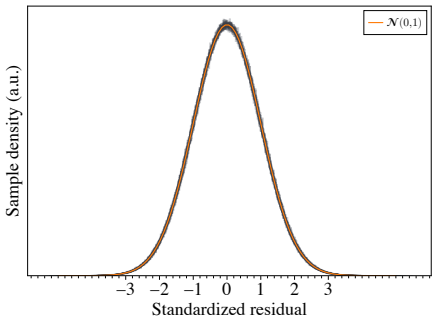


(b) KNM2.

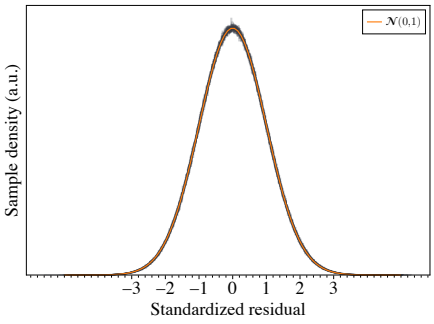


(c) KNM3-SAP.

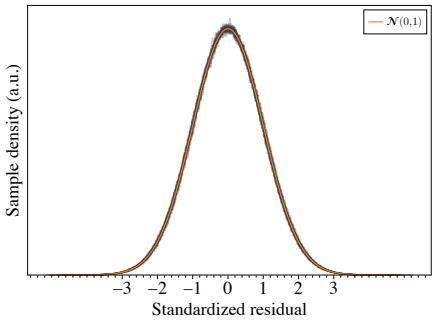


(d) KNM3-NAP.

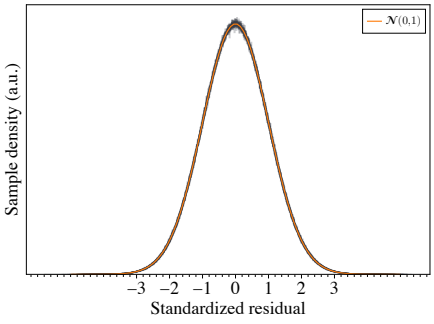


(e) KNM4-NOM.

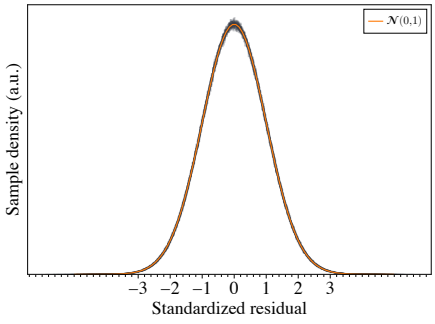


(f) KNM4-OPT.

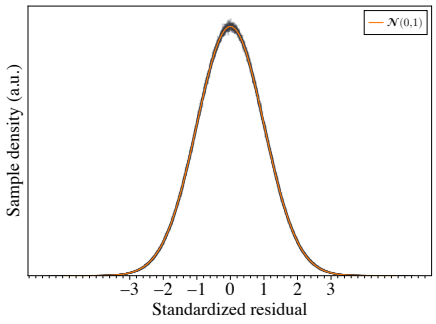


(g) KNM5.

Figure B.5: Posterior predictive check with posterior samples for the individual KATRIN campaigns using a flat prior $m_\nu^2 \sim \mathcal{U}(-10,10)$. Shown are the standardized residuals for all energies in the form of gray step histograms. The residual distributions should follow a standard Normal distribution, indicated with an orange curve.

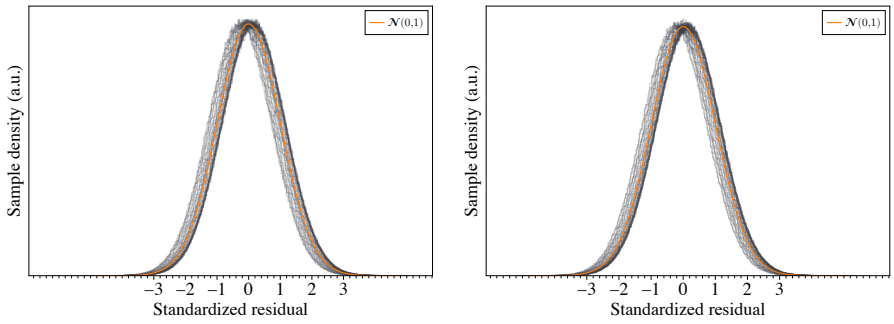


(a) KNM1.




(b) KNM2.

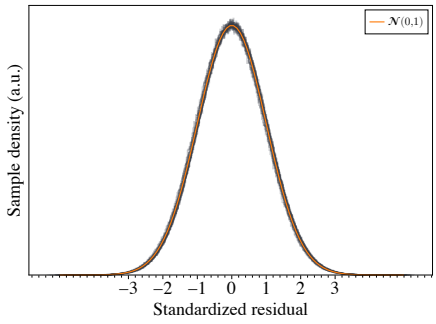


(c) KNM3-SAP.

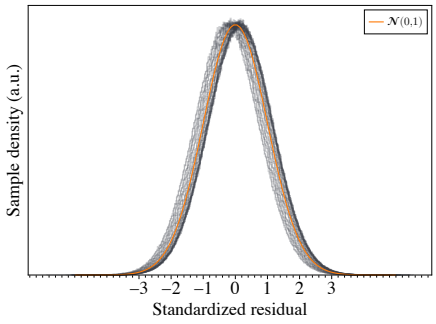


(d) KNM3-NAP.

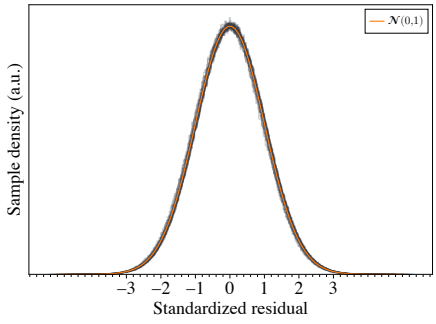


(e) KNM4-NOM.

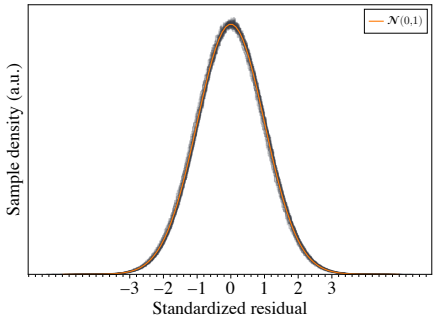


(f) KNM4-OPT.

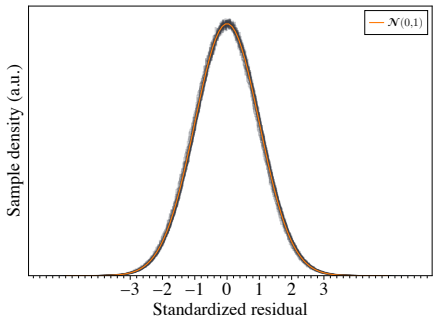


(g) KNM5.

Figure B.6: Posterior predictive check with posterior samples for the individual KATRIN campaigns using a flat, positive prior $m_\nu^2 \sim \mathcal{U}(0,3)$. Shown are the standardized residuals for all energies in the form of gray step histograms. The residual distributions should follow a standard Normal distribution, indicated with an orange curve.

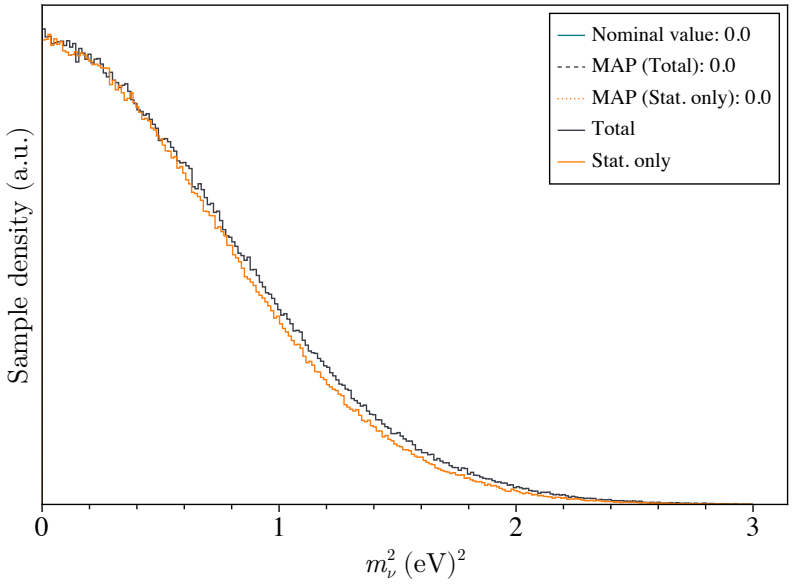


| Type | Quantile values for $m_\nu^2$ in eV$^2$ | | | | | | |
|---|---|---|---|---|---|---|---|
| | **5%** | **15.9%** | **50%** | **68.3%** | **84.1%** | **90%** | **95%** |
| **Total** | 0.0476 | 0.1535 | 0.5199 | 0.7728 | 1.0928 | 1.2792 | 1.5311 |
| **Stat. only** | 0.0459 | 0.1481 | 0.4989 | 0.7417 | 1.0474 | 1.2262 | 1.4662 |

(a) Results for a flat, positive prior: $m_\nu^2 \sim \mathcal{U}(0,3)$.

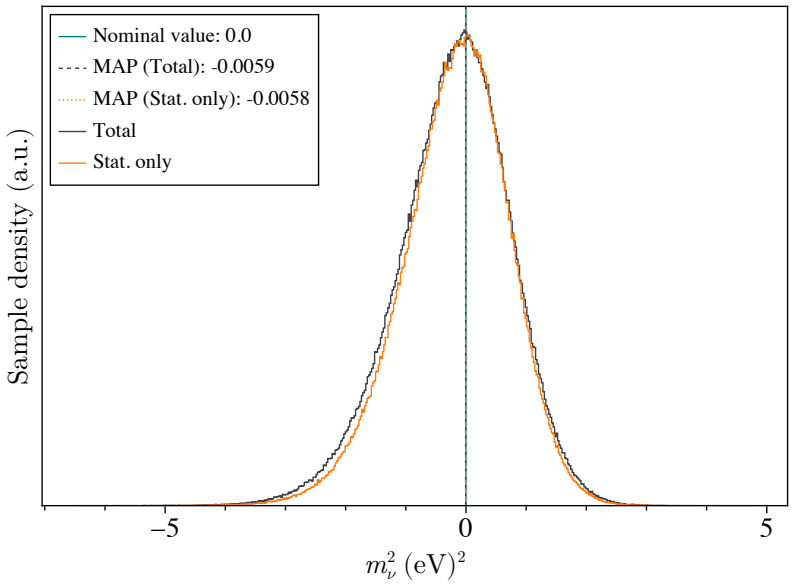


| Type | Quantile values for $m_\nu^2$ in eV$^2$ | | | | | | |
|---|---|---|---|---|---|---|---|
| | **5%** | **15.9%** | **50%** | **68.3%** | **84.1%** | **90%** | **95%** |
| **Total** | -1.8432 | -1.1235 | -0.1509 | 0.2606 | 0.6949 | 0.9277 | 1.2245 |
| **Stat. only** | -1.7095 | -1.0408 | -0.1244 | 0.2672 | 0.6789 | 0.8981 | 1.1815 |

(b) Results for a flat prior: $m_\nu^2 \sim \mathcal{U}(-10,10)$.

Figure B.7: Results for KNM1 are shown for different priors on $m_\nu^2$ as well as for (Stat. only) and (Total) fits. Displayed are the marginal distributions and the corresponding quantile values. The nominal value and the MAP estimates are shown as vertical lines. Numbers are rounded to four digits.

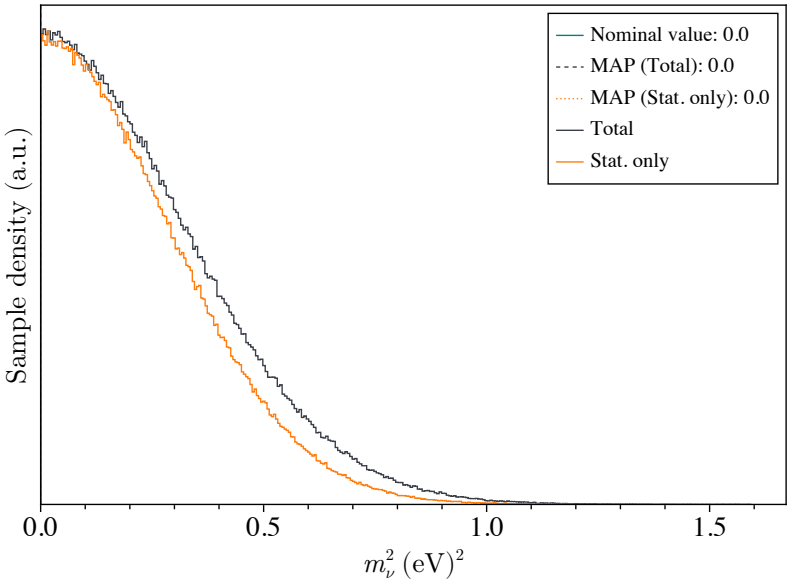


| Type | Quantile values for $m_\nu^2$ in eV$^2$ | | | | | | |
|---|---|---|---|---|---|---|---|
| | **5%** | **15.9%** | **50%** | **68.3%** | **84.1%** | **90%** | **95%** |
| **Total** | 0.0200 | 0.0639 | 0.2166 | 0.3229 | 0.4575 | 0.5360 | 0.6412 |
| **Stat. only** | 0.0179 | 0.0573 | 0.1930 | 0.2869 | 0.4051 | 0.4737 | 0.5654 |

(a) Results for a flat, positive prior: $m_\nu^2 \sim \mathcal{U}(0,3)$.

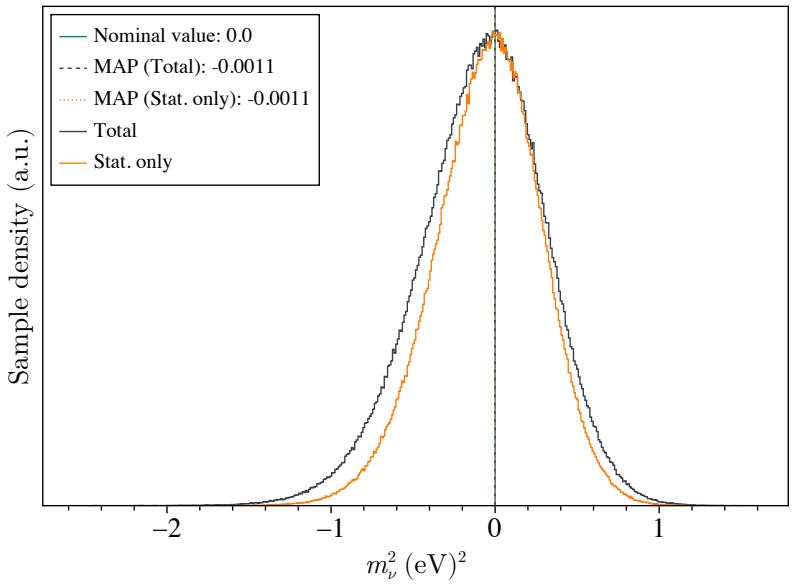


| Type | Quantile values for $m_\nu^2$ in eV$^2$ | | | | | | |
|---|---|---|---|---|---|---|---|
| | **5%** | **15.9%** | **50%** | **68.3%** | **84.1%** | **90%** | **95%** |
| **Total** | -0.7389 | -0.4573 | -0.0629 | 0.1081 | 0.2893 | 0.3857 | 0.5105 |
| **Stat. only** | -0.6037 | -0.3688 | -0.0336 | 0.1139 | 0.2707 | 0.3543 | 0.4625 |

(b) Results for a flat prior: $m_\nu^2 \sim \mathcal{U}(-10,10)$.

Figure B.8: Results for KNM2 are shown for different priors on $m_\nu^2$ as well as for (Stat. only) and (Total) fits. Displayed are the marginal distributions and the corresponding quantile values. The nominal value and the MAP estimates are shown as vertical lines. Numbers are rounded to four digits.

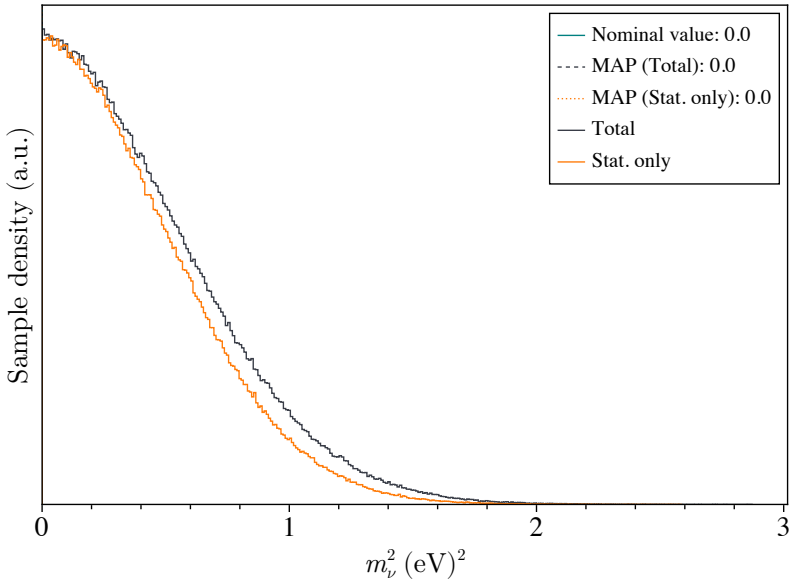


| Type | Quantile values for $m_\nu^2$ in eV$^2$ | | | | | | |
|---|---|---|---|---|---|---|---|
| | **5%** | **15.9%** | **50%** | **68.3%** | **84.1%** | **90%** | **95%** |
| **Total** | 0.0340 | 0.1094 | 0.3724 | 0.5574 | 0.7917 | 0.9287 | 1.1142 |
| **Stat. only** | 0.0309 | 0.0993 | 0.3375 | 0.5046 | 0.7146 | 0.8379 | 1.0039 |

(a) Results for a flat, positive prior: $m_\nu^2 \sim \mathcal{U}(0,3)$.

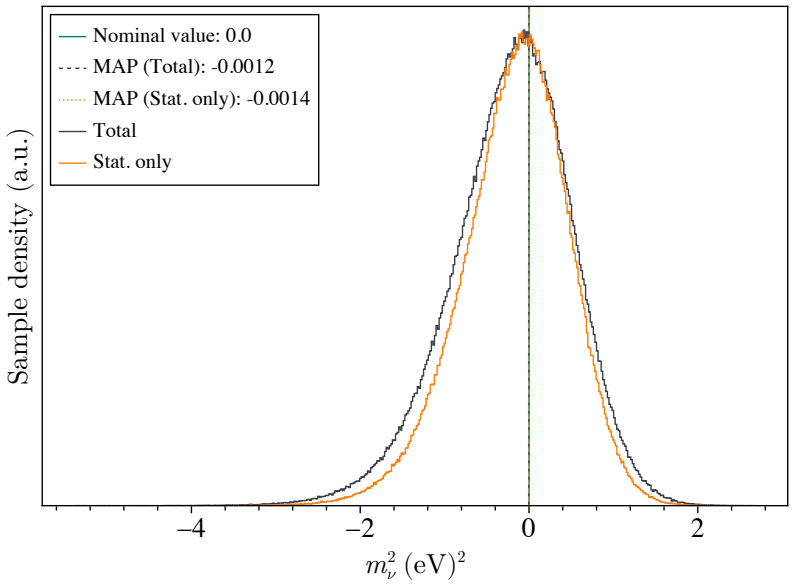


| Type | Quantile values for $m_\nu^2$ in eV$^2$ | | | | | | |
|---|---|---|---|---|---|---|---|
| | **5%** | **15.9%** | **50%** | **68.3%** | **84.1%** | **90%** | **95%** |
| **Total** | -1.4598 | -0.9061 | -0.1635 | 0.1487 | 0.4736 | 0.6474 | 0.8691 |
| **Stat. only** | -1.2700 | -0.7866 | -0.1284 | 0.1473 | 0.4382 | 0.5931 | 0.7906 |

(b) Results for a flat prior: $m_\nu^2 \sim \mathcal{U}(-10,10)$.

Figure B.9: Results for KNM3-SAP are shown for different priors on $m_\nu^2$ as well as for (Stat. only) and (Total) fits. Displayed are the marginal distributions and the corresponding quantile values. The nominal value and the MAP estimates are shown as vertical lines. Numbers are rounded to four digits.

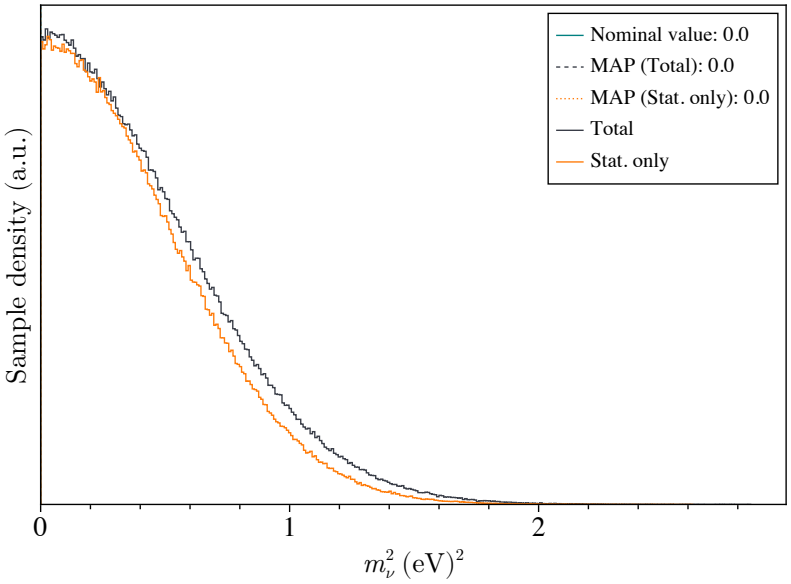


| Type | Quantile values for $m_\nu^2$ in eV$^2$ | | | | | | |
|---|---|---|---|---|---|---|---|
| | **5%** | **15.9%** | **50%** | **68.3%** | **84.1%** | **90%** | **95%** |
| **Total** | 0.0348 | 0.1109 | 0.3770 | 0.5619 | 0.7953 | 0.9318 | 1.1136 |
| **Stat. only** | 0.0322 | 0.1034 | 0.3468 | 0.5147 | 0.7269 | 0.8499 | 1.0143 |

(a) Results for a flat, positive prior: $m_\nu^2 \sim \mathcal{U}(0,3)$.

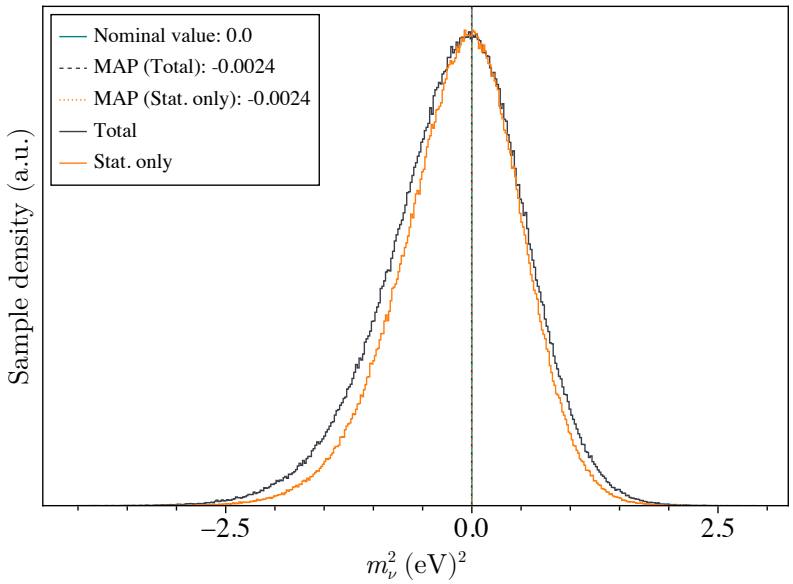


| Type | Quantile values for $m_\nu^2$ in eV$^2$ | | | | | | |
|---|---|---|---|---|---|---|---|
| | **5%** | **15.9%** | **50%** | **68.3%** | **84.1%** | **90%** | **95%** |
| **Total** | -1.3748 | -0.8426 | -0.1235 | 0.1797 | 0.4972 | 0.6678 | 0.8868 |
| **Stat. only** | -1.1878 | -0.7233 | -0.0860 | 0.1851 | 0.4705 | 0.6238 | 0.8184 |

(b) Results for a flat prior: $m_\nu^2 \sim \mathcal{U}(-10,10)$.

Figure B.10: Results for KNM3-NAP are shown for different priors on $m_\nu^2$ as well as for (Stat. only) and (Total) fits. Displayed are the marginal distributions and the corresponding quantile values. The nominal value and the MAP estimates are shown as vertical lines. Numbers are rounded to four digits.

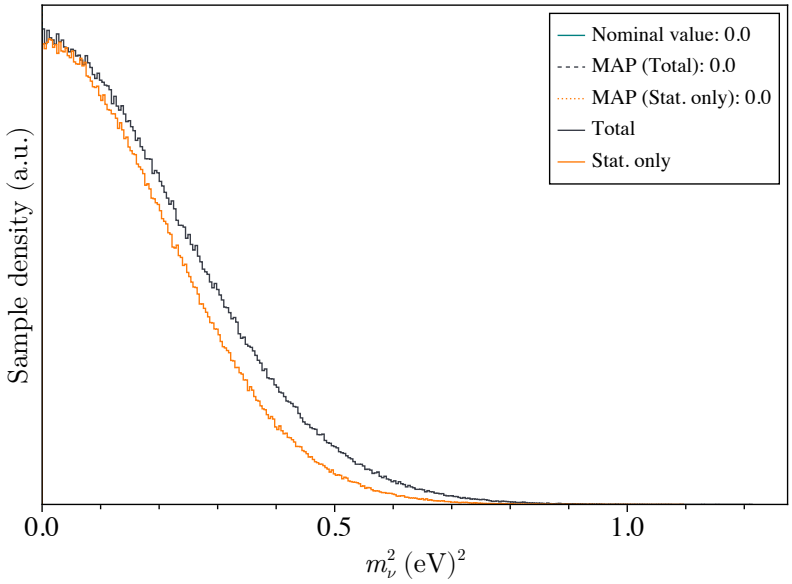


| Type | Quantile values for $m_\nu^2$ in eV$^2$ | | | | | | |
|---|---|---|---|---|---|---|---|
| | 5% | 15.9% | 50% | 68.3% | 84.1% | 90% | 95% |
| **Total** | 0.0150 | 0.0482 | 0.1632 | 0.2435 | 0.3449 | 0.4040 | 0.4832 |
| **Stat. only** | 0.0134 | 0.0428 | 0.1443 | 0.2146 | 0.3032 | 0.3548 | 0.4244 |

(a) Results for a flat, positive prior: $m_\nu^2 \sim \mathcal{U}(0,3)$.

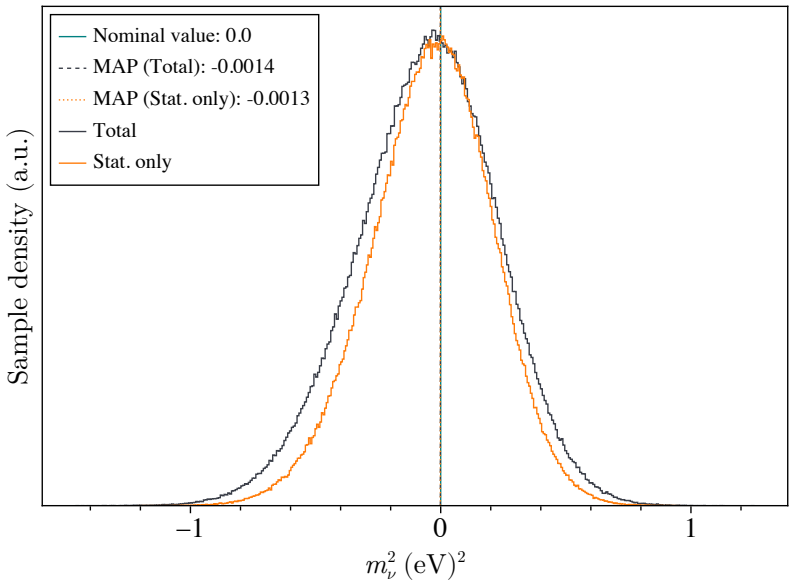


| Type | Quantile values for $m_\nu^2$ in eV$^2$ | | | | | | |
|---|---|---|---|---|---|---|---|
| | 5% | 15.9% | 50% | 68.3% | 84.1% | 90% | 95% |
| **Total** | -0.5351 | -0.3365 | -0.0460 | 0.0821 | 0.2188 | 0.2923 | 0.3864 |
| **Stat. only** | -0.4484 | -0.2771 | -0.0285 | 0.0825 | 0.2006 | 0.2637 | 0.3450 |

(b) Results for a flat prior: $m_\nu^2 \sim \mathcal{U}(-10,10)$.

Figure B.11: Results for KNM4-NOM are shown for different priors on $m_\nu^2$ as well as for (Stat. only) and (Total) fits. Displayed are the marginal distributions and the corresponding quantile values. The nominal value and the MAP estimates are shown as vertical lines. Numbers are rounded to four digits.

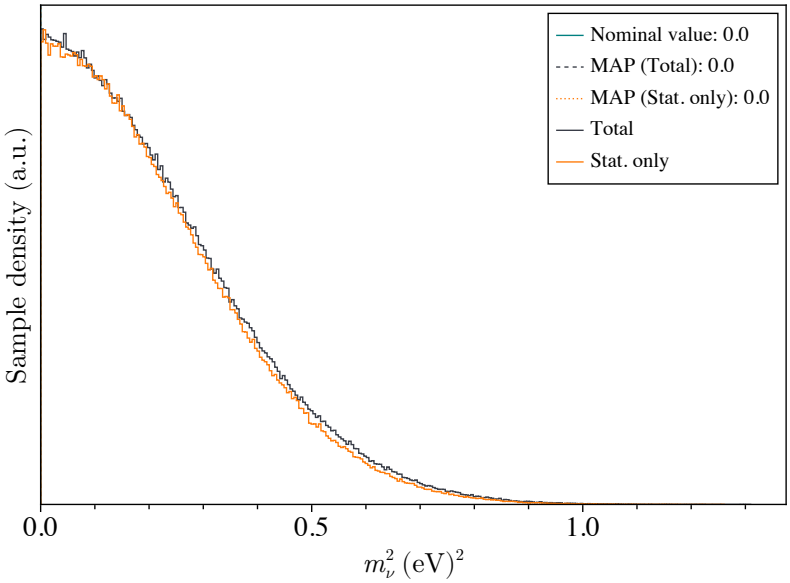


| Type | Quantile values for $m_\nu^2$ in eV$^2$ | | | | | | |
|---|---|---|---|---|---|---|---|
| | **5%** | **15.9%** | **50%** | **68.3%** | **84.1%** | **90%** | **95%** |
| **Total** | 0.0172 | 0.0554 | 0.1880 | 0.2800 | 0.3960 | 0.4641 | 0.5545 |
| **Stat. only** | 0.0169 | 0.0544 | 0.1826 | 0.2718 | 0.3840 | 0.4493 | 0.5364 |

(a) Results for a flat, positive prior: $m_\nu^2 \sim \mathcal{U}(0,3)$.

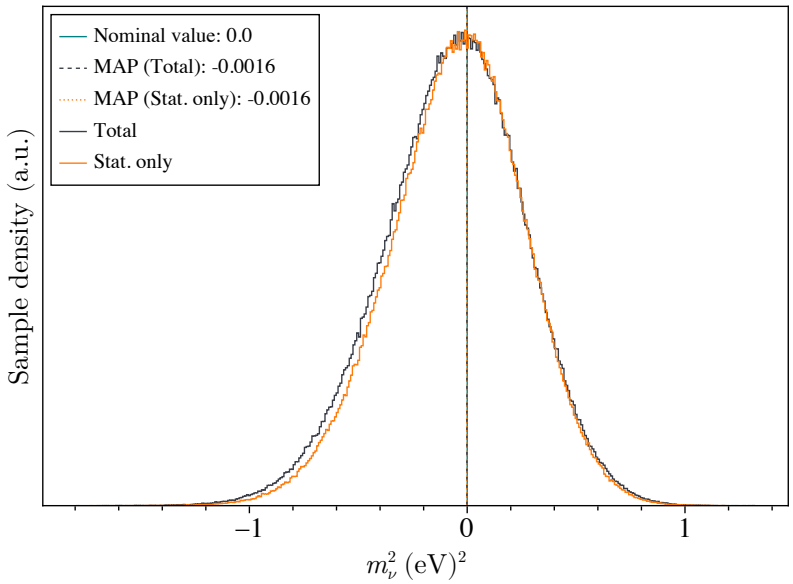


| Type | Quantile values for $m_\nu^2$ in eV$^2$ | | | | | | |
|---|---|---|---|---|---|---|---|
| | **5%** | **15.9%** | **50%** | **68.3%** | **84.1%** | **90%** | **95%** |
| **Total** | -0.6146 | -0.3848 | -0.0508 | 0.0966 | 0.2527 | 0.3372 | 0.4442 |
| **Stat. only** | -0.5734 | -0.3544 | -0.0365 | 0.1041 | 0.2545 | 0.3352 | 0.4372 |

(b) Results for a flat prior: $m_\nu^2 \sim \mathcal{U}(-10,10)$.

Figure B.12: Results for KNM4-OPT are shown for different priors on $m_\nu^2$ as well as for (Stat. only) and (Total) fits. Displayed are the marginal distributions and the corresponding quantile values. The nominal value and the MAP estimates are shown as vertical lines. Numbers are rounded to four digits.

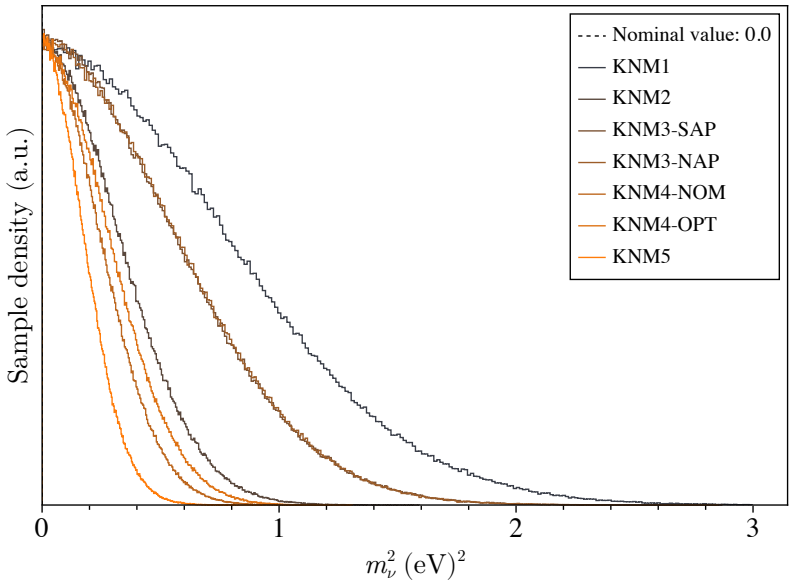


(a) Results for a flat, positive prior: $m_\nu^2 \sim \mathcal{U}(0,3)$.

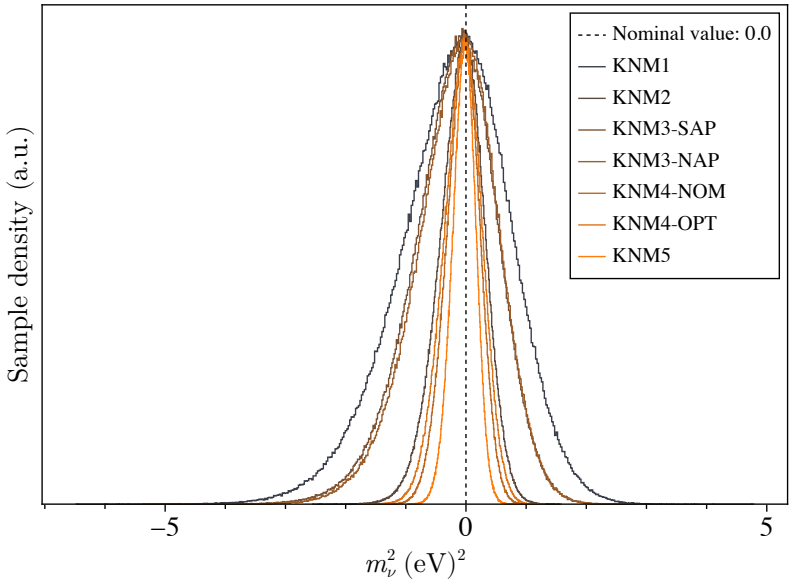


(b) Results for a flat prior: $m_\nu^2 \sim \mathcal{U}(-10,10)$.

Figure B.13: The marginal distribution of $m_\nu^2$ are shown for KNM1-5. The results are obtained by using Asimov twins and taking statistical and systematic uncertainties into account. The results using different priors for $m_\nu^2$ are compared: (a) flat prior and (b) flat, positive prior.

## B.2 Chained analysis

### B.2.1 Initial priors for forwarded parameters

In the following equations, the initial priors for the 12 forwarded parameters $m_\nu^2$, $B_{\text{max}}$, $B_{\text{src}}$, $\vec{E}_{\text{loss,amp}}$, $\vec{E}_{\text{loss,exp}}$ and $\vec{E}_{\text{loss,std}}$ are defined which are used in the first step of a chained analysis. Their form and numerical values are identical for each of the first five KATRIN campaigns. The priors take the form:

$$m_\nu^2 \sim \mathcal{U}(0,3) \;||\; \mathcal{U}(-10,10), \tag{B.1}$$

$$B_{\text{max}} \sim \mathcal{N}\left(1.000,\ 1.000\times10^{-3}\right), \tag{B.2}$$

$$B_{\text{src}} \sim \mathcal{N}\left(2.507,\ 6.000\times10^{-3}\right), \tag{B.3}$$

$$E_{\text{loss}} \sim \mathcal{N}(\mu,\ \Sigma), \tag{B.4}$$

with the expectation value $\mu$ (rounded to three significant digits):

$$\mu := \begin{pmatrix} \mu_{\vec{E}_{\text{loss,amp}}} \\ \mu_{\vec{E}_{\text{loss,exp}}} \\ \mu_{\vec{E}_{\text{loss,std}}} \end{pmatrix} = \begin{pmatrix} 3.280\times10^{-2} \\ 2.957\times10^{-1} \\ 7.575\times10^{-2} \\ 1.192\times10^{1} \\ 1.280\times10^{1} \\ 1.497\times10^{1} \\ 1.836\times10^{-1} \\ 4.677\times10^{-1} \\ 9.070\times10^{-1} \end{pmatrix}, \tag{B.5}$$

and the corresponding covariance matrix $\Sigma$ shown in Table B.2. The values of all other priors used in the first five KATRIN campaigns can be found in Ref. [KATRIN et al., 2025c].

### B.2.2 Parameter transformations

The result of transforming a multivariate non-Gaussian distribution to a standard Gaussian multivariate distribution, as is necessary in the chained analysis, is shown in Fig. B.14.

### B.2.3 MCMC convergence diagnostics

The Markov chain Monte Carlo convergence diagnostics of the performed chained analyses are shown in Tables B.3 to B.5.

### B.2.4 Results

The results for the chained-analysis of the first five KATRIN campaigns, forwarding only information about $m_\nu^2$, can be found in Figs. B.15 and B.16. The results when forwarding all possible 12 parameters, are shown in the main text in Fig. 7.12.

Table B.2: Covariance matrix $\Sigma$ for the $E_{\text{loss}}$-parameters: $\vec{E}_{\text{loss,amp}}$, $\vec{E}_{\text{loss,exp}}$ and $\vec{E}_{\text{loss,std}}$ (rounded to three significant digits).

$$\begin{pmatrix}
1.169\times10^{-4} & 7.818\times10^{-6} & -3.608\times10^{-6} & 3.624\times10^{-4} & 1.074\times10^{-4} & -8.035\times10^{-5} & 1.985\times10^{-4} & -1.404\times10^{-4} & 2.676\times10^{-4} \\
7.818\times10^{-6} & 3.665\times10^{-5} & 3.905\times10^{-6} & -5.202\times10^{-5} & 1.810\times10^{-5} & -1.020\times10^{-5} & -7.794\times10^{-7} & -4.120\times10^{-5} & -1.615\times10^{-4} \\
-3.608\times10^{-6} & 3.905\times10^{-6} & 1.084\times10^{-5} & -5.260\times10^{-6} & 1.515\times10^{-5} & -4.935\times10^{-5} & -1.472\times10^{-5} & 1.947\times10^{-5} & -3.323\times10^{-4} \\
3.624\times10^{-4} & -5.202\times10^{-5} & -5.260\times10^{-6} & 5.552\times10^{-3} & 8.271\times10^{-4} & -2.712\times10^{-4} & 3.629\times10^{-3} & -6.384\times10^{-4} & 6.475\times10^{-4} \\
1.074\times10^{-4} & 1.810\times10^{-5} & 1.515\times10^{-5} & 8.271\times10^{-4} & 3.602\times10^{-4} & 5.916\times10^{-5} & 6.612\times10^{-4} & -9.648\times10^{-5} & -6.902\times10^{-4} \\
-8.035\times10^{-5} & -1.020\times10^{-5} & -4.935\times10^{-5} & -2.712\times10^{-4} & 5.916\times10^{-5} & 1.313\times10^{-3} & -3.782\times10^{-4} & 2.771\times10^{-4} & -1.797\times10^{-4} \\
1.985\times10^{-4} & -7.794\times10^{-7} & -1.472\times10^{-5} & 3.629\times10^{-3} & 6.612\times10^{-4} & -3.782\times10^{-4} & 3.886\times10^{-3} & -7.143\times10^{-4} & 1.203\times10^{-3} \\
-1.404\times10^{-4} & -4.120\times10^{-5} & 1.947\times10^{-5} & -6.384\times10^{-4} & -9.648\times10^{-5} & 2.771\times10^{-4} & -7.143\times10^{-4} & 3.797\times10^{-4} & -1.216\times10^{-3} \\
2.676\times10^{-4} & -1.615\times10^{-4} & -3.323\times10^{-4} & 6.475\times10^{-4} & -6.902\times10^{-4} & -1.797\times10^{-4} & 1.203\times10^{-3} & -1.216\times10^{-3} & 1.306\times10^{-2}
\end{pmatrix}$$

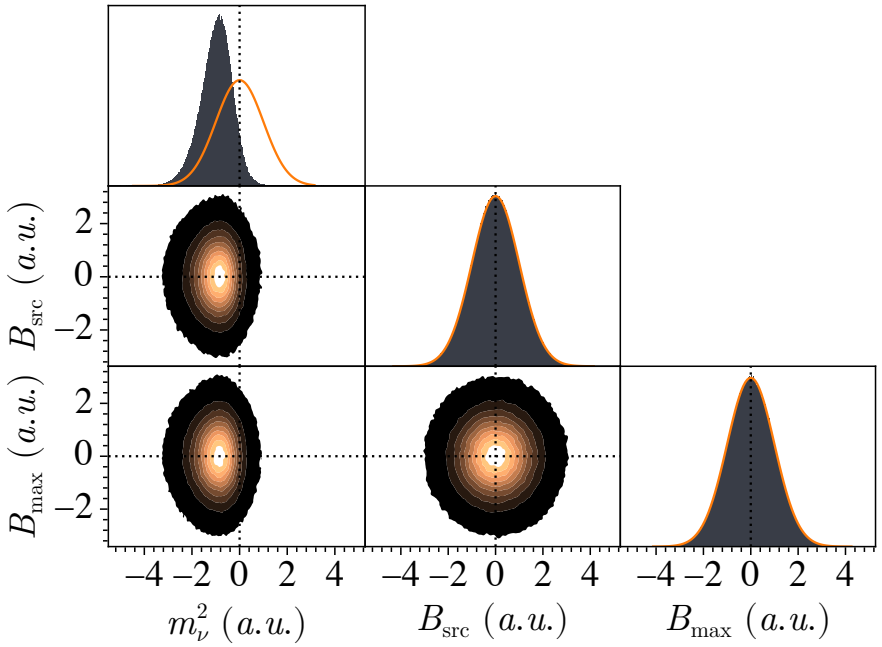


(a) Forwarded parameters in space-1. The correlation between parameters are visible and especially the marginal distribution of $m_\nu^2$ is skewed and does not follow a standard normal distribution.

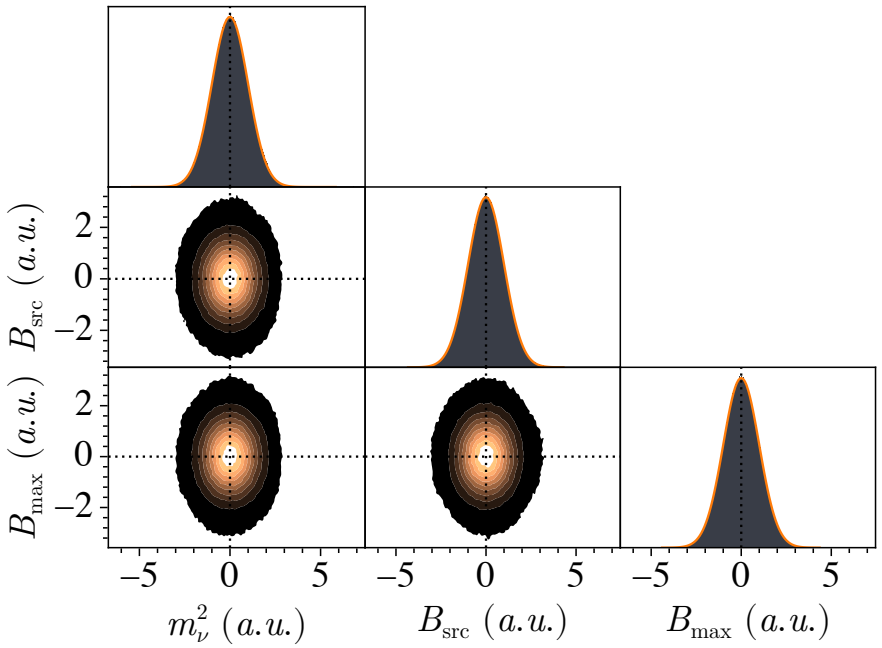


(b) Forwarded parameters in space-2. The parameters follow a multivariate standard normal distribution.

Figure B.14: Illustration of a parameter transformation from space-1 to space-2. For the sake of visualization, only three of the 12 forwarded parameters are shown, namely $m_\nu^2, B_{\mathrm{src}}$ and $B_{\mathrm{max}}$. The anticipated standard normal distribution is indicated in the 1-d histograms with orange lines. For the 2-d histograms dashed black lines are drawn, horizontally and vertically, at a value of zero.

Table B.3: Summary of MCMC convergence diagnostics for the chained analysis where only $m_\nu^2$ are forwarded between campaigns. Reported are the largest values from all parameters of a campaign for $\widehat{\mathrm{R}}$ and the relative MCMCSE for the 90%-quantile. Asimov data were analyzed and an initial flat prior $m_\nu^2 \sim \mathcal{U}(-10,10)$ was used in the first step. The diagnostics are shown for two different sequences, both analyzed taking only statistical uncertainties or statistical and systematic uncertainties into account.

(a) Permutation 1. Taking only statistical uncertainties into account.

| **Step** | **Campaign** | $\widehat{\mathbf{R}}$ | **MCMCSE for 90%-quantile** |
|---|---|---|---|
| 1 | KNM1 | $\leq 1.000037$ | 0.27% |
| 2 | KNM2 | $\leq 1.000033$ | 0.23% |
| 3 | KNM3-NAP | $\leq 1.000019$ | 0.21% |
| 4 | KNM3-SAP | $\leq 1.000023$ | 0.17% |
| 5 | KNM4-NOM | $\leq 1.000017$ | 0.19% |
| 6 | KNM4-OPT | $\leq 1.000017$ | 0.16% |
| 7 | KNM5 | $\leq 1.000019$ | 0.17% |

(b) Permutation 2. Taking only statistical uncertainties into account.

| **Step** | **Campaign** | $\widehat{\mathbf{R}}$ | **MCMCSE for 90%-quantile** |
|---|---|---|---|
| 1 | KNM5 | $\leq 1.000041$ | 0.21% |
| 2 | KNM4-OPT | $\leq 1.000021$ | 0.15% |
| 3 | KNM4-NOM | $\leq 1.000030$ | 0.18% |
| 4 | KNM3-SAP | $\leq 1.000017$ | 0.16% |
| 5 | KNM3-NAP | $\leq 1.000016$ | 0.20% |
| 6 | KNM2 | $\leq 1.000014$ | 0.19% |
| 7 | KNM1 | $\leq 1.000023$ | 0.18% |

(c) Permutation 1. Taking statistical and systematic uncertainties into account.

| **Step** | **Campaign** | $\widehat{\mathbf{R}}$ | **MCMCSE for 90%-quantile** |
|---|---|---|---|
| 1 | KNM1 | $\leq 1.000027$ | 0.17% |
| 2 | KNM2 | $\leq 1.000031$ | 0.18% |
| 3 | KNM3-NAP | $\leq 1.000018$ | 0.18% |
| 4 | KNM3-SAP | $\leq 1.000038$ | 0.49% |
| 5 | KNM4-NOM | $\leq 1.000119$ | 0.48% |
| 6 | KNM4-OPT | $\leq 1.000032$ | 0.51% |
| 7 | KNM5 | $\leq 1.000124$ | 0.22% |

(d) Permutation 2. Taking statistical and systematic uncertainties into account.

| **Step** | **Campaign** | $\widehat{\mathbf{R}}$ | **MCMCSE for 90%-quantile** |
|---|---|---|---|
| 1 | KNM5 | $\leq 1.000156$ | 0.27% |
| 2 | KNM4-OPT | $\leq 1.000058$ | 0.49% |
| 3 | KNM4-NOM | $\leq 1.000106$ | 0.50% |
| 4 | KNM3-SAP | $\leq 1.000032$ | 0.53% |
| 5 | KNM3-NAP | $\leq 1.000023$ | 0.17% |
| 6 | KNM2 | $\leq 1.000020$ | 0.19% |
| 7 | KNM1 | $\leq 1.000018$ | 0.18% |

Table B.4: Summary of MCMC convergence diagnostics for the chained analysis where only $m_\nu^2$ are forwarded between campaigns. Reported are the largest values from all parameters of a campaign for $\widehat{\mathrm{R}}$ and the relative MCMCSE for the 90%-quantile. Asimov data were analyzed and an initial flat, positive prior $m_\nu^2 \sim \mathcal{U}(0,3)$ was used in the first step. The diagnostics are shown for two different sequences, both analyzed taking only statistical uncertainties or statistical and systematic uncertainties into account.

(a) Permutation 1. Taking only statistical uncertainties into account.

| Step | Campaign | $\widehat{\mathrm{R}}$ | MCMCSE for 90%-quantile |
|---|---|---|---|
| 1 | KNM1 | $\leq 1.000019$ | 0.16% |
| 2 | KNM2 | $\leq 1.000034$ | 0.14% |
| 3 | KNM3-NAP | $\leq 1.000016$ | 0.12% |
| 4 | KNM3-SAP | $\leq 1.000023$ | 0.10% |
| 5 | KNM4-NOM | $\leq 1.000027$ | 0.11% |
| 6 | KNM4-OPT | $\leq 1.000023$ | 0.10% |
| 7 | KNM5 | $\leq 1.000023$ | 0.10% |

(b) Permutation 2. Taking only statistical uncertainties into account.

| Step | Campaign | $\widehat{\mathrm{R}}$ | MCMCSE for 90%-quantile |
|---|---|---|---|
| 1 | KNM5 | $\leq 1.000018$ | 0.11% |
| 2 | KNM4-OPT | $\leq 1.000017$ | 0.10% |
| 3 | KNM4-NOM | $\leq 1.000015$ | 0.10% |
| 4 | KNM3-SAP | $\leq 1.000018$ | 0.09% |
| 5 | KNM3-NAP | $\leq 1.000020$ | 0.11% |
| 6 | KNM2 | $\leq 1.000013$ | 0.11% |
| 7 | KNM1 | $\leq 1.000022$ | 0.11% |

(c) Permutation 1. Taking statistical and systematic uncertainties into account.

| Step | Campaign | $\widehat{\mathrm{R}}$ | MCMCSE for 90%-quantile |
|---|---|---|---|
| 1 | KNM1 | $\leq 1.000022$ | 0.15% |
| 2 | KNM2 | $\leq 1.000023$ | 0.15% |
| 3 | KNM3-NAP | $\leq 1.000021$ | 0.15% |
| 4 | KNM3-SAP | $\leq 1.000047$ | 0.52% |
| 5 | KNM4-NOM | $\leq 1.000067$ | 0.52% |
| 6 | KNM4-OPT | $\leq 1.000062$ | 0.50% |
| 7 | KNM5 | $\leq 1.000183$ | 0.15% |

(d) Permutation 2. Taking statistical and systematic uncertainties into account.

| Step | Campaign | $\widehat{\mathrm{R}}$ | MCMCSE for 90%-quantile |
|---|---|---|---|
| 1 | KNM5 | $\leq 1.000094$ | 0.16% |
| 2 | KNM4-OPT | $\leq 1.000056$ | 0.55% |
| 3 | KNM4-NOM | $\leq 1.000065$ | 0.46% |
| 4 | KNM3-SAP | $\leq 1.000032$ | 0.52% |
| 5 | KNM3-NAP | $\leq 1.000021$ | 0.16% |
| 6 | KNM2 | $\leq 1.000026$ | 0.15% |
| 7 | KNM1 | $\leq 1.000018$ | 0.15% |

Table B.5: Summary of MCMC convergence diagnostics for the chained analysis where $m_\nu^2$, $B_{\text{max}}$, $B_{\text{src}}$, $\vec{E}_{\text{loss,amp}}$, $\vec{E}_{\text{loss,exp}}$, $\vec{E}_{\text{loss,std}}$ and their correlations are forwarded between campaigns. Reported are the largest values from all parameters of a campaign for $\widehat{\text{R}}$ and the relative MCMCSE. Asimov data were analyzed and different initial priors on $m_\nu^2$ was used in the first step. The diagnostics are shown for two different sequences, both analyzed taking statistical and systematic uncertainties into account.

(a) Permutation 1. With a flat prior $m_\nu^2 \sim \mathcal{U}(-10, 10)$ used in the first step.

| **Step** | **Campaign** | $\widehat{\mathbf{R}}$ | **MCMCSE for 90%-quantile** |
|---|---|---|---|
| 1 | KNM1 | $\leq 1.000026$ | 0.17% |
| 2 | KNM2 | $\leq 1.000015$ | 0.17% |
| 3 | KNM3-NAP | $\leq 1.000017$ | 0.18% |
| 4 | KNM3-SAP | $\leq 1.000029$ | 0.50% |
| 5 | KNM4-NOM | $\leq 1.000073$ | 0.50% |
| 6 | KNM4-OPT | $\leq 1.000091$ | 0.53% |
| 7 | KNM5 | $\leq 1.000173$ | 0.23% |

(b) Permutation 2. With a flat prior $m_\nu^2 \sim \mathcal{U}(-10, 10)$ used in the first step.

| **Step** | **Campaign** | $\widehat{\mathbf{R}}$ | **MCMCSE for 90%-quantile** |
|---|---|---|---|
| 1 | KNM5 | $\leq 1.000170$ | 0.29% |
| 2 | KNM4-OPT | $\leq 1.000062$ | 0.49% |
| 3 | KNM4-NOM | $\leq 1.000126$ | 0.47% |
| 4 | KNM3-SAP | $\leq 1.000031$ | 0.52% |
| 5 | KNM3-NAP | $\leq 1.000023$ | 0.17% |
| 6 | KNM2 | $\leq 1.000029$ | 0.19% |
| 7 | KNM1 | $\leq 1.000031$ | 0.17% |

(c) Permutation 1. With a flat, positive prior $m_\nu^2 \sim \mathcal{U}(0, 3)$ used in the first step.

| **Step** | **Campaign** | $\widehat{\mathbf{R}}$ | **MCMCSE for 90%-quantile** |
|---|---|---|---|
| 1 | KNM1 | $\leq 1.000022$ | 0.15% |
| 2 | KNM2 | $\leq 1.000019$ | 0.16% |
| 3 | KNM3-NAP | $\leq 1.000025$ | 0.15% |
| 4 | KNM3-SAP | $\leq 1.000028$ | 0.50% |
| 5 | KNM4-NOM | $\leq 1.000101$ | 0.47% |
| 6 | KNM4-OPT | $\leq 1.000029$ | 0.46% |
| 7 | KNM5 | $\leq 1.000133$ | 0.15% |

(d) Permutation 2. With a flat, positive prior $m_\nu^2 \sim \mathcal{U}(0, 3)$ used in the first step.

| **Step** | **Campaign** | $\widehat{\mathbf{R}}$ | **MCMCSE for 90%-quantile** |
|---|---|---|---|
| 1 | KNM5 | $\leq 1.000119$ | 0.16% |
| 2 | KNM4-OPT | $\leq 1.000067$ | 0.49% |
| 3 | KNM4-NOM | $\leq 1.000025$ | 0.49% |
| 4 | KNM3-SAP | $\leq 1.000028$ | 0.51% |
| 5 | KNM3-NAP | $\leq 1.000022$ | 0.15% |
| 6 | KNM2 | $\leq 1.000020$ | 0.16% |
| 7 | KNM1 | $\leq 1.000023$ | 0.16% |

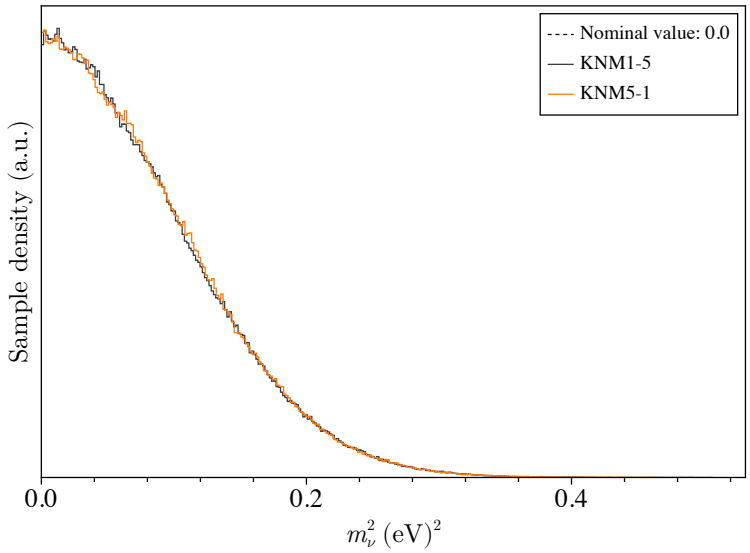


| Type | Quantile values for $m_\nu^2$ in eV$^2$ | | | | | | |
|---|---|---|---|---|---|---|---|
| | **5%** | **15.9%** | **50%** | **68.3%** | **84.1%** | **90%** | **95%** |
| **KNM1-5** | 0.0063 | 0.0200 | 0.0679 | 0.1009 | 0.1427 | 0.1668 | 0.1993 |
| **KNM5-1** | 0.0063 | 0.0201 | 0.0685 | 0.1016 | 0.1426 | 0.1669 | 0.1988 |

(a) Taking only statistical uncertainties into account.

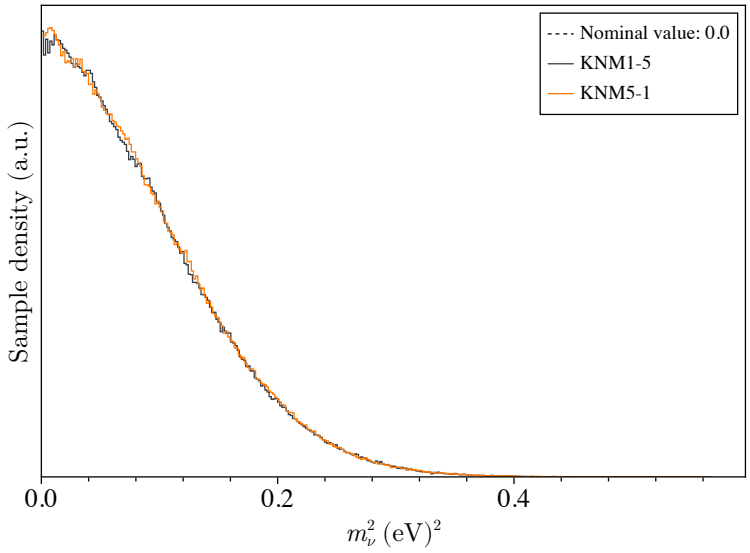


| Type | Quantile values for $m_\nu^2$ in eV$^2$ | | | | | | |
|---|---|---|---|---|---|---|---|
| | **5%** | **15.9%** | **50%** | **68.3%** | **84.1%** | **90%** | **95%** |
| **KNM1-5** | 0.0066 | 0.0209 | 0.0716 | 0.1070 | 0.1523 | 0.1785 | 0.2140 |
| **KNM5-1** | 0.0065 | 0.0208 | 0.0718 | 0.1074 | 0.1525 | 0.1790 | 0.2137 |

(b) Taking statistical and systematic uncertainties into account.

Figure B.15: Results of the chained analysis forwarding only $m_\nu^2$ between campaigns. The sequences KNM1 → KNM2 → KNM3-NAP → KNM3-SAP → KNM4-NOM → KNM4-OPT → KNM5 and its reversed order are compared for an initial flat, positive prior $m_\nu^2 \sim \mathcal{U}(0,3)$. In addition, the results are shown for (a) taking only statistical uncertainties and (b) taking statistical and systematic uncertainties into account.

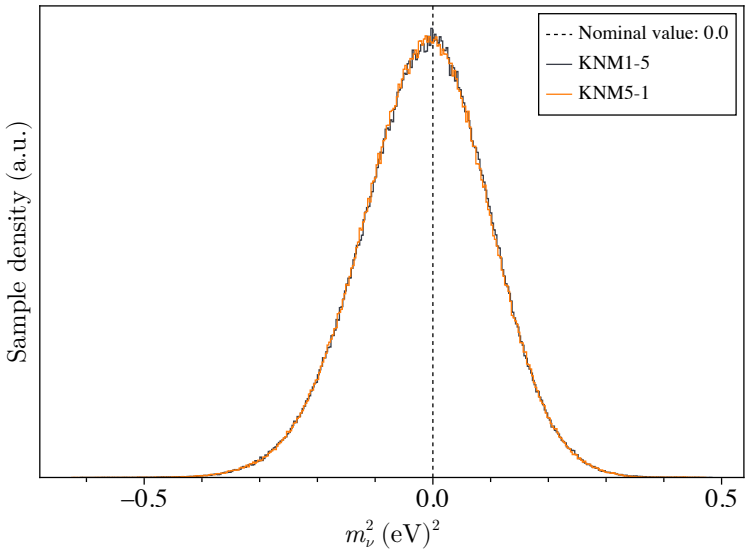


| Type | Quantile values for $m_\nu^2$ in eV$^2$ | | | | | | |
|---|---|---|---|---|---|---|---|
| | 5% | 15.9% | 50% | 68.3% | 84.1% | 90% | 95% |
| **KNM1-5** | -0.1982 | -0.1222 | -0.0100 | 0.0408 | 0.0957 | 0.1250 | 0.1629 |
| **KNM5-1** | -0.1982 | -0.1225 | -0.0112 | 0.0397 | 0.0948 | 0.1247 | 0.1626 |

(a) Taking only statistical uncertainties into account.

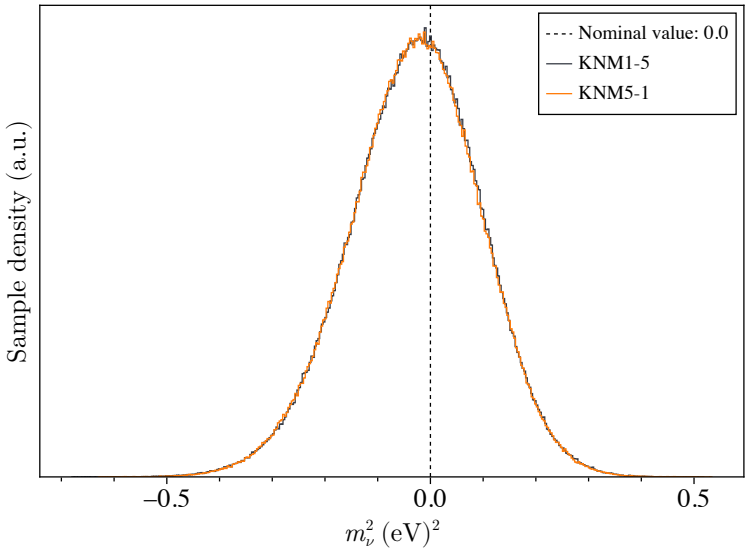


| Type | Quantile values for $m_\nu^2$ in eV$^2$ | | | | | | |
|---|---|---|---|---|---|---|---|
| | 5% | 15.9% | 50% | 68.3% | 84.1% | 90% | 95% |
| **KNM1-5** | -0.2378 | -0.1515 | -0.0250 | 0.0324 | 0.0940 | 0.1268 | 0.1686 |
| **KNM5-1** | -0.2383 | -0.1522 | -0.0263 | 0.0311 | 0.0931 | 0.1264 | 0.1680 |

(b) Taking statistical and systematic uncertainties into account.

Figure B.16: Results of the chained analysis forwarding only $m_\nu^2$ between campaigns. The sequences KNM1 → KNM2 → KNM3-NAP → KNM3-SAP → KNM4-NOM → KNM4-OPT → KNM5 and its reversed order are compared for an initial flat prior $m_\nu^2 \sim \mathcal{U}(-10, 10)$. In addition, the results are shown for (a) taking only statistical uncertainties and (b) taking statistical and systematic uncertainties into account.

# Appendix C

# Further scientific contributions

## C.1 Supervised students

**Masterthesis**:

- Jakob Krause, "Determination of the beam asymmetry $\Sigma$ in $\eta$- and $\eta'$-photoproduction using Bayesian statistics", 2022
- Jean Noël, "Truncated partial-wave analysis of the reaction $\gamma p \to \pi^0 p$ using Bayesian statistics", 2022

**Bachelorthesis**:

- Aleksander Wagner, "Truncated partial wave analysis of the reaction $\gamma p \to K\Lambda$", 2023

## C.2 Conference contributions

1. **CB-Collaboration Meeting**, **2023**, Talk with the title "Truncated partial-wave analysis of $\eta$-Photoproduction with Bayesian statistics"
2. **MENU**, **2023**, 16th International conference on meson-nucleon physics and the structure of the nucleon, Talk with the title "Combination of Bayesian statistics with truncated partial-wave analysis"
3. **Invited Talk Glasgow University**, **2023**, "Combination of Bayesian statistics with truncated partial-wave analysis"
4. **HADRON**, **2021**, 19th International conference on hadron spectroscopy and structure, Talk with the title "Minimal complete sets for two-pseudoscalar-meson photoproduction"
5. **ISNET**, **2021**, Information and statistics in nuclear experiment and theory, Talk with the title "Bayesian statistics for partial-wave analysis"

6. **KATRIN collaboration Meeting**, **2024**, Talk with the title "Bayesian Analysis of KNM1-5 using Netrium.jl" (multiple speakers)
7. **KATRIN collaboration Meeting**, **2025**, Talk with the title "Bayesian analysis of KNM1-5, First looks on combined data" (multiple speakers)
8. **KATRIN collaboration Meeting**, **2025**, Talk with the title "Chained Bayesian Analysis of KNM1-5 with Netrium"

# List of Tables

# List of Figures

# Bibliography


[Aaij et al., 2015] Aaij, R. et al. (2015). Observation of $J/\psi p$ resonances consistent with pentaquark states in $\Lambda_b^0 \to J/\psi k^- p$ decays. *Physical Review Letters*, 115(7):072001.

[Aaij et al., 2017] Aaij, R. et al. (2017). Observation of $J/\psi\phi$ structures consistent with exotic states from amplitude analysis of $B^+ \to J/\psi\phi K^+$ decays. *Physical Review Letters*, 118:022003.

[Adame et al., 2025] Adame, A. et al. (2025). DESI 2024 VI: cosmological constraints from the measurements of baryon acoustic oscillations. *Journal of Cosmology and Astroparticle Physics*, 2025(02):021.

[Ahmad et al., 2001] Ahmad, Q. R. et al. (2001). Measurement of the rate of $\nu_e + d \to p + p + e^-$ interactions produced by $^8B$ solar neutrinos at the sudbury neutrino observatory. *Physical Review Letters*, 87:071301.

[Ahmad et al., 2002] Ahmad, Q. R. et al. (2002). Direct evidence for neutrino flavor transformation from neutral-current interactions in the sudbury neutrino observatory. *Physical Review Letters*, 89:011301.

[Aitchison and Hey, 2012] Aitchison, I. J. and Hey, A. J. (2012). *Gauge Theories in Particle Physics: A Practical Introduction, -2 Volume set.* Taylor & Francis.

[Aker et al., 2021a] Aker, M. et al. (2021a). Analysis methods for the first KATRIN neutrino-mass measurement. *Physical Review D*, 104(1):012005.

[Aker et al., 2021b] Aker, M. et al. (2021b). The design, construction, and commissioning of the KATRIN experiment. *Journal of Instrumentation*, 16(08):T08015.

[Aker et al., 2021c] Aker, M. et al. (2021c). Precision measurement of the electron energy-loss function in tritium and deuterium gas for the KATRIN experiment. *The European Physical Journal C*, 81:1–16.

[Akhmedov and Smirnov, 2009] Akhmedov, E. K. and Smirnov, A. Y. (2009). Paradoxes of neutrino oscillations. *Physics of Atomic Nuclei*, 72(8):1363–1381.

[Alef et al., 2020] Alef, S. et al. (2020). The BGOOD experimental setup at ELSA. *The European Physical Journal A*, 56:1–27.

[Amsbaugh et al., 2015] Amsbaugh, J. et al. (2015). Focal-plane detector system for the KATRIN experiment. *Nuclear Instruments and Methods in Physics Research Section A: Accelerators, Spectrometers, Detectors and Associated Equipment*, 778:40–60.

[Anisovich et al., 2013] Anisovich, A. et al. (2013). Study of ambiguities in $\pi^- p \to \Lambda K^0$ scattering amplitudes. *The European Physical Journal A*, 49:1–14.

[Anisovich et al., 2016] Anisovich, A. et al. (2016). The impact of new polarization data from Bonn, Mainz and Jefferson Laboratory on multipoles. *The European Physical Journal A*, 52(9):284.

[Arenhövel and Fix, 2014] Arenhövel, H. and Fix, A. (2014). Complete set of observables for photoproduction of two pseudoscalars on a nucleon. *Physical Review C*, 89(3):034003.

[ATLAS-Collaboration et al., 2012] ATLAS-Collaboration et al. (2012). Observation of a new particle in the search for the standard model Higgs boson with the ATLAS detector at the LHC. *Physics Letters B*, 716(1):1–29.

[Ball, 1961] Ball, J. S. (1961). Application of the Mandelstam representation to photoproduction of pions from nucleons. *Phys. Rev.*, 124:2014–2028.

[Bartalini et al., 2005] Bartalini, O. et al. (2005). Measurement of $\pi$-photoproduction on the proton from 550 to 1500 Mev at GRAAL. *The European Physical Journal A-Hadrons and Nuclei*, 26:399–419.

[Bayes, 1763] Bayes, T. (1763). LII. An essay towards solving a problem in the doctrine of chances. By the late Rev. Mr. Bayes, FRS communicated by Mr. Price, in a letter to John Canton, AMFR S. *Philosophical transactions of the Royal Society of London*, 53:370–418.

[Besançon et al., 2021] Besançon, M. et al. (2021). Distributions.jl: Definition and modeling of probability distributions in the Juliastats ecosystem. *Journal of Statistical Software*, 98(16):1–30.

[Bezanson et al., 2017] Bezanson, J. et al. (2017). Julia: A fresh approach to numerical computing. *SIAM Review*, 59(1):65–98.

[Bloom et al., 1969] Bloom, E. D. et al. (1969). High-energy inelastic $e-p$ scattering at $6^\circ$ and $10^\circ$. *Physical Review Letters*, 23:930–934.

[Breidenbach et al., 1969] Breidenbach, M. et al. (1969). Observed behavior of highly inelastic electron-proton scattering. *Physical Review Letters*, 23:935–939.

[Capstick, 1992] Capstick, S. (1992). Photo- and electroproduction of nonstrange baryon resonances in the relativized quark model. *Physical Review D*, 46:2864–2881.

[Capstick and Roberts, 1998] Capstick, S. and Roberts, W. (1998). Strange decays of nonstrange baryons. *Physical Review D*, 58:074011.

[CBELSA/TAPS et al., 2017] CBELSA/TAPS et al. (2017). Double-polarization observable G in neutral-pion photoproduction off the proton. *The European Physical Journal A*, 53:1–12.

[Chadwick, 1914] Chadwick, J. (1914). The intensity distribution in the magnetic spectrum of $\beta$ particles from radium (B + C). *Verh. Phys. Gesell.*, 16:383–391.

[Chadwick, 1932] Chadwick, J. (1932). The existence of a neutron. *Proceedings of the Royal Society of London. Series A, Containing Papers of a Mathematical and Physical Character*, 136(830):692–708.

[Chew et al., 1957] Chew, G. F. et al. (1957). Relativistic dispersion relation approach to photomeson production. *Phys. Rev.*, 106:1345–1355.

[Chiang and Tabakin, 1997] Chiang, W.-T. and Tabakin, F. (1997). Completeness rules for spin observables in pseudoscalar meson photoproduction. *Physical Review C*, 55(4):2054.

[CMS-Collaboration et al., 2012] CMS-Collaboration et al. (2012). Observation of a new boson at a mass of 125 Gev with the CMS experiment at the LHC. *Physics Letters B*, 716(1):30–61.

[Coleman, 1979] Coleman, S. (1979). The 1979 Nobel Prize in Physics. *Science*, 206(4424):1290–1292.

[Cowan Jr et al., 1956] Cowan Jr, C. L. et al. (1956). Detection of the free neutrino: a confirmation. *Science*, 124(3212):103–104.

[Danisch and Krumbiegel, 2021] Danisch, S. and Krumbiegel, J. (2021). Makie.jl: Flexible high-performance data visualization for Julia. *Journal of Open Source Software*, 6(65):3349.

[Davis et al., 1968] Davis, R. et al. (1968). Search for neutrinos from the sun. *Physical Review Letters*, 20:1205–1209.

[Edwards et al., 2011] Edwards, R. G. et al. (2011). Excited state baryon spectroscopy from lattice QCD. *Physical Review D*, 84:074508.

[Efron, 1992] Efron, B. (1992). Bootstrap methods: another look at the jackknife. In *Breakthroughs in statistics: Methodology and distribution*, pages 569–593. Springer.

[Englert and Brout, 1964] Englert, F. and Brout, R. (1964). Broken symmetry and the mass of gauge vector mesons. *Physical Review Letters*, 13:321–323.

[Esteban et al., 2020] Esteban, I. et al. (2020). The fate of hints: updated global analysis of three-flavor neutrino oscillations. *Journal of High Energy Physics*, 2020(9):1–22.

[Esteban et al., 2024a] Esteban, I. et al. (2024a). Nufit 5.3. www.nu-fit.org.

[Esteban et al., 2024b] Esteban, I. et al. (2024b). Nufit 5.3 included data. http://www.nu-fit.org/sites/default/files/v53.release-notes.pdf.

[Fix and Arenhövel, 2013] Fix, A. and Arenhövel, H. (2013). Truncated partial-wave analysis of a complete experiment for photoproduction of two pseudoscalar mesons on a nucleon. *Physical Review C—Nuclear Physics*, 87(4):045503.

[Fukuda et al., 1998] Fukuda, Y. et al. (1998). Evidence for oscillation of atmospheric neutrinos. *Physical Review Letters*, 81:1562–1567.

[Gell-Mann, 1964] Gell-Mann, M. (1964). A schematic model of baryons and mesons. *Physics Letters*, 8(3):214–215.

[Gelman et al., 2013] Gelman, A. et al. (2013). *Bayesian data analysis*. CRC press.

[Gelman and Rubin, 1992] Gelman, A. and Rubin, D. B. (1992). Inference from iterative simulation using multiple sequences. *Statistical Science*, 7(4):457–472.

[Geyer, 1992] Geyer, C. J. (1992). Practical Markov chain Monte Carlo. *Statistical science*, pages 473–483.

[Geyer, 2005] Geyer, C. J. (2005). Markov chain Monte Carlo lecture notes. https://www.stat.umn.edu/geyer/f05/8931/n1998.pdf.

[Geyer, 2011] Geyer, C. J. (2011). Introduction to Markov chain Monte Carlo. In *Handbook of Markov chain Monte Carlo*. Chapman and Hall/CRC.

[Giunti and Kim, 2007] Giunti, C. and Kim, C. W. (2007). *Fundamentals of neutrino physics and astrophysics*. Oxford university press.

[Goodman and Weare, 2010] Goodman, J. and Weare, J. (2010). Ensemble samplers with affine invariance. *Communications in applied mathematics and computational science*, 5(1):65–80.

[Gottschall et al., 2021] Gottschall, M. et al. (2021). Measurement of the helicity asymmetry E for the reaction $\gamma p \rightarrow \pi^0$. *The European Physical Journal A*, 57:1–22.

[Gross et al., 2023] Gross, F. et al. (2023). 50 years of quantum chromodynamics: Introduction and review. *The European Physical Journal C*, 83(12):1125.

[Halzen and Martin, 2008] Halzen, F. and Martin, A. D. (2008). *Quark & Leptons: An introductory course in modern particle physics*. John Wiley & Sons.

[Higgs, 1964] Higgs, P. W. (1964). Broken symmetries and the masses of gauge bosons. *Physical Review Letters*, 13:508–509.

[Hosaka et al., 2006] Hosaka, J. et al. (2006). Solar neutrino measurements in Super-Kamiokande-I. *Physical Review D*, 73:112001.

[Karl et al., 2022] Karl, C. et al. (2022). Fast and precise model calculation for KATRIN using a neural network. *The European Physical Journal C*, 82(5):439.

[Karl, 2022] Karl, C. R. (2022). *First sub-electronvolt direct neutrino mass measurement with the KATRIN experiment*. PhD thesis, Technische Universität München.

[KATRIN et al., 2022] KATRIN et al. (2022). Direct neutrino-mass measurement with sub-electronvolt sensitivity. *Nature Physics*, 18(2):160–166.

[KATRIN et al., 2024a] KATRIN et al. (2024a). Direct neutrino-mass measurement based on 259 days of KATRIN data.

[KATRIN et al., 2024b] KATRIN et al. (2024b). Measurement of the electric potential and the magnetic field in the shifted analysing plane of the KATRIN experiment. *The European Physical Journal C*, 84(12):1258.

[KATRIN et al., 2025a] KATRIN et al. (2025a). Data of KNM1-5. https://www.katrin.kit.edu/publikationen/KATRIN_data_KNM1-5.json. Accessed: 23.05.2025.

[KATRIN et al., 2025b] KATRIN et al. (2025b). Direct neutrino-mass measurement based on 259 days of KATRIN data. *Science*, 388(6743):180–185.

[KATRIN et al., 2025c] KATRIN et al. (2025c). Model inputs for KNM1-5. https://www.katrin.kit.edu/publikationen/KATRIN_inputs_KNM1-5.json. Accessed: 23.05.2025.

[Kessy et al., 2018] Kessy, A. et al. (2018). Optimal whitening and decorrelation. *The American Statistician*, 72(4):309–314.

[Kiefer, 2012] Kiefer, C. (2012). *Quantum Gravity*. Oxford University Press.

[Kleesiek et al., 2019] Kleesiek, M. et al. (2019). $\beta$-decay spectrum, response function and statistical model for neutrino mass measurements with the KATRIN experiment. *The European Physical Journal C*, 79(3):204.

[Kraus et al., 2005] Kraus, C. et al. (2005). Final results from phase II of the Mainz neutrino mass searchin tritium decay. *The European Physical Journal C-Particles and Fields*, 40(4):447–468.

[Kroenert et al., 2021] Kroenert, P. et al. (2021). Minimal complete sets for two-pseudoscalar-meson photoproduction. *Phys. Rev. C*, 103:014607. https://doi.org/10.1103/PhysRevC.103.014607.

[Kroenert et al., 2024] Kroenert, P. et al. (2024). Truncated partial-wave analysis for $\eta$-photoproduction observables via Bayesian statistics. *Phys. Rev. C*, 109:045206. https://doi.org/10.1103/PhysRevC.109.045206.

[Lokhov et al., 2022] Lokhov, A. et al. (2022). Background reduction at the KATRIN experiment by the shifted analysing plane configuration. *The European Physical Journal C*, 82(3):258.

[Mecking et al., 2003] Mecking, B. et al. (2003). The CEBAF large acceptance spectrometer (CLAS). *Nuclear Instruments and Methods in Physics Research Section A: Accelerators, Spectrometers, Detectors and Associated Equipment*, 503(3):513–553.

[Mogensen et al., 2018] Mogensen, P. K. et al. (2018). Optim: A mathematical optimization package for Julia. *Journal of Open Source Software*, 3(24):615.

[Moravcsik, 1985] Moravcsik, M. J. (1985). Resolving the discrete ambiguities in amplitude determinations. *Journal of Mathematical Physics*, 26(1):211–213.

[Muramatsu et al., 2022] Muramatsu, N. et al. (2022). SPring-8 LEPS2 beamline: A facility to produce a multi-GeV photon beam via laser compton scattering. *Nuclear Instruments and Methods in Physics Research Section A: Accelerators, Spectrometers, Detectors and Associated Equipment*, 1033:166677.

[Nakayama, 2019] Nakayama, K. (2019). Explicit derivation of the completeness condition in pseudoscalar meson photoproduction. *Phys. Rev. C*, 100:035208.

[Navas et al., 2024] Navas, S. et al. (2024). Review of Particle Physics. *Physical Review D*, 110:030001.

[Neal, 2011] Neal, R. M. (2011). MCMC using Hamiltonian dynamics. In *Handbook of Markov chain Monte Carlo*. Chapman and Hall/CRC.

[Otten and Weinheimer, 2008] Otten, E. W. and Weinheimer, C. (2008). Neutrino mass limit from tritium $\beta$ decay. *Reports on Progress in Physics*, 71(8):086201.

[Pauli, 1978] Pauli, W. (1978). Dear radioactive ladies and gentlemen. *Phys. Today*, 31N9:27.

[Povh et al., 1995] Povh, B. et al. (1995). Particles and nuclei. *An introduction to the physical concepts, Berlin and Heidelberg: Springer-Verlag (Italian Translation:(1998), Particelle e nuclei. Un'introduzione ai concetti sici, Torino: Bollati Boringhieri editore).*

[Roberts and Oed, 2005] Roberts, W. and Oed, T. (2005). Polarization observables for two-pion production off the nucleon. *Phys. Rev. C*, 71:055201.

[Rönchen et al., 2022] Rönchen, D. et al. (2022). Light baryon resonances from a coupled-channel study including $K\Sigma$-photoproduction. *The European Physical Journal A*, 58(11):229.

[Rutherford, 2010] Rutherford, E. (2010). Collision of $\alpha$ particles with light atoms. IV. An anomalous effect in nitrogen. *Philosophical Magazine*, 90(sup1):31–37.

[Sandorfi et al., 2011] Sandorfi, A. et al. (2011). Determining pseudoscalar meson photoproduction amplitudes from complete experiments. *Journal of Physics G: Nuclear and Particle Physics*, 38(5):053001.

[Schulz et al., 2021] Schulz, O. et al. (2021). Bat.jl: A Julia-based tool for Bayesian inference. *SN Computer Science*, 2(3):210.

[Schwemmer and Kroenert, 2025] Schwemmer, A. and Kroenert, P. (2025). knm-analysis. https://nuserv.uni-muenster.de:8443/aschwemm/knm-analysis/. Commit SHA: 179ced130af14b4b87d27a4341244f791dd9fd1f.

[Smirnov, 2017] Smirnov, A. (06.03.2017 – 10.03.2017). Bethe forum lecture series on 'neutrinos'. From my personal notetaking.

[Super-Kamiokande-Collaboration, 2023] Super-Kamiokande-Collaboration (2023). Data release: Atmospheric neutrino oscillation analysis with neutron tagging and an expanded fiducial volume in Super-Kamiokande I-V. https://doi.org/10.5281/zenodo.8401262.

[Thiel et al., 2022] Thiel, A. et al. (2022). Light baryon spectroscopy. *Progress in Particle and Nuclear Physics*, 125:103949.

[Thomson, 2013] Thomson, M. (2013). *Modern particle physics*. Cambridge University Press.

[Tiator, 2018] Tiator, L. (2018). The MAID legacy and future. *Few-Body Systems*, 59:1–9.

[Tiator et al., 2017] Tiator, L. et al. (2017). Amplitude reconstruction from complete electroproduction experiments and truncated partial-wave expansions. *Physical Review C*, 96(2):025210.

[Tiator et al., 2018] Tiator, L. et al. (2018). Eta and etaprime photoproduction on the nucleon with the isobar model EtaMAID2018. *The European Physical Journal A*, 54(12):210.

[Vehtari et al., 2021] Vehtari, A. et al. (2021). Rank-normalization, folding, and localization: An improved $\widehat{R}$ for assessing convergence of mcmc (with discussion). *Bayesian Analysis*, 16(2):667 – 718.

[Walcher, 1990] Walcher, T. (1990). The Mainz microtron facility MAMI. *Progress in Particle and Nuclear Physics*, 24:189–203.

[Watanabe, 2010] Watanabe, S. (2010). Asymptotic equivalence of Bayes cross validation and widely applicable information criterion in singular learning theory. *Journal of Machine Learning Research*, 11(116):3571–3594.

[Wester et al., 2024] Wester, T. et al. (2024). Atmospheric neutrino oscillation analysis with neutron tagging and an expanded fiducial volume in Super-Kamiokande I–V. *Physical Review D*, 109(7):072014.

[Wilson, 1974] Wilson, K. G. (1974). Confinement of quarks. *Physical Review D*, 10:2445–2459.

[Workman et al., 2022] Workman, R. L. et al. (2022). Review of Particle Physics. *PTEP*, 2022:083C01.

[Wunderlich, 2021] Wunderlich, Y. (2021). New graphical criterion for the selection of complete sets of polarization observables and its application to single-meson photoproduction as well as electroproduction. *Phys. Rev. C*, 104(4):045203.

[Wunderlich et al., 2017] Wunderlich, Y. et al. (2017). Determining the dominant partial wave contributions from angular distributions of single-and double-polarization observables in pseudoscalar meson photoproduction. *The European Physical Journal A*, 53:1–66.

[Wunderlich et al., 2020] Wunderlich, Y. et al. (2020). Moravcsik's theorem on complete sets of polarization observables reexamined. *Phys. Rev. C*, 102:034605.

[Xu et al., 2020] Xu, K. et al. (2020). Advancedhmc. jl: A robust, modular and efficient implementation of advanced HMC algorithms. In *Symposium on Advances in Approximate Bayesian Inference*, pages 1–10. PMLR.

[Xu, 2025] Xu, W. (2025). kafit-mcmc. https://nuserv.uni-muenster.de:8443/katrin-git/kafit/kafit-mcmc/. Commit SHA: f62a052c081c0a5ba04ce1cf1c4483af0d9e1213.

[Yannick Wunderlich, 2019] Yannick Wunderlich (2019). *The complete experiment problem of pseudoscalar meson photoproduction in a truncated partial wave analysis.* PhD thesis, Rheinische Friedrich-Wilhelms-Universität Bonn.

[Zweig, 1964] Zweig, G. (1964). An SU(3) model for strong interaction symmetry and its breaking. Technical report, CM-P00042884.